ISTANBUL TECHNICAL UNIVERSITY ★ GRADUATE SCHOOL OF SCIENCE ENGINEERING AND TECHNOLOGY

GROWTH AND CHARACTERIZATION OF SOL-GEL DERIVED $CuIn_{1-X}Ga_XSe_2$ (CIGS) THIN-FILMS AND BETA IRRADIATION EFFECT

M.Sc. THESIS

Şengül AKYOL

Department of Metallurgical and Materials Engineering

Material Engineering Programme

MAY 2015

ISTANBUL TECHNICAL UNIVERSITY ★ GRADUATE SCHOOL OF SCIENCE ENGINEERING AND TECHNOLOGY

GROWTH AND CHARACTERIZATION OF SOL-GEL DERIVED $CuIn_{1-X}Ga_XSe_2$ (CIGS) THIN-FILMS AND BETA IRRADIATION EFFECT

M.Sc. THESIS

Şengül AKYOL
(506001226)

Department of Metallurgical and Materials Engineering

Material Engineering Programme

Thesis Advisor: Prof. Dr. Hüseyin ÇİMENOĞLU

MAY 2015

İSTANBUL TEKNİK ÜNİVERSİTESİ ★ FEN BİLİMLERİ ENSTİTÜSÜ

$CuIn_{1-X}Ga_XSe_2$ (CIGS) İNCE FİLMLERİN SOL-JEL TEKNİĞİYLE BÜYÜTÜLMESİ, KARAKTERİZASYONU VE BETA IŞINLARININ ETKİSİNİN İNCELENMESİ

YÜKSEK LİSANS TEZİ

Şengül AKYOL
(506001226)

Metalurji ve Malzeme Mühendisliği Anabilim Dalı

Malzeme Mühendisliği Programı

Tez Danışmanı: Prof. Dr. Hüseyin ÇİMENOĞLU

MAYIS 2015

Şengül Akyol, a **M.Sc.** student of ITU **Graduate School of Science Engineering and Technology** student ID 506001226, successfully defended the **thesis** entitled " **GROWTH AND CHARACTERIZATION OF SOL-GEL DERIVED $CuIn_{1-X}Ga_XSe_2$ (CIGS) THIN-FILMS AND BETA IRRADIATION EFFECT** ", which she prepared after fulfilling the requirements specified in the associated legislations, before the jury whose signatures are below.

Thesis Advisor :	**Prof. Dr. Hüseyin ÇİMENOĞLU** İstanbul Technical University	.....
Co-Advisor :	**Prof. Dr. Nilgün BAYDOĞAN** İstanbul Technical University	.....
Jury Members :	**Prof. Dr. Sakin ZEYTİN** Sakarya University	.....
	Assoc. Prof. Dr. Erdem ATAR Gebze Technical University	.....
	Assoc. Prof. Dr. Murat BAYDOĞAN İstanbul Technical University	.....

Date of Submission : 04 May 2015
Date of Defense : 22 May 2015

For Love and Presence...
To All Member's of My Lovely Family,

FOREWORD

I would like to express my deepest gratitude and thanks to my supervisor, Prof. Dr. Hüseyin ÇİMENOĞLU, Department of Metallurgical and Materials Engineering, for his support and patience with friendly and encouraging attitude. He gave me the opportunity to work in his research group and introduced me to thin-film and solar cell studies. I always feel an admiration about his positive energy, scientific knowledge and creative criticism.

I express my endless sincere thanks to my co-supervisor Prof. Dr. Nilgün Baydoğan, Department of Nuclear Researchers, for her scientific guadience, helpful suggestions, keeping her eyes on me at every steps of the experimental stages, continous support and kind friendship.

I would like to offer my deepest appreciation and sincere gratitude to all academic and administrative staff of the Department of Metallurgy and Material Enginnering, for their precious support and valuable comments during my scientific preparation period. I am also grateful to Prof. Dr. Fatma Tepehan from Physics Dept. It was a great pleasure to have lectures from her class.

I would like to thank to the jury members Prof. Dr. Sakin Zeytin, Assoc. Prof. Dr. Erdem Atar and Assoc. Prof. Dr. Murat Baydoğan for their beneficial criticism on this thesis.

I would also like to present my sincere thanks to Assoc. Prof. Dr. Murat Baydoğan; Assoc. Prof. Dr. Birgül Benli from ITU Mineral Processing Engineering Dept. for her help in AFM analysis; Assoc. Prof. Dr. Mustafa Okutan for his help in sheet resistance measurements and Assoc. Prof. Dr. Süreyya Aydın Yüksel for her help in I-V measurements of p-n junction from Yildiz Technical University Physics Dept.

I would like to thank to my lab-mate, my beloved friend Lecturer Utku Cancı Matur from Gedik University for her cooperation and friendship throughout this study. I am so grateful for her existence in this study.

I am also so much thankful to my beloved friends Burak İzmirlioğlu and Dr. Seniz Türküz from ŞişeCam Science and Technology Center for their help in XRD, SEM/EDS analysis, 4-point probe measurements and for their endless support, assist in all parts of this study. Their valuable patience, encouragement and support led to the completion of this thesis.

It is a pleasure to convey my gratitude to Hüseyin Ateş Parlar from ŞişeCam Science and Technology Center for providing the opportunity to use all the required analysis for the academical studies. I thank also to the laboratory member Oğuzhan Kafalı, for his technical and personal support and friendly behavior.

I wish to thank Research Assistant Faiz Muhaffel, Res. Asst. Onur Tazegül, Res. Asst. Yakup Yürektürk from I.T.U. Metallurgical and Materials Engineering Dept., Res. Asst. Türker Türken from I.T.U. MEM-TEK Laboratory and Res. Asst. Ertuğrul Demir from ITU Energy Institute, to all my lab-mates Gürol Aldıç, Dilek Teker Aydoğan, Tayfun Bel and to my lecture-mates Begüm Vural, Didem Ovalı, Dilek Demiroğlu and all the rest I couldn't mention here for their precious helps, sharing of knowledge and valuable friendship.

My special thanks go to my family for their endless love and encouragement all through my lifetime.
Finally, I am thankful to all my beloved friends Duygu Özdemir, Tülay Tombul, Ümit Arhan Gürel, Elif İbiş Akşit, of whom I have felt all their encouragement support and endless love during this term of my life.
I sincerely acknowledge that this study is financially supported by I.T.U. B.A.P. - Scientific Research Projects–Division under I.T.U. the Graduate School of Natural and Applied Sciences with the project number 37792. I thank to I.T.U. the Graduate School of Natural and Applied Sciences for the support on this study and supporting me to join to Diffusion Solid Liquid Conference 2014. And thanks to all administrative staff of I.T.U. the Graduate School of Natural and Applied Sciences for their patience and help.

May 2015 Şengül AKYOL

TABLE OF CONTENTS

Page

ABBREVIATIONS

a.u.	**:** Arbitrary Unit
at.%	**:** Atomic Percentage
AFM	**:** Atomic Force Microscopy
a.m.u.	**:** Atomic Mass Unit
ATARC	**:** Prof.Adnan Tekin Material Sciences & Production Technologies Applied Research Center
Bq	**:** Becquerel
CIGS	**:** Copper Indium Gallium Diselenium-Cu(In,Ga)Se_2
DEA	**:** Diethanolamine-$(CH_2CH_2OH)_2$
dps	**:** Disintegrations (decay) per second
DTA	**:** Differential Thermal Analysis
EC	**:** Ethyl Cellulose
EDS	**:** Energy Dispersive Spectrometer
FWHM	**:** Full Width Half Maximum
Gy	**:** Gray
IR	**:** Infrared
ITO	**:** Indium Tin Oxide
I.T.U.	**:** Istanbul TeknicalUniversity
JCPDS	**:** Joint Committee for Powder Diffraction Data
MEM-TEK	**:** Prof.Dr. Dinçer Topacık National Research Center on **:** Membrane Technologies
M.E.T.U.	**:** Middle East Technical University
M.I.T.	**:** Massachusetts Institute of Technology
M.Sc.	**:** Master of Science
NIR	**:** Near Infrared
NREL	**:** National Renewable Energy Laboratory
ZnO:Al (AZO)	**:** Aluminium Doped Zinc Oxide
LED	**:** Light Laser Emitting Diode
LET	**:** Linear Energy Transfer
Ph.D.	**:** Doctor of Philosophy
ppm	**:** Parts Per Million
PV	**:** Photovoltaic
R	**:** Roentgen
rad	**:** Radiation absorbed dose
SEM	**:** Scanning Electron Microscopy
Sv	**:** Sieverts
XRD	**:** X-Ray Diffraction
XRF	**:** X-Ray Fluorescence
TCO	**:** Transparent Conductive Oxide
TEOS	**:** Tetraethyl Orthosilicate
TGA	**:** Thermo Gravimetric Analysis
UV/VIS	**:** Ultraviolet/Visible

SYMBOLS

A	**:** Atomic Weight
A	**:** Optical Absorbance (%)
A	**:** Specific Activity at t Time
$\mathbf{A_0}$	**:** Initial Acitivity Value
B	**:** Intensity Equal to Half the Maximum Intensity-FHWD (radian)
c	**:** Light Speed (2.99793×10^8 m.s^{-1})
CdS	**:** Cadmium Sulphur
Ci	**:** Curie (the activity of 1 gram of Radium-226)
$\mathbf{Cu(NO_3)_2 \cdot 3H_2O}$	**:** Copper(II) Nitrate Hydrate
$\mathbf{C_2H_5OH}$	**:** Ethanol
d	**:** Interatomic Distance (nm)
d	**:** Thickness of the Film (cm)
D	**:** Crystallite Size (nm)
$\mathbf{E_b}$	**:** Maximum Energy of Beta Particle
$\mathbf{E_g}$	**:** Optical band gap energy (Transition Energy)
$\mathbf{E_{hv}}$	**:** Bremsstrahlung Radiation Energy
$\mathbf{E_{k1}}$	**:** Energy of Incident Electron
$\mathbf{E_{k2}}$	**:** Decelareted Energy Amount
g	**:** Gravity
$\mathbf{Ga(NO_3)_3 \cdot H_2O}$	**:** Gallium(III) Nitrate Hydrate
h	**:** Planck constant (6.625 x 10-27 erg-sec)
h	**:** Thickness of the Coating
HCl	**:** Hydrochloric Acid
$\mathbf{H_2SO_4}$	**:** Sulfuric Acid
(hkl)	**:** Miller Indexes
I	**:** Current (Amper)
$\mathbf{I_o}$	**:** Initial Intensity of Light
I	**:** Intensity of Light Passing Through
$\mathbf{In(NO_3)_2 \cdot 3H_2O}$	**:** Indium(III) Nitrate Hydrate
k	**:** Extinction Coefficient
$\mathbf{K_2Cr_2O_7}$	**:** Potassium Dichromate
L	**:** Spacing between the contacts
n	**:** Neutron
n	**:** Refractive Index
p	**:** Proton
R	**:** Optical Reflectance (%)
$\mathbf{Ra_{226}}$	**:** Radium-226
$\mathbf{Rn_{222}}$	**:** Radon-222
REM	**:** Roentgen Equivalent Man
$\mathbf{SeO_2}$	**:** Selenium(IV) Oxide
$\mathbf{Sr_{90}}$	**:** Strontium-90 Radioisotope

T	**:** Optical Transmittance (%)
$\mathbf{T_{1/2}}$	**:** Half-life of Radioactive Material
t	**:** Time
u	**:** Speed of Substrate
w	**:** Width of Thin-Film
V	**:** Voltage (V)
$\mathbf{Y_{90}}$	**:** Yttrium-90
Z	**:** Atomic Number
Zr-O-n-propyl	**:** Zirkon-n-propoxid
$\boldsymbol{\alpha}$	**:** Absorption Coefficient (cm^{-1})
Å	**:** Angstrom
$\boldsymbol{\beta^-}$	**:** Negatron (Beta-minus)
$\boldsymbol{\beta^+}$	**:** Positron (Beta-plus)
$\boldsymbol{\gamma_{LV}}$	**:** Liquid-Vapour Surface Tension
$\boldsymbol{\gamma}$	**:** Gamma Ray
$\boldsymbol{\sigma}$	**:** Conductivity (cm^{-1})
$\boldsymbol{\eta}$	**:** Viscosity of Sol
ηˌ	**:** Neutron Particle
$\boldsymbol{\theta_B}$	**:** Diffraction (Bragg) Angle (theta)
$\boldsymbol{\lambda}$	**:** Wavelength (nm)
$\boldsymbol{\lambda}$	**:** Decay Constant
$\boldsymbol{\rho}$	**:** Density of Sol
ρ	**:** Resistivity (Ω-cm)
ν	**:** Frequency
$\boldsymbol{\nu^+}$	**:** Antineutrino
$\boldsymbol{\nu^-_e}$	**:** Neutrino

LIST OF TABLES

Page

LIST OF FIGURES

Page

GROWTH AND CHARACTERIZATION OF SOL-GEL DERIVED $CuIn_{1-X}Ga_XSe_2$ (CIGS) THIN-FILMS AND BETA IRRADIATION EFFECT

SUMMARY

One of the most promising absorber material for the thin-film solar modules is polycrystalline chalcopyrite thin-film solar cell based on Cu(In, Ga)Se_2 (CIGS) by having the direct energy band gap and high absorption coefficient. CIGS compounds have high solar to electricity conversion efficiency, reliability and stability.

Solar cells using CIGS as an absorber block, having a direct band gap within the maximum solar absorption region, a high absorption coefficient (10^5 cm^{-1}) and appropriate electrical and optical properties for production, as has been demonstrated by the ~ 20% conversion efficiency.

Cu(In,Ga)Se_2 (CIGS) thin-films were prepared by economical sol–gel dip coating technique of aqueous solution of $Cu(NO_3)_2 \cdot 3H_2O$, $In(NO_3)_2 \cdot 3H_2O$, $Ga(NO_3)_3 \cdot H_2O$ and SeO_2 onto soda-lime silicate glass substrates. Sol–gel dip coating technique is the most economical way for depositing CIGS thin-films by utilizing a non-vacuum technology and involving cheap equipments and lower temperature.

The optimum optical properties of CIGS thin-films is obtained by varying the film thickness. Beside that, the sol-gel derived CIGS thin-films with determined thickness were thermally treated at different temperatures from 135 °C up to 200 °C with a colloidal solution prepared in an air ambiance under the standard laboratory conditions and in an inert atmosphere. The ultra CIGS thin-films deposited from the colloidal solution prepared under argon gas exhibit quasi-amorphous structure while in air ambiance it was amorphous structure.

Cu(In,Ga)Se_2 thin-films were deposited at different pH-values changing from 1 to 4 by using sol-gel dip coating technique at 150 ^oC annealing temperature, in an air ambiance. The structural, optical and electrical properties were investigated for the different pH-values to determine the optimum pH-value. The optimum optical properties for the use of a potential absorber material depending on its favorable energy band gap (~ 1.6 eV) and optimum electrical conductivity is obtained by controlling the pH-value of the CIGS solution between 1.5-2.0 pH. These results indicate that the CIGS thin-films obtained by sol-gel process can be good candidates for applications in optoelectronic devices.

The effect of ionization radiation on the optical materials is promising in the radiation science and air & space science. The ionized radiation causes changes at the physical and chemical properties with exciting the free carriers and forming the electron-hole pairs. The irradiation effect on the CIGS thin-films is evaluated by determining optical energy band gap of the films exposed to the beta radiation source by using Sr-90 radioisotope. The variations in structural, optical and electrical properties were considered with respect to the absorbed dose level to investigate the characteristic properties of CIGS thin-films. The observed effects in electrical resistivity are attributed to beta irradiation-induced formation of defects in the CIGS thin-film structure. The significant blue shift of absorption edge was improved by

beta irradiation with the reduced elapsed time of colloidal solution and the increased of thickness. The irradiation treatment was conducted by using Sr-90 radioisotopes which played an important role in enhancing electrical properties. The beta irradiation was a key parameter to decrease the electrical resistivity of CIGS thin-film.

$CuIn_{1-X}Ga_XSe_2$ (CIGS) İNCE FİLMLERİN SOL-JEL TEKNİĞİYLE BÜYÜTÜLMESİ, KARAKTERİZASYONU VE BETA IŞINLARININ ETKİSİNİN İNCELENMESİ

ÖZET

Güneş enerjisi, fotovoltaik modüller yardımıyla doğrudan elektrik enerjisine dönüştürülebilmesi ile sınırsız varsayılan, sürekli ve tekrar tekrar kullanılabilen yenilenebilir enerji kaynakları arasında en güçlü ve sonsuz olanıdır. Petrol ve doğalgaz gibi bazı fosil yakıt rezervlerinin giderek azalması, bütün enerji kaynaklarının verimli bir şekilde kullanılmasının önemini hatırlatmaktadır. Dünyamız üzerinde enerji ihtiyacının sürekli artması ama buna müteakip kaynakların gittikçe azalması güneş kaynağını kullanılarak enerji ihtiyacının karşılanabilmesinin yolunu açmış; ucuz ve yüksek verimli güneş pillerinin elde edilmesine yönelik Ar-Ge çalışmalarına ivme kazandırmıştır. Fotovoltaik modüller için, yarıiletken malzemeler kullanılarak üretilen ince filmler, esnek tabanlar üzerine, daha az malzeme ve ucuz yöntemlerle elde edilebilme özelliklerinden ötürü yoğun ve güncel araştırma konuları arasında yer almaktadır. İnce filmlerin fotovoltaik paneller için değişik yöntemler kullanılarak elde edilmesinin de mümkün olması önem arz etmektedir.

Fotovoltaik panellerde kullanılan $CuIn_{1-x}Ga_xSe_2$ (CIGS) ince film katmanı güneş piller ikinci nesil teknolojilerde ulaşılmış en yüksek laboratuvar verimine sahip olması nedeniyle son yıllarda üzerinde pek çok çalışmaların yapılmasına neden olmuştur. $Cu(In,Ga)Se_2$ ya da bir başka deyişle Bakır İndiyum Galyum DiSelenür, polikristalin yapıda fotovoltaik etkisinin iyi bir şekilde gözlenebildiği bir yarıiletkendir. Ulusal Yenilenebilir Enerji Laboratuvarlarında (NREL) üretilen ve ölçümlerinin de burada yapıldığı CIGS güneş pillerinden elde edilen %19,6 verimlilik birinci nesil teknolojilerden GaAs güneş pillerinden sağlanan %27,6 verimlilikle mukayese edilebilir niteliktedir. Yüksek verim özelliğinin yanı sıra esnek yüzeylere uygulanabilmesi nedeni ile giysilerde ya da çatılarda kullanılabilmektedir.

İsviçre'deki Empa Laboratuvarı'nda 2013 yılında esnek polimer yüzey üzerine ince film CIGS güneş hücreleri yerleştirerek, enerji dönüşümü verimliliğinde %20,4 gibi yüksek bir değere ulaşılmıştır.

Kalkopirit kristal yapıdaki CIGS ince filmler direkt bant aralığına sahip p-tipi yarıiletkenlerdir ve (1,0-1,7 eV) bant aralığı değerlerinde, oldukça yüksek soğurma katsayısı (10^5 cm^{-1}) ile güneş pili üretiminde soğurucu katman olarak hayli popüler bir güneş gözesi teknolojisi haline gelmiştir.

$CuIn_{1-x}Ga_xSe_2$ (CIGS) ince filmler, bu tez kapsamında sol-jel daldırma yöntemi ile enerji tasarrufu sağlanarak ekonomik bir şekilde üretilebilmiştir. Bu yöntem sayesinde diğer yöntemlerde ihtiyaç gösteren yüksek maliyetli cihazlara gereksinim duyulmamıştır. Sol-jel daldırma tekniğiyle üretilen nanopartiküler yapının fiziksel özelliklerinin kontrolü, hazırlanan koloidal solüsyonun konsantrasyonunun atomik düzeydeki kontrolüyle elde edilebilmektedir.

Bu çalışmayla, $CuIn_{1-x}Ga_xSe_2$ (CIGS) yarıiletken ince filmlerin sol-jel daldırma teknikleri kullanılarak elde edilmesi, üretilen filmlerin karakterize edilerek güneş pili yapılarına uyumluluğu incelenmiştir. Taşıyıcı yüzeyler üzerinde nitelikli filmlerin ekonomik bir şekilde üretiminin mümkün olması amaçlanmıştır.

CIGS kolloidal çözelti için bakır(II) nitrat hidrat (Aldrich, $Cu(NO_3)_2 \cdot 3H_2O$; 99.999%), indiyum(III) nitrat hidrat (Aldrich, $In(NO_3)_2 \cdot 3H_2O$; 99.9%), galyum(III) nitrat hidrat (Aldrich, $Ga(NO_3)_3 \cdot H_2O$; 99.9%) ve selenyum(IV) oksit (Merck Millipore, SeO_2; 99.999%) 60 ml' lik etanol içinde 1:0,7:0,3:2 oranında çözdürülerek ve uygun miktarlarda dietanolamin, terpineol, etil selüloz dahil edilerek hazırlanmıştır. CIGS solüsyonu, laboratuvar ortam koşullarında ve de inert ortamda argon gazı altında üretilmiştir. Ultrasonik banyoda temizlenmiş soda-kireç cam altlıkları hazırlanan CIGS kolloidal solüsyona daldırılıp 5 saniye solüsyon içinde bekletildikten sonra 1 $mm.s^{-1}$ hız oranıyla çekilmiştir. Kaplanan CIGS ince film 100 °C sıcaklıkta 10 dakika bekletilerek kurutulmuştur. 3 ila 11 arasında değişen farklı kaplama sayılarında çekilen numuneler fırın hava ortamında 135 °C ila 200 °C arasında değişen farklı tavlama sıcaklıklarında 30 dakika süreyle tavlanmıştır.

Üretilmis CIGS filmlerin yapısal özellikleri X-ışınları kırınım cihazı (XRD) kullanılarak; yüzey morfolojisi Atomik Kuvvet Mikroskobu (AFM), kimyasal analizi ise Taramalı Elektron Mikroskobu (SEM/EDS) ve X-Işını Floresans Spektrometresi (XRF) kullanılarak incelenmiştir. Kaplama kalınlığı yüzey profilometre cihazıyla belirlenmiş. 3 kat kaplanmış CIGS ince filmin 80±5 nm kalınlık değeri saptanmıştır. Farklı kaplama kalınlıklarında üretilen numunelerin yüzey görüntüleri Taramalı Elektron Mikroskobu (SEM) kullanılarak nano-yapıların morfolojisi ve film-porozitesi incelenmiştir. Filmlerin optik karakterizasyonu için [190,1100] nm dalga boyu aralığında R (yansıtma) ve T (geçirme) ölçümleri gerçekleştirilmiştir. Elektriksel özelliklerinin değerlendirilmesinde 4 nokta prob sistemi kullanılmıştır. DTA ve TGA analizleri ile CIGS ince filmi oluşturmak için yapılan ısıl işlemin 150 °C ile 200 °C arası olması gerektiği tespit edilmiştir.

CIGS ince filmlerin karakterizasyonu üretim parametreleri değiştirilerek yapısal, optik ve elektriksel özellikleri incelenmiş ve en ideal üretim parametreleri oluşturulmuştur. Tez kapsamına dahil edilen parametreler ise ısıl işlem sıcaklığı, film kalınlığı, kullanılan koloidal çözeltinin pH değeri şeklindedir. Farklı sürelerde yaşlandırılmış koloidal solüsyonlara ve farklı kalınlıklardaki ince filmlere beta parçacık etkisi ise ayrıca incelenmiştir.

Laboratuvar ortam şartlarında hazırlanan CIGS solünün 1 ila 4 pH aralığındaki farklı pH değerlerinin film üzerindeki etkisi incelendiğinde optimum bir pH değerinin sağlanmasının gerekliliği ortaya çıkmıştır. CIGS ince film katmanının güneş pillerinde soğurucu tabaka olarak tüm güneş spektrumunu soğurması istendiğinden 1,24-1,60 eV enerji bant aralığını sağlayan 1,5-2,0 pH değerleri optimum değer olarak belirlenmiştir. Ultra ince CIGS filmin, çok ince bir katman oluşturması sebebiyle yapısal özelliklerin ölçümlerinde net bilgi sağlanamamıştır. X-Işınları Kırınım desenleri mukayeseli olarak incelendiğinde 2 pH değerinde amorf yapıdan yarı-amorf yapıya dönüşüm gözlenmiştir. CIGS ince filmlerin elektriksel özellikleri dikkate alındığında $8{,}69x10^2$ $(\Omega\text{-cm})^{-1}$ iletkenlik değeri 2 pH değerinde sağlanmıştır. Üretilen koloidal solüsyonun sahip olması gereken pH değerinin optimum aralığının 1,5 ila 2,0 pH arasında olduğu tespit edilmiştir.

Tavlama sıcaklığı etkisinin incelenmesinde laboratuvar ortam koşullarında ve argon ortamında iki farklı solüsyon hazırlanmıştır. İnert ortamda elde edilen solüsyondan üretilen ince filmler yarı-amorf yapı özelliği göstermiş, buna karşın oda koşullarında üretilen ince filmler ise daha amorf yapıda olduğu tespit edilmiştir. Oda koşullarında

havada bulunan oksijenin yapıya tutunması kristal yapıyı önemli ölçüde etkilemiş olduğu söylenebilir.
Kalınlığı ~ 60 nm olan çok ince filmlerin, klasik soğurucu ince film katmanlarının kalınlıklarıyla mukayese edildiğinde, ki bu kalınlık değeri mikron düzeyindedir, çok ince bir filmden bahsedilmektedir. Çok ince CIGS filmlerin X-Işınları Kırınım deseni temel amorf yapı sonucunun elde edildiği çok ince filmlere benzemektedir. Yarı-amorf yapı ultra ince CIGS filmleri 80±5 nm kalınlıkta çok ince filmlerde gözlenebilmiştir.
Filmlerin enerji bant aralığı UV-VIS spektrofotometresi kullanılarak yaklaşık 1,50-1,75 eV aralığında bulunmuştur.
İyonizan radyasyon, optik malzemeler üzerinde serbest taşıyıcıları uyarmak suretiyle elektron-boşluk çiftlerini oluşturarak fiziksel ve kimyasal özelliklerin değişimine neden olmaktadır. Sol-jel tekniğiyle üretilmiş CIGS ince filmlerin fiziksel özellikleri beta radyasyonuna maruz bırakıldıktan sonra incelenmiştir. Beta radyasyon etkisinin incelenmesinde beta radyasyon kaynağı olarak Stronsiyum-90 (Sr-90) radyoizotopu kullanılmıştır. Farklı yaşlandırma sürelerinde üretilen solüsyonlardan elde edilmiş ve farklı kalınlıklarda kaplanmış ince filmlerin artan radyasyon soğurma dozlarındaki etkileri incelenmiştir. Beta parçacıklarına maruz bırakılmadan önce ve bırakıldıktan sonra X-Işınları Kırınım yöntemi kullanılarak çekilen görüntüler farklı kalınlıklarda üretilen ince filmlerin yarı-amorf yapıda olduğunu doğrulamıştır. Debye-Sherrer formülü kullanılarak hesaplanan kristal boyutları mukayese edildiğinde; beta radyasyonun kristal boyutlarının küçülmesine neden olduğu tespit edilmiştir. Büyük tane boyutları, tane sınırlarında olabilecek saçılmaları azaltması nedeniyle elektriksel iletkenliğinde iyileşme sağlamaktadır. Farklı kalınlıklardaki ince filmlerin beta radyasyon etkisinden önceki ve sonraki 4-nokta prob cihazıyla dirençleri ölçülerek, iletkenlikleri hesaplandığında ise iletkenliğin arttığı görülmüştür. Kristal boyutlar, beta radyasyon etkisinden sonra küçülmüş olmasına rağmen iletkenlik artmıştır. 11 kat kaplanmış beta ışınına maruz bırakılmış CIGS ince filmin iletkenlik değeri 21.897×10^{3} $(\Omega\text{-cm})^{-1}$ olarak hesaplanmıştır. Kristal boyut küçülmesine rağmen iletkenlik artışının nedeni ise yapılan EDS analizleriyle doğrulanabilmiştir. Bakır (Cu) miktarınında doğru orantılı olarak artışı Sr-90 radyoizotopundan yayımlanan beta negatif parçacıkların CIGS ince filmde Cu-kaynaklı hatalar (Cu-related defects) oluşturarak efektif alıcı yoğunluğunu (acceptor density) artırmıştır. Negatif yüklü parçacıklar Frenkel-çiftlerini oluşturarak elektrik direncini düşürmüştür.

1. INTRODUCTION

1.1 Solar Cell

Solar energy plays a significant role in the future energy demands [1], which is the major part of the renewable energy. Renewable energy is continuous, again and again usable and assumed as endless natural resources [2]. The definitive source of green, clean and renewable energy is obtained by the photovoltaics. Photovoltaic (PV) system is a method of converting solar energy into electrical energy by using semiconductors. To accelerate the usage of solar energy, the main issue is to develope the cost-effective and environmentally friendly alternative. However, today's technologies use relatively rare and expensive semiconductors [3].

For the past 30 years, the PV Technology's dominant material is based on crystalline silicon [4]. PV solar industry has two main production routes; one is crystalline silicon technology, which includes monocrystalline silicon and polycrystalline silicon solar technology; another is the alternative PV technologies like the thin-film technologies, called as second generation. Even though silicon is a highly abundant material (Figure 1.1), the purifying and crystallization processes require intensive energy consumption; consist of many complex stages [1,5]. The fabricating methods emit for every ton of silicon some 10 tons of CO_2 and at the purifying stage moreover 45 tons of CO_2 as well as some other toxic gases [5].

The contradiction is that such an environmentally destroying process of 95% of the produced silicon serves for the PV industry, which is benefit of a clean and sustainable energy source [5].

Among the alternative PV technologies, one of the most dominant and potential one is Copper Indium Gallium Diselenium (CIGS) semiconductor thin-film solar technology. CIGS thin-films have been studied extensively for solar energy conversion applications [6], these studies increased more in recent years. On the other hand, it signifies insufficient production of CIGS solar cells [7].

This thesis contributes to the field of CIGS thin-films production with the sol-gel method to reduce the production cost and to control the chemical composition on the surface of films in atomic scale. The sol-gel derived CIGS thin-film uses less materials and is produced by cheaper processing methods to reduce the cost-price of solar energy.

Producing those materials into the solar cell devices is one another important topic. Solar cells are consisting of semiconductor materials for transforming solar radiation into electrical energy [8]. The principle of these devices is based on absorbing photons from the solar energy and releasing the electrons that can be channeled into an electrical current. This effect is known as photovoltaic effect. In two main steps the process runs, which are releasing free electrons, called generation step, and then falling of these electrons into its original position, called recombination [3].

Solar cell industry is rapidly growing in Europe and America by 20% a year [Url-1]. Solar cell using thin-film PV technologies is showing efficiency between 18-20%. Table 1.1 presents the solar conversion efficiency by any single-junction photovoltaic device [9]. The III-V PV technology results in the highest conversion efficiencies. A 27.6% efficiency of III-V cells of Ga-As thin-films has been taken at the National Renewable Energy Laboratory (NREL) for a $1cm^2$ thin-film GaAs device produced by Alta Devices, Inc. [9]. III-V materials are mainly used in space applications and in concentrator systems [10]. Copper– Indium–Gallium–Diselenium (CIGS) solar cell fabricated by and measured at NREL has showed the efficiency improvement to 19.6% for a 1-cm2 single-junction [9]. Higher than this efficiency has been reported as 20% and higher for less than $1cm^2$ in area application [9].

Table 1.1 : The conversion efficiency (%) of solar cells and submodules.

Classification	Efficiency (%)
Silicon	
Si (crystalline)	25.0 ± 0.5
Si (multicrystalline)	20.4 ± 0.5
Si (thin-film transfer)	16.7 ± 0.4
Si (thin-film submodule)	10.5 ± 0.3
III-V cells	
GaAs (thin-film)	27.6 ± 0.8
GaAs (multicrystalline)	18.4 ± 0.5
InP (crystalline)	22.1 ± 0.7
Thin-film chalcogenide	
CIGS (cell)	19.6 ± 0.6
CIGS (submodule)	16.7 ± 0.4
CdTe (cell)	16.7 ± 0.5
Amorphous/nanocrystalline Si	
Si (amorphous)	10.1 ± 0.3
Si (nanocrystalline)	10.1 ± 0.2
Photochemical	
Dye sensitied	10.4 ± 0.3
Dye sensitied (submodule)	9.9 ± 0.4
Organic	
Organic thin-film	10.0 ± 0.3
Organic (submodule)	4.2 ± 0.2

1.2 CIGS Thin-Films

CIGS thin-films are I-III-VI_2 chalcopyrite semiconductor materials, which have high absorption coefficient, low mass and flexibility [11]. CIGS stands for Copper Indium Gallium Diselenium and formulated as Cu(In,Ga)Se_2. The first investigations of the chalcopyrite solar cell have started 35 years ago [12]. Chalcopyrite-based solar cells are one of the leading technologies for solar energy generators being champions in terms of efficiency (which is about 20%) among thin-film devices [Url-1]. Chalcopyrites enclose wide range of energy band gap energies -from 3.5 eV ($CuAlS_2$) to 1.04 eV ($CuInSe_2$)- which makes these compounds as promising candidates for LEDs and detectors in wide wavelength range [13]. The compounds of the chalcopyrite structures such as $CuInSe_2$, $CuGaSe_2$, Cu(In,Ga)Se_2 have exhibited good photovoltaic properties among the other ternary compounds [12]. In the solar cell production using this as an absorber layer has attracted much attention last couple of years. For this reason, studies on CIGS solar cells continue to increase in recent years and subject to active research all over the world.

$Cu(In,Ga)Se_2$ (CIGS) exhibits the highest efficiency among all materials for the use of thin-film in solar cells [14]. Chalcopyrite $Cu(In,Ga)Se_2$ (CIGS) compound is a direct band gap p-type semiconductor material used as an absorber layer in the solar cells [15], which has a light absorption coefficient higher than 10^5 cm^{-1} [16].

Nowadays, there is a significant lack in the production of CIGS solar cells. There are various methods to growth CIGS thin-films which are electrodeposited stacked elemental layer, rapid thermal processing, coatings of Nano-particles precursor layer (non-vacuum), selenization with H_2Se, magnetron sputtering in Se atmosphere, screen printing of nanoparticles, co-evaporation and doctor-blade [17,18]. The main method that use for deposition CIGS is conventional vacuum-based processes [19,20]. Each of the evaporation deposition, the sputtering deposition, and electrochemical deposition involves a vacuum processing which needs expensive equipment investment [7]. The sol-gel method is the most economical way for depositing CIGS thin-films with a non-vacuum technology, involves cheap equipment. This study contributes to the field of the physical properties of CIGS thin-films produced by the sol-gel method to reduce the cost of the production and to control the chemical composition on the surface of the thin-films in atomic scale [11]. Sol-gel method is one of the best candidates for producing CIGS thin-films for the solar modules economically [21].

To investigate the possibility of the production of CIGS understanding the resources of each element on the earth crust is also important. Figure 1.1 shows the relative abundance of the chemical elements in earth's upper continental crust, atoms of element per 10^6 atoms of Si versus to Atomic number. The elements written in black bold characters are major industrial metals Fe, Al, Mg, Mn, Ti, Cr, Cu, Zn, Ni, Mo, Sn, Pb, W; precious metals are Au, Ag, Pt, Ir, Os, Ru, Rh, Pd; rare earth elements are Lanthanides group, including Y and Sc given in red. The challenge in the CIGS technology is that it includes the element Indium. In Figure 1.1, the red line is a limit level for the critical abundance of a source material that can be used for large-scale production. As can be seen in this diagram Indium is close to the rare element area and not a very abundant element. Indium might be the limiting step for the future CIGS PV technology. Consequently, one alternative to replace the CIGS absorber layer is Copper Zinc Tin Sulfide (CZTS), which is based on non-toxic and

abundantly available elements. The current record efficiency of CZTS solar cells on lab-scale is around 11% [22,23,24].

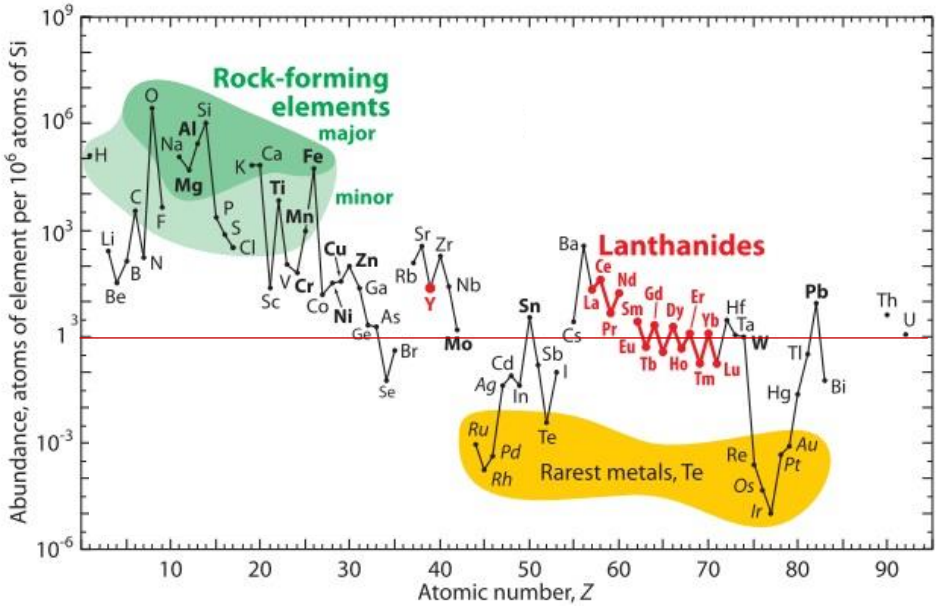

Figure 1.1 : Relative abundance of the chemical elements in earth's upper continental crust [25]

1.3 Thesis Statement

This study investigates the formation process of the compound $Cu(In,Ga)Se_2$ via sol-gel method. Crystallographic, morphological, optical and electrical properties of the films were characterized.

The aim of this study is to make a contribution for the improvement of the cost-effective method by using a sol-gel deposition technique and investigate the properties for the usage of solar cell devices.

This study contributes to determine the production parameters by analyzing the effect of production parameters and beta irradiation effect on the structural, optical and electrical properties of sol-gel derived CIGS thin-films.

1.4 Thesis Outline

This thesis covers the growth and characterization of the $CuIn_{1-x}Ga_xSe_2$ (CIGS) absorber layer for the solar cell structures and the effect of beta irradiation. Chapter 1 introduces the solar cell, PV technology and CIGS thin-film. The theoretical consideration is summarized into four sections. Chapter 2 describes some theoretical

items. The semiconductors and how the solar cell works; crystal structure of the I–III–VI_2 thin-film and CIGS; sol-gel technique and radiation theory were briefly presented for understanding the principle behind the thesis. Brief information on the physical principle of semiconductor materials and how the semiconductor materials are used in devices to directly convert solar light into electricity (photovoltaic devices) is introduced.

The experimental technique details and the growth of sol-gel derived CIGS thin-film absorber for solar cell applications are described in Chapter 3. The CIGS sol was produced via sol-gel technique in an air ambiance under the standard laboratory conditions and under the inert gas atmosphere. The characterization of Sol and the characterization techniques are introduced, as well as the beta irradiation process.

Chapter 4 illustrates results of the characterization of the CIGS thin-film. The results are summarized under different parameters' effect. The pH-value of sol, the production parameters such as annealing temperature, number of coating layers and beta irradiation effects are investigated by considering the structural, optical and electrical properties. The surface of absorber layers by AFM and SEM supported with EDS and the structural properties with the aid of XRD technique are investigated. The optical properties of $Cu(In,Ga)Se_2$ absorber layer by means of absorption, reflectance, and transmission employing UV-VIS Spectrophotometer and the electrical properties by using 4-point resistivity probe to figure out the conductivity were examined. The techniques contribute to determine absorber layer of CIGS thin-film for solar cell devices, are the main tools to assess the quality of the thin-film.

2. THEORETICAL CONSIDERATIONS

2.1 Physics of Solar Cell

2.1.1 Semiconductors

Materials can be classified in terms of their electrical properties. Metals conduct electricity very well [26]. The high conductivity of the metals is depended on the weakly bounded outer electrons of the atoms in a metal which form the free mobile electrons ocean [27]. As electrons are negatively charged, the conduction in a metal is based on mobile negative charge. In Figure 2.1, the free mobile electrons are showed with the red dots which move around core of the atom referred to the blue circle. The core can be considered as positively charged ion as the atom gives away the valence electrons. Materials which do not conduct electricity are called insulators [28]. The electrons of the insulator materials are bounded to the core of the atom. There is no free mobile electrons ocean [29]. In the Figure 2.1, the red dots representing the electrons are adhered to the blue circles indicating the core of the atoms.

Semiconductor materials can be defined simply by their conductivity range between that of a metal and an insulator [30]. The valence –outer- electrons of the atoms are less weakly bounded to the core of the atoms than in insulators and more strongly bounded to the core of the atoms than in metals. Some certain conditions can cause them to become freely mobile electrons and leave the core of the atoms. These donated electrons create positively charged core. This positively charged core is called a hole which is represented by the small blue dots (Figure 2.1). These holes can move like electrons easily. Negatively charged electrons and positively charged holes are the transported charges in the semiconductor materials [31].

Electronic band structure of metals, insulators and semiconductors can be explained briefly at Figure 2.1 [27]. The potential energy levels that an electron could occupy in the material defines the electronic band. Metals have a wide electronic band corresponding to the energy levels in which the electrons can freely move. Contrary

to the metals, insulators and semiconductors have two different bands -valence band and conduction band- separated with a large gap called energy band gap or forbidden energy band gap [31]. Valence band is the lower electronic band filled with most of the electrons. The upper electronic band is the conduction band where electrons are mobile and move freely. In the gap there is no energy state. The difference between insulators and semiconductors is that the energy band gap of an insulator is much larger than the energy band gap of a semiconductor, 3 eV energy level can be defined as a limit for the semiconductors [28]. The larger the forbidden gap, the smaller the probability that an electron can have enough energy to occupy a state in the conduction band [31].

In semiconductor, the energy from light can be big enough to excite some electrons from the valence band to the conduction band. if the photon has an energy equal or larger than the energy band gap, semiconductor can be more conductive. While electrons in the valence band are bonded to their core atoms, the positively charged holes can diffuse through the valence band, just like the electrons in the conduction band [31]. The conductivity properties are determined by the electrons in the conduction band and the holes in the valence band.

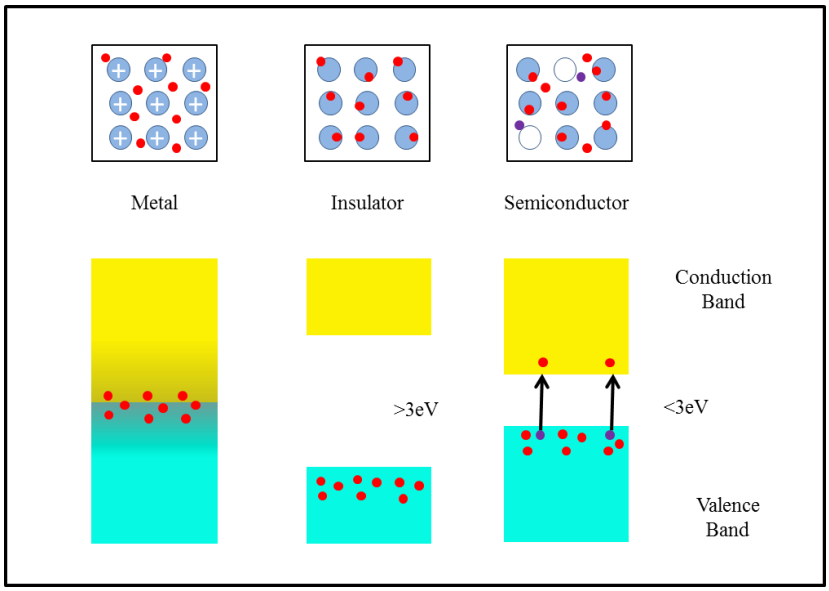

Figure 2.1 : Materials' categorization with energy band level.

Energy band gap (Pauli' s exclusion)

What is the principle of an energy band gap? How do electrons bond in an atom? The most simple atom in our universe is the hydrogen atom. The hydrogen atom has a positively charged proton in the nucleus and around this proton, the much lighter

negatively charged electron is moving in orbits [31]. This system can be described by laws of quantum mechanics, with Schrödinger Equation. Quantum mechanics and the Schrödinger equation tell that in the hydrogen atom the electron can only occupy certain energy level. The lowest energy position close to the nucleus is the ground state known as first electron shell indicated by 1s and the electron is strongly bound to the proton in an orbit. More energy excites the electron to a higher energy level, to the second shell in which the electron is less strongly bound to the atom and its averaged orbit is further away from the nucleus. In the second shell two types of electronic energy levels are found, 2s and 2p. If even more energy is given, it can be excited to the upper shell [31].

The important property of the electron is that electrons can have spins. The important law in quantum mechanics is Pauli's Exclusion Principle [6]. Electrons have spins. Spin can be explained briefly a charged body in classical electrodynamics, like the spheres in Figure 2.2.

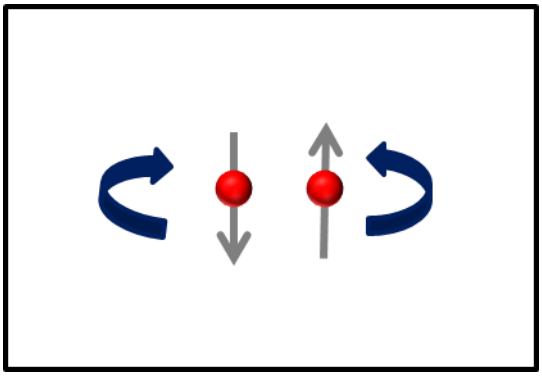

Figure 2.2 : Illustration of electrons' spins in classical electrodynamics.

When these bodies rotate, the rotation of the charge will induce a magnetic dipole. Depending on the rotation clockwise or counter-clockwise, the magnetic dipole will point up or will point down. This means that an electron can be in two different quantum states: spin up (magnetic dipole pointing up) and spin down (magnetic dipole pointing down) [31]. The Pauli Exclusion Principle tells us that two identical electrons can not occupy the same quantum state simultaneously [32]. Basically, Pauli's exclusion principle allows every electronic energy level to be filled by at maximum two electrons [31].

Energy band gap of materials can be classified as direct energy band gap and indirect energy band gap. The momentum of electrons and holes at valence and conduction bands are equal to each other for a direct energy band gap. In the direct transition

event, the energy of photon excites the electrons and it moves from valence band to conduction band easily. The highest energy level in the valence band is vertically aligned with the lowest energy in the conduction band. It means that only transfer of energy is required to excite an electron from the valence to the conduction band. No transfer of momentum is required [27,30].

Indirect energy band gap term is defined as the energy band gap when the momentum of the electrons and holes at valence and conduction bands are not equal to each other. In the indirect transition event, the enery of photon is not sufficient for excitation of electron. In addition to a photon, additional energy corresponding to the difference in the momentum of the valence band electrons and holes is also necessary to excite valence band electrons of indirect energy band gap material. Photon and momentum are exist and simultaneously absorbed by the electron. For indirect transition, the maximum of valence band and minimum of conduction band do not take place at the same wave vector [27,30]. Therefore, during the excitation of electrons, momentum and energy have to be conserved. These conditions are satisfied by absorption or emission of phonon for indirect band transitions. The absorption coefficient for indirect transition involves phonon absorption and emission. Crystal lattice energy can be the source of this momentum change. A phonon is described as the vibration energy of atoms in the crystal. Absorption or emission of phonons can cause the momentum change which is needed for the excitaton of the electron in an indirect band structure [33]. Direct and indirect energy band gap structures are depicted in Figure 2.3.

The photovoltaic conversion process occurs with the incident photons. If the photons' energy is larger than the energy band gap energy, the electrons are excited from the valence band into the empty states of the conduction band. The photon energy is $h\nu$ whereas the ν is the frequency of the incident light [34].

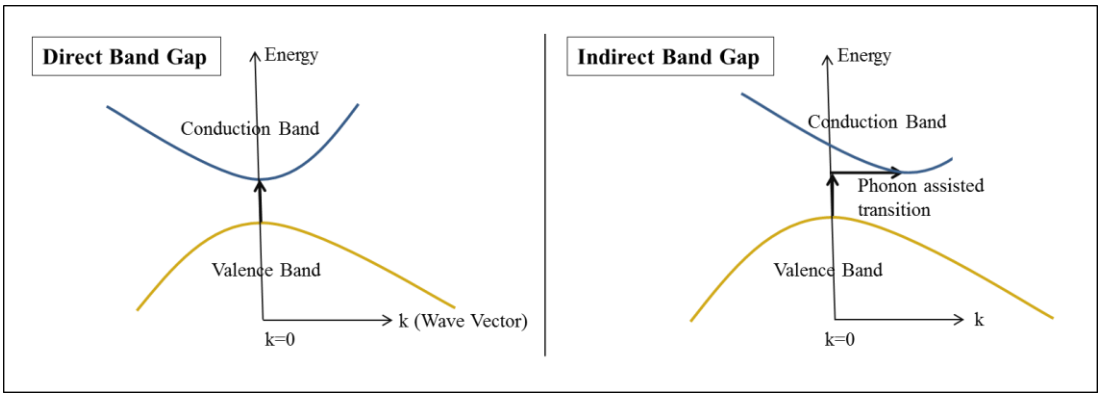

Figure 2.3 : Schematic diagram of direct and indirect transition.

Semiconductors can be generally classified as Intrinsic or extrinsic semiconductors. Intrinsic semiconductors are named for the undoped semiconductors like silicon. Extrinsic semiconductors are the doped semiconductors with two different types; n-type and p-type [35]. In the n-type semiconductors electrons are the majority charge carriers and the doping atoms that give away an electron are set positive charge in the network. In a p-type semiconductors holes are the majority charge carriers and the doping atoms that take an electron are set negative charges in the network. On the p-type semiconductor, the fermi level is closer to the valence band than to the conduction band. The Fermi level of n-type semiconductor material is closer to the conduction band. When these n-type and p-type semiconductor materials touch each other, this is called a p-n junction. The charge carriers is distributed over the p-region and the n-region; On the n-type semiconductor a majority of holes, on p-region a majority of electrons exist. The p-n junction has an enormous density gradient close to the interface between the p- and n-region. The hole density is much lower in the n-region than in the p-region, whereas the electron density is much lower in the p-region than the n-region [27,31].

Si, Ge, InSb, GaAs, SiC semiconductors can be given as an example for Intrinsic semiconductors. Intrinsic semiconductors possess low conductivity at room temperature and they do not have any charge carriers at the temperature of absolute zero, resulting to behave as an insulator. Their valence band is completely filled with electrons and the conduction band is empty. If a valence band electron is excited, it leaves an unoccupied state in the valence band and promotes to the conduction band. This unoccupied state is called as a hole.There is a corresponding empty state in the valence band for each of the electrons in the conduction band in Intrinsic semiconductors, thus electron and hole concentration are equal to each other [36,37].

2.2 Material Properties (Thin-Films)

2.2.1 Chalcopyrite structure (I-III-VI_2 group)

I-III-VI_2 (I=Cu, Ag, III=In, Ga, VI=S, Se, Te) ternary compounds have attracted much attention due to their interesting optical and electrical properties. These types of compounds are the ternary analogue of the II-VI binary compounds having a structure called zincblende as illustrated in Figure 2.4a [38]. The crystallization of I-III-VI_2 materials occurs with a structure called chalcopyrite, which is a super lattice of Zinc-blende II-VI compounds structure (Figure 2.4b) [39].

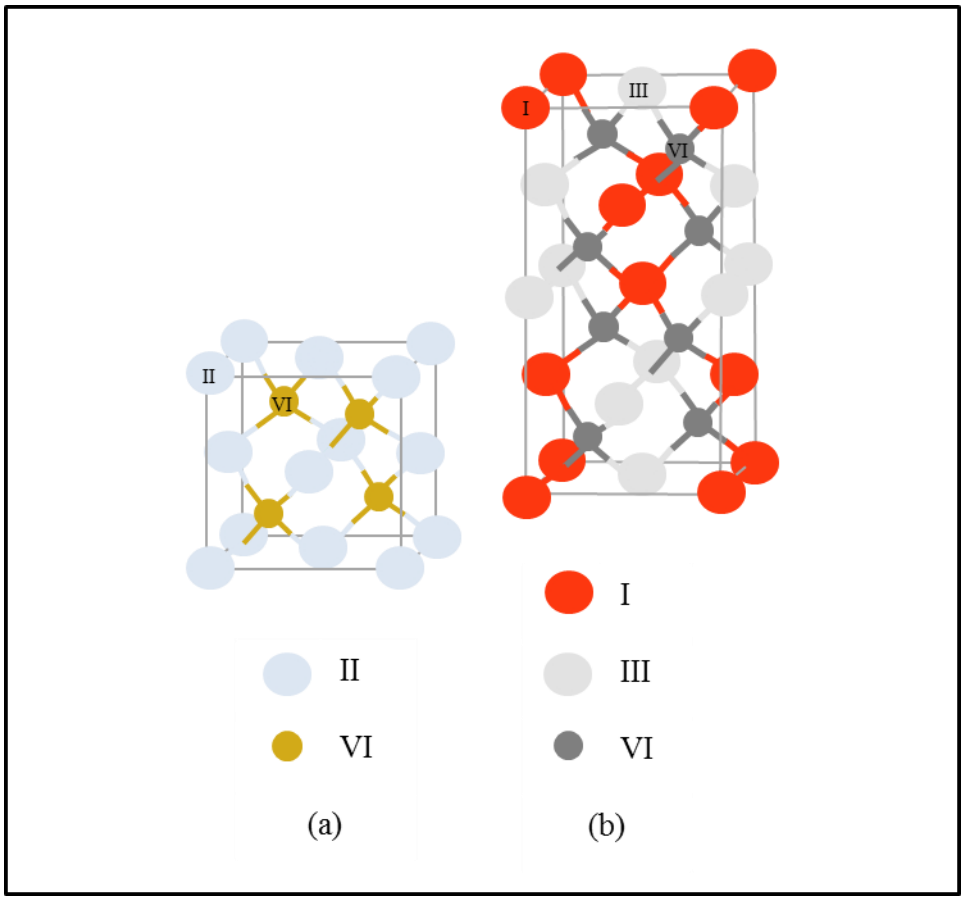

Figure 2.4 : Unit cell crystal structure of (a) Zinc-blende and (b) Chalcopyrite.

As can be seen from the unit cell in Figure 2.4 (b), I-III-VI_2 semiconductors crystallize in the tetragonal structure ($a = b \neq c,\ \alpha = \beta = \gamma = 90°$) and space group symmetry I(-4)2d with four formula units in each unit cell, which is constructed by doubling the unit cell of the zinc-blende in vertical direction [40]. The c/a ratio for the most of chalcopyrite compounds may differ. It is defined two for the ideal chalcopyrite structure [13]. The zincblende structure is supperlattice but still it is important to consider some deviations relative to binary analogues called anomalies

which determines structural and optical properties of chalcopyrite materials [13]. For example; when an anion (II) deflects from its ideal position, it may effect on the energy band gap of such types of compounds. Consequently cause a variation in degree of hybridization between anion and cation orbitals. In the Figure 2.4a, in zinc-blende structure each cation (VI) has bounds with four anions (II), whereas each anion coordinates with two different cations and each cation with four anions in chalcopyrite structure (Figure 2.4b) [13,41-42].

Generally, chalcopyrite ternary compounds are defined in two different groups, copper (Cu-III-VI_2) and silver (Ag-III-VI_2) based compounds.

Cu-based chalcopyrites are the most promising materials for photovoltaic applications [43]. For the light-emitting devices (LEDs) and detectors in wide wavelength range varying from ultraviolet to infrared, these compounds are potential candidates which tune the energy band gap energies (ranging from 3.5 eV ($CuAlS_2$) to 1.04 eV ($CuInSe_2$)) [13,44]. With a control of the different dopants these properties can be extended [40]. As the structural likeness between I-III-VI_2 and II-VI compounds was explained briefly with Figure 2.4, it is obvious that these two different groups semiconductors form p-n heterojunction with high-efficient solar cell devices [39].

One of its unique features is super high tolerance to any radiation. Compare to amorphous silicon solar cells in space their life-time is at least 50 times more [Url-1]. “In fact, irradiation with quite high doses of MeV protons and electrons improves their performance. It seems the material repairs itself at room temperature” [Url-1].

2.2.2 CIGS thin-films

Among the Cu-based materials, the ternary compounds $CuGaSe_2$, $CuInS_2$, $CuInSe_2$ and $Cu(In,Ga)Se_2$ have shown better photovoltaic properties. The structural, electrical and optical properties of $Cu(In,Ga)Se_2$ crystal structures have been investigated both experimentally and theoretically by Chen et al. [39,45].

The crystal structure of $Cu(In,Ga)Se_2$ is shown in Figure 2.5 [45]. The lattice atoms are tetrahedrally bonded with a chalcopyrite structure. As a common characteristic of all other chalcopyrite, $Cu(In,Ga)Se_2$ unit cell is a supperlattice of two zinc blende unit cell with $I\bar{4}2d$ space group symmetry [39,43]. $Cu(In,Ga)Se_2$ unit cell consist of four cation (Cu and In,Ga) and eight anion (Se) atom. The symmetrical position of

these atoms are represented by (x, y, z), (-x, - y, -z), (y, -x, -z), (-y, x, -z), (-x+1/2, y, -z+3/4), (x+1/2, -y, -z+3/4), and (-y+1/2, -x, z+3/4), respectively.

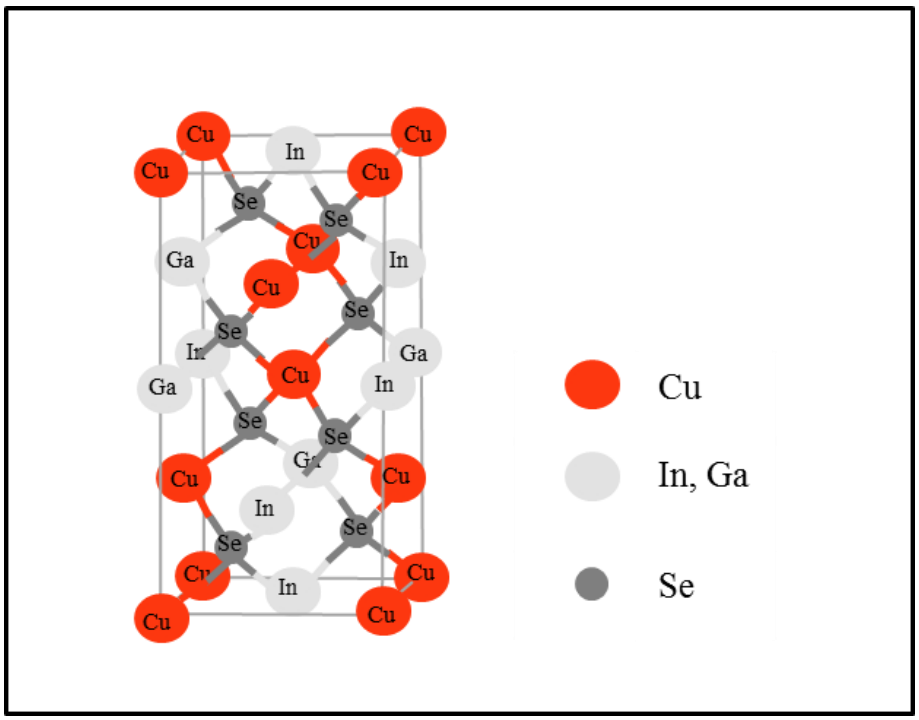

Figure 2.5 : Crystal structure of Cu(In,Ga)Se_2.

CIGS alloys are heterogeneous materials consisting of a phase of copper-indium-selenide, (CIS), and copper indium gallium diselenium.

Formulated with Cu(In_xGa_{1-x})Se_2 which changes with the value of x in the chemical formula. The $CuGaSe_2$ material corresponds to x=0 and $CuInSe_2$ material to x=1. That explains the importance of the Cu/Ga ratio which tunes the energy band gap from 1.7 eV at x=0 $CuGaSe_2$ to 1.0 eV for x=1.0. $CuInSe_2$ Cu(In,Ga)Se_2 having a energy band gap of 1.6 eV. [43,45-46]. The absorber layer CIGS is a p-type semiconductor layer. Related to Cu deficiencies, the doping is a result of intrinsic defects in the material. With the Cu deficiencies and these vacancies efficiently act as an acceptor, it means electrons excited from the valence band can get easily trapped. As a result the holes become the majority charge carrier density [40].

Meanwhile Cu(In,Ga)Se_2 CIGS thin-film solar cells are subject to active research all over the world and have been studied extensively due to the high absorption coefficients (10^5 cm^{-1}) for visible light [12,47].

The CIGS material is a direct energy band gap semiconductor material having a large absorption coefficient. 1-2 microns thickness will be enough to absorb a large fraction of the light above the energy band gap [40].

In Figure 2.6, the absorption coefficient versus the wavelength is presented. The absorption coefficient of GaAs is significantly greater than of silicon that defines GaAs absorbs the same amount of light in reference to a silicon wafer with a possible thinner magnititude of thickness [31].

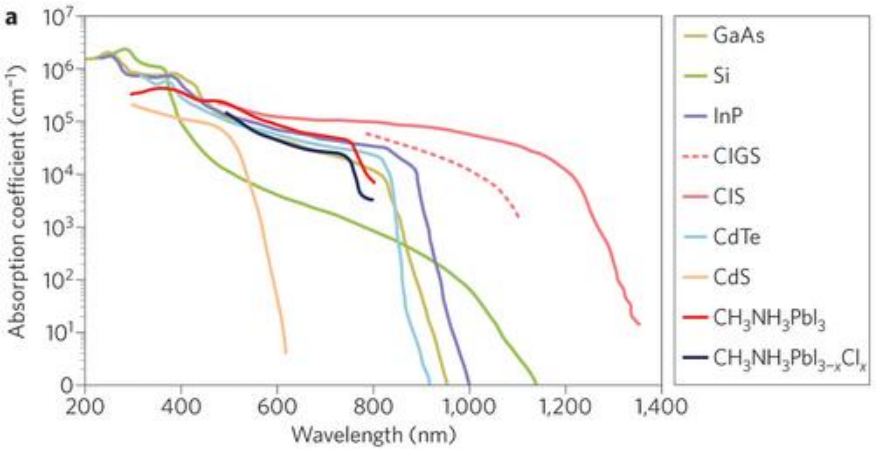

Figure 2.6 : Absorption coefficient (cm^{-1}) versus wavelength (nm) [48].

The absorption coefficient of crystalline silicon compare to the direct energy band gap materials, such as CIGS, GaAs and InP is considerably lower (Figure 2.6). Crystalline silicon is indicated by the green line and CIGS by the red dashes whereas GaAs and InP is indicated in dark yellow and purple. In the visible light range crystalline silicon absorbs less than the GaAs and InP just below the ~ 364 nm, it absorbs as much as GaAs and InP, because silicon has direct band to band transition here as well [40].

The absorption coefficient of $Cu(In_xGa_{1-x})Se_2$ versus photon energy with the different Gallium amount is presented in Figure 2.7. The absorption coefficient range is shown here to make comparison with the calculated values of the produced CIGS thin-films at Chapter 4.

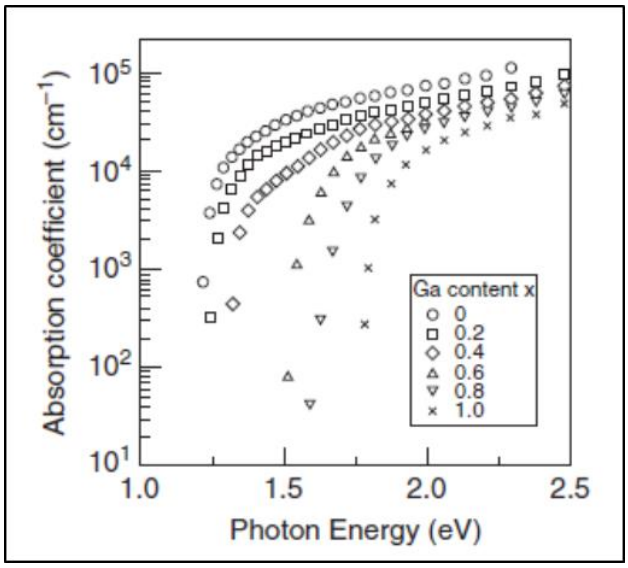

Figure 2.7 : Absorption coefficient (cm^{-1}) of $Cu(In_xGa_{1-x})Se_2$ versus photon energy (eV) [47].

2.2.2.1 Deposition technologies of CIGS thin-films

A variety of deposition techniques can be used by depositing CIGS thin-films. One of the processing techniques is co-evaporation or co-sputtering under vacuum conditions. The sputtering and co-evaporation on a substrate at high temperatures. During the process there is an additional selenium source so that a CIGS thin-film is formed. In another application at sputtering and co-evaporation is depositing on a substrate at room temperature and thermally annealed in presence of a selenide vapor to form the CIGS structure. One another option is to deposit a selenium rich layer on top of the initial deposited alloy and this is annealed. Because of the variety and complexity of the reactions taking place during such 'Selenization' process, the properties of CIGS are difficult to control [31]. Also the required vacuum processing needs expensive equipment investment.

The sol-gel method is the most economical way for depositing CIGS thin-films with a non-vacuum technology, involves cheap equipments. This study contributes to the field of the optical properties of CIGS thin-films produced by the sol-gel method to reduce the cost of the production and to control the chemical composition on the surface of films in atomic scale [11].

2.2.2.2 CIGS solar cell

Figure 2.8 is a typical $Cu(In,Ga)Se_2$ solar cell structure [49,Url-1]. The CIGS solar cell typically includes a glass substrate. On top of the glass an approximately 1 μ m

thick polycrystalline molybdenum (Mo) layer is deposited with sputtering technique. This layer acts as the back electrode conducting electricity [46,49]. On top of the back electrode, the polycrystalline p-type semiconductor $Cu(In,Ga)Se_2$ about 2 up to 4 μm thick layer, for absorbing light. The p-n junction is formed by a thin n-type semiconductor CdS buffer layer of around 25−50 nm on top of p-type CIGS. This layer is referred to as the buffer layer which is produced with chemical bath deposition [50]. The n-type CIGS layer can be also replaced between the p-type CIGS and the CdS interface so that it prevents loss mechanism of the defects at the interface. The n-type CIGS is an Indium rich alloy, like $Cu(In,Ga)_3Se_5$ [31].

The n-type region is extended with an n-type TCO (transparent conductive oxide). First an intrinsic ZnO is placed followed by an Al doped ZnO. The Al-doping makes the ZnO n-type. The Aluminum doped ZnO acts like a transparent front contact for the solar cell which has high light transparency and a high electric conductivity [49]. On top of this transparent conductive oxide, antireflective coatings can be placed.

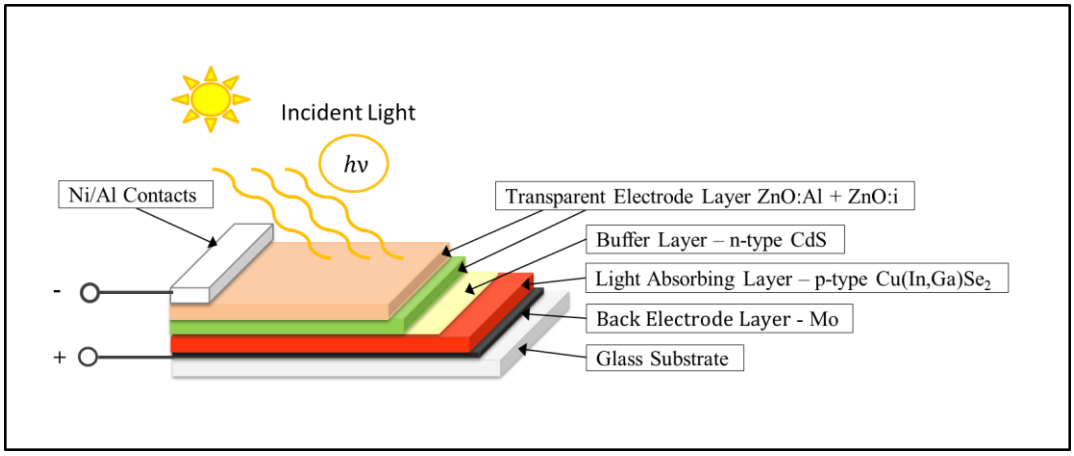

Figure 2.8 : Illustration of a conventional CIGS Solar-Cell.

The CIGS light absorbing layer absorbs the sunlight and produces electron hole pairs having electric potential energy [49]. The front transparent electrode layer and the back electrode layer then output the electric potential for power supplying, collecting the current [12].

As can be seen from the Figure 2.9, the incident light enters the solar cell from the ZnO side with a high transparency. The energy band gap of p-type CIGS absorber layers is around 1.1-1.2 eV in the industrial modules. This energy band gap is performed by a ratio of Ga to In of around 0.3. The energy band gap of n-type semiconductor CdS buffer layer is 2.5 eV. As the energy band gap of the

n- and p-type junction materials are different, this CIGS solar cell can be considered as a heterojunction. The excited minority electrons in the CIGS layers diffuse to the CdS/CIGS interface to be separated. Molybdenum back contact collects the diffused holes. Here, the holes recombine with the electrons supplied from this Molybdenum back contact. ZnO behaves like the front contact. The energy band gap of the ZnO is 3.3 eV which is large enough that helps to minimize the parasitic absorption losses [31,50].

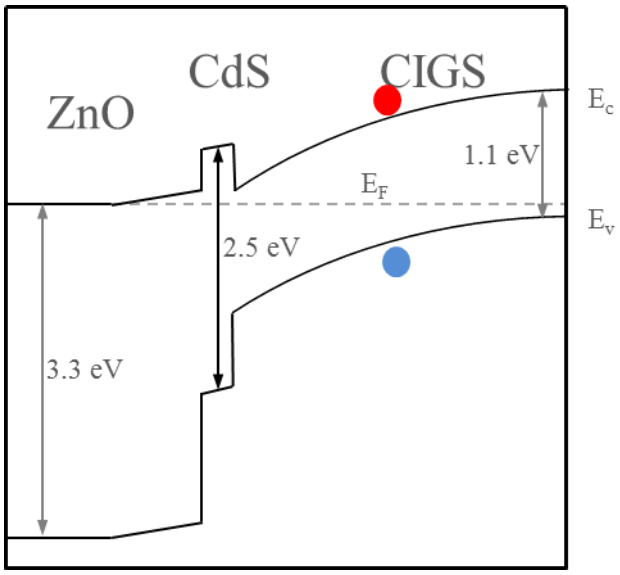

Figure 2.9 : CI(G)S Solar Cell Electronic Band Diagram.

In Cu deficient p-type, the role of Sodium is important for the CIGS solar cells. Low contamination of Sodium increases the conductivity in the p-type CIGS materials which increases in the averaged grain size [9,12]. Similar to multi-crystalline silicon, the larger the grain size, the less grain boundaries and less recombination are present in the material. This results in higher energy band gap utilization and higher open circuit voltages. Typical optimum concentration of sodium in the CIGS layers is 0.1%. The Sodium source in the growth mechanism can be the soda-lime glass used as substrate. In CIGS solar cell concepts, where this soda-lime glass is missing, the Sodium has to be intentionally added during the deposition process [12].

CIGS thin-film PV technology has the highest achieved efficiencies on both laboratory scale and module level. Solar cells using CIGS as an absorber block have already reached a 19.5% efficiency [51].

2.3 Sol-Gel

The sol-gel process involves the preparation of a sol, the gelation of the sol, and the removal of the liquid. A sol is a colloidal suspension of solid particles in Brownian motion within a fluid matrix. Two different sol-gel processing routes are commonly distinguished: Colloidal gel route in which the sol consist of dense colloidal particles between 1 nm (10 Å) and 1 μm (10^4 Å) and the polymeric gel route in which the sol consists of polymer chains but has no dense particles >1 nm [52-53].

The starting compounds (precursors) for the preparation of the inorganic sols are *metal alkoxides* and metal salts; but often *metal alkoxides*, compounds of a metal with an alkoxy group, i.e. with an oxygen atom the metal atom is bonded to an alkyl group like methyl or n-propyl. Zirkon-n-propoxid is Zr-O-n-propyl. Tetraethyl orthosilicate (TEOS) is oxygen bonds silicon and ethyl [54].

In the first step of the production of a sol this precursor is dissolved in an appropriate solvent and by adding a catalyst and maybe water it is hydrolyzed (Fig. 2.10) [Url-2].Figure 2.10 shows the representative schematics of hydrolysis-condensation process of the sol generation and the reactions accompanying. In this step the system requires water and with the bond between the metal ion and the oxygen and additional hydrogen atom from the water an unstable hydroxyl compound is formed and further the alkyl group reacts to alcohol.

Hydrolysis reaction is accompanied by condensation of hydrolyzed moieties (M-OH, M: metal) to form the oxygen bridge bonds (M-O-M) [54]. In this step the hydroxyl compounds condense by oxygen bridge bonds and demerge water (Figure 2.10). With all molecules in the system is condensed via oxygen bridge bonds, the gel formation is determined. This is also called polymerization [55]. When it is partially hydrolyzed, demerges alcohol [55].

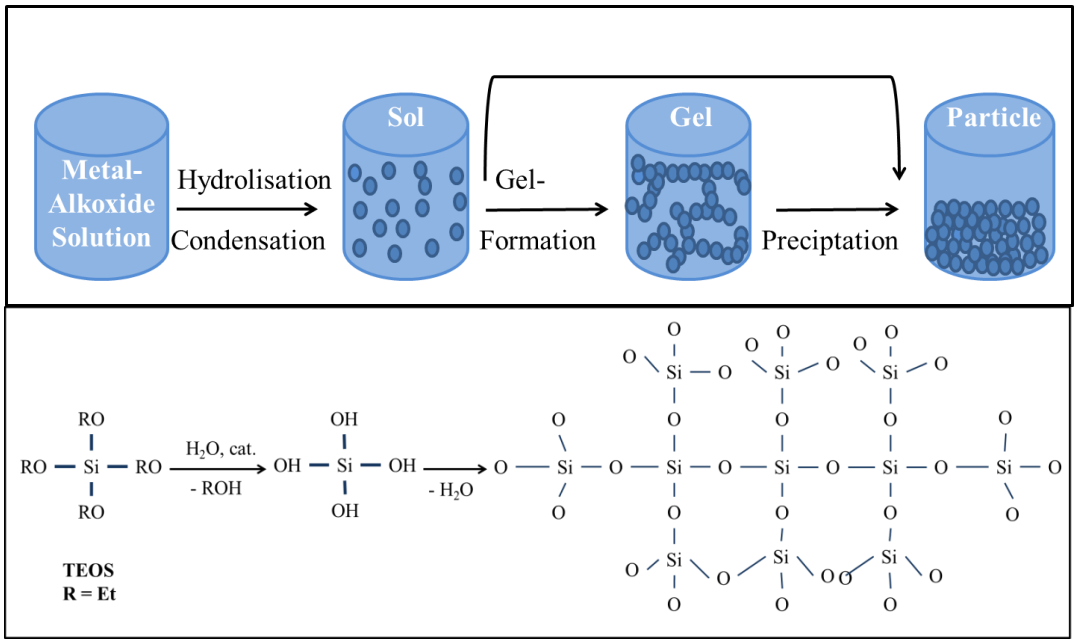

Figure 2.10 : Hydrolysis-Condensation process of Sol-Gel Generation.

Due to an electrochemical double layer that is absorbed by OH-groups on the surface the particles reject each other. The repelling forces overwhelm the attracting Van-der-Waals forces so that the sol is stabilized. This inorganic sol consists of solvent and polymeric particles with the size of only a few nanometers that don't interact with each other. It is also called a *colloidal dispersion* and because of the small size of the particles these sols are often translucent and often show thixotropic behavior. The thixotropic behavior is because of the micro ionic cloud on the surface or weak hydrogen bridge bonds [53].

In dip-coating the destabilization of the sol is a result of the particles drawing closer to each other and at the same time more cross linking oxygen bridging bonds occurs. For a critical distance, the repelling forces convert into attracting forces, see Figure 2.11. In the green area sol is stabilized, in the yellow area interaction between particles occurs [56].

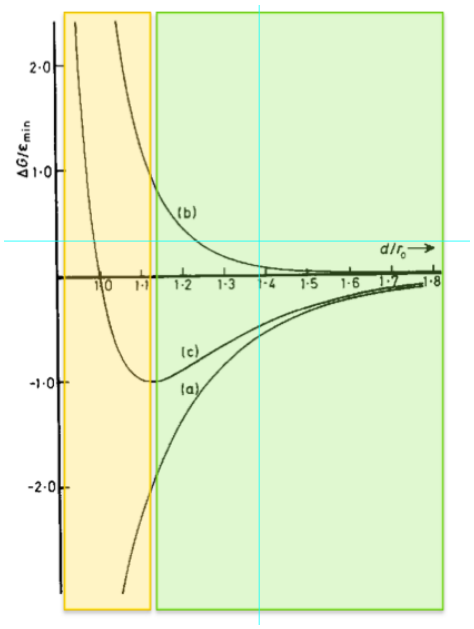

Figure 2.11 : Free Energy as a function of distance between particles [57].

A cross-linked structure filled with a liquid phase is called a hydrogel. If the solvent evaporated completely it is called xerogel. In a heat treatment the coating is already starting to compact, due to the high surface area. Volatile matter and organic remains are removed and with further sintering processes a thin, compact coating, <1µm, of crystalline or amorphous structure can be achieved. With a smart temperature-time program different crystalline phases can be achieved for e.g. for alumina coatings. Silica coatings are of amorphous kind [57].

2.3.1 Sol-Gel Process

Sol-Gel is a coating technique which can be applied on various material surfaces such as glass, metal, ceramic and polymer to improve the physical (optical, electrical), chemical and mechanical properties. Sol-gel methods can be used to produce any single or multilayer coatings. The application areas of sol-gel method include but not limited to optical coatings, electronic films, porous films and protective films. Providing "coloration, antireflection, selective reflection, electrochromism and photochromism, selective absorption, wave guiding, reduced friction, anti-soiling reduced adhesion, transparent conductors, electro-optics, dye lasers" [58].

Ferroelectric and superconductor thin-films can also be prepared by sol-gel method. Sol-gel protective coatings impart strength, corrosion resistance and abrasion

resistance to improve material properties. Sol-gel derived highly porous films can be utilized in sensor applications as well [54].

There are five main sol-gel processing steps such as preparing the sol, preparing the substrates, thin-film deposition, pre-heating and annealing. In the first step the sol is prepared by mixing all the required chemicals in appropriate ratios to form homogeneous and transparent solution. The prepared solution is precipitated in a required time period. In the second step, the substrates are cleaned with a suitable cleaning process, could be cleaned ultrasonically with alcohol, acetone or any kind of appropriate solvent. Film deposition step starts with one of those sol-gel coating technique. Mostly dip-coating, spin coating or spray coating is used. In pre-heating organic residuals are evaporated, dried. The annealing process determines the crystal structure of the thin-film. The very strong radicals decompose already in this step.

The sol-gel process offers a high number of varieties affecting thin-film microstructure and physical properties;

under the sol preparation; pH, composition and concentration of chemicals, time and temperature of mixing process, atmospheric conditions of preparation process; under the substrate-film interaction; sol viscosity, spin-dip coating parameters; under the thermal processing of the deposited thin-film; time and temperature of preheating between each layer deposition, time-temperature-atmosphere of post heating, time, temperature and atmosphere of final annealing can be considered [59].

One of the major parameter is the variation in pH-values of the sol. The differences between acid and base catalyzed reactions and the consequences for particle morphology are conceptually represented. Figure 2.12 represents the effect of pH-value to the structure of the particles and coating. Depending on the application, in acid media solid, compact coatings can be achieved; in basic media on the other hand more porous coating will result. In this thesis, the pH effect to the CIGS thin-film is considered as well. The exact pH-value is determined via the experiments similar with the literature (the details are presented in the results of this thesis) [60].

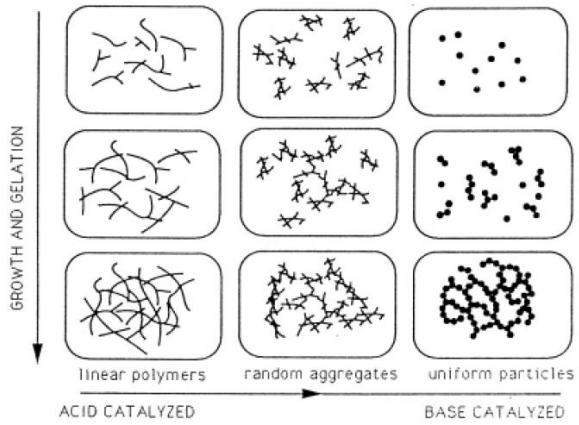

Figure 2.12 : Influence of the pH-value on the structure [60].

Advantages and Disadvantages of Sol-Gel Processing

Compared to conventional techniques the sol-gel offers a number of important advantages that makes the method interesting for the production of materials customized to specific applications [53]. There is an ability to synthesize highly pure and homogeneous products by employing simple and low cost coating techniques with inexpensive equipments compare to vacuum techniques [56]. The possibility to coat large, curved or complex-shaped substrates by using simple deposition techniques and the ability to obtain homogenous coatings. Sol-gel methods can be conveniently used to produce multilayer coatings, permitting the fabrication of layers with widely varying optical characteristics, such as transmission and reflection [53]. On the other hand, vacuum coating processes, unlike dip processes, permit continuous adjustment of the film parameters easily during deposition [54].

Additionally, low processing temperatures make sol-gel method suitable for industrial scale production. Moreover, sol-gel method not only enables the deposition of thin-films, but also monoliths, fibers and powders can be produced [61]. An additional advantage is the ability to produce porous structure, which is sometimes also required in some systems. Major advantage of this process is that it doesn't have any air-pollution and on the other hand it has the contribution of energy save. Additionally, solutions with precise amount of dopants can be prepared easily without the need for expensive equipment. Moreover, manipulation of sol chemistry at the atomic scale by use of different precursors, solvents, and additives enable researchers to improve the optical and electrical properties of CIGS thin-films [61].

On the other hand, there are also some drawbacks linked to sol-gel method. Many metal alkoxides are fairly expensive, and most are very sensitive to changes in temperature and moisture content of processing atmosphere so that they must be handled in a dry environment (e.g., an inert atmosphere glove box) [52,56]. This problem can be avoided if metal salts are used in processing instead of alkoxides. Moreover, the density of films is generally lower when compared to vacuum methods such as sputtering. The residual pores in the films may deteriorate the functional and structural properties of films and coatings, except porous films [56]. Also material loss can be one another important case. The quality of the thin-film can be affected by carbon impurities [55].

Nevertheless, sol-gel method enables researchers and industrialists to produce a wide variety of products through relatively simple and cheap processes. In these respects, CIGS thin-film deposition through sol-gel method has attracted numerous researchers and resistivity comparable to that of sputtered films can be obtained [61].

2.3.2 Deposition Techniques of Sol-Gel

Deposition techniques can be categorized into three groups mainly;

- Dip Coating,
- Spin Coating,
- Spray Coating.

Beside these techniques some additional methods can be expressed like flow coating, laminar coating and roll coating. Dip coating is the most widely used, favored sol-gel deposition technique because of its easy application procedure and low cost.

2.3.2.1 Dip Coating Technique

Dip coating techniques can be described as a process where the substrate to be coated is immersed in a solution for a certain time until the substrate is completely wetted and then withdrawn with a well-defined withdrawal speed under controlled temperature and atmospheric conditions that the film thickness reaches satisfactory levels [62].

The coating thickness is mainly defined by the withdrawal speed, by the solid content and the viscosity of the liquid. If the withdrawal speed is chosen such that the

sheer rates keep the system in the Newtonian regime, the coating thickness can be calculated by the Landau-Levich Equation **(2.1**) [62, Url-3].

$$h = 0.94 \times \frac{(\eta \cdot u)^{2/3}}{\gamma_{LV}^{1/6} \cdot (\rho \cdot g)^{1/2}} \quad \textbf{(2.1)}$$

h = Thickness of the Coating

η = Viscosity of Sol

u = Speed of Substrate

γ_{LV} = liquid-vapour surface tension

ρ = Density of Sol

g = gravity

The thickness of the thin-film increases with the increase of the dip-velocity. This is due to the thixotropic behavior of the sol, so at fast dip-velocities the material has no chance to flow down on the substrate. Another way to achieve thicker coatings is multiple dipping.

Figure 2.13 shows the representative schematics for thin-film formation in dip coating technique of sol-gel process. The dip coating process can be summarized in five main steps. The process starts with the immersion of the substrate to be coated into the coating solution which is followed by either drawing the substrate from solution or drawing the reaction vessel away from the substrate to deposit thin-films. The substrate is immersed into a solution of the material to be deposited at a constant immersion rate. At the second stage the substrate which has been dipped into the solution for a determinate period of time starts to be pulled up. The wet layer is formed on the substrate while withdrawing the substrate. The withdrawal is carried out at a constant rate, avoiding any undesired vibration. The withdrawal speed determines the thickness of the deposited film (a higher speed produces a thicker film). At the fourth stage the excess of liquid is drained from the surface. At the last stage the solvent is evaporated from the deposited liquid film, resulting gelation of the layer on the coating. For volatile solvents, such as alcohols, the evaporation process starts during the deposition and drainage steps. During substrate removal, organics and water are evaporated leading to the formation of a thin-film. In the continuous process, the steps are carried out directly after each other [Url-4].

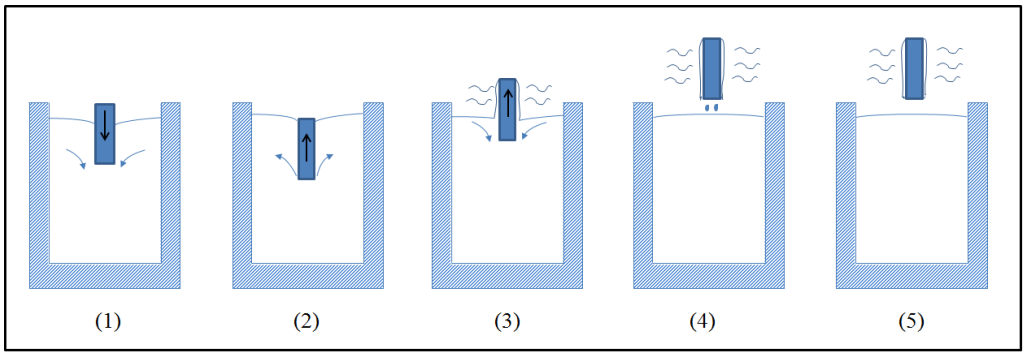

Figure 2.13 : Stages of the dip coating process: (1) Immersion (2) Withdraw (3) Deposition-Drainage (4) Drainage (5) Evaporation

The conversion of sol to the gel form schematically is shown in Figure 2.14. Gelation process during dip coating process is obtained by evaporation of the solvent and subsequent destabilization of the sol. The atmosphere controls the evaporation of the solvent and the subsequent destabilization of the sols by solvent evaporation, leads to a gelation process and the formation of a transparent film due to the small particle size in the sols (nm range) [63, Url-3].

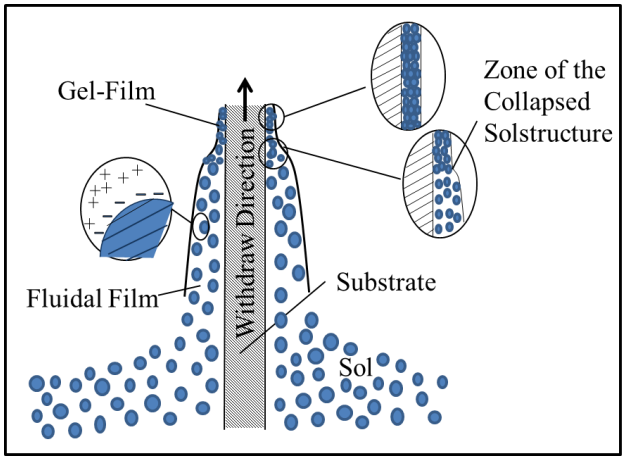

Figure 2.14 : The conversion of sol to gel for dip-coating process.

Dip coating technique is advantageous in terms of allowing the coating complex shaped substrates such as hollow, concave and convex pieces. Additionally, both sides of the substrates can be coated simultaneously. The thickness of the deposits depends on the viscosity and density of the solution and the withdrawal speed. Dipping technique can be continuous or batch, both of which are fully adaptable to large scale manufacturing [54,64].

The chemical reactions are controlled by the processing variables such as chemical composition of the precursor, concentration of reactants, pH of the solution, and temperature [52].

2.4 Radiation

Scientists have studied radiation for over 100 years and radiation is part of nature. All living creatures, from the beginning of time, have been, and are still being exposing radiation. Radiation is any form of energy transmitted through space by means of: waves, particles. In another way; radiation is an energy in the form of electromagnetic waves or energetic particles (particulate matter), traveling in the air [65, Url-5].

"Radiation is defined as the particles with sufficient energy to cause ionization" [66].

One form of radiation is electromagnetic radiation pure energy with no weight. This is like vibrating or pulsating rays or "waves" of electrical and magnetic energy. Electromagnetic radiation has both electric and magnetic field components. This pure energy is emitted in the form of a photon of wavelength predicted by the energy relationship (**2.2)**:

$$E = \frac{hc}{\lambda} \qquad \textbf{(2.2)}$$

where h is Planck' s constant (6.625 x 10^{-27} erg-sec), c is the speed velocity of light (2.99793 x 10^{8} m.s^{-1}), and λ is the wavelength of the photon in nm. In vacuum, electromagnetic radiation propagates at a characteristic speed, the speed of light. The wavelength of electromagnetic radiation depends on their energy (Figure 2.15) [66].

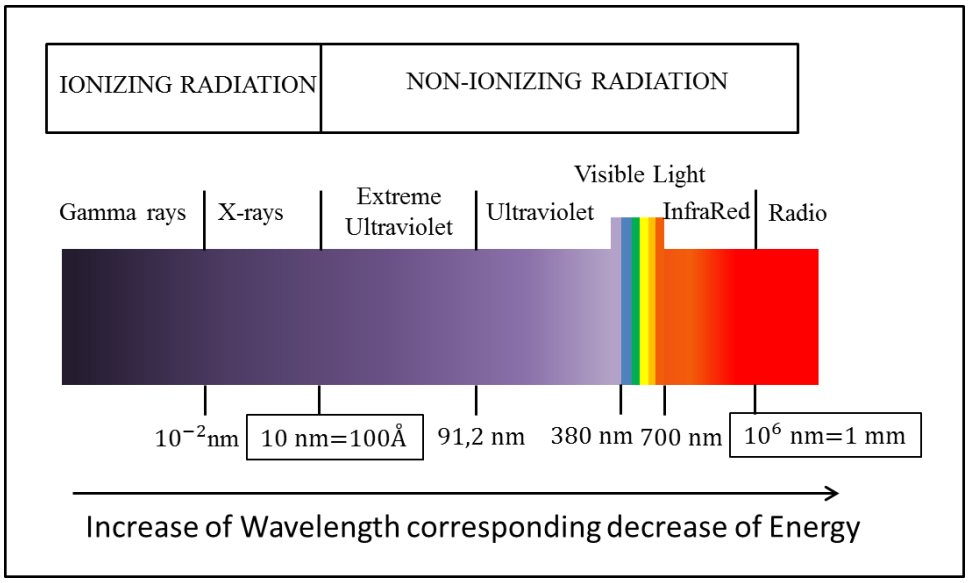

Figure 2.15 : Electromagnetic Spectrum.

The other form of radiation, which is known as particle radiation, is tiny fast-moving particles that have both energy and mass (weight). This less-familiar form of radiation includes positively charged alpha particles, negatively charged beta particles and neutrons, as explained in Figure 2.16 [Url-5]. The wave-like form of radiation gamma rays and x-rays are also mentioned in Figure 2.16.

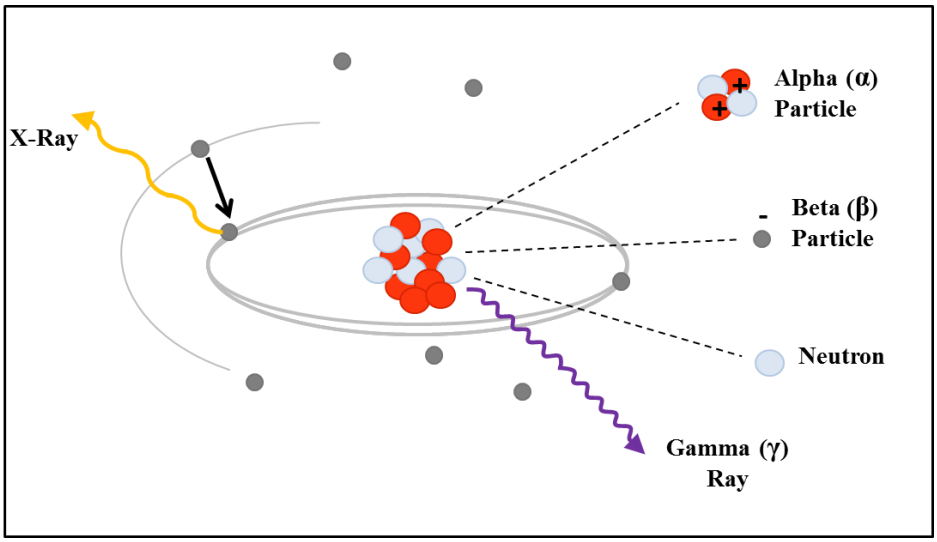

Figure 2.16 : Some Wave-Particle Radiation Type.

The unstable atoms spontaneously transform into new atoms to get stability and loses energy by emitting ionizing particles and/or photons. This process is called the decay of the nucleus [66]. In order to reach stability, these atoms give off, or emit, the excess energy or mass. These emissions are called radiation.

The "amount" of radioactivity, which is called activity, is given by the number of nuclear decays. Activity occurs per unit time or decays per minute. An atom with an unstable nucleus will "decay" until it becomes a stable atom. Before it reaches a stable state the atom undergoes several radioactive decays, as the new formed atom can be also unstable, creating a "decay chain". Through this process radioisotopes lose their radioactivity over time. This gradual loss of radioactivity is measured in half-lives. The half-life of a radioactive material tells us how quickly it decays away. Essentially, a half-life of a radioactive material is the time it takes one-half of the atoms of a radioisotope to decay away by emitting radiation [Url-5]. It is measured in units of time. For example; some natural isotopes, like Uranium and Thorium, have half-life that is billions of years.

Radiation is classified into two main groups depending on how it affects matter (Figure 2.15):

- Non-ionizing radiation
- Ionizing radiation

Non-ionizing radiation includes sunlight, radio waves, microwaves, infra-red waves, visible light waves and lasers. As the incident photon has generally low energy this photon cannot pull electron from orbit.

Ionizing Radiation includes electromagnetic waves with higher energy or heavy particles (such as beta and alpha) which are high enough to pull electron from orbit (Figure 2.16).

2.4.1 Ionizing radiation

Ionizing radiation is a type of radiation that is able to disrupt atoms and molecules on which they pass through, giving rise to ions and free radicals [65]. This is the case of alpha and beta radiations, as well as of electromagnetic radiations such as gamma rays, X-rays and some ultra-violet rays.

Two types of ionizing radiation can be considered: direct ionizing radiation and indirect ionizing radiation. The phenomena of direct ionizing radiation are the charged particles such as alpha particles, beta particles, electrons, because though Coulomb Interaction with matter it directly causes ionization and excitation of atoms. Indirect ionizing radiation (such as neutrons and gamma photons) is radiation of particles or photons, which have no charge and during interaction with matter can transfer energy to charged particles, nuclei and atom electrons due to electromagnetic or nuclear interaction [Url-6].

Ionizing radiation is produced by unstable atoms. Unstable atoms differ from stable atoms because they have an excess of energy or mass or both. There are five different types of radiation emitted from radio-active bodies [67]; alpha (α) particles, beta (β) particles, neutrons (η), gamma (γ) rays (or photons), x-rays (Figure 2.16).

2.4.1.1 Alpha (α) radiation

Alpha (α) radiation is a result of alpha particle which is emitted from the nucleus of an atom, having 2 neutrons and 2 protons. +2 charged nucleus is identical to the nucleus of a Helium atom. Helium nucleus has large mass (4 a.m.u.). Hence it is a heavy particle with a big charge. Figure 2.17 represents the primary types of ionizing radiation with different radioactive substances.

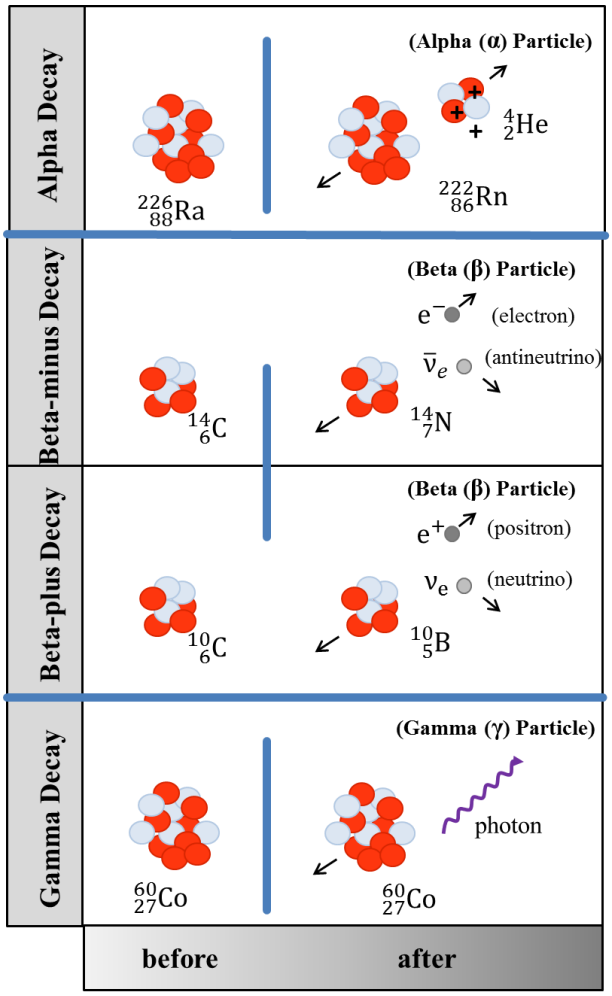

Figure 2.17 : Types and characteristics of ionizing radiation.

Radioactive substances possess the property of spontaneously emitting ionizing radiations [67]. As it is shown clearly $^{226}_{88}$Ra decays into $^{222}_{86}$Rn [68] by emitting α- particles which is nucleus of ^{4}He, called alpha decay. Eventually it loses too much energy to ionize; become He. Alpha particles travel short distances with a limited range and their path is smaller than 10 cm in air and smaller than 60 µm in tissue.

Typical Energy level is 4-8 MeV, having high LET- Linear Energy Transfer. Hence, it can cause great biological damage with heavy damage (4K-9K ion pairs/µm in tissue) [65]. LET is defined as the total energy dissipated divided by the path length required for the particle to stop **(2.3)** in (J/m or keV/m) where *E* is the kinetic energy of the incident particle and *l* is its stopping distance [68].

$$\text{LET} = {}^{E}/_{l} \qquad \textbf{(2.3)}$$

Uranium, Thorium, Radon, Polonium and Plutonium are main alpha emitters. Especially Plutonium is the strategic material in nuclear technology. Alpha particles

can be shielded easily. Internal radiation hazard can be stopped by a piece of paper or the top layer of human skin (Figure 2.18).

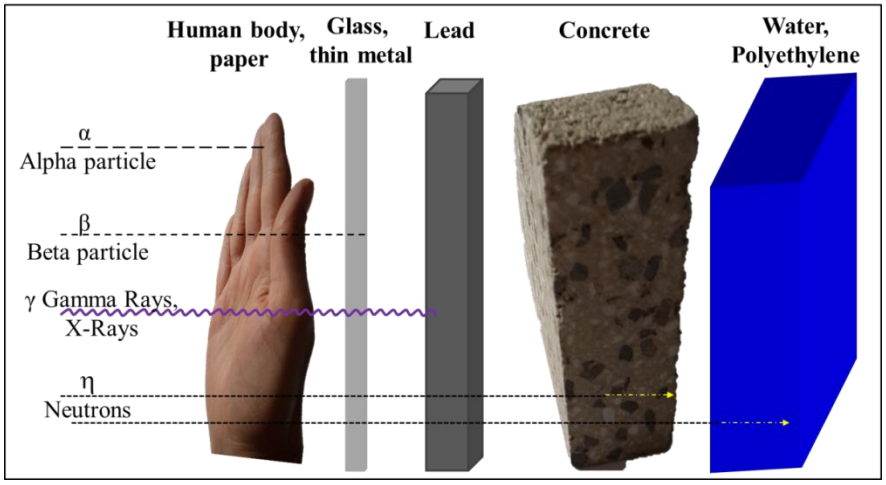

Figure 2.18 : The shielding of ionizing radiation with several materials.

2.4.1.2 Beta (β) radiation

Beta radiation is emitted by many different radioisotopes sources, can be sometimes alone, but mostly emitted with gamma rays. It can be positively or negatively charged (+/- 1) [66,68].

Negative beta particle is identical to the electron except that it has kinetic energy to ensure conservation of energy. It is emitted with speed of light from the nucleus called negatron and is shown as β^-. After interaction with a matter it loses its energy and transforms into free electron [66,68].

Negatrons form when a neutron transforms into a proton which disseminating an electron or high speed electron ejected from nucleus and an antineutrino (ν+). Negatron forms as given in **(2.4)** [67].

$$n \rightarrow p + \beta^- + \nu^+ + \text{Energy} \qquad \textbf{(2.4)}$$

The standard description for the β- decay is presented in **(2.5)** [67].

$$^{A}_{Z}X \rightarrow {}_{Z+1}{}^{A}Y + e + \bar{\nu}_e \qquad \textbf{(2.5)}$$

Positive beta particle is called as positron, symbolized with β^+ and formulated in **(2.6)**. Some nuclei disintegrate by emitting a positively charges electron and a neutrino [68]. It is the disintegration of proton into neutron.

$$p \rightarrow n + \beta^+ + \nu^- + \text{Energy} \qquad \textbf{(2.6)}$$

The beta decay of the nucleus with different examples is shown in Figure 2.17. They are relatively light particle having small mass as 0.00055 AMU and variable energy. Typical energy level is several keV to 5 MeV. The beta energy is approximately 1/3 of the maximum energy (E_{av}=1/3E_{max}). The speed of beta particles changes with the rise of the energy, and the speed is an indication of its energy level [65].

Beta radiation travels through matter with a distance depending on their initial kinetic energy For example, beta particle with energy about 2 MeV will travel up to 9 m in air and about 10 mm in water. Beta radiation can penetrate air and paper. It is shielded by wood or other low density materials such as lucite or plexiglass or aluminum foil and other light (Z<14) materials, glass plate or 2.5 cm of virtually anything (Figure 2.18) [65,Url-6].

Body penetration is around 0.2-1.3 cm depending on energy. Range is approximately 30.48 cm/MeV in air, a few mm in tissue; low LET causing light damage (6-8 ion pairs/μm in tissue) [65,69].

Beta radiation penetrates human skin in a fast process breaking chemical bonds and destroying certain living cells. It causes primarily skin burns or an internal hazard (such as ingestion and inhalation) but high beta can be an external hazard to skin. On the other side, using beta radiation, in some medical treatment (cancer and pharmacological studies etc.) is also so effective [65].

Beta radiation sources

Strontium, Phosphorus, Carbon, Sulfur are famous beta emitters. Strontium-90 is a commonly used beta emitter in industrial areas. Phosphorus-32 is a short lived high energy beta emitter, which is used in research in radiotracers. It can be used in DNA research. Carbon-14 is used commonly as a radiotracer in organic compounds. Paper, plastic and aluminum can shield beta radiation considerably [68].

Mechanisms of beta interaction with matter

Two main mechanisms can be defined for the interaction of beta with matter [Url-7]:

Excitation and ionization

Beta particles can interact with electrons as well as nuclei. Beta particles passing near nucleus is deviated by the coulomb forces (Figure 2.19). The interaction between the electric field of a beta particle and the orbital electrons leads to inelastic collisions that generate electronic excitation and ionization due to the coulomb

repulsion. The lost energy amount of the beta particles is equivalent to the kinetic energy of the electron plus the energy used to be donated from the atom. With the donated electron, core atom becomes positively charged. This donated electron and core atom forms the ion pair. A beta particle may produce 50 to 150 ion pairs per centimeter of air before its kinetic energy is completely annihilated. Because of the continuous spectrum of beta particles, the specific ionization decreases. With the replacement of other electrons to the vacant orbits the characteristic X-rays are emitted. Beta particles also excite the external orbital electrons, which can lead to UV photon emission [Url-6,Url-7].

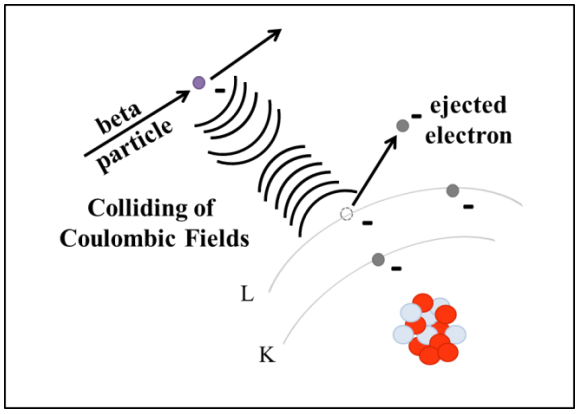

Figure 2.19 : Coulomb Interaction of Beta Particle (Ionization by a Beta Particle).

Positrons extinguish their kinetic energy just like beta particles through ionization and excitation. When a positron slowed down sufficiently, it will be attracted by an electron. As the electron and positron collide, they are both extinct and an amount of energy equal to the sum of the particle masses is released in the form of two photons. These photons are referred to as "annihilation radiation". Both annihilation photons carry energy of 0.512 MeV, which is equivalent to the rest mass of the electron or the positron [Url-6].

Bremsstrahlung radiation

The second important mechanism is "bremsstrahlung". When a high-speed charged particle passes through a medium, it sometimes goes through a significant nuclear scattering resulting with the emission of continuous electromagnetic energy called bremsstrahlung or "braking radiation" [Url-7]. The bremsstrahlung radiation energy (E_{hv}) occurs with an amount of the difference between the energy of incident electron (E_{k1}) and the decelerated energy amount (E_{k2}) [68] (Figure 2.20).

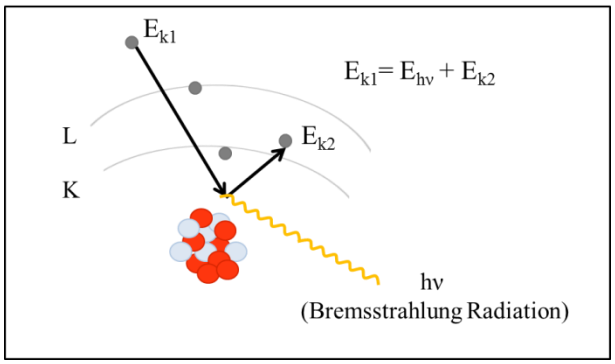

Figure 2.20 : Bremmstrahlung radiation.

This energy is in the range of X-rays so that if the shielding material is made of a material having high atomic number, it becomes more energetic. The light materials such as plexiglass are utilized to reduce "bremsstrahlung" and to absorb beta radiation [Url-7].

2.4.1.3 Neutrons (η) radiation

Neutron radiation has the same mass as protons but is uncharged. Small neutral particles (same size as a proton) travel many kilometers in air. These particles are stopped by 30 cm of water, polyethylene or paraffin. Self-fission radioactive materials like plutonium, californium give off neutrons. Large doses can do significant damage to people. Neutron shielding material depends on the energy of the neutrons [68] (Figure 2.18).

2.4.1.4 Gamma (γ) radiation

Gamma radiation (ray) is result of an energy release in the nucleus, usually after an alpha, negatron (beta) or positron transition. Gamma (γ) rays (photons) are emitted from the nucleus of an atom with no mass and no charge. These are wave-like electromagnetic radiations, often as a part of radioactive decay (Figure 2.17) which moves at or near the speed of light. Gamma rays typically have higher energy (MeV' s) than X-rays (KeV' s), but both are unlimited [68].

Gamma Rays (photons) travels many kilometers/miles in air which has a high penetration ability. Therefore, extensive shielding is required. Lead (>10 cm thickness) or steel materials or concrete are used as shielding (Figure 2.18). Lead is good for the shielding of x-rays and gamma rays as it has high electron density. For example; gamma rays of Iodine-125 having 30 keV can be easily stopped with 3.18 mm (1/8”) of lead [68].

External radiation hazard occurs deep into organs and tissues. Via ingestion or inhalation of gamma emitter, internal hazard happens. On the other hand it is normal to be exposed to small amounts every day from ground radiation and cosmic rays [68].

Gamma interaction with matter

Gamma interactions differ from charged particle interactions. Interactions transfer the energy to atom. Therefore, it has three fundamental interactions:

- May pass through and there will be no interaction.
- Compton Effect: Incident photon interacts with free electron and loses its energy [Url-8]. Incident photon disappears and secondary scattered photon appears with lower energy changing its direction, the free electron recoils with remaining energy [66] (Figure 2.21).

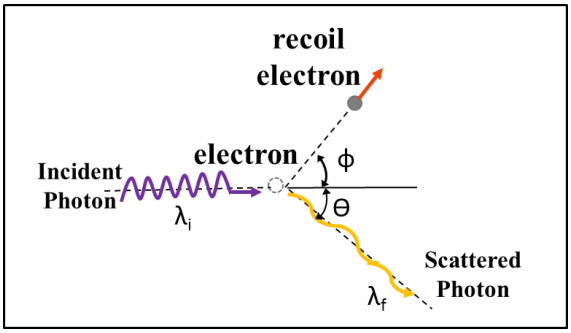

Figure 2.21 : Compton Effect.

- Photoelectric Effect: An Incident photon interacts with free electron and transfers all its energy to this free electron and primary photon disappears [Url-8]. If the incident photon collides with an atom with an energy greater than the binding energy of the electron of this atom, it ejects the electron of the atom. The electron scatters with this absorbed energy and leaves its orbit [69]. The electron from one upper shell orbit fills the scattered electron's orbit stabilizing its energy with a lower energy and release its energy (Figure 2.22).

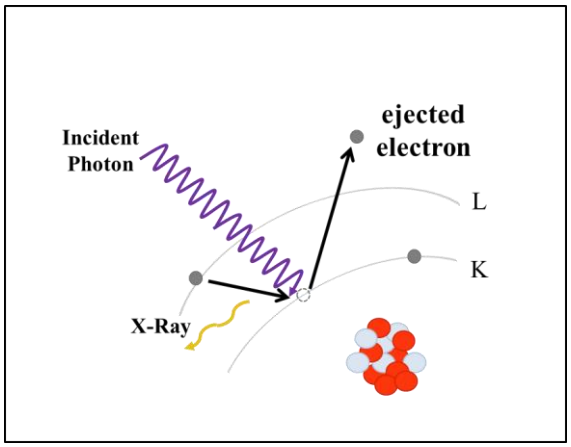

Figure 2.22 : Photoelectric Effect.

➢ Pair Production : An incident photon interacts with positively charged nucleus. The incident photon energy is big enough that creates an positron-electron pair (charge conserving) which has kinetic energy equal to excess over pair rest mass energy (1.02 MeV). When positron finds a different electron, it demolishes and emits two gamma rays photons, each with 0.511 MeV energy [69,Url-8].

2.4.1.5 X-rays

X-rays are wave-like electromagnetic radiations emitted from electron orbits that is non-particulate (Figure 2.16). It is disseminated with various energies & wavelengths usually machine produced. Same properties as gamma rays relative to mass, charge, distance traveled, and shielding. X-rays are highly penetrating so extensive shielding is required (Figure 2.18).

2.4.2 Quantification of radiation

By quantifying radioactive decay, disintegrations per second (dps) is used for the measurement of activity. The number of decays per unit time tell us how radioactive a source is. This is called activity and measured in Curies (Ci) or Becquerels (Bq). 1 disintegrations (decay) per second (dps) corresponds to 1 becquerel (Bq); 1 curie (Ci) equals to 3.7 x 10^{10} Bq and 1 Ci defined as the activity of 1 gram of Radium-226 [68]. Activity of substances are expressed as activity per weight or volume (e.g., Bq/gm or Ci/l).

Specific Activity refers to the activity of 1 gram of a radioactive material and all different isotopes have different specific activities. The longer the half-life of the

isotope has lower specific activity of the isotope. 1 gram of cobalt-60 has the same activity as 3300 metric tons of uranium-238 [68,70].

By quantifying exposure, roentgen is used as unit. 1 roentgen (R) equals to the amount of X or gamma radiation that produces ionization resulting in 1 electrostatic unit of charge in 1 cm^3 of dry air. It is the measure of how much radiation "hits" an object (or person). Instruments often measure exposure rate in mR/hr [68,70].

By quantifying absorbed dose, rad (Radiation absorbed dose) is used and equals to the absorption of 100 ergs of energy from any radiation in 1 gram of any material; 1 gray (Gy) equals to 100 rad which corresponds to 1 joule/kg; exposure to 1 Roentgen approximates 0.9 rad in air [70]. Absorbed dose defines how much energy is imparted on/transferred to the object by the radiation. It can be visualized as how much the skin heats up from the sunlight hitting it.

Biologically equivalent dose is used to quantify the effects of radiation on biological tissue (radiation-weighted dose). It is measured in Rem (Roentgen Equivalent Man) or Sieverts (Sv) that equivalents to dose in rad multiply by Quality Factor. 1 Sievert (Sv) equals to 100 rems [70]. Visualization can be as how sun burnt get an object/person from sitting out in the sun.

3. EXPERIMENTAL TECHNIQUES

3.1 Introduction

In this chapter, the details of the $CuIn_{1-x}Ga_xSe_2$ (CIGS) thin-film production on the glass substrate and the measurement methods of the physical properties such as structural, electrical and optical characterization methods are introduced. The main objective is to provide the basic information about the deposition process of thin-films and description of experiment setup used for the investigation of structural, electrical, and optical properties of the deposited thin-films. The sections are organized as follows; the deposition process of thin-films by using sol-gel dip-coating technique. This is followed by characterization of the CIGS sol and a brief introduction of basic structural, optical and electrical characterization methods. As the deposited samples were irradiated by beta radiation source, the beta irradiation process is also mentioned.

In this study, CIGS thin-films were prepared by sol-gel dip-coating technique with a Cu, In and Ga nitrate and Selenium oxide containing solution. Soda-lime silicate glass slides were used as the substrates for the thin-film deposition. The effect of different parameters were investigated such as annealing temperature, annealing time, number of coating layers, selenium concentration, withdraw speed. The effect of pH and aging of the sol were observed. The radiation effect on the sol-gel derived CIGS substrates were considered on the different aged sol and different number of layers. For the investigation of annealing effect on the samples, the deposited substrates were annealed at different temperatures under the air atmosphere. In order to examine the effect of the thickness of the films, the coating process was repeated by increasing the number of layers. The solution properties were investigated employing TG (Thermogravimetry) and DTA (Differential Thermal Analysis). The films were characterized by a surface profilometer, X-Ray diffractometer (XRD), a scanning-electron-microscopy (SEM), an atomic force microscopy (AFM), X-Ray fluorescence (XRF), UV/VIS spectrophotometer and 4-point resistivity probe.

3.2 Production of CIGS Thin-Films

3.2.1 Chemical materials

The chemical materials employed used in this study supplied with high chemical purities. The materials, which were listed in Table 3.1 with their formulas and supplier information, used to prepare CIGS coating solutions. All chemicals were used as purveyed without any further purification treatment.

Table 3.1 : The information of purities and formulas of the employed chemical materials.

Material	Supplier	Chemical Formula	Purity
Copper(II) Nitrate Hydrate	Sigma-Aldrich	$Cu(NO_3)_2 \cdot 3H_2O$	99.999%
Indium(III) Nitrate Hydrate	Sigma-Aldrich	$In(NO_3)_2 \cdot 3H_2O$	99.9%
Gallium(III) Nitrate Hydrate	Sigma-Aldrich	$Ga(NO_3)_3 \cdot H_2O$	99.9%
Selenium(IV) Oxide	Merck Millipore	SeO_2	99.999%
Ethyl Cellulose (EC)	Sigma-Aldrich	-	48.0-49.5%
Terpineol	Fluka	$C_{10}H_{18}O$	≥99.5%
Diethanolamine (DEA)	Merck	$C_4H_{11}NO_2$	98%
Ethanol	Merck	C_2H_5OH	Absolute
Hydrochloric Acid	Merck	HCl	37%

3.2.2 Preparation of CIGS solution

The CIGS coating solution was prepared by conventional sol-gel approaches at the room temperature with the chemical materials presented in Table 3.1. The precursor materials copper(II) nitrate hydrate ($Cu(NO_3)_2.3H_2O$; 99.999 %), indium(III) nitrate hydrate ($In(NO_3)_2.3H_2O$; 99.999 %) and gallium(III) nitrate hydrate ($Ga(NO_3)_3.H_2O$; 99.9 %) were weighed in the composition ratio of 1:0.7:0.3:2 [71] with a METTLER TOLEDO AB54-S Analytical Balances (Figure 3.1). These chemicals were dissolved in 60 ml ethanol as material (C_2H_5OH; 99.6%).

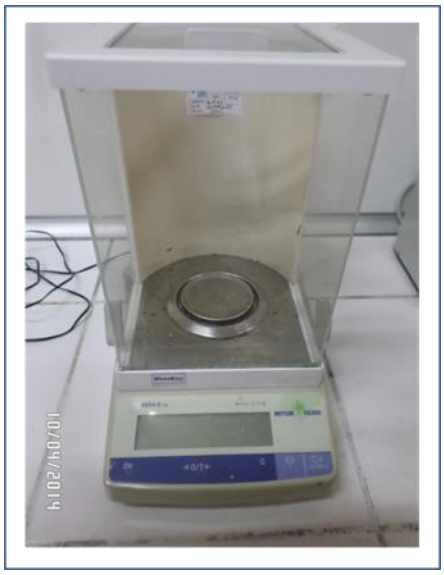

Figure 3.1 : Analytical Balances METTLER TOLEDO AB54-S.

Ethyl-cellulose (EC) (Aldrich, 0.75 g) and terpineol (Fluka, 15mL) were dissolved in 20 ml ethanol solution and this viscous solution was mixed with Cu-, In- and Ga-containing ethanol solution [71] with a Heidolph MR3001K magnetic stirrer for 1 hour (Figure 3.2).

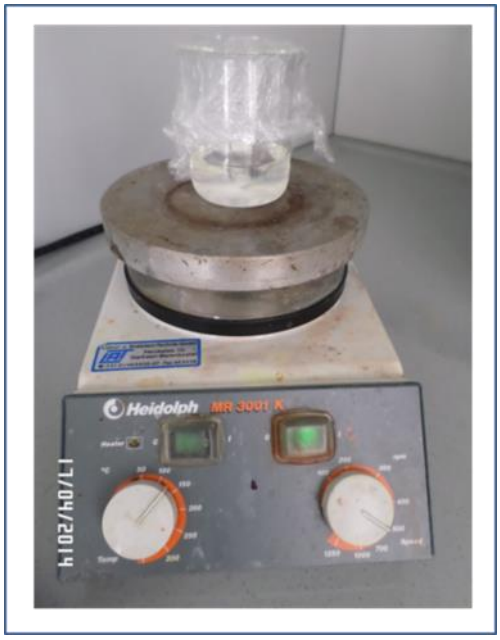

Figure 3.2 : Magnetic Stirrer Heidolph MR3001K.

The addition of terpineol effects the adhesive of the chalcopyrite Cu(In,Ga)Se_2 structure to the soda-lime-silicate glass substrate and provides the pH adjustment lower than 2.5. SeO_2 (Merck, 99.9%) was mixed in 10ml ethanol and added to the CIG solution. SeO_2 was dissolved seperately to avoid rapid oxidation with

Cu-, In-, Ga- solution [21]. The pH of the mixture is lower than 1, indicating proton generation from alcohols [72].

The solution was stabilized with diethanolamine DEA $(CH_2CH_2OH)_2$ [49], to coordinate metal cations in order to improve chemical homogeneity. The reactions leading to formation of oxide network initiate firstly by the hydrolysis of alkoxide chains.

The final mixture becomes blue opak colour initially (Figure 3.3a). The pH-value was controlled with the aid of hydrochloric acid and acetic acid. The solution turned to clear, transparent green colour (Figure 3.3b).

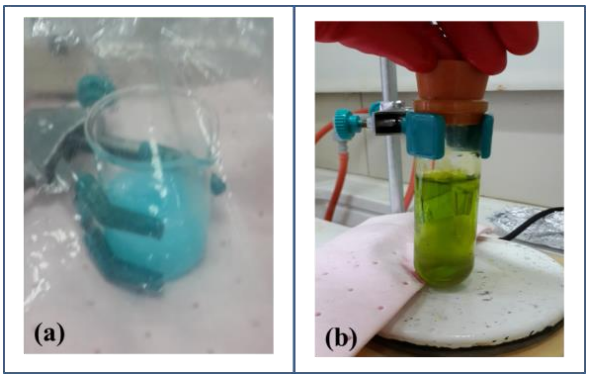

Figure 3.3 : The CIGS sol **(a)** before **(b)** after pH adjustment.

The resulting mixture was stirred with a magnetic stirrer to ensure effective homogenization (Figure 3.4). The colour of the solution changes considerably due to the increase of pH effect.

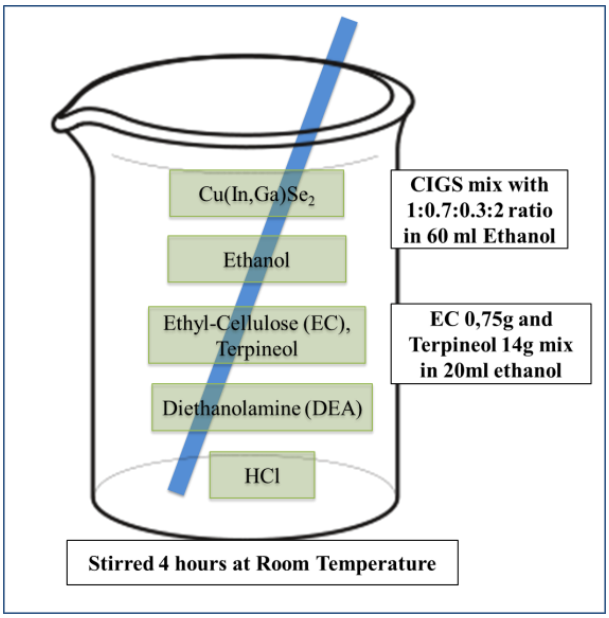

Figure 3.4 : The Preparation of CIGS Sol [73].

The preparation of solution was performed at room temperature in an air atmosphere. The relative humidity of the laboratory environment was held as constant at ~ 43% by using a dehumidifier while preparing the solution and during the dip-coating process (Figure 3.5).

Figure 3.5 : The laboratory conditions.

3.2.3.2 The pH adjustment

The pH-value of CIGS solution is controlled meticulously to obtain the colloidal transparent solution (Figure 3.3b). Hence it was possible to obtain a suspension consisting of a mixture of liquids with CIGS particles. CIGS particles may not dissolve in the obtained solution. The exact shifting point from the suspension mixture to the transparent colloidal structure is observed carefully. The rise of the transparency of the solution corresponds to the decrease in their pH-value. The acidity of the solution has increased until a certain value with the decrease of the pH-value. The pH-value of this colloidal structure was accepted as the exact pH-value of the produced CIGS solution. The colloidal structure was dispersed in the CIGS based transparent liquid.

CIGS solution was prepared via the sol–gel route employing DEA and hydrochloric acid to stabilize pH level of the solution. To achieve different pH-value by obtaining the desired colloidal solution, terpineol is used as a main chemical material/ingredient. By adding terpineol the lower pH-values between 1 and 2 was

obtained. However, without the addition of terpineol the pH of the solution was adjusted precisely between 2.5 and 4.0. The addition of terpineol provided the decrease of the pH-value between 1 and 2.

The addition of terpineol effected the adhesion of the chalcopyrite $Cu(In,Ga)Se_2$ structure to the soda-lime-silicate glass substrate. On the other hand the addition of terpineol improved adhesion of the film with decreasing the uniformity of the thin-film structure. The pH-value was controlled with hydrochloric acid and/or acetic acid and measured with WTW pH3110 SET2 pH meter (Figure 3.6).

Figure 3.6 : The used pH meter in the preparation of CIGS thin-film.

The CIGS solution prepared at first has 0.5 pH-value which signifies high acidity [74]. Some stabilizing agents were used to coordinate metal cations in order to improve chemical homogeneity. Acidity was controlled after the addition of stabilizing agent-DEA into the solution and there is a saturation condition of pH-value at 9-10. The pH-value at 9 gives the opaque appearance and a blue colour to the solution [74] (Figure 3.3 a). Hydrochloric acid (HCI) and/or acetic acid were added to the solution to perform a clear and a transparent colloidal solution. The effect of pH of the transparent colloidal solution was investigated at different pH-values between 1 and 4 by adding acetic acid and/or hydrochloric acid.

3.2.3.2 Sol aging

The thin-films were deposited from the aged colloidal solution which kept at -5 °C in a dark environment in order to prevent precipitation and to extend the life of the solution (Figure 3.7). The CIGS solution was aged at two different elapsed time as 18 and 35 days.

Figure 3.7 : The aged sol samples at -5 °C in a dark environment.

3.2.3.2 Preparation of sol in the inert conditions

Some parameters such as thickness, annealing temperature, annealing time were investigated with the CIGS solution produced under the inert gas atmosphere at room temperature. The experiment set-up was performed inside a vacuum–bag as seen in Figure 3.8. The air inside the vacuum-bag was sucked at first and the inert gas was pumped inside this vacuum-bag. The atmosphere was obtained with Argon Gas (Linde, %99.998).

Figure 3.8 : The experiment set-up at the inert ambiance.

All the new precursors were openned and used for the experiment in the inert atmosphere. The weightining and stiring proccesses were done inside this vacuum-bag as shown in Figure 3.9.

Figure 3.9 : The experiment set-up at the inert ambiance with the holding unit.

The mixing was finalized inside this bag properly with holding apparats (Figure 3.9). Till the sol formation it was kept inside the bag and the sol inside the beaker was covered with a parafilm and taken for the dip-coating process.

3.2.3 Substrate preparation

Thin-film growth and adhesion of the film to the substrate can be related to the cleaning process of substrate considerably. After subjugated to the proper cleaning process the surface of the substrates contain plenty of hydroxyl groups. Sufficient amount of hydroxyl (–OH) groups inside the sol helps to determine the good adhesion onto soda-lime silicate glass substrates [75]. Therefore, it is essential to clean the substrate thoroughly before the deposition process. Ultrasonic cleaning method was used to clean the surface throughout the study. For ultrasonic cleaning Bondelin Sonorex Ultrasonic Bath was utilized (Figure 3.10).

Figure 3.10 : Bondelin Sonorex ultrasonic bath for substate preparation.

The microscope slides of ISOLAB in 76 x 26 mm [3 x 1 inch] dimensions were used as soda-lime silicate glass substrate. The glass pieces are first sinked in a dilute solution of chemical detergent prepared from highly pure water to dissolve the unwanted contaminants like organic molecules from the surface at a temperature of about

100 °C. Then, the deionized water solution containing substrate pieces is put into ultrasonic cleaner to increase the efectiveness of remove of the unwanted contaminants and the layer of residue on the surface. Same procedure was repeated for acetone solution in ultrasonic bath for 15 minutes to increase the efectiveness of the rinsed in pure deionized water process and rinsed with acetone than dried in drying oven.

All laboratory equipment that were used for sol and substrate preparation were cleaned with detergent at first, rinsed with water and kept inside the water for some time. Than rinsed with the solution of sulfuric acid (H_2SO_4), Potassium dichromate ($K_2Cr_2O_7$) and then rinsed with water. Again kept inside the water for some time. De-ionized water was used for clear rinsing and dried in drying oven at 100 °C.

3.2.4 Coating process of CIGS thin-film

After completing the cleaning process, the cleaned soda-lime silicate glass substrates were immersed in the readily-prepared CIGS colloidal solution into and withdrawn from the solution at a rate of 1 mm.s^{-1}, and were kept in the solution for 5 seconds by employing a computer-controlled dip coater (KSV-LMX2) (Figure 3.11). The films were then dried at 100 °C for 10 min in an air ambiance as a pre-annealing process.

Dipping process was repeated three times while investigating pH effect and beta effect for the aged sol and five times by observing temperature effect [11]. Hence it is eventual to make an assessment for the effect of withdraw speed to the improvement of optical and electrical properties of the CIGS thin-film.

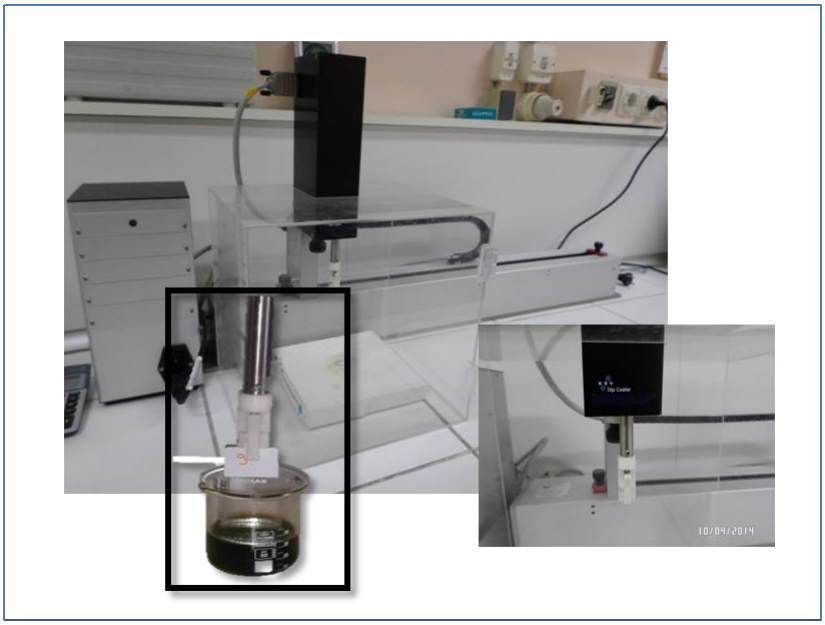

Figure 3.11 : Computer-Controlled Dip Coater Equipment (KSV-LMX2).

3.2.5 Annealing process of CIGS thin-film

The CIG thin-films were annealed at different temperatures between 135-200 °C for 30 min in air ambiance. Consequently, it is possible to make an improvement in the crystalline properties with the change in annealing temperatures. The used furnace for the annealing process was Binder 300 °C FD53 model which is presented in Figure 3.12.

Figure 3.12 : The furnace used in the thin-film preparation.

3.3 Characterization of Solution

Differential thermal and thermo gravimetric analyses (DTA/TGA) were performed using Perkin Elmer Diamond TG-DTA thermal analyses equipment in order to investigate the thermal behaviours of CIGS thin-films. These analysis were performed in an air atmosphere with a 10 °C.min^{-1} heating and cooling rate from room temperature to 500 °C and from 500 °C to room temperature, respectively. A noticeable mass loss was observed at the endothermic peak up to ~ 170 °C according to the analysis in Figure 3.13. There is a set value for the crystallisation of deposited film at an annealing temperature [11]. The annealing is performed for 30 min in air after the final drying.

Figure 3.13 shows that approximately 15 % of the total weight loss occurred up to ~ 150 °C. This slight weight loss may indicate the evaporation of water and solvents. DTA results may associate with the creation of slight crystallittes at ~ 200°C. Besides, DTA curve of the endothermic peaks at around 250 °C may associate with the evaporation of water, solvents and other organic compounds, respectively. Surface morphology of CIGS thin-films were investigated after annealing at 150 °C and 200 °C, respectively. The annealing temperature was defined as 150 °C for the crystallization of film annealed at the lowest temperature in economic conditions.

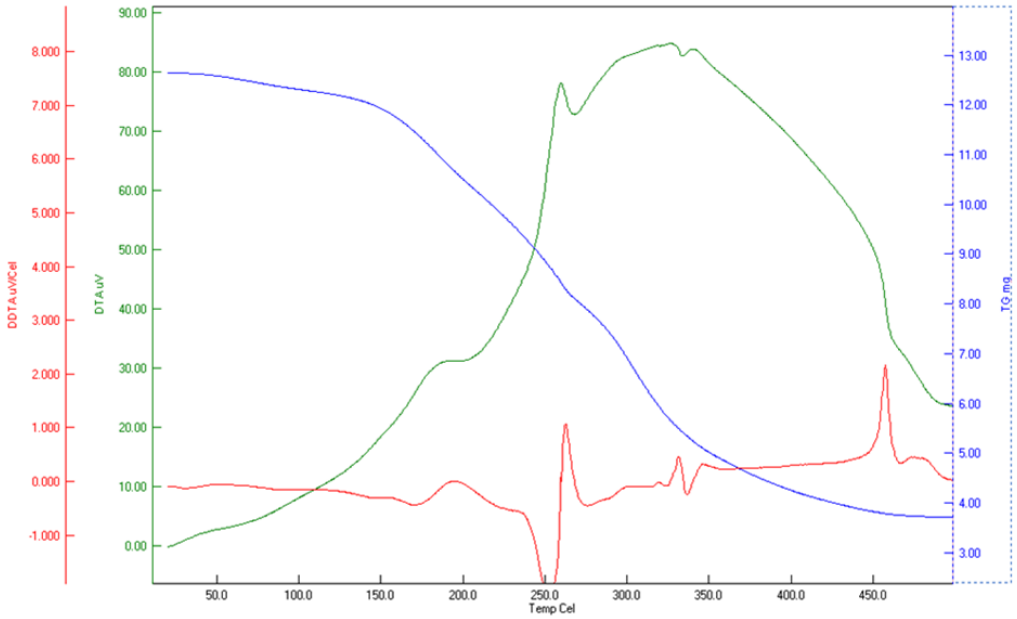

Figure 3.13 : DTA/TG analysis of the CIGS powder without Terpineol.

Figure 3.14 presents DTA/TG analysis of the CIGS powder with Terpineol. There was a slight change their results with repect the results of DTA/TG analysis of the CIGS powder with Terpineol. Besides, there was more weight loss with addition of terpinol into the solution.

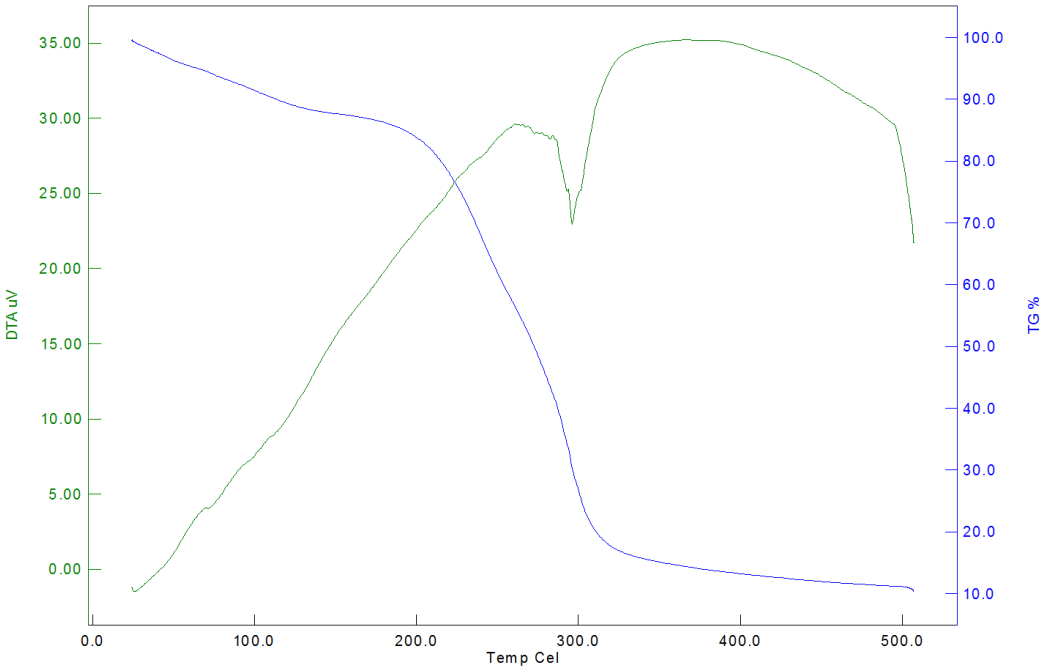

Figure 3.14 : DTA/TG analysis of the CIGS powder with Terpineol.

3.4 Characterization Methods of CIGS Thin-Films

In this study, CIGS thin-films were produced in Characterization Laboratories of ITU Metallurgical and Materials Engineering Department and ATARC Prof.Dr. Adnan Tekin Material Sciences & Production Technologies Applied Research Center. Irradiation process, XRF analysis and optical measurements by using a UV/VIS spectrophotometer were performed in ITU Energy Institute. Electrical resistivity was determined by using four point prob technique and surface morphology were examined by SEM images in the Research and Development Department of ŞişeCam and MEM-TEK Prof.Dr. Dinçer Topacık National Research Center on Membrane Technologies. AFM images of the films were obtained in ITU Mineral Processing Engineering Department. The structural behaviors of CIGS thin-films were investigated by using X-Ray diffractometer in the ŞişeCam Research and Development Department and Characterization Laboratories of ITU Metallurgical and Materials Engineering Department.

3.4.1 Structural characterization methods

Structural characterization of the CIGS thin-films was performed by X-Ray diffraction (XRD) and the compositional analyses of the thin-films was determined by Scanning Electron Microscope (SEM) equipped with Energy Dispersive Spectrometer (EDS), X-Ray fluorescence (XRF) and atomic force microscopy (AFM).

The thickness of the thin-film was measured by using a Veeco Dektak 6M surface profilometer. Partially coated on soda-lime silicate glass were scanned along a number of lines. The scanning begins from the uncoated part and forward to the coated parts. The height difference between the uncoated and coated sections were taken as the average film thickness. The thickness of the film was measured by using the surface profilometer [76]. Three layers coated CIGS thin-films of thickness ~ 82 nm are grown by sol-gel dip coating at a rate of 1 $mm.s^{-1}$ withdraw speed onto 76 x 26 mm [1 x 3 x 1 / 20 inch] soda-lime silicate glass substrate. Five layers coated CIGS thin-films has a thickness of ~ 150 nm.

Thin-film solar cells become feasible with this absorber layer with a thickness below two micrometer that absorb most of the incident solar power [77].

The decrease of the thickness of the absorber layer saves raw materials as well as energy input in the production process.

3.4.1.1 XRD analysis

X-ray diffraction (XRD) is an important tool for the structural investigation of crystalline materials, is used to investigate crystal structure and orientation of the films. XRD is a non-destructive technique studying information on structure, crystal orientation, phase, lattice parameter of the thin-film samples.

The X-Ray diffraction patterns of the thin-films were taken employing a Rigaku D/Max-2200PC X-Ray diffractometer (Figure 3.15) with a X-Ray source of 1.54059 Å-wavelength Cu-Kα radiation in the scan range of 2θ=10°-90° with 2° min^{-1} constant scan speed. X-Ray diffractometer was operated at 50 kV and 30 mA, with a power of 1.2 kWatt. The XRD peaks were analyzed with JCPDS – Joint Committee for Powder Diffraction Data and Database of computer program, Windows-Qualitative Analysis Version 6.0.

Figure 3.15 : X-Ray diffractometer (XRD).

3.4.1.2 SEM-EDS analysis

A focused beam of high-energy electrons is used to generate a variety of signals at the surface of the substrates. From the reveal information the electron-sample interactions form signals about the sample including chemical composition, external

morphology (texture) and crystalline structure and orientation of materials making up the sample [Url-9]. SEM is also non-destructive technique.

The surface morphology of the films was investigated using JEOL JSM-6360LV Scanning Electron Microscope (SEM) with a 15kV accelerating voltage, magnification ranging from 100X to approximately 3,000X (Figure 3.16). The SEM is also capable of performing analyses of selected point locations on the sample; this approach is especially useful in determining chemical compositions qualitatively or semi-quantitatively by using EDS [Url-9]. The composition of the film was analyzed with an ThermoNoran System Six Energy Dispersive Spectrometer (EDS) attached to SEM.

Figure 3.16 : Scanning Electron Microscope (SEM)- Energy Dispersive Spectrometer (EDS) - JEOL JSM-6360LV.

The surface morphology of the films was investigated also with FEI Quanta FEG 250 Scanning Electron Microscope (SEM) with a 10kV accelerating voltage, magnification ranging from 3,000X to approximately 12,000X (Figure 3.17).

Figure 3.17 : Scanning Electron Microscope (SEM) Quanta FEG 250 [Url-10].

3.4.1.3 XRF analysis

XRF Spectrometry is used to identify elements in a substance and quantify the amount of those elements present. An element is determined by its characteristic X-ray emission wavelength (λ) or energy (E). The amount of an element present is quantified by measuring the intensity of its characteristic line. XRF Spectrometry ultimately determines the elemental composition of a material [78]. X-Ray Fluorescence (XRF) technique was used to determine the possible chemical contamination in the CIGS thin-film composition by using Innovative XRF Technologies Alpha Series 2003 (Figure 3.18).

Figure 3.18 : X-Ray Fluorescence Spectrometers.

3.4.1.4 AFM analysis

The samples were characterized with the AFM operating, which allowed us to determine their morphological surface properties such as roughness, mean grain size, grain boundaries and power spectrum density. The surface morphology of the films was evaluated by using XE-Series Park Systems SPM Controller XE-70 Atomic Force Microscopy (AFM).

3.4.1.5 Determination of Structural Parameters

The incident photon beam scatters from each lattice planes at a certain angle. The peak intensity, which is determined by the XRD analysis, of a given reflection is proportional to the number of lattice planes according to diffraction condition.The diffracting planes, are shown with (hkl) Miller Indices, angles (the incident beams and diffracted beams) are equal [79].

The interatomic distances between the crystal planes are calculated according to the Bragg Law using the results of XRD analysis. The basis of this law is briefly illustrated in Figure 3.19 which shows the diffraction from the atomic planes.

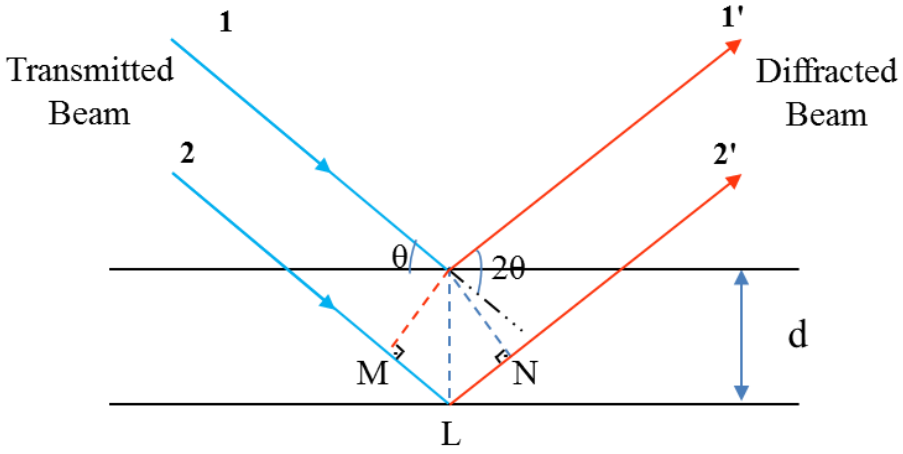

Figure 3.19 : The illustration of the diffraction from atomic planes.

The incident beam scatters from the parallel lattice planes with an angle θ and wavelength λ (Figure 3.19) [79]. The diffracted beam and the transmitted beam makes always 2θ angle with each other, which is known as the diffraction angle and is usually measured experimentally.

The optical path difference can be written as **(3.1)**. The **(3.1)** is the diffraction conditions called as Bragg Law [80].

$$ML + LN = d'\sin\theta + d'\sin\theta \quad \textbf{(3.1)}$$

From the geometrical approach **(3.1)** is easily determined as in (**3.2)**.

$$\sin\theta = \frac{ML}{d'} = \frac{LN}{d'} \quad \textbf{(3.2)}$$

The condition for diffraction happens when the difference between the transmitted beam 1 and 1' and the diffracted beam 2 and 2' are equal with an integer (n) number of wavelengths of the incident photon which is X-rays in here **(3.3)**. Bragg scattering can occur with a condition of $\lambda \leq 2d$ [79].

$$ML + LN = 2d'\sin\theta = n\,\lambda \quad \textbf{(3.3)}$$

"A reflection of any order can be considered as a first-order reflection from planes, spaced at a distance 1/n of the previous spacing. So that, d=d'/n can be set and the Bragg law can be written in the form of **(3.4)**" [80].

$$\lambda = 2d\sin\theta \quad \textbf{(3.4)}$$

In this expression **(3.4)**, λ is the wavelength of the X-rays, *d* is the spacing of the planes (interatomic distance), and θ the glancing angle at which the X-rays are diffracted [81].

The XRD analysis is also used to estimate the particle size of very small crystals from the measured width of the diffraction curves as a rough measure [80].

The average crystallite (grain) sizes are calculated from the XRD data using Debye-Scherrer formula **(3.5)** [80].

$$D = \frac{0.9\lambda}{B\cos\theta_B} \quad \textbf{(3.5)}$$

The crystallite size is determined by D in nanometer; θ_B (theta) is the diffraction angle [82], is called also Bragg angle, in degree and B is measured in radian at an intensity equal to half the maximum intensity, is expressed as FWHM (Full Width Half Maximum) (Figure 3.20) [80]. Less FWHM means more crystallinity [47]. As can be seen in Figure 3.20 the increase of the width of the diffraction curve result with decrease of the crystal thickness [80].

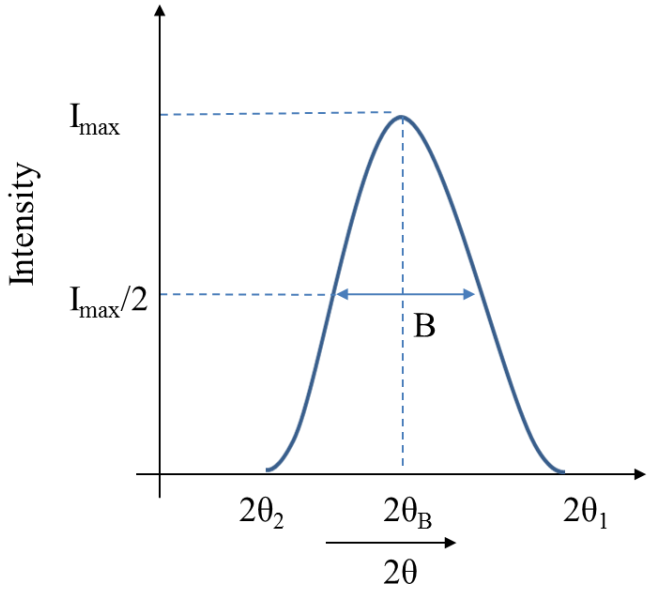

Figure 3.20 : The illustration of X-Ray Diffraction Peak.

3.4.2 Optical characterization method

For many applications such as optoelectronics, solar power engineering, optical sensor technology, integrated optics, microelectronics the optical properties of thin-films are very important. Investigation of optical properties of materials generally focuses on optical energy band gap, absorption, refraction index and photoconductivity.

3.4.2.1 UV/Visible spectrophotometer

The UV/VIS Spectrophotometer was used for the optical measurements (Figure 3.21). UV, visible and near-ultraviolet regions were examined to focus on the investigation of optical properties and energy gap of the deposited CIGS thin-films and optical properties such as absorbance, transmittance and reflectance as a function of wavelength.

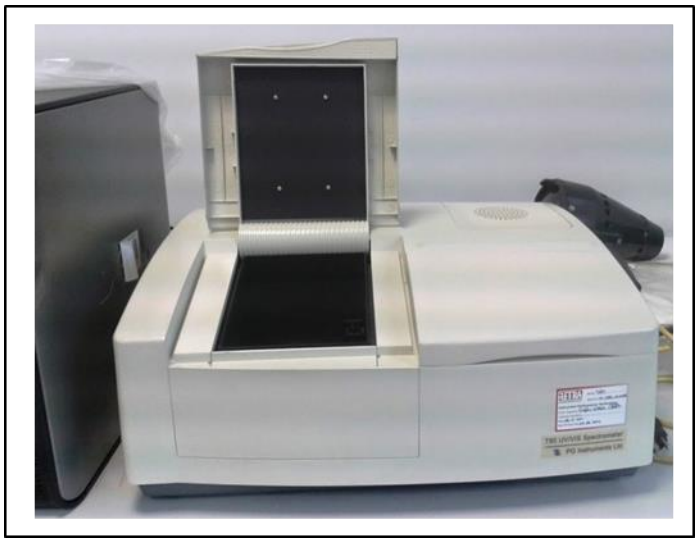

Figure 3.21 : The UV/Vis Spectrophotometer.

The absorption measurement is one of the significant techniques for the determination of energy band gap of semiconductor materials. This technique is based on interaction of the photons with the material, which gives rise to transmission or absorption according to the energy of the photons [79]. The optical measurements have been carried out by PG Instruments T80UV/VIS Model, double beam spectrophotometer in the 190 - 1100 nm wavelength range. The measurements were performed with a 0.5 % T (0 ~ 100 % T) photometric accuracy. The bare glass substrate has been used for reference. All measurements were performed at room temperature (295 K).

In a double beam spectrophotometer, the light source splits into two separate beams before it reaches the sample [Url-11]. One beam passes through the CIGS deposited glass sample and the second one is used for reference.

3.4.2.2 Determination of optical parameters

In transmission measurements, the spectrophotometer quantitatively compares the amount of light passing through the reference and test sample. For reflectance, it compares the amount of light reflecting from the test and reference sample solutions [Url-11].

The intensity of light passing through a sample (I) and the intensity of light (through the reference cell) before it passes through the sample (I_o) are measured. The ratio (I/I_0) is called the optical transmittance, and is usually expressed as a percentage (%T). The absorbance (A) is based on the transmittance as given in **(3.6)**;

$$A = \ln\left(I_0/I\right) = -\ln T \tag{3.6}$$

The absorption coefficient (α) is calculated from the obtained optical measurement values as Manifacier model in **(3.7)** [83],

$$\alpha = \frac{\ln\left((1-R)/T\right)}{d} \tag{3.7}$$

where *R* is optical reflectance (%) and *d* is the thickness of the film in cm.

The relation between the absorption coefficient and the incident photon energy is given in Equation **(3.8)**,

$$\alpha(hv) = A\left(hv - E_g\right)^{1/n} \tag{3.8}$$

where A is a constant and a function of reduced electron and hole masses, E_g is the optical energy band gap energy (transition energy) of semiconductor and n is an index, which changes according to the transition types. In an allowed direct transition n value is determined as 1/2, for indirect transition as 2 [84-85]. The optical energy band gap is determined by extrapolating the linear portion of the $(\alpha h\nu)^2$ versus hν graph to hν=0.

The refractive index is one of the optical parameters investigated in this study. It is an effective parameter for optical materials and applications. "It is closely related to the electronic polarizability of ions and the local field inside materials" [86]. Refractive index is an efficient parameter which set forth the optical quality of CIGS thin-films.

The reflectance (R) is related with refractive index (n) and extinction coefficient (k) and can be determined by using the relation (**3.9)** [87].

$$\mathrm{R} = \frac{(\mathrm{n}-1)^2+\mathrm{k}^2}{(\mathrm{n}+1)^2+\mathrm{k}^2} \tag{3.9}$$

From **(3.9)** the equation **(3.10)** can be derived;

$$\mathrm{n} = \left\{\frac{(1+\mathrm{R})}{(1-\mathrm{R})}\right\} + \left\{\left[\frac{1+\mathrm{R}}{1-\mathrm{R}}\right]^2 - (1+\mathrm{k})^2\right\}^{1/2} \tag{3.10}$$

The extinction coefficient is conjugated to absorption coefficient (α) with **(3.11)** equation [88].

$$k = \frac{\alpha\lambda}{4\pi} \quad \textbf{(3.11)}$$

3.4.3 Electrical characterization method

Electrical characterization measurements are to determine important parameters which are very important aspects of estimating the material quality and device behavior. Electrical characterization contains plenty of measurement one of those includes surface resistivity measurement. Electrical conductivity can be found from surface resistivity measurement. The electrical conductivities of CIGS thin-films were measured to investigate the electrical characteristics of the samples [79].

3.4.3.1 Four-point probe

The surface resistivity of CIGS thin-films were determined as sheet resistance in Ω/□ (omega/ square) by using a four-point resistivity probe, employing SIGNATONE four point probe mounting stand in Figure 3.22.

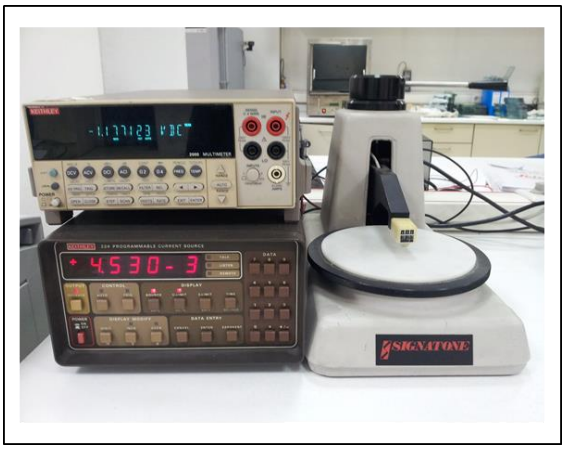

Figure 3.22 : Manual four point resistivity probing equipment.

A four point probe is a simple apparatus for measuring the surface resistivity (sheet resistance) of semiconductor samples. By passing a current through two outer probes and measuring the voltage through the inner probes allows the measurement of the substrate resistivity. This method is called as Van der Pauw method (4-points) [Url-12].

3.4.3.2 Determination of electrical parameter

One of the most important electrical parameter of the semiconductors is resistivity. Electrons and holes contribute to the current and determine the resistivity (and also conductivity) in semiconductors [79]. The resistivity is expressed in Equation **(3.12)**;

$$\rho = \frac{V}{I}\frac{wt}{L} \quad \textbf{(3.12)}$$

I is current, w is the width of film, t is thickness and L is the spacing between the contacts across the voltage (V) is measured.

The resistivity (ρ) values that depend on thickness were calculated in (Ω-cm). Conductivity of material can also be found from resistivity. The surface conductivity (σ) of the film was calculated regarding the resistivity in **(3.13)** [28].

$$\sigma = {}^{1}/_{\rho} \quad \textbf{(3.13)}$$

3.5 Beta Irradiation Process

In this study, Strontium-90 (Sr-90) radioisotope was used as radioactive source to investigate the radiation effects on CIGS thin-film properties. Sr-90 radioisotope has a half-life of 28.1 years and undergoes β^- decay into Yttrium-90, with a decay energy of 0.546 MeV (Figure 3.23) [89,90].

The equation of the Sr-90 decay is presented at equation **(3.14)** [89]:

$$^{90}_{38}\mathrm{Sr} \rightarrow {}^{90}_{39}\mathrm{Y} + \mathrm{e} + \bar{\nu}_e \quad \textbf{(3.14)}$$

Strontium emits electrons with a continuous distribution of kinetic energies, having a maximum kinetic energy value which can not be reached by most of the electrons. Specific range for nucleus decay can be between 0.5-2 MeV. Yttrium element is denoted with (Y) symbol. Nevertheless, energy conservation and momentum must be considered as well. In 1930 Wolfgang Pauli hypothesized a third undetected particle which is included to the parent nuclide (in here Sr), daugther nuclide (Y) and electron. This undetected third particle was found empirically afterwards and called antineutrino ($\overline{\nu_e}$). The difference between maximum kinetic energy and kinetic energy of electrons is absorbed by antineutrino. Neutrinos has no charge and possess a very small mass. In air, the range of Negatron (Beta-minus-β^-) radiation is about 1.5 to 8.5 m depending on their kinetic energy. Due to the electric charge of the electrons these particles can be deviated by electric and magnetic fields [Url-13].

Energy-level diagram of Sr-90 [Url-13] is presented in Figure 3.23.

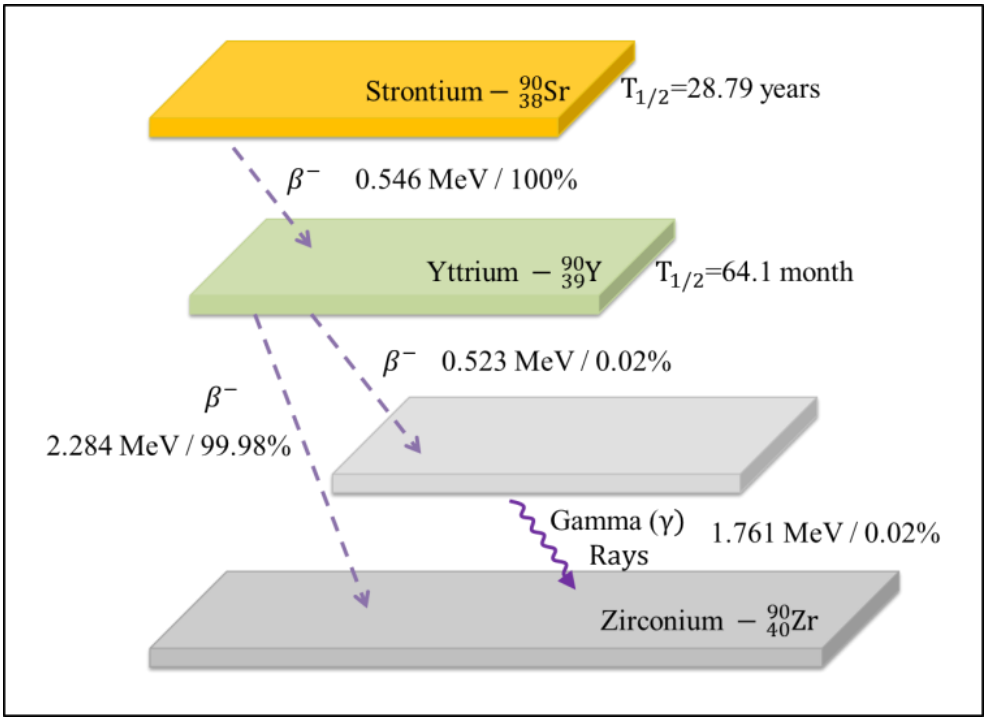

Figure 3.23 : Energy-level diagram of Sr-90.

The details of the produced beta radiation are presented in Table 3.2 [89,90].

Table 3.2 : Details of the beta irradiation source.

Radioisotopes	Maximum Kinetic Energy (MeV)	Half-life
38-Sr-90	0.546	28.1 year
39-Y-90	2.284	64.1 hours

The parent nuclide is decaying into Yttrium, with a half-life of 64.1 hours, emitting electrons with a maximum kinetic energy of 0.546 MeV [66,Url-14]. Yttrium is the intermediate nuclide and can decay further by two different decay channels into Zirconium which is a stable nuclide. The probability of the electrons emission of Yttrium daughter nuclide via the channel with maximum kinetic energy of 2.284 MeV is 99.98 %. The rest 0.02 %probability is the emission of electrons via the other channel. In the second emission channel, the excited nuclide emits Gamma (γ)-rays with maximum kinetic energy of 1.761 MeV [66,Url-14].

3.5.1 Irradiation setting

The certified beta source of a Strontium-90 radioisotope with 2.86 mCi activity at 0.546 MeV max electron energy [89] was used as the beta radiation source and the radius of the radioisotope was 0.015 cm. Properties of used Sr-90 radioisotope are presented in Table 3.3 [89].

Table 3.3: Properties of used Sr-90 radioisotope.

Radioisotope	**Activity (mCi)**	**Half-Life $T_{1/2}$ (y)**	**E_b (MeV)**	**Abundance (%)**
Strontium-90	3.58	28.1	0.546	~ 100

Samples were replaced around the beta irradiation source, panaromically, with a distance of 1.0 cm (Figure 3.24). Irradiation process was performed at room temperature.

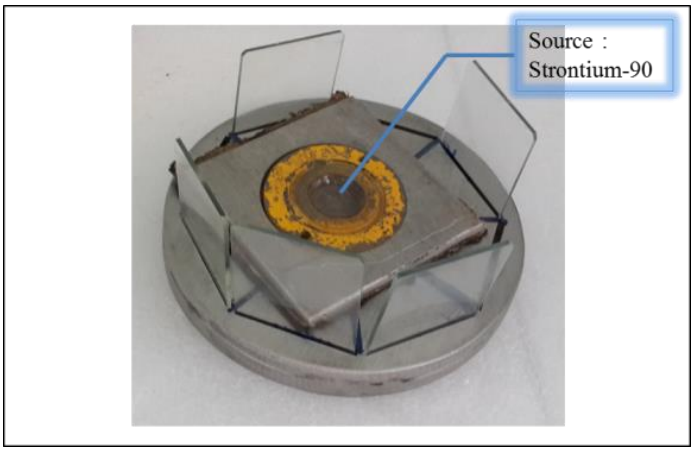

Figure 3.24 : Samples around the beta irradiation source.

The irradiation treatment was performed in a plexiglass cell in terms of shielding and besides, aluminium disks were placed on this cell to protect the environment from radiation (Figure 3.25).

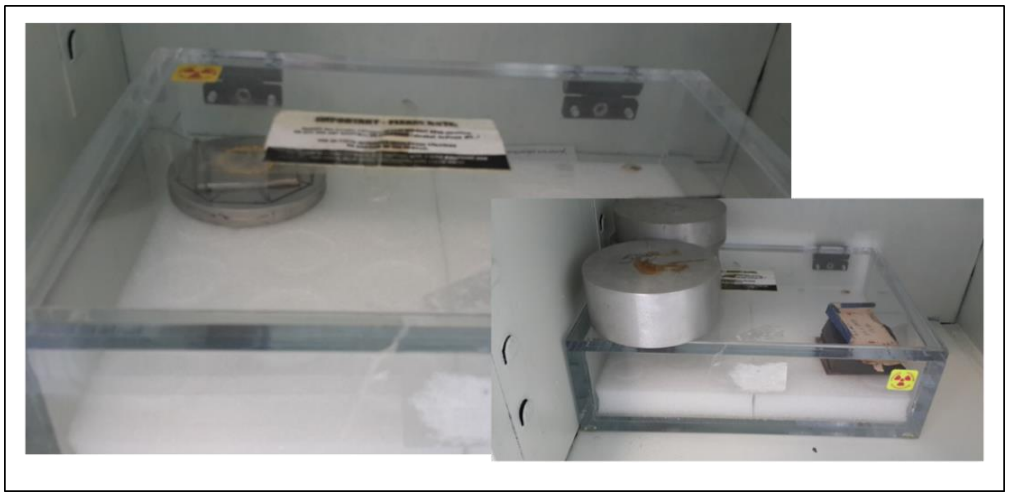

Figure 3.25 : Irradiation settlement of the samples.

The applied dose levels were selected as three different absorbed dose levels such as ~ 0.8; 1.5 and 4.3 Gy to examine the characteristic changes in the CIGS thin-film samples [11].

The selection of the radioisotope is very important depending on energy and half-life of the radioisotopes for the determination of the irradiation effect on the CIGS thin-film. Radioisotopes whose energy have under 0.5 MeV causes insufficient excitation and ionization at the glass structure [91]. If E > 1 keV, the electrons of the atoms at the CIGS thin-film structure can be excited by Compton Effect. The excess energy is converted to the kinetic energy. Therefore they will either recombine with positively charged holes, become trapped or if the energy is sufficiently high to produce a secondary electron cascade by knock on collisions with other bound electrons. Additional bound electrons are ionized by the secondary electrons through Coulomb interactions, secondaries losing approximately 20 eV for each ionization [92].

3.5.2 Irradiation dose calculation

The activity of the radioactive material may be calculated by a decay equation [93-94] which predicts activity at any time. **A** is the specific activity at t time; A_0 stands for initial acitivity value **(3.15)**. λ is the decay constant **(3.15** and **3.16**). There is a constant relation between half-life ($T_{1/2}$) of the radioactive material and the decay constant given in **(3.16)**

$$\mathbf{A} = A_0 \cdot e^{-\lambda t} \qquad \textbf{(3.15)}$$

$$T_{1/2} = \frac{0.69315}{\lambda} \qquad \textbf{(3.16)}$$

The activity of strontium-90 has been measured as 9.6 mCi in september 1959. From this year till the time it was used in the experiment it makes 54.75 year. So, initial activity was taken as 9.6 mCi and time as 54.75 year. the activity was calculated 2.4762 mCi.

The dose was calculated with a direct proportion. Ratio was based on for 154834.01 hour and the absorbed dose of the sample was 0.998 kGy. According to the irradiated time period, the irradiation amount was estimated.

4. RESULTS

This section of this study is to investigate the production parameters of CIGS thin-films to make a contribution for the improvement of the cost-effective method by using a sol-gel deposition technique and to obtain polycrystalline CIGS thin-films.

4.1 Production Parameters Effect

4.1.1 The pH effect

This section contributes to the effect of pH-value on the structural, optical and electrical properties of the sol-gel derived CIGS thin-films. The effect of pH on the structural, optical and electrical properties was investigated to determine the suitable pH-value with optimum electrical conductivity for the use of a potential absorber material depending of its favourable energy band gap (~ 1.6 eV) [74].

For this purpose $Cu(In,Ga)Se_2$ thin-films were deposited at different pH-values changing from 1 to 4 by using sol-gel dip coating technique [74]. The pH of the CIGS colloidal solution was adjusted by the addition of terpineol into the solution and by obtaining solution with different Se concentration. The substrates were immersed in this colloidal suspension and dried at 100 °C in an air ambiance for 10 min. This procedure was repeated three times. After the final drying, the samples were annealed at 150 °C, for 30 min, in an air ambiance.

Some data about the effect of the pH-values of CIGS solution and the response of the CIGS thin-films to the different pH-values in terms of the effect of the optical energy band gap at an optimum pH-value is investigated. The pH-value leads to variations in structural, optical and electrical properties of CIGS thin-films. Hence, it is neccessary to determine the details about optimum pH-values for the production of CIGS thin-film by sol-gel process [74].

4.1.1.1 Structural characterization

CIGS thin-films having thicknesses of about 80±5 nm were deposited on soda-lime silicate glass substrates to investigate the crystallinity and phase composition of the films by using X-Ray diffractometer. Figure 4.1 illustrates the X-ray diffraction patterns of the CIGS thin-films, prepared at various pH-values at 150 °C annealing temperature.

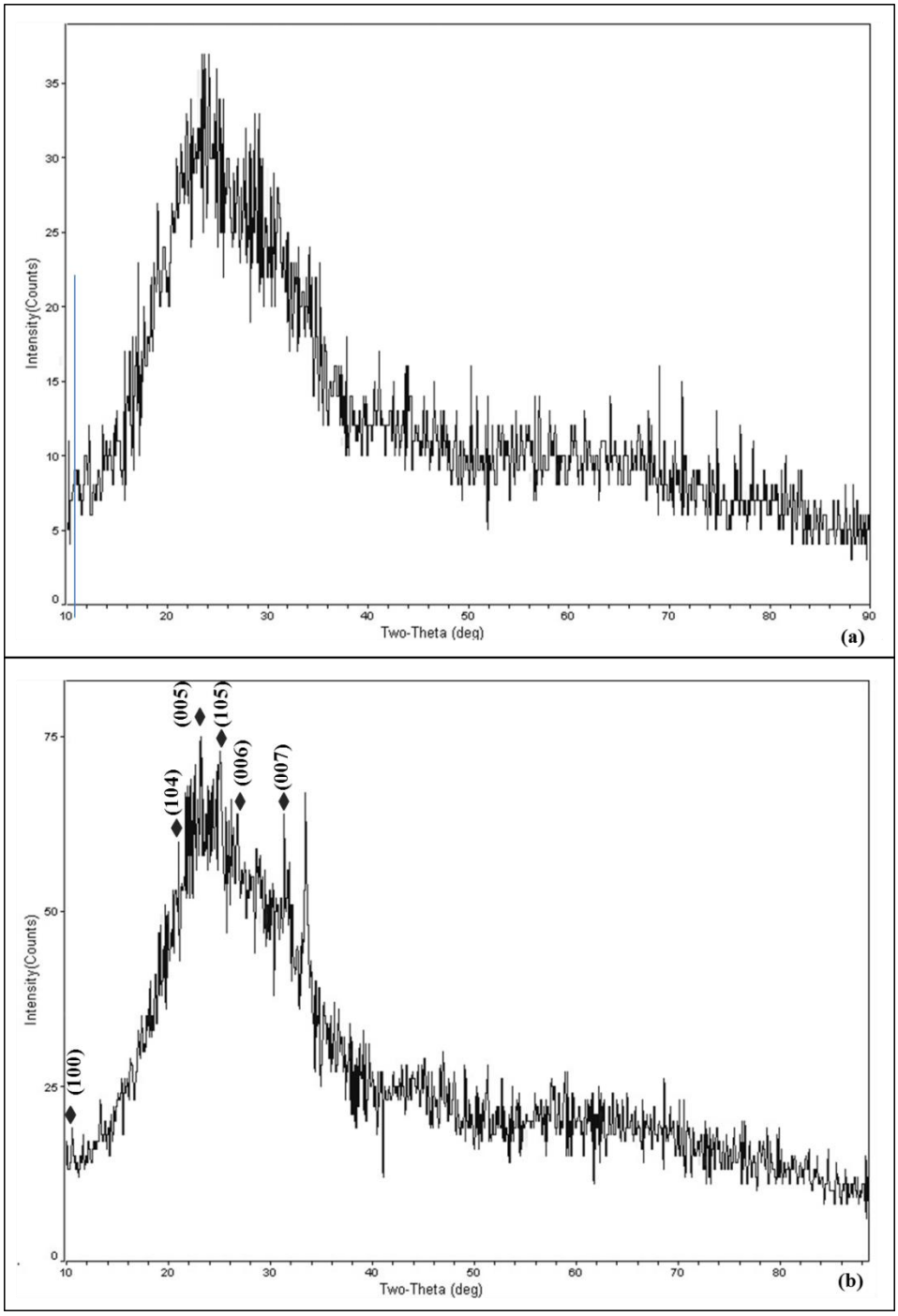

Figure 4.1 (Continued) : XRD patterns of 80 nm thick CIGS film at pH-values **(a)** 1.40; **(b)** 2.00; **(c)** 3.95.

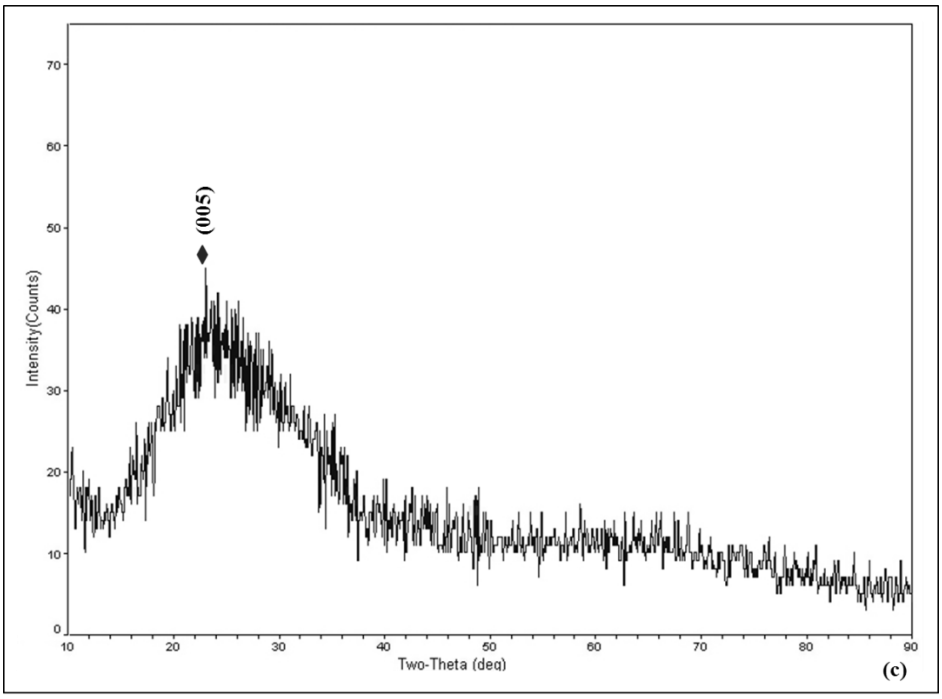

Figure 4.1 : XRD patterns of 80nm thick CIGS film at pH-values **(a)** 1.40; **(b)** 2.00; **(c)** 3.95.

X-Ray Diffraction data of ultra-thin CIGS film deposited on soda-lime silicate glass, which were produced from the solutions of 1.40; 2.00; 3.95 pH-values, is presented in Figure 4.1a, b, c, respectively. It was observed that although the intensity values of diffraction peaks of XRD patterns are not too high, yet they are slightly dependent on the pH-values as a result of the ultra-thin thickness of the film and makes slight differences in the intensity values.

The maximum intensity was observed at 2 pH-value. However, the peak intensity was weakly decreased at the smaller and bigger than 2 pH-values. The change in pH affects slightly the crystal structure of the film. Figure 4.1(b) shows that the XRD patterns of ultra-thin CIGS film matches with that of chalcopyrite $Cu_{0.28}In_{1.72}Se_{2.72}$ from Joint Committee for Powder Diffraction Data (JCPDS) of 39-0758 card number [95]. Those characteristic reflection peaks of $Cu_{0.28}In_{1.72}Se_{2.72}$ (JCPDS-39-0758) are indexed in the Figure 4.1b. The presence of reflection peaks placed on the diffuse halo of amorphous confirms the quasi-amorphous structure [96]. Due to the too thin film with a thickness of ~ 80 nm, XRD analysis was presented the quasi-amorphous structure at 2 pH-value.

The Theoretical X-Ray diffraction data of chalcopyrite $Cu_{0.28}In_{1.72}Se_{2.72}$ (JCPDS 39-0758) is presented in Table 4.1 [95,97].

Table 4.1 : Theoretical X-Ray diffraction data of chalcopyrite $Cu_{0.28}In_{1.72}Se_{2.72}$ (JCPDS 39-0758).

	JCPDS 39-0758		
(*hkl*)	d (Å)	2θ	I/I_0
(100)	8.120	10.886	5
(104)	4.143	21.429	20
(005)	3.917	22.681	100
(105)	3.519	25.287	10
(007)	3.273	27.223	80
(007)	2.805	31.876	60

The adjustment of the pH-value was based on the Se concentration and the inclusion of terpineol. To investigate the terpineol effect the samples were characterized with the AFM operating, which gives the morphological surface properties such as roughness (Figure 4.2a-b). Figure 4.2a presents terpineol included CIGS thin-film which exhibits very smooth top surface morphology and a dense, uniform and compact film. In contrast to Figure 4.2a, Figure 4.2b illustrates thin-film without inclusion of terpineol having a rough top surface [74].

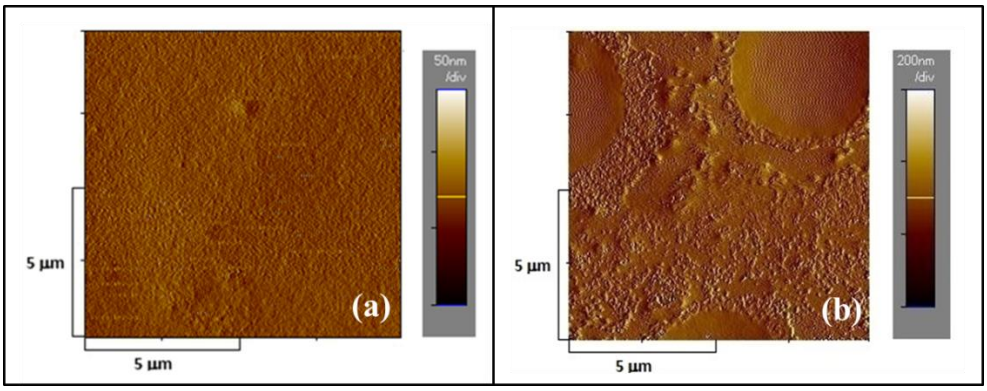

Figure 4.2 : AFM micrograph of the CIGS thin-film pH-values between **(a)** 1.0-2.0 (with terpineol); **(b)** 2.5-4.0 (without terpnieol).

SEM micrographs of the CIGS thin-film at 1.40, 2.46 and 3.95 pH-values of the colloidal solution are illustrated in Figure 4.3. SEM micrographs of CIGS thin-film annealed at 150°C in the air atmosphere magnified by 1,000X magnification. Figure 4.3 presents the pH effect on the surface of the electrical conductive

CIGS thin-film. Figure 4.3a illustrates ~ 1.5 pH-value which exhibits higher electrical conductivity as ~ 10^3 $(\Omega\text{-cm})^{-1}$ and shows relatively smooth surface and elongated pores in one single direction, might be from the withdraw direction of the substrate during the deposition process. In general, electrical conductive CIGS thin-films at ~ 1.5 pH-values exhibit elongated morphology on the surface. Some surface debris is also present which is more than 1.5 pH-value in Figure 4.3b-c. Figure 4.3b-c confirms the in homogeneity of the thin-film and some cracks which might cause less electrical conductivity and optical transmittance.

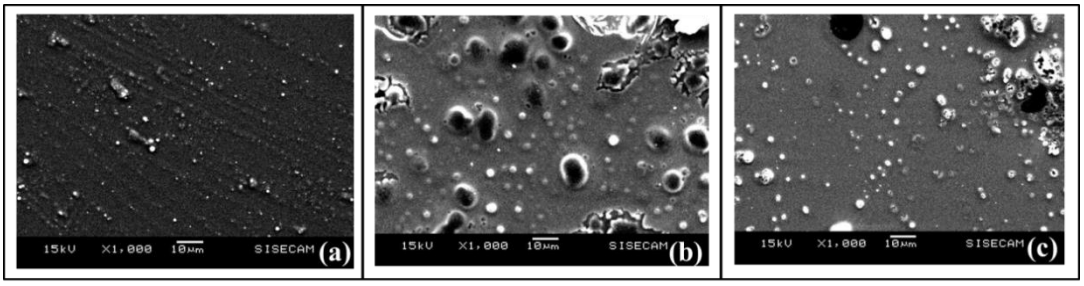

Figure 4.3 : SEM Image of the surface of CIGS thin-film at pH-values **(a)** 1.40; **(b)** 2.46; **(c)** 3.95.

The XRF results of the CIGS thin-films were given at different pH-values (Table 4.2). The change of the Cu and Se concentration on the surface with the rise of the pH can be observed. The increase of pH-value of solution from 1.40 to 3.95 indicates that the increase of selenium content improved the bonding of selenium to the chalcopyrite $Cu(In,Ga)Se_2$ crystal structure.

Table 4.2 : XRF analysis of CIGS thin-films with different pH-values.

	Elements (ppm)	
pH-value	**Cu**	**Se**
1.40	47 ± 10	88 ± 4
3.00	63 ± 10	122 ± 5
3.95	191 ± 14	265 ± 8

4.1.1.2 Optical characterization

The optical changes were considered with the spectral changes in the electromagnetic spectrum between 190 - 1100 nm. Figure 4.4 illustrates the transmittance and absorbance spectrum of the examined CIGS thin-films at various pH-values between 1-2. There is a considerable decrease of transmittance with the rise of pH-values which is corresponding a rise at absorbance.

The CIGS thin-films are non-absorbing beyond ~ 250 nm in the UV range of CIGS thin-film for all pH-values. A significant increase in the optical transmittance was performed at ~ 1.5 pH-values (Figure 4.4).

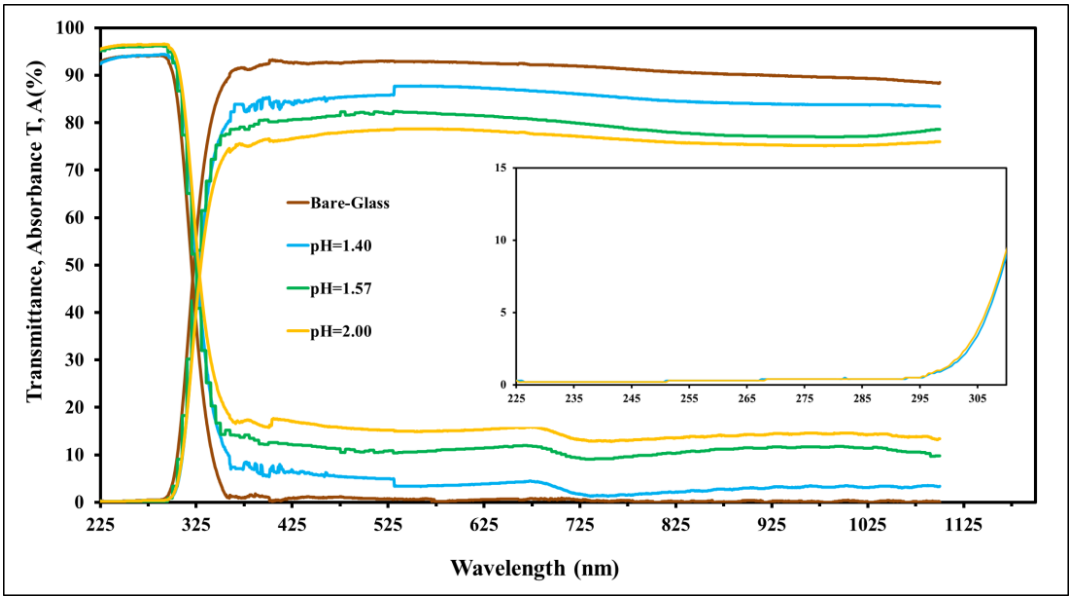

Figure 4.4 : Optical transmittance and absorbance spectra at 1-2 pH-values.

The increase in the optical transmittance of the thin-films is investigated with the decrease of pH-values between 1-4 at 550 nm wavelength clearly in Figure 4.5. The details of the optical transmittance are investigated for the visual sensation of human eye in the visible range at 550 nm.

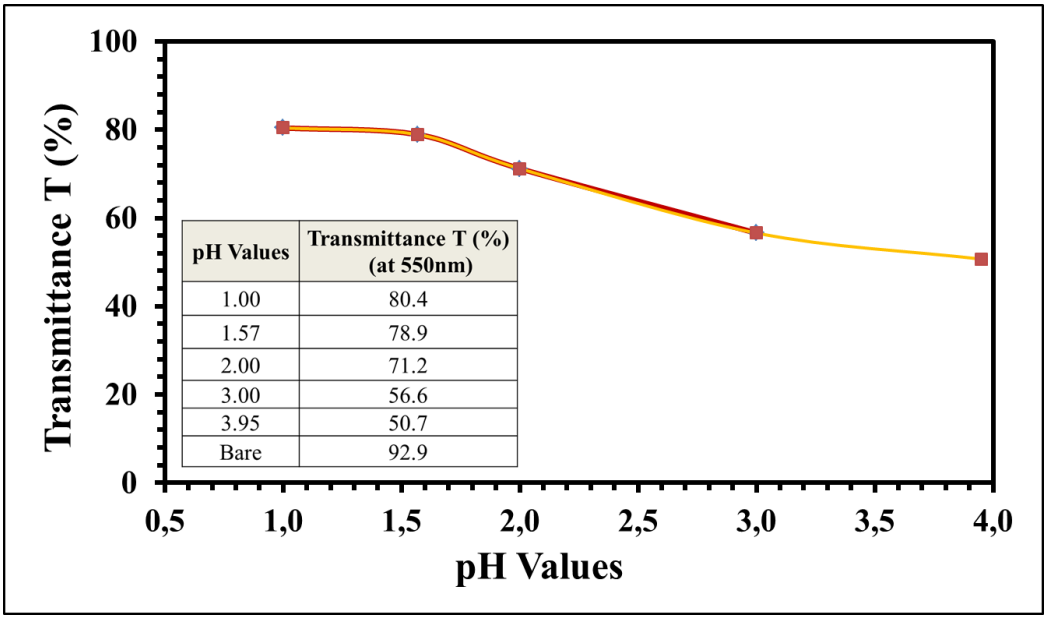

Figure 4.5 : The changes in the transmittance with the pH change at 550 nm wavelength.

Figure 4.6 shows the plots of $(\alpha h\nu)^2$ versus hν, drawn for CIGS thin-films. It is determined that there is an allowed direct transition of $(\alpha h\nu)^2$ for CIGS thin-film. The lowest optical band gap value was obtained at 2 pH-value. It is obvious that the changes in the optical energy band gap portray a blue shift at the 2 pH-value (Figure 4.6). The absorbance increases at the ideal pH-value which indicates 2 pH-value. The optical band gap is determined at 1.6 eV which achieves a high photoelectric conversion efficiency up to 19 %, as stated in the literature [16], at ~ 1.5 pH-value.

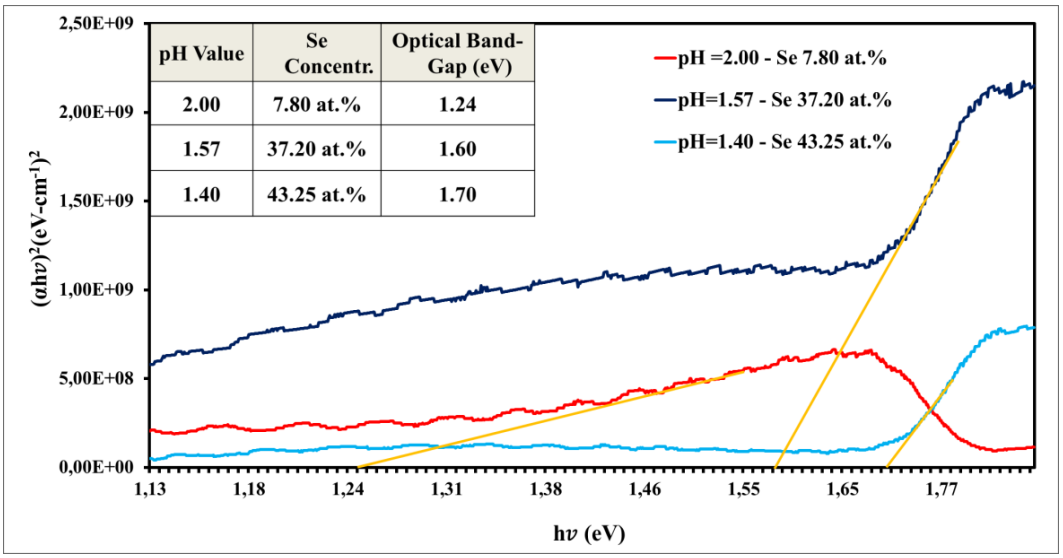

Figure 4.6 : The changes in the optical energy band gap with different pH-values.

4.1.1.3 Electrical characterization

The surface conductivity of the film was calculated from the measured resistivity values. The results were presented indicating variation of conductivity of the examined CIGS thin-films with respect to pH-value in Figure 4.7 [74].

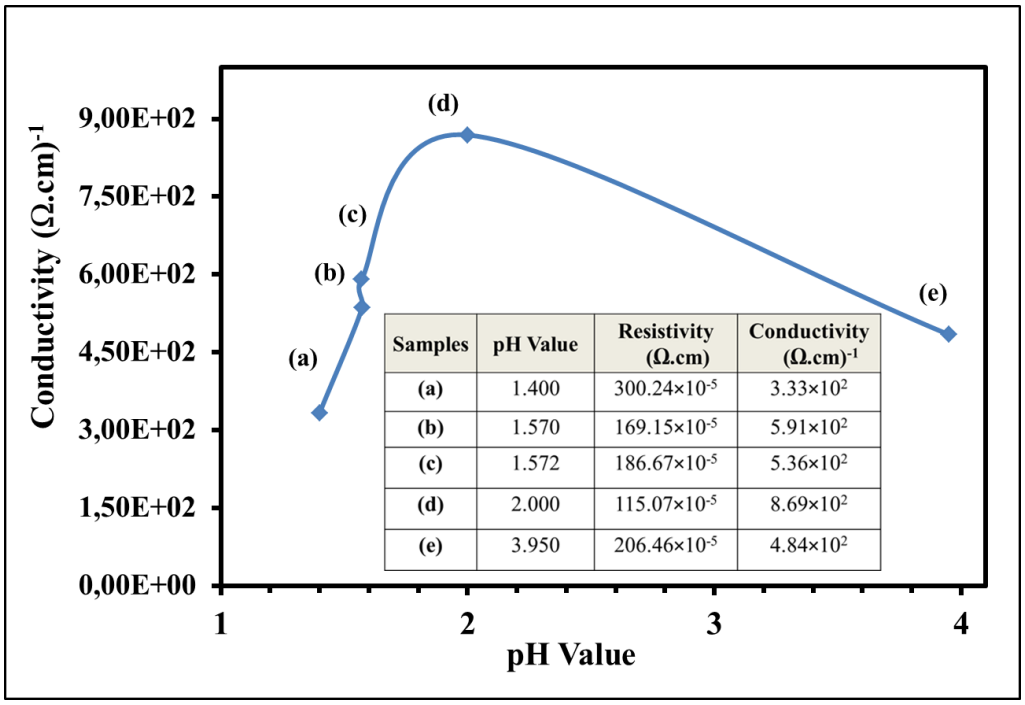

Samples	pH Value	Resistivity (Ω.cm)	Conductivity $(\Omega.cm)^{-1}$
(a)	1.400	300.24×10^{-5}	3.33×10^{2}
(b)	1.570	169.15×10^{-5}	5.91×10^{2}
(c)	1.572	186.67×10^{-5}	5.36×10^{2}
(d)	2.000	115.07×10^{-5}	8.69×10^{2}
(e)	3.950	206.46×10^{-5}	4.84×10^{2}

Figure 4.7 : The changes in electrical conductivity at different pH-values.

The electrical conductivity increased with the increase of pH of CIGS solution till 2 pH-value. However, the electrical conductivity was affected adversely with the raise of pH after 2 pH-value. The highest conductivity is obtained at ~ 2 pH-value which is 8.69 x 10^{2} $(\Omega.cm)^{-1}$.

The decrease of electrical resistivity of the CIGS thin-film annealed at 150 °C for 30 min in air atmosphere indicates the improvement of the crystallinity of the thin-film produced at ~ 2 pH-value from the solution [74].

4.1.2 Heat treatment effect

The quantum efficiency is accepted as the ratio of the number of carriers collected by the solar cell to the number of photons of a given energy incident on the solar cell. The quantum efficiency can be given either as a function of wavelength or as an energy. If all of the photons at a certain wavelength are absorbed and the resulting minority carriers are collected, then the quantum efficiency at this wavelength is unity [Url-14].

Several annealing processes provides better quantum efficiency due to the disappearance of non-radiative recombination centers [98]. Hence the enhancement of the annealing process in an economical way was a key parameter to improve the quantum efficiency of CIGS thin-film in this study.

The sol-gel derived CIGS thin-films were thermally treated at different temperatures for the further investigations. Two different types of solution were prepared; one of them is under the inert atmosphere and the other one is under the standard laboratory conditions to examine the temperature effect.

The visual quality control for the CIGS thin-film samples was presented in Figure 4.8. The coated and uncoated sides of the unannealed and annealed samples are seen clearly (Figure 4.8).

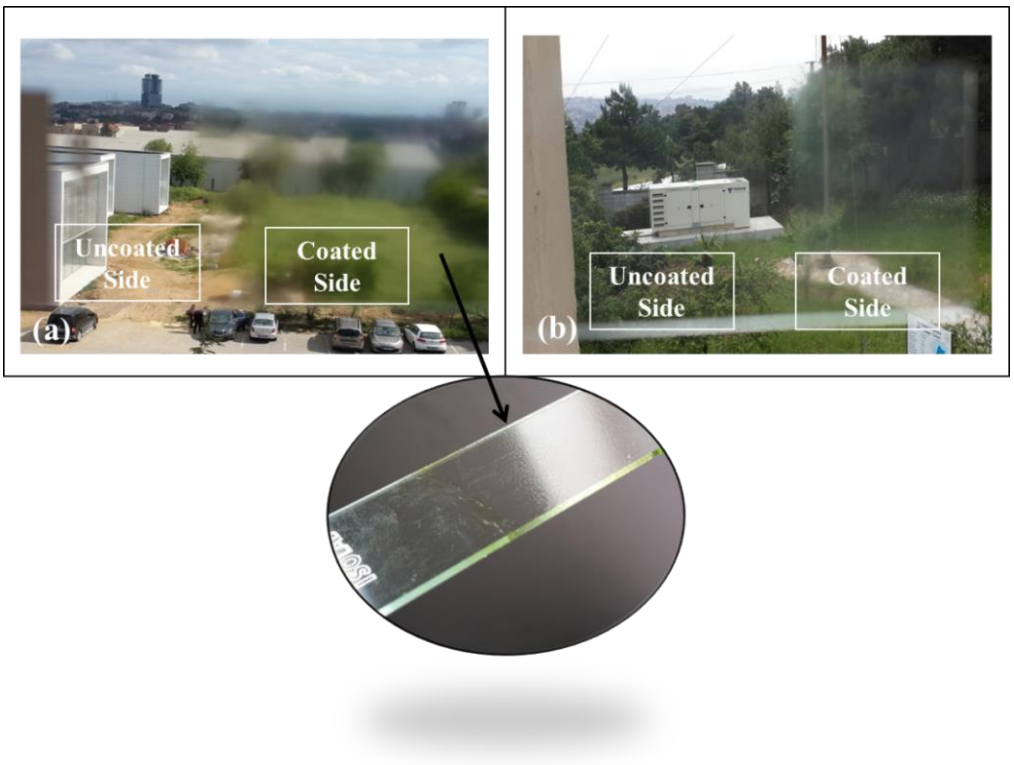

Figure 4.8 : The visual quality control **a)** before **b)** after the heat treatment.

4.1.2.1 Heat treatment effect of solution prepared in air

The CIGS sol was prepared in an air ambiance under the standard laboratory conditions. The details of the coating and drying processes were presented in the previous chapter. The drying process in each deposition was performed at 100 °C for 10 min in an air ambiance.

The three layers coated CIGS thin-film of 30 at.% Se concentration were annealed at 150 °C and 200 °C temperatures for 30 minutes under air ambiance. The optimum annealing temperature is determined according to the structural, optical and electrical characterization.

Structural characterization

The films derived from the solution prepared in the air are predominantly amorphous in nature (Figure 4.9). No visible peak exists in the XRD patterns. The CIGS thin-film samples are too thin to provide good crystalline structure unless grazing incidence is carried out. Very thin-films are pronounced at ~ 60 nm thickness which is too thin according to classical thin layer absorbers in the literature. In this study, XRD peaks of diffraction planes are weak for the produced CIGS thin-film. Ultra-thin CIGS film presents principally the results of very thin-film similar with halo of amorphous material (Figure 4.9). The collected XRD patterns of the CIGS thin-film were examined in order to compare the changes in the structural properties of before and after annealing processes. The difference of XRD patterns of CIGS thin-film samples annealed at 150 °C and 200 °C for 30 min are compared with as-grown CIGS thin-film in Figure 4.9, which signifies the annealing temperature at 150 °C provides higher intesity and narrower amorphous peak around 22.68° (2θ) which is the most characteristic peak of JCPDS-39-0758.

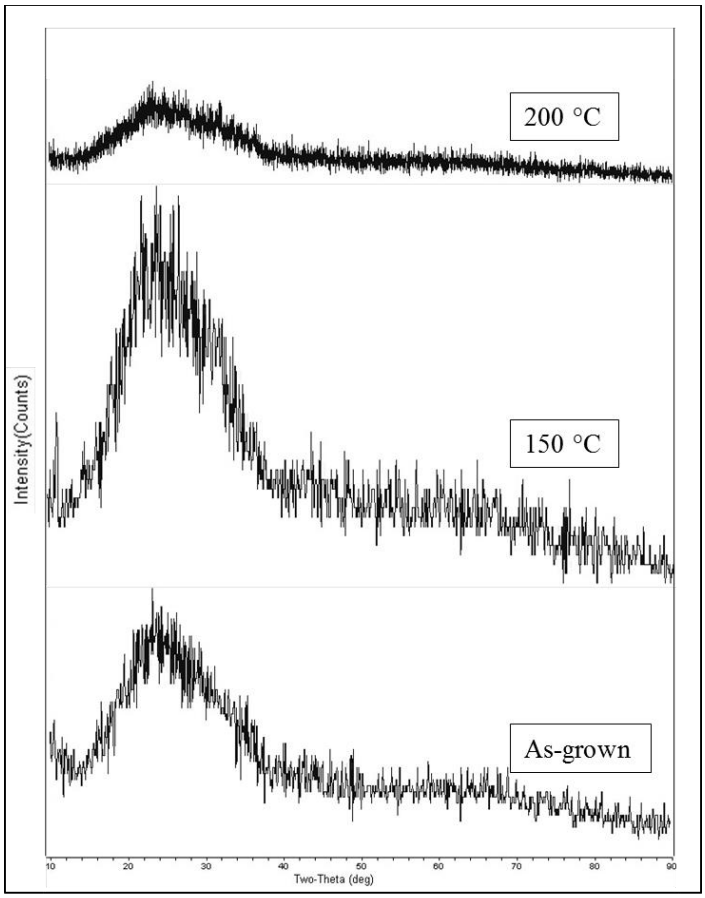

Figure 4.9 : XRD pattern of CIGS thin-films produced from CIGS solution prepared in the air ambiance.

Surface morphology of CIGS thin-films was investigated by using SEM micrographs at different annealing temperatures in Figure 4.10a-c. SEM image of the CIGS thin-film presented the cracked surface before the annealing process as shown in Figure 4.10c. Annealing process caused to agglomeration of the CIGS grains on the surface of the film (Figure 4.10a,b). The cracks on the surface of the film disappeared by the annealing treatment at 150 °C in air as the annealing treatment caused the diffusion on the surface of the film [99]. SEM image of the film annealed at 200 °C was presented in Figure 4.10a. The increase of the annealing temperature from 150 °C to 200 °C resulted with the finer grains on the surface.

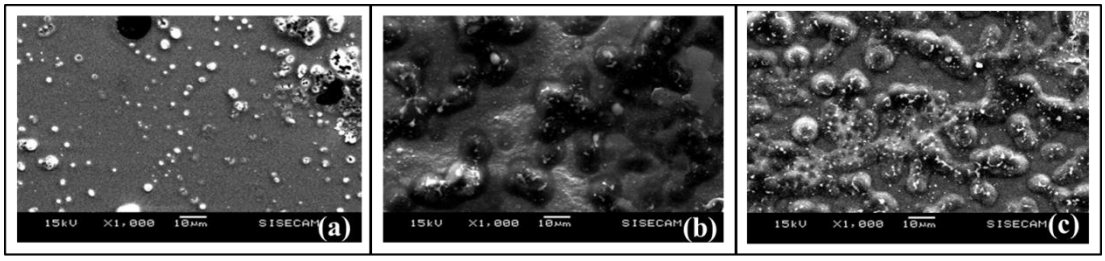

Figure 4.10 : SEM images of CIGS thin-film
(a) as-grown state; **(b)** 150 °C; **(c)** 200 °C.

Optical characterization

The energy band gap of the annealed samples at 150 °C and unannealed samples were presented in Figure 4.11. Annealing process at 150 °C improves the crystallity and decreases the optical band to 1,14 eV value.

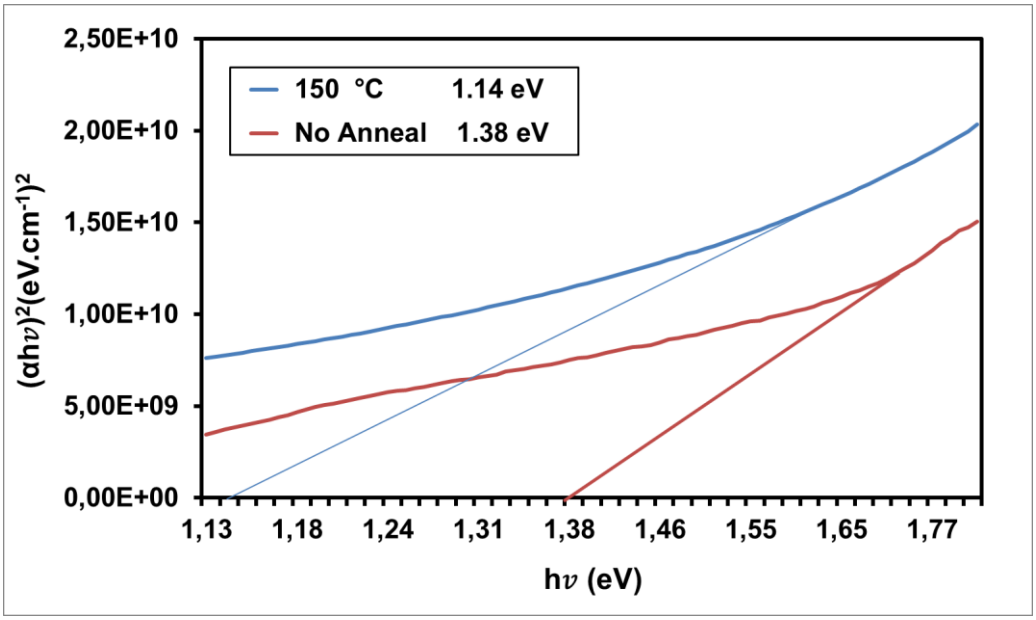

Figure 4.11 : The energy band gap at 150 °C annealing temperature and as-grown state.

Electrical characterization

The changes in electrical conductivity at different annealing temperatures such as (a) no anneal, (b) 137 °C, (c) 150 °C and (d) 200 °C are shown in Figure 4.12. The highest conductivity value was obtained at 150 °C annealing temperature with $74{,}034.56 \times 10^{2}$ $(\Omega.cm)^{-1}$.

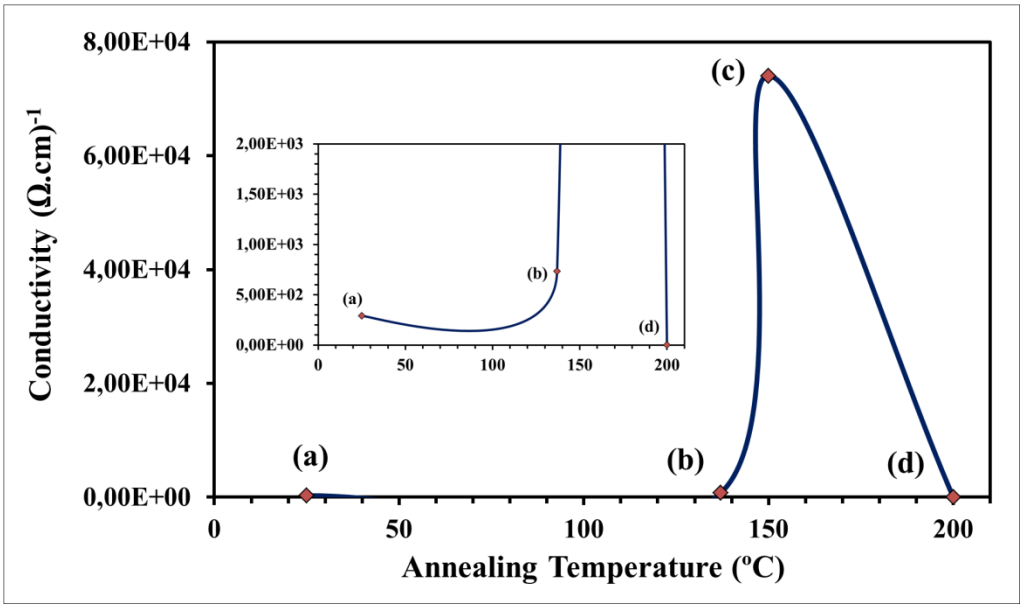

Figure 4.12 : Effect of annealing temperature on electrical properties
(a) as-grown; **(b)** 137 °C; **(c)** 150 °C; **(d)** 200 °C.

4.1.2.2 Heat treatment effect of solution prepared in inert atmosphere

The CIGS sol was prepared in argon to avoid the oxidation effect on the solution. The five layers coated CIGS thin-film of 30 at.% Se concentration have been annealed at different temperatures from 135 °C up to 200 °C during 30 minutes in air ambiance. The drying process in each deposition has been continued at room temperature for 10 min five times. The optimum annealing temperature is determined according to the structural, optical and electrical properties.

Structural characterization

The XRD patterns were presented for each of the annealing temperature in Figures 4.13 - 4.18. Although the thickness of the film with ~ 140 nm is too thin to achieve a good crystalline structure, such a development of crystallinity can be attributed to the settlement of the atoms caused by annealing [100] and the preparation of sol in the inert atmosphere, which ensured the inhibition of the oxygen bonding. XRD analyses, “the broad background diffraction pattern of the amorphous structure became overlapped by peaks corresponding to the diffraction” [101] from

the $Cu_{0.28}In_{1.72}Se_{2.72}$. The different annealing temperatures led to the formation of quasi-amorphous [102] chalcopyrite $Cu_{0.28}In_{1.72}Se_{2.72}$ (JCPDS 39-0758) structure (Table 4.1) [95, 97]. The XRD patterns of ultra-thin CIGS film shows that the annealed CIGS film at 135 °C is almost amorphous and after heat treatment, the structure of the films was improved, the presence of the characteristic diffraction peaks of $Cu_{0.28}In_{1.72}Se_{2.72}$ on the amorphous structure between 150-180 °C were appeared slightly which is consistent with TG/DTA results [100]. The strongest diffraction peak (007) plane of ultra-thin CIGS film at 31.88° (2θ) can be identified in the XRD analysis.

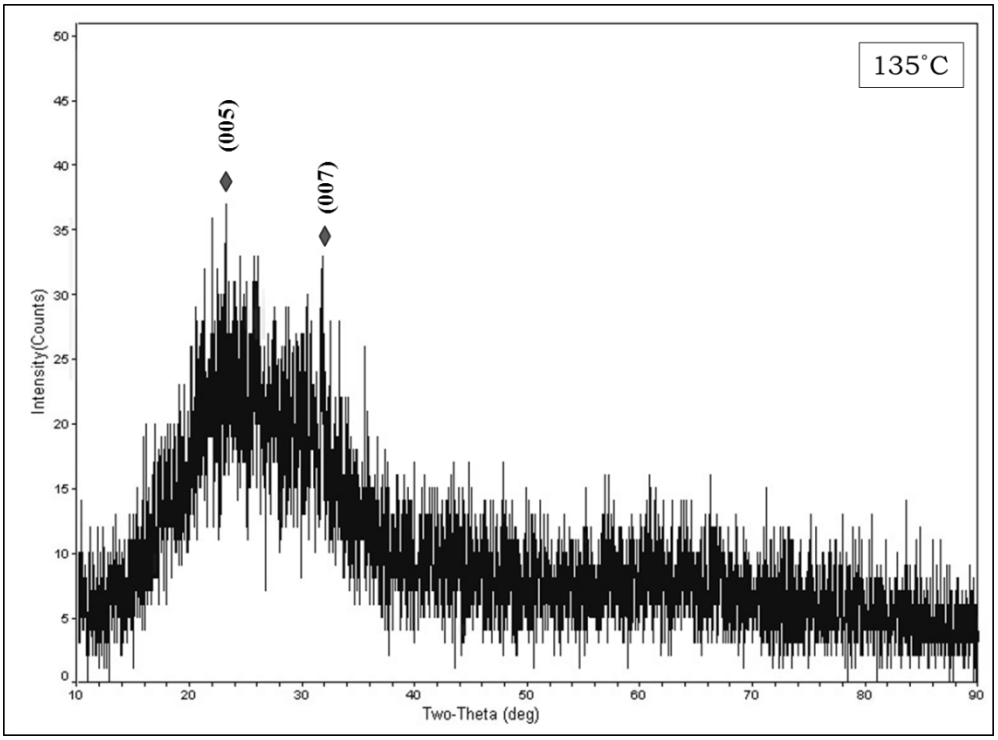

Figure 4.13 : XRD pattern of CIGS thin-films produced from CIGS solution prepared in argon annealed at 135 °C.

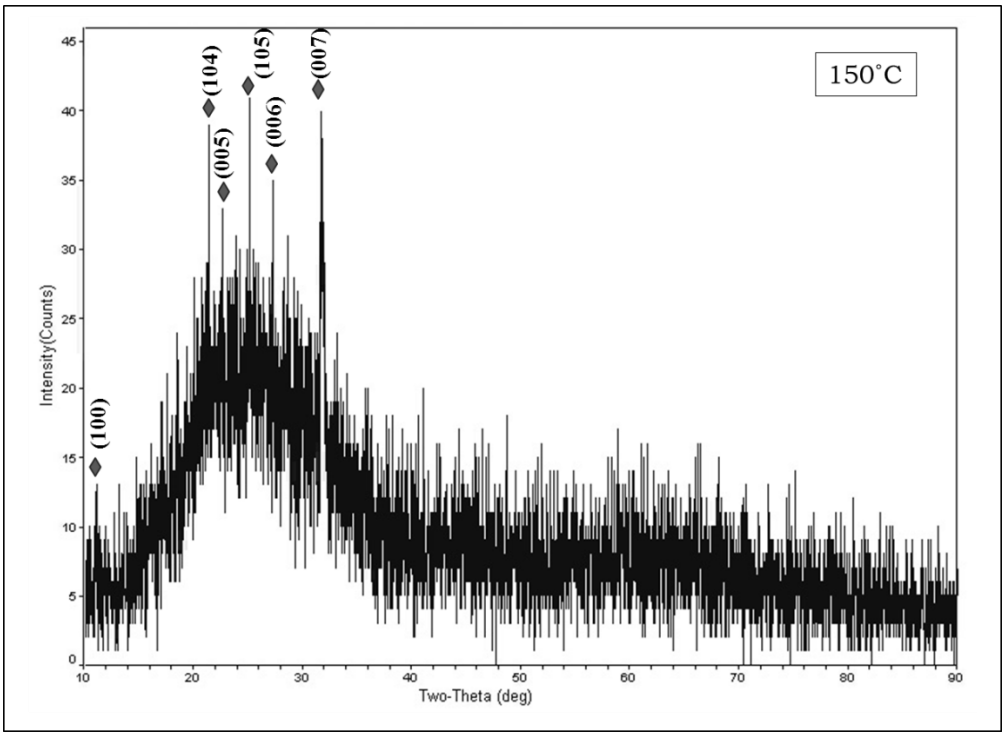

Figure 4.14 : XRD pattern of CIGS thin-films produced from CIGS solution prepared in argon annealed at 150 °C.

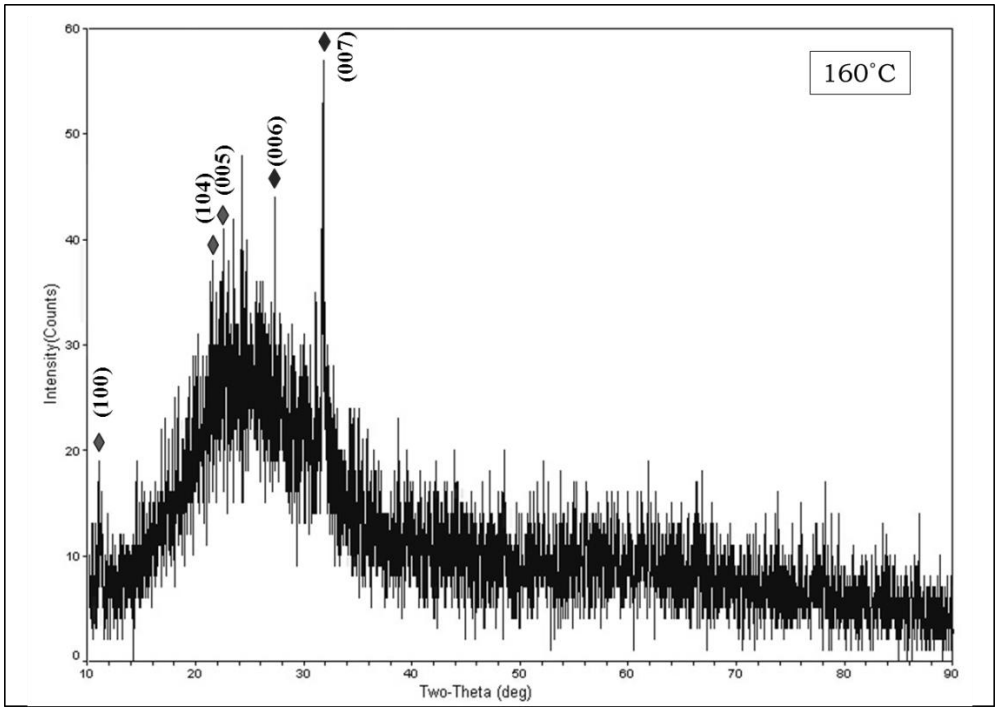

Figure 4.15 : XRD pattern of CIGS thin-films produced from CIGS solution prepared in argon annealed at 160 °C.

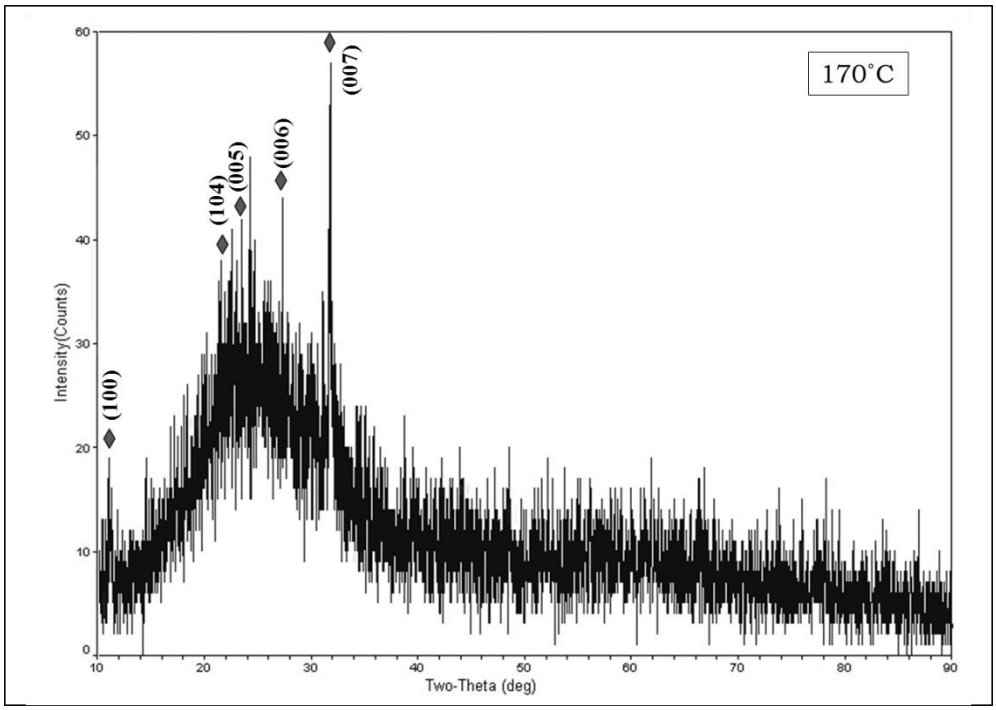

Figure 4.16 : XRD pattern of CIGS thin-films produced from CIGS solution prepared in argon annealed at 170 °C.

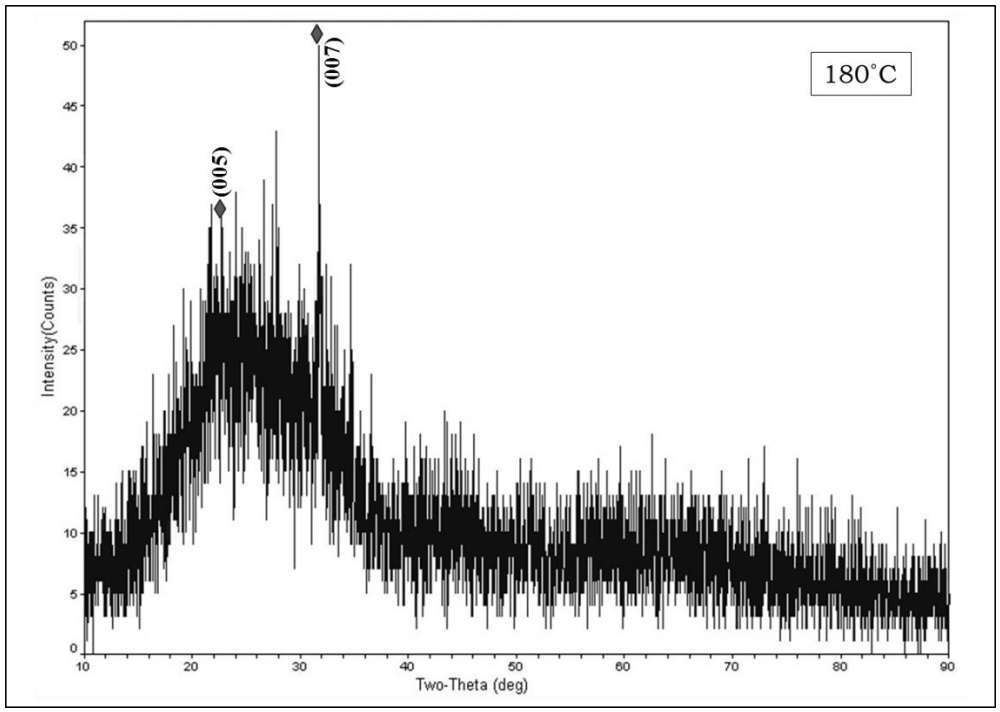

Figure 4.17 : XRD pattern of CIGS thin-films produced from CIGS solution prepared in argon annealed at 180 °C.

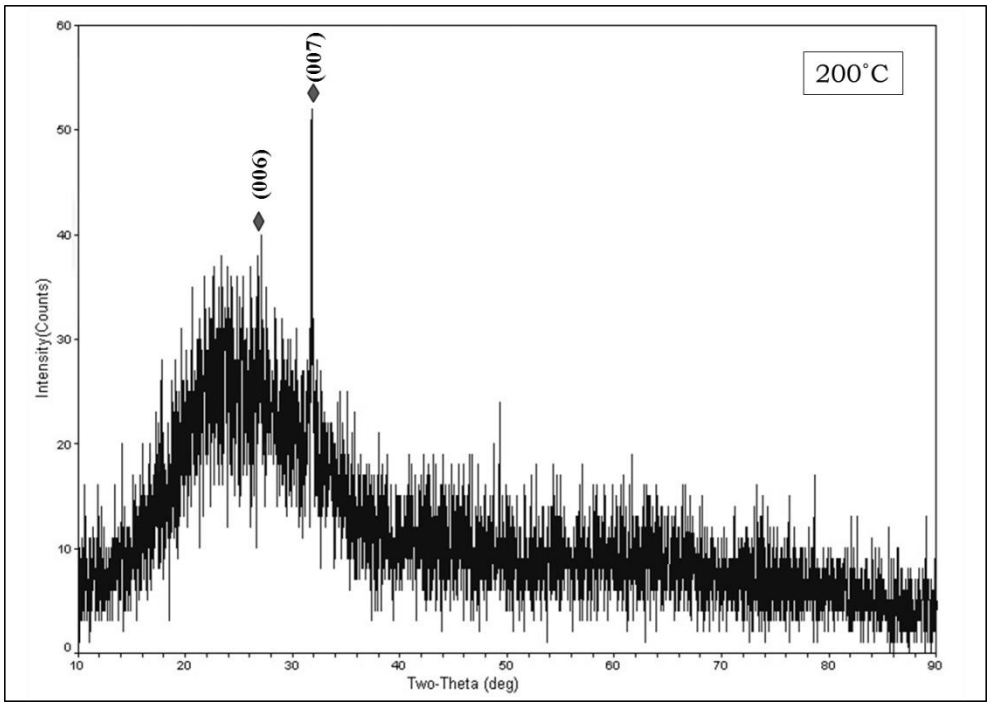

Figure 4.18 : XRD pattern of CIGS thin-films produced from CIGS solution prepared in argon annealed at 200 °C.

EDS Analysis

The EDS patterns of the samples annealed at different temperatures were presented in Figure 4.19 - 4.24, the films composition were only slightly Cu-poor and In-poor with respect to the different annealing temperatures. Cu amount was determined as 3.90 % and In amount was 3.31 % according to EDS analyses after annealing at 160 °C. Cu (with 14.63 %) and In (with 12.66 %) amounts of the thin-films were determined as the highest amount with respect to the samples annealed at other temperatures. At 160 °C and 170 °C annealing temperature Cu and In amount are considerably higher. That corresponds to the result of the TG/DTA analysis result in Figure 3.13. As the deposited film was too thin-film, the used amounts of Ga and Se elements were not enough to determine according to EDS analysis. Besides, some of the elements coming from the soda-lime silicate glass substrate were detected at EDS analysis.

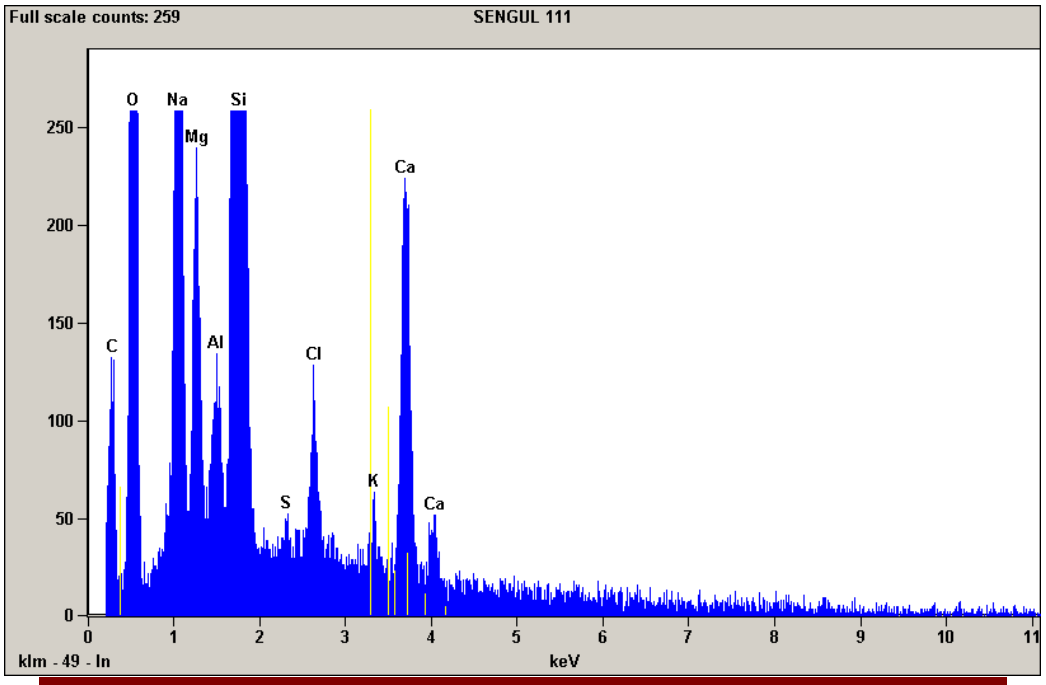

Element	*Weight %*	*Formula*	*Compound %*
O	46.61	***S***	---
Na	8.70	***Na_2O***	11.73
Mg	2.13	***MgO***	3.53
Al	0.83	***Al_2O_3***	1.56
Si	34.00	***SiO_2***	72.73
S	0.23	***SO_3***	0.57
Cl	1.33	***Cl***	1.33
K	0.52	***K_2O***	0.62
Ca	5.65	***CaO***	7.91
Total	100.00		100.00

Figure 4.19 : EDS pattern of CIGS thin-films annealed at 135 °C.

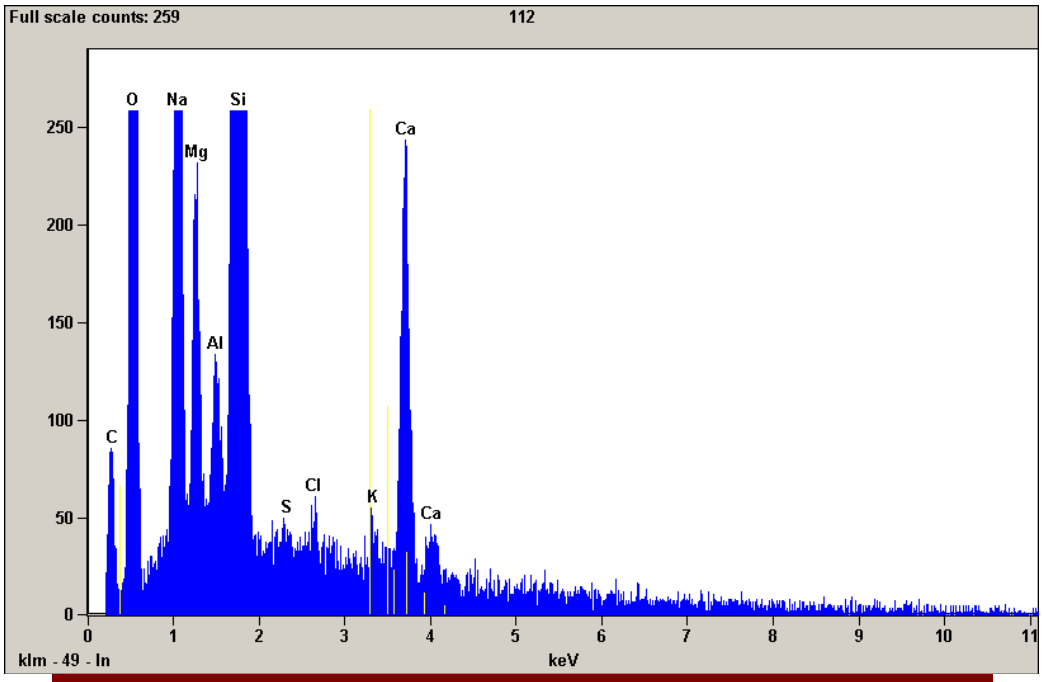

Element	*Weight %*	*Formula*	*Compound %*
O	47.08	***S***	---
Na	9.05	***Na_2O***	12.20
Mg	2.22	***MgO***	3.69
Al	0.80	***Al_2O_3***	1.52
Si	34.49	***SiO_2***	73.77
S	0.14	***SO_3***	0.35
Cl	0.39	***Cl***	0.39
K	0.39	***K_2O***	0.47
Ca	5.44	***CaO***	7.61
Total	100.00		100.00

Figure 4.20 : EDS pattern of CIGS thin-films annealed at 150 °C.

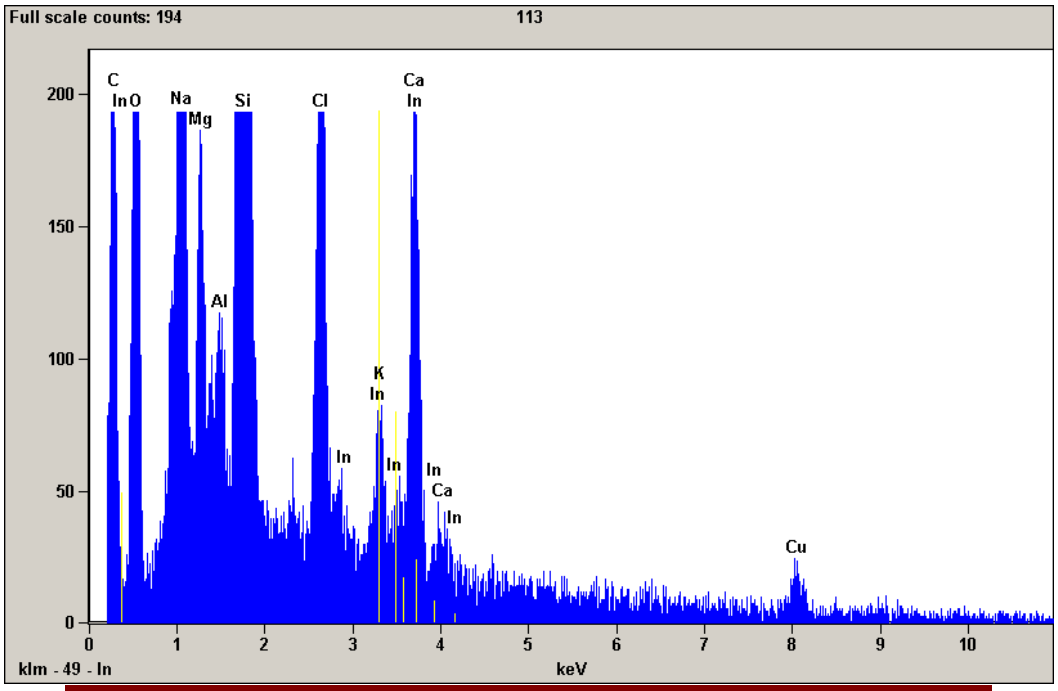

Element	*Weight %*	*Formula*	*Compound %*
O	42.26	***S***	---
Na	7.22	***Na_2O***	9.74
Mg	1.05	***MgO***	1.74
Al	0.46	***Al_2O_3***	0.87
Si	30.97	***SiO_2***	66.26
Cl	5.25	***Cl***	5.25
K	0.25	***K_2O***	0.30
Ca	5.32	***CaO***	7.45
Cu	3.90	***Cu_2O***	4.39
In	3.31	***In_2O_3***	4.00
Total	100.00		100.00

Figure 4.21 : EDS pattern of CIGS thin-films annealed at 160 °C.

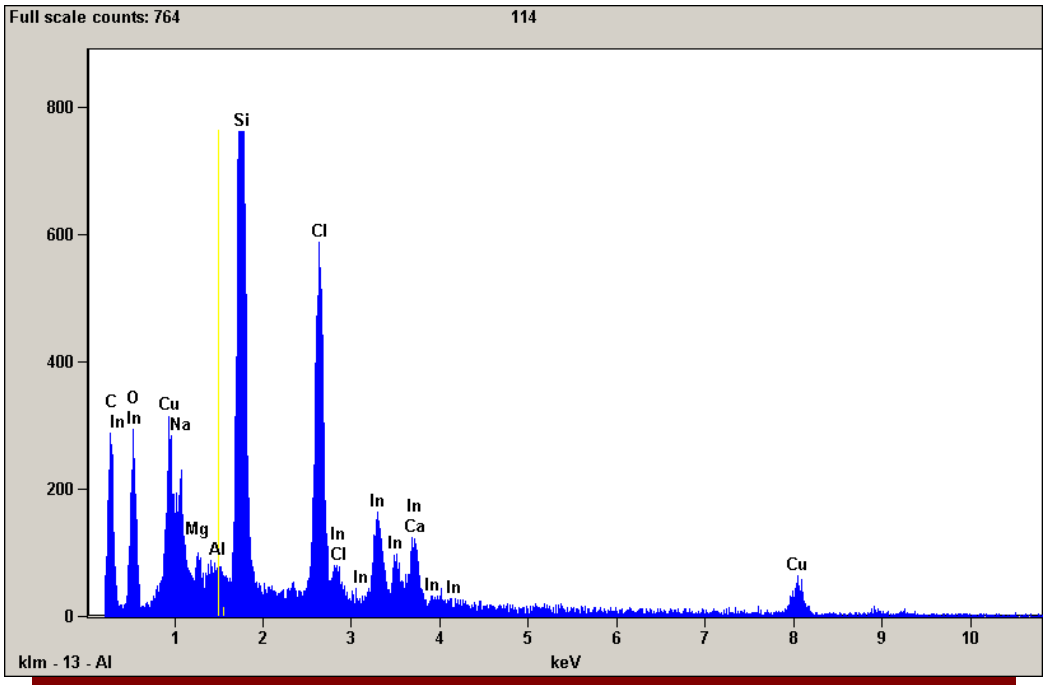

Element	*Weight %*	*Formula*	*Compound %*
O	30.09	***S***	---
Na	4.80	***Na_2O***	6.47
Mg	0.14	***MgO***	0.23
Al	0.39	***Al_2O_3***	0.74
Si	19.56	***SiO_2***	41.85
Cl	14.73	***Cl***	14.73
Ca	3.00	***CaO***	4.20
Cu	14.63	***Cu_2O***	16.48
In	12.66	***In_2O3***	15.31
Total	100.00		100.00

Figure 4.22 : EDS pattern of CIGS thin-films annealed at 170 °C.

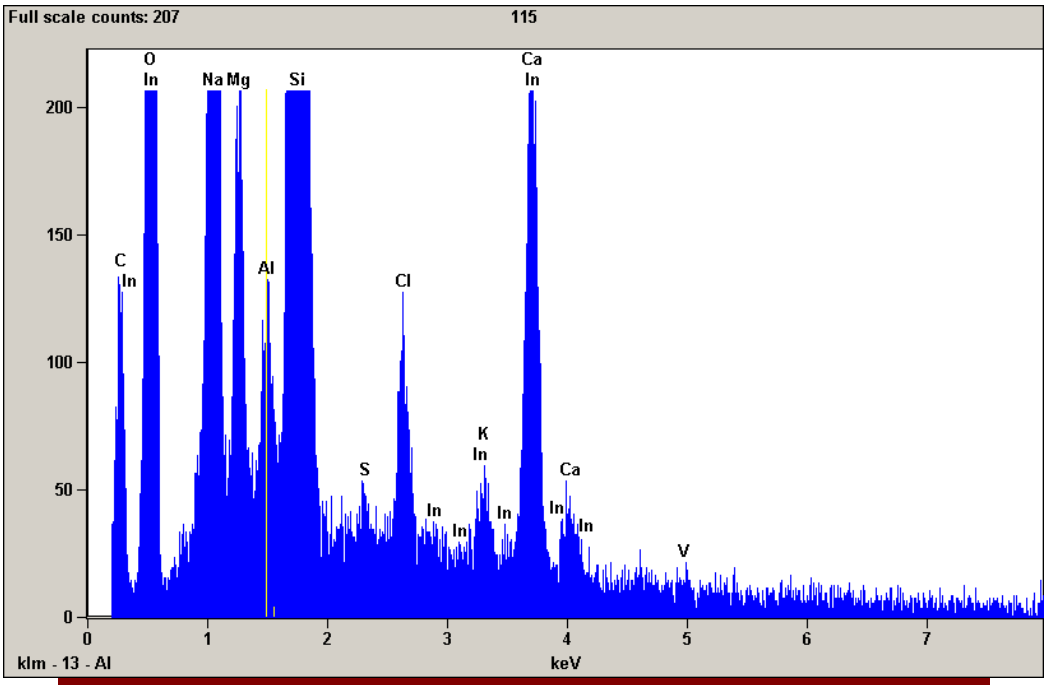

Element	*Weight %*	*Formula*	*Compound %*
O	45.96	***S***	---
Na	8.25	***Na_2O***	11.12
Mg	2.14	***MgO***	3.55
Al	0.77	***Al_2O_3***	1.46
Si	33.11	***SiO_2***	70.83
S	0.22	***SO_3***	0.55
Cl	1.72	***Cl***	1.72
K	0.29	***K_2O***	0.34
Ca	5.93	***CaO***	8.30
V	0.31	***V_2O_5***	0.55
In	1.30	***In_2O_3***	1.57
Total	100.00		100.00

Figure 4.23 : EDS pattern of CIGS thin-films annealed at 180 °C.

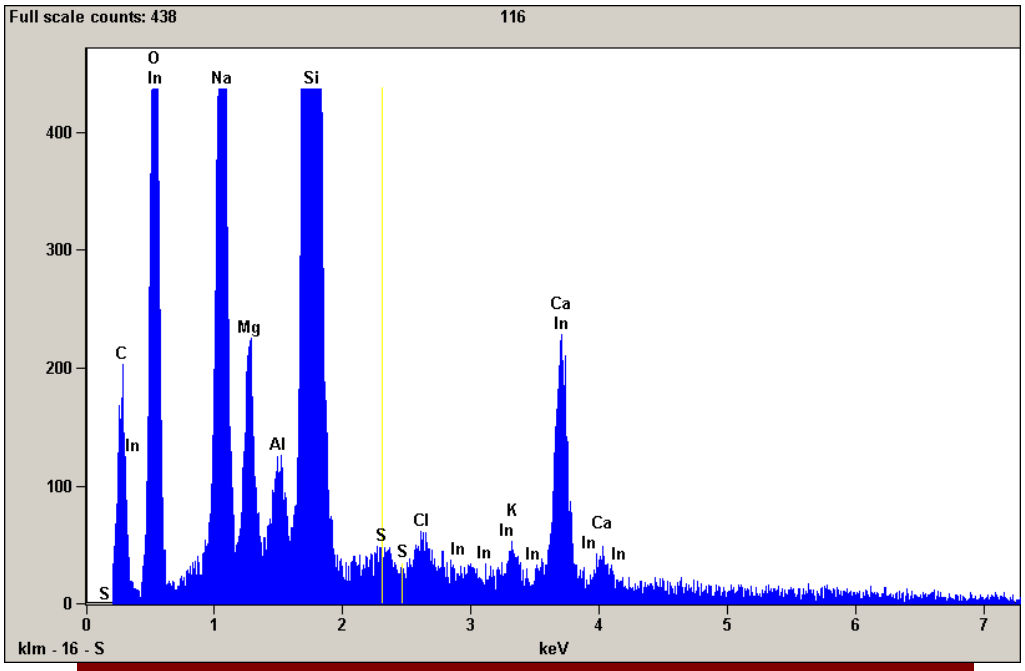

Element	*Weight %*	*Formula*	*Compound %*
O	46.83	***S***	---
Na	8.76	***Na_2O***	11.81
Mg	2.17	***MgO***	3.59
Al	0.76	***Al_2O_3***	1.43
Si	34.19	***SiO_2***	73.13
S	0.24	***SO_3***	0.59
Cl	0.70	***Cl***	0.70
K	0.46	***K_2O***	0.55
Ca	5.54	***CaO***	7.75
In	0.38	***In_2O_3***	0.45
Total	100.00		100.00

Figure 4.24 : EDS pattern of CIGS thin-films annealed at 200 °C.

Optical characterization

The optical properties of the CIGS thin-films changed with the increase of the annealing temperature in Figure 4.25. The transmittance and absorbance changed at different annealing temperature. The details on the changes of transmittance and absorbance of CIGS thin-film annealed at different temperatures were presented in different ranges of electromagnetic spectrum in Table 4.3.

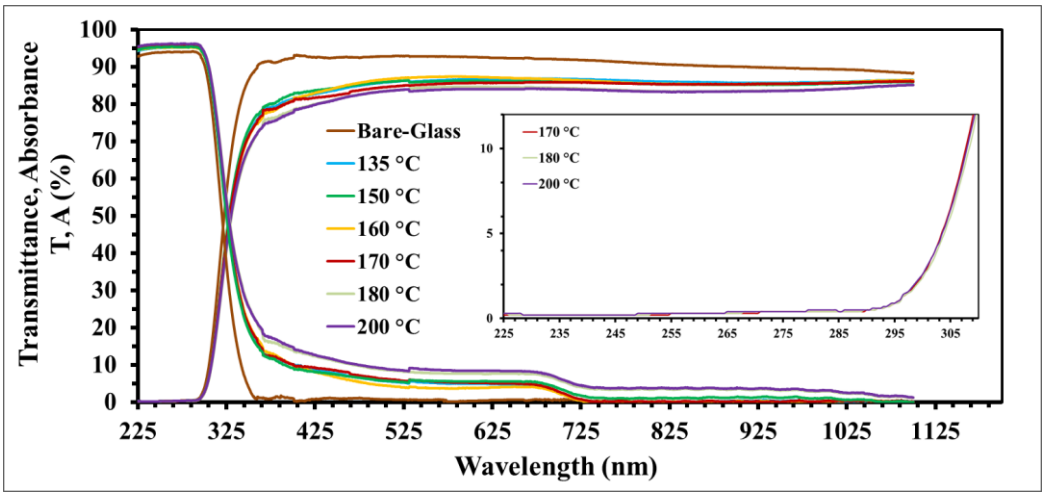

Figure 4.25 : Transmittance and absorbance spectra of the CIGS annealed at different temperatures.

Table 4.3 : The changes of transmittance and absorbance with the rise of the annealing temperature.

	UV (190-380 nm)			Visible (380-780 nm)			NIR (780-1100 nm)		
	T (%)	R (%)	A (%)	T (%)	R (%)	A (%)	T (%)	R (%)	A (%)
135 °C	22.98	5.78	71.24	85.60	9.31	5.09	86.05	13.69	0.26
150 °C	23.41	5.54	71.05	85.48	9.06	5.46	85.51	13.49	1.00
160 °C	22.71	5.78	71.51	85.90	9.74	4.36	85.73	14.05	0.23
170 °C	22.85	5.53	71.62	84.61	9.98	5.41	85.63	14.09	0.28
180 °C	21.73	4.94	73.33	83.23	8.57	8.20	83.96	13.07	2.97
200 °C	21.89	4.65	73.46	82.89	8.34	8.76	83.86	12.92	3.22
BareGlass	27.90	7.06	65.04	92.44	6.88	0.68	89.85	9.96	0.19

With the increase of annealing temperature, the absorbance increases as well. The absorbance spectrum between 250-550 nm wavelength is presented in Fig. 4.26 for the different annealing temperatures to observe more clearly. The CIGS thin-films are non-absorbing beyond ~ 300 nm in the UV range of CIGS thin-film for all annealing temperatures.

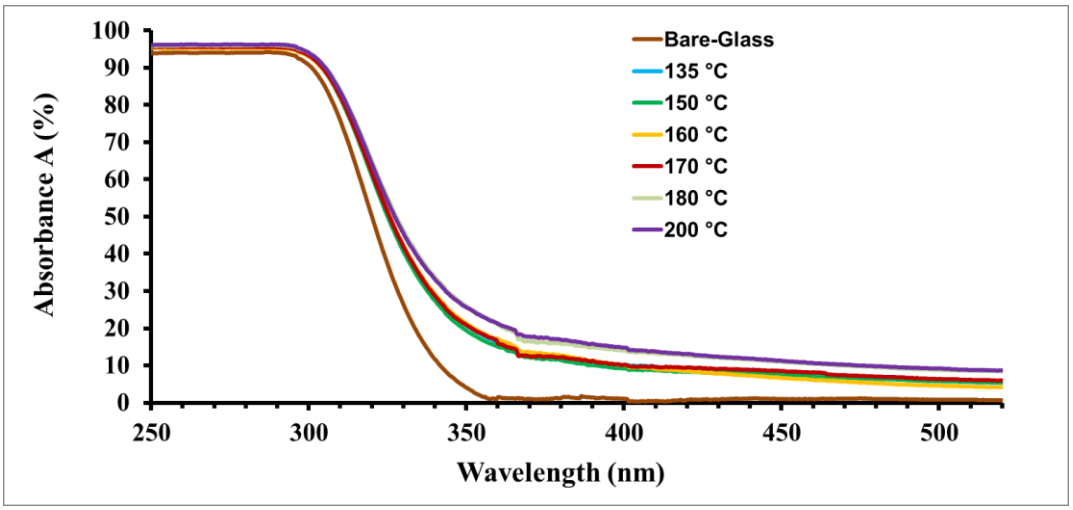

Figure 4.26 : Absorbance spectra of the annealed samples at different temperatures.

The absorption coefficient of $Cu(In,Ga)Se_2$ thin-films annealed at a temperature of 200 °C is 7.3 x 10^3 cm^{-1} at fundamental absorption region of 500 nm (Table 4.4). The refractive index (n) of $Cu(In,Ga)Se_2$ is 2.10 at 1.25 eV and 2.97 at 1.53 eV, whereas it is 2.5 at 0.5 eV and 1.68 at 2.25 eV in the thin-films (Table 4.4). The lower refractive index in the thin-films may be due to lower density of thin-films [47].

Table 4.4 : The calculated optical parameters of the annealed samples at different temperature.

Samples	Wavelength (nm)	Photon Energy (eV)	Absorption Coeff. α (cm^{-1})	Extinction Coeff. (k)	Refractive Index (n)
135 °C	992	1.25	145.43	0.001	2.19
	550	2.25	7.450,21	0.033	1.76
	350	3.54	31.974,80	0.089	1.56
150 °C	992	1.25	1.599,79	0.013	2.15
	550	2.25	8.148,95	0.036	1.73
	350	3.54	29.315,34	0.082	1.56
160 °C	992	1.25	291.38	0.002	2.20
	550	2.25	5.600,04	0.025	1.80
	350	3.54	32.754,96	0.091	1.57
170 °C	992	1.25	249.90	0.002	2.20
	550	2.25	4.698,81	0.021	1.82
	350	3.54	18.339,02	0.051	1.67
180 °C	992	1.25	2.424,37	0.019	2.11
	550	2.25	6.383,96	0.028	1.71
	350	3.54	23.215,14	0.065	1.53
200 °C	992	1.25	2.591,61	0.020	2.10
	550	2.25	7.294,96	0.032	1.68
	350	3.54	22.765,74	0.063	1.52

The absorption coeffiecient versus wavelength graph is given in Figure 4.27. The optical energy band gap graphs of the different annealing temperatures were presented in Figure 4.28. The energy band gaps of 135 °C and 200 °C are 1.73 and 1.68 eV, respectively (Figure 4.28).

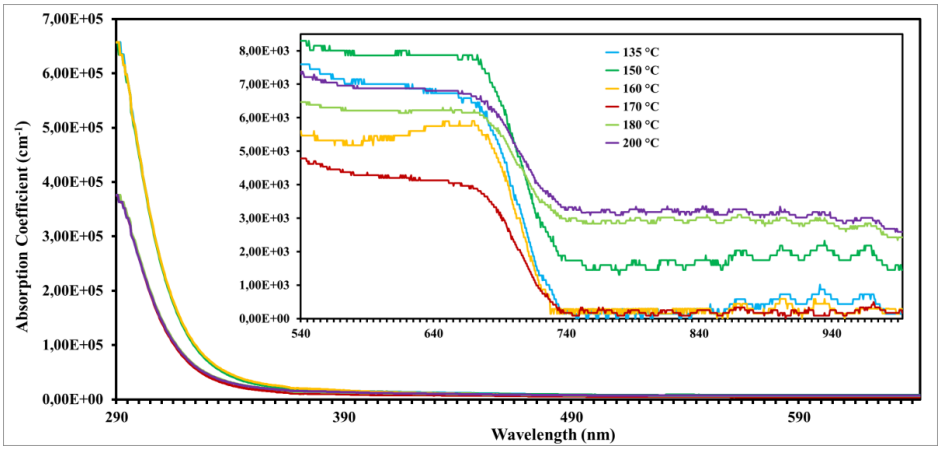

Figure 4.27 : Absorption coefficient of Cu(In,Ga)Se_2 thin-films with function of wavelength for different annealing temperatures.

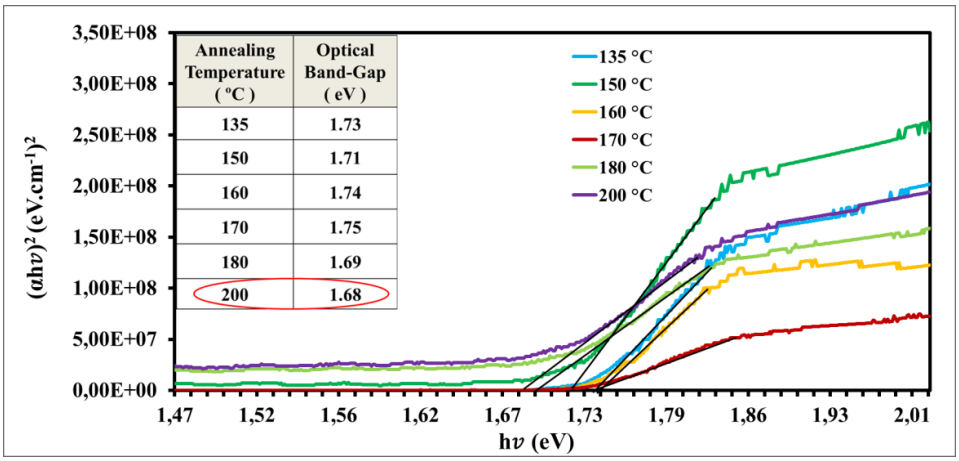

Annealing Temperature (°C)	Optical Band-Gap (eV)
135	1.73
150	1.71
160	1.74
170	1.75
180	1.69
200	1.68

Figure 4.28 : The variation of optical energy band gap with the change of annealing temperature.

Electrical characterization

The sheet resistance was measured for the each temperature value. The resistance was detected at the samples annealed at 150 °C and 160 °C. The thin-films coated with the sol prepared in the inert atmosphere achieved the higher conductivity at 160 °C annealing temperature. The conductivity was calculated 10.869,57 $(\Omega\text{-cm})^{-1}$. The sample annealed at 150 °C for 30 min shows 3.467,71 $(\Omega\text{-cm})^{-1}$. Most of the productions the annealing temperature was taken as 150 °C due to the achieving lower cost. This thesis is based on the basis to produce an absorber layer for the solar cells economically.

4.1.3 Thickness effect

The cleaned substrates were immersed into CIGS solution and withdrawn at a rate of 1 $mm.s^{-1}$ and then the films were then dried at room temperature for 10 min in an air

ambiance. To investigate thickness effect dipping process was repeated 3, 5, 7, 9, 11 times. Layers 3, 5, 7, 9 and 11 were deposited on different glass substrates. The sol-gel derived CIGS thin-films were thermally treated at 150 °C for 30 min. Then the thickness of the film was measured by using surface profilometer. The layers and thickness dependence in the CIGS thin-film was presented in Table 4.5.

Table 4.5 : The layers and thickness dependence at the CIGS thin-film.

Layers	Thickness (± 5 nm)
3	80
5	140
7	195
9	235
11	300

The increase of the thin-film layers affected the structural, optical and electrical properties of CIGS thin-films slightly. The optimum optical properties of CIGS thin-films are evaluated by varying the film layers. The visual quality control for the samples was done in Figure 4.29 - 4.30.

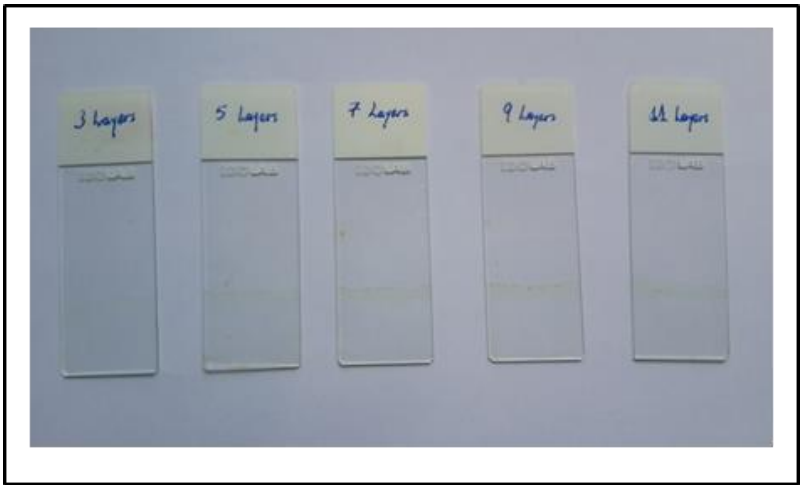

Figure 4.29 : The samples with different number of coating layers.

Figure 4.30 : The visual control of the each samples with different coated layers.

4.1.3.1 Structural characterization

SEM Analysis

The surface morphology was evaluated between the 3 layers and 9 layers coated samples. The SEM images were taken 6,000, 12,000 and 24,000 magnified (Fig. 4.31 - 4.33). The SEM images show that the colloidal structure of the thin-film needs to cover the vacancies with the increase of the thickness. The porousity reduced absolutely which would improve optical and electrical properties as well.

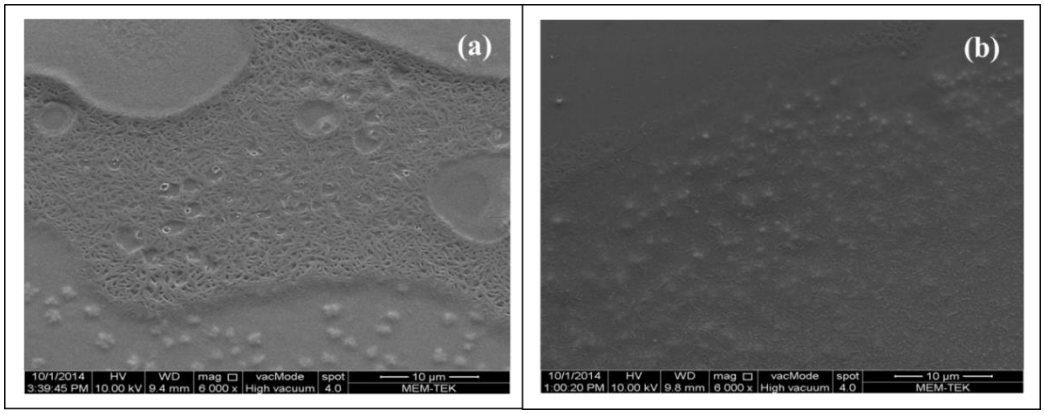

Figure 4.31 : SEM images magnified 6,000x of **(a)** 3 layers and **(b)** 9 layers.

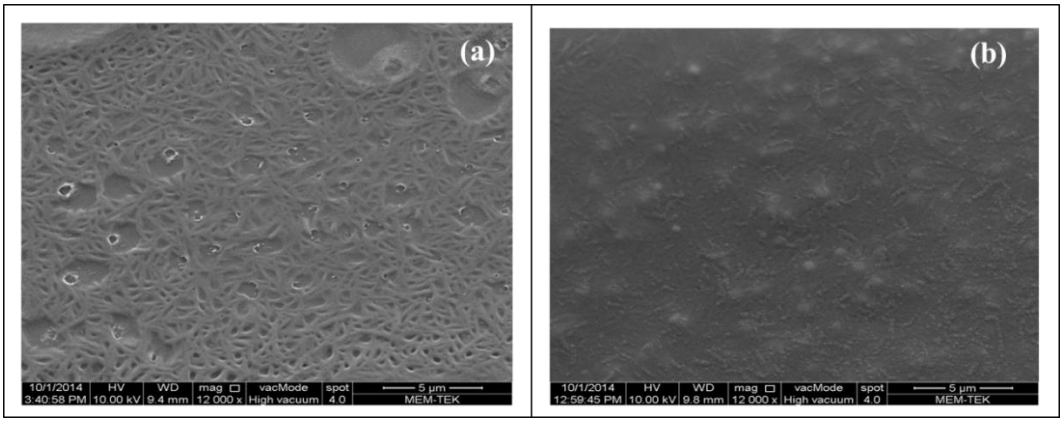

Figure 4.32 : SEM images magnified 12,000x of **(a)** 3 layers and **(b)** 9 layers.

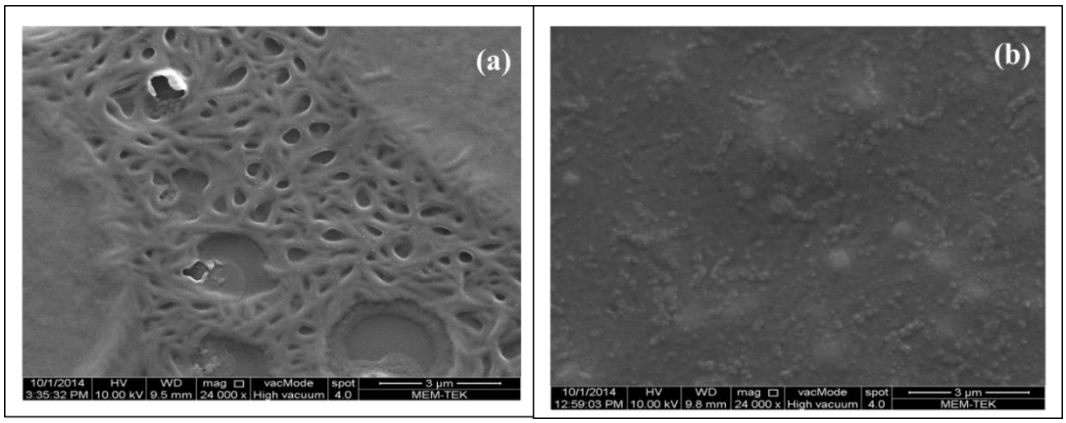

Figure 4.33 : SEM images magnified 24,000x of **(a)** 3 layers and **(b)** 9 layers.

X-Ray Diffraction Analysis

The XRD patterns of the sol-gel derived CIGS thin-film with the different number of coating layers (80, 195, 235 and 300 nm thicknesses) were presented in Figure 4.34a-e. Although the peak intensities are so low in the nanometric scale, there is a possibility matching with suggested the Joint Committee for Powder Diffraction Data (JCPDS) of chalcopyrite $Cu_{0.28}In_{1.72}Se_{2.72}$ structure (Card Number: 39-0758) [95,97]. In the general trend, the XRD diffraction peak identified at (007) plane clearly (Figure 4.34). The presence of sharp narrow peak placed on the diffuse halo of amorphous [103]. Here, the (007) plane is preferably grown with the short-range. With increasing film thickness above 300 nm, the long-range order is starting to show itself which is placed on the broad background diffraction pattern of the amorphous structure [101,102].

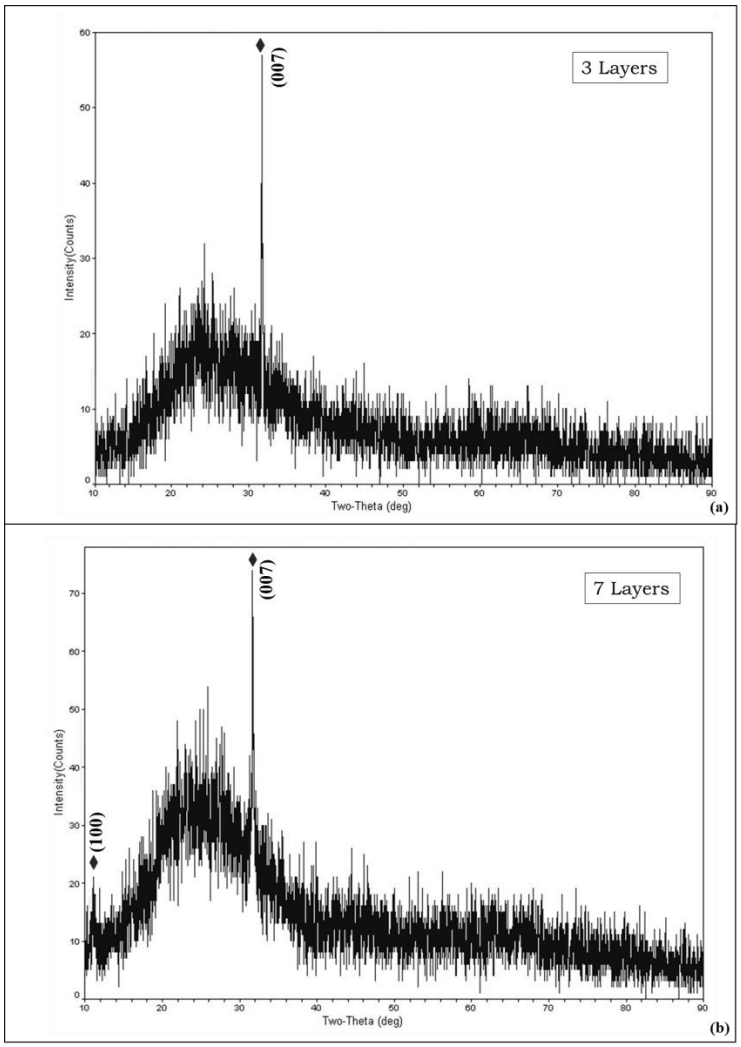

Figure 4.34 (Continued) : XRD patterns of $Cu(In,Ga)Se_2$ thin-films deposited **(a)** 3 layers; **(b)** 7 layers; **(c)** 9 layers; **(d)** 11 layers.

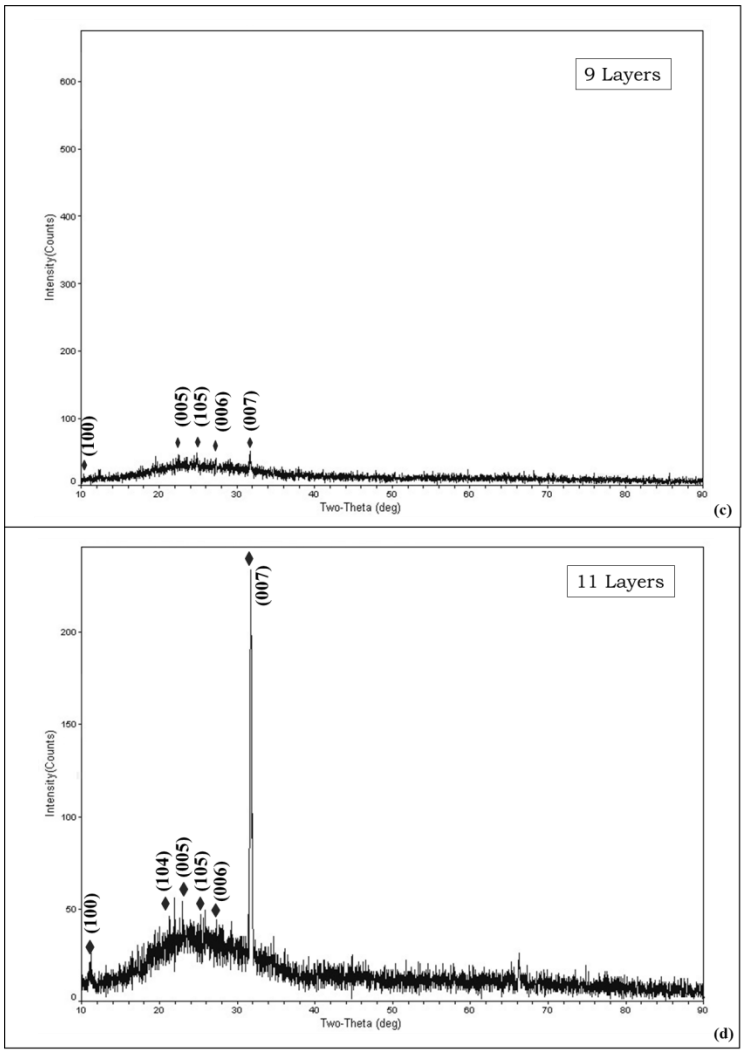

Figure 4.34 : XRD patterns of Cu(In,Ga)Se_2 thin-films deposited **(a)** 3 layers; **(b)** 7 layers; **(c)** 9 layers; **(d)** 11 layers.

However, the peak at about 31.88°, corresponding to (007), are clearly visible in XRD patterns of the samples with different thicknesses (Figure 4.34), indicating the development of crystallinity with the thickness increase [100].

The calculated interatomic distances according to Bragg equation **(3.4)** and the measured diffraction angles are presented in Table 4.6 with the theoretical XRD result of JCPDS 39-0758 card for (007) diffraction plane.

Table 4.6 : X-Ray diffraction data with different number of coating layers.

Samples	(*hkl*)	Calculated		JCPDS 39-0758	
		d (Å)	2θ	d (Å)	2θ
3 Layers	(007)	2.81	31.83	2.81	31.88
7 Layers	(007)	2.81	31.78		
9 Layers	(007)	2.82	31.74		
11 Layers	(007)	2.82	31.74		

Grain size (Crystallite size) of the (007) plane was calculated from the XRD data using the Debye-Scherrer formula **(3.5)**. Table 4.7 depicts the calculated crystallite size.

Table 4.7 : The average crystallite size and the intensity of (007) peak diffraction.

Layer	Thickness (nm)	I_0	Aver.Cryst. Size (nm)
3	80±5	57	232.02
7	195±5	74	185.59
9	235±5	50	115.98
11	300±5	234	231.97

Large grain size is one of the fundamental requirements in photovoltaics to reduce grain boundary scattering and improve conductivity [Url-15].

4.1.3.2 Optical characterization

The transmittance and absorbance of CIGS thin-film of different number of layers are illustrated in Figure 4.35 and Figure 4.36. It was determined that there was a decrease in the transmittance of the CIGS thin-film with the rise of the film layers in Figure 4.35 and Figure 4.36. However, the rise of the layers of the CIGS thin-films resulted with the increase in the absorbance depending on the enhancement of the thickness.

The transmittance of CIGS thin-films between 230 - 310 nm are also shown in Figure 4.35. The CIGS thin-films were non-absorbing beyond ~ 246 nm in the UV range of CIGS thin-film for all the number of layers (Figure 4.35).

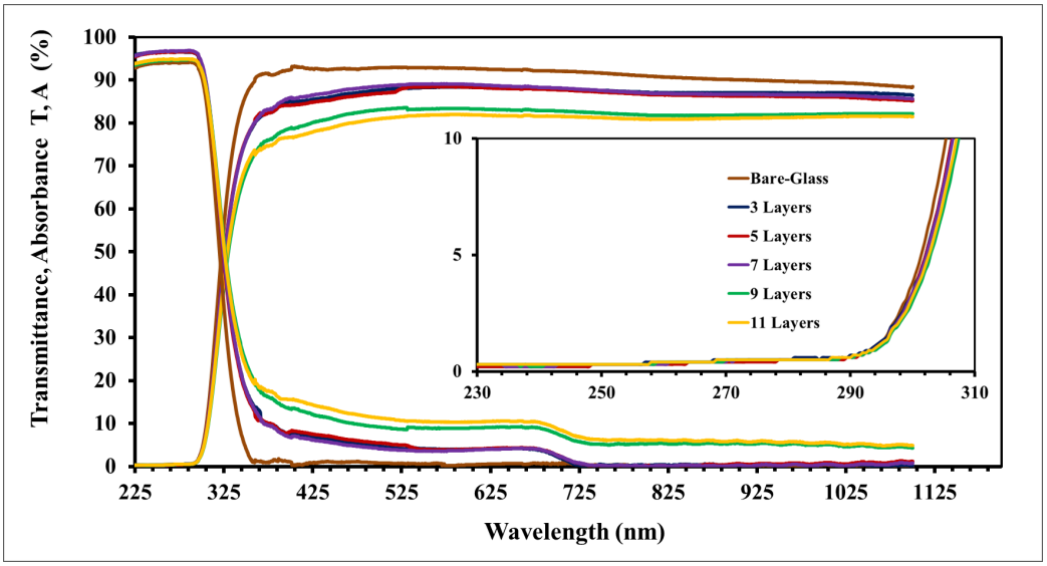

Figure 4.35 : Optical transmission and absorbance spectrum of CIGS thin-film with different thicknesses.

Figure 4.36 indicates transmittance and absorbance values versus different coating layers at 550 nm wavelength. Optical transmittance and absorbance were evaluated at 550 nm since the maximum human visual sensitivity is ~ 550 nm (Figure 4.36). The transmittance of the bare glass is 92.9 %.

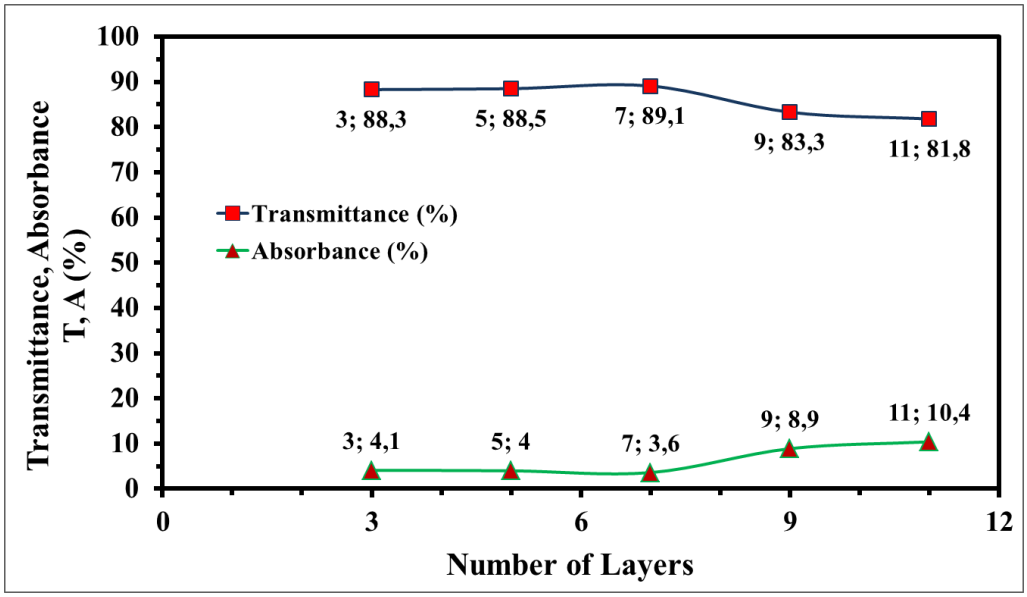

Figure 4.36 : Transmittance and absorbance variations at 550 nm wavelength versus number of layers.

The average transmittance and absorbance of CIGS films at 3, 5, 7, 9 and 11 layers were presented at ultraviolet, visible and near infrared ranges in Table 4.8. There was a decrease in transmittance of CIGS thin-film at ultraviolet range of electromagnetic spectrum as well as at the visible and the near-infrared ranges.

Table 4.8 : The average transmittance and absorbance of CIGS thin-film with different number of layers.

	UV (190-380 nm)			Visible (380-780 nm)			NIR (780-1100 nm)		
	T (%)	R (%)	A (%)	T (%)	R (%)	A (%)	T (%)	R (%)	A (%)
3 Layers	24.72	4.23	71.06	87.41	8.51	4.09	87.03	12.60	0.37
5 Layers	24.76	4.68	70.56	87.10	8.54	4.36	86.19	13.24	0.57
7 Layers	24.70	4.38	70.91	88.00	8.19	3.81	86.57	13.12	0.31
9 Layers	22.18	6.17	71.65	82.29	8.62	9.09	81.97	12.96	5.07
11 Layers	22.44	5.94	71.61	80.69	8.61	10.70	81.26	13.08	5.66
Bare-Glass	27.90	7.06	65.04	92.44	6.88	0.68	89.85	9.96	0.19

Figure 4.37 shows the plot of $(\alpha h\nu)^2$ vs. hν. The optical transition was determined as an allowed direct transition of $(\alpha h\nu)^2$ for CIGS thin-film. The linear nature of the plot near the higher energy range indicates that the films have direct energy band gaps [104]. Optical energy band gap, E_g for allowed direct transition was determined by extrapolating the linear part of $(\alpha h\nu)^2$ versus hν plot. There was a change in optical energy band gap in CIGS thin-films with the increase of the film layers from 3 to 11 layers (Figure 4.37).

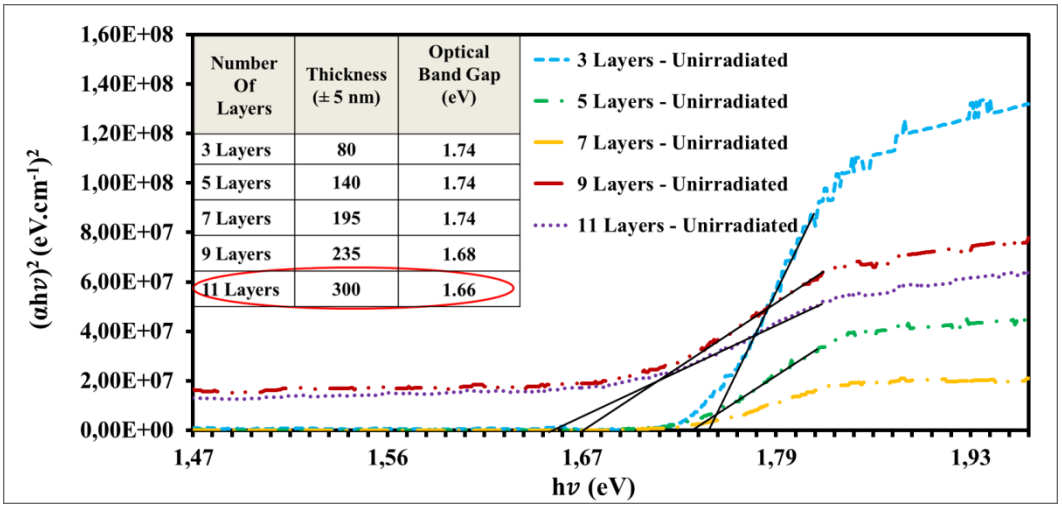

Figure 4.37 : The variation of optical energy band gap with the change of thickness.

The optical energy band gap of CIGS absorber layer of 9-11 layers is determined as ~ 1.68 eV by extrapolating the plot of $(\alpha h\upsilon)^2$ as a function of hυ.

The optical parameters of thin-films such as absorption coefficient (α), extinction coefficient (k) and refractive index (n) were calculated for the photon energy of 1.25, 2.25 and 3.54 eV (Table 4.9).

Table 4.9 : The calculated optical parameters of CIGS film at different number of layers.

Samples	Wavelength (nm)	Photon Energy (eV)	Absorption Coeff. α (cm^{-1})	Extinction Coeff. (k)	Refractive Index (n)
3 Layer	992	1.25	573.40	0.005	2.09
	550	2.25	5,673.36	0.025	1.72
	350	3.54	26,272.77	0.073	1.48
5 Layer	992	1.25	578.37	0.005	2.14
	550	2.25	3,157.58	0.014	1.73
	350	3.54	14,350.62	0.040	1.61
7 Layer	992	1.25	177.55	0.001	2.14
	550	2.25	2,031.24	0.009	1.72
	350	3.54	10,656.58	0.030	1.60
9 Layer	992	1.25	4,384.36	0.03	2.08
	550	2.25	7,519.38	0.03	1.72
	350	3.54	22,381.79	0.06	1.61
11 Layer	992	1.25	8,172.84	0.06	2.05
	550	2.25	14,960.36	0.07	1.65
	350	3.54	35,513.03	0.10	1.49

The raise of the thin-film layer resulted with a high absorption coefficient (Figure 4.38). As CIGS thin-film has a high absorption coefficient, it may absorb incident photon energy strongly. So that, a much thinner film is sufficient than of other semiconductor materials [105].

The literature presents the absorption coefficient of the CIGS thin-films for 1 - 2 μm (Figure 2.7 and Figure 2.8). In this study the very too thin-films were investigated. Therefore, the comparison with the literature must be done according to the thickness amount.

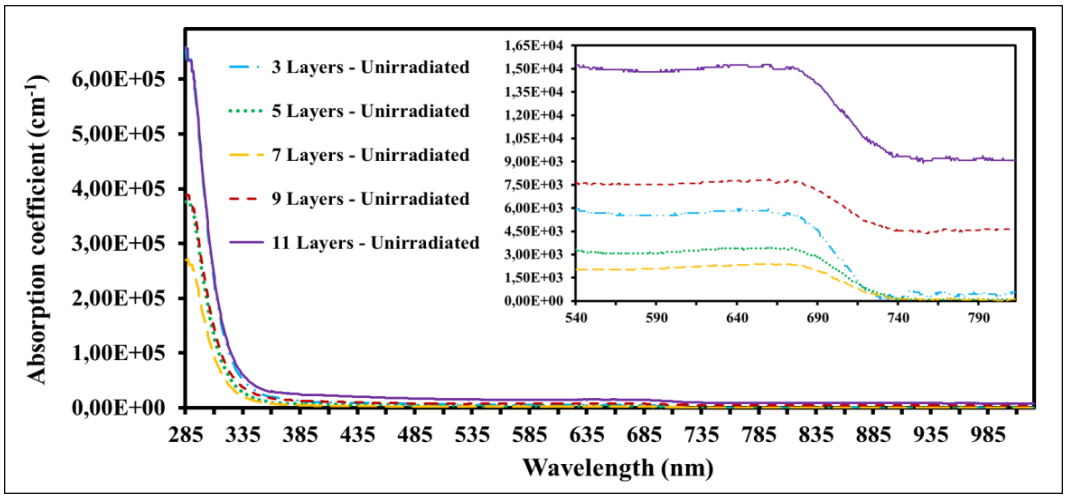

Figure 4.38 : Absorption coefficient of Cu(In,Ga)Se_2 thin-films with function of wavelength for different thicknesses.

4.2 Beta Irradiation Effect

The effect of ionization radiation on the optical materials is promising in the radiation science and air & space science. The ionized radiation causes changes at physical and chemical properties with exciting the free carriers and forming the electron-hole pairs [11].

In this chapter, the changes of physical properties of sol-gel derived CIGS thin-films were investigated after the beta irradiation. The coated CIGS thin-films were irradiated by using Strontium-90 radioisotope as beta radiation source.

The activity of Sr-90 radioisotope was enough to effect the characteristic properties of CIGS thin-film. As the electrons of Sr-90 radioisotope have high energy for the creation of colour centers in the film structure its electrons interact with the structure and penetrate homogeneously to the thin-film. Sr-90 radioisotope source emits beta radiation (max electron energy is 0.546 MeV) with the negative charge and besides its progeny Yttrium-90 from Sr-90.

Depending on the microstructural changes of the film structure, beta particles cause defects centers. When the electrons of the irradiation source -Sr-90 radioisotope-, are slowing down in the force field of the atoms on the film structure, the radiation is brought about that has a continuous energy spectrum. Beta particles emitted from Sr-90 radioisotope interact with the conduction electrons of the ions at the film structure depending on the coulomb screening effect. Beta irradiation can lead to change via knock-on momentum transfer in the thin-film structure [11].

4.2.1 Beta irradiation effect on thickness

The CIGS solution was prepared in the inert atmosphere under argon gas. The deposition of the CIGS thin-films were performed on the different glass substrates 3; 5; 7; 9 and 11 times in air. Drying process was for 10 min at room temperature. Annealing of the samples were performed at 150 °C for 30 minutes in air. The thickness of CIGS thin-film with 3 Layers and 5 Layers were in the range of 80 ± 5 nm and 140 ± 5 nm, respectively.

The samples were irradiated by the Sr-90 radioisotope resource. The optical measurements were taken at different absorbed doses such as 1.1; 1.9; 2.5; 3.1; 7.0 and 9.0 Gy. The structural and electrical properties were investigated before irradiation process and after the 9.0 Gy absorbed dose. The optical properties were evaluated at the different absorbed doses.

4.2.1.1 Structural characterization

The deposits of $Cu(In,Ga)Se_2$ with different thicknesses were characterized by X-Rays diffraction before and after ~ 9 Gy absorbed dose of beta irradiation. XRD patterns of the unirradiated and irradiated ultra thin CIGS films are given in Figure 4.39 - 4.43.

Figure 4.39-4.43 imply that the intensity of the irradiated ultra thin CIGS films is higher than the unirradiated films. This can be associated with the higher crystallinity rather than unirradiated [106].

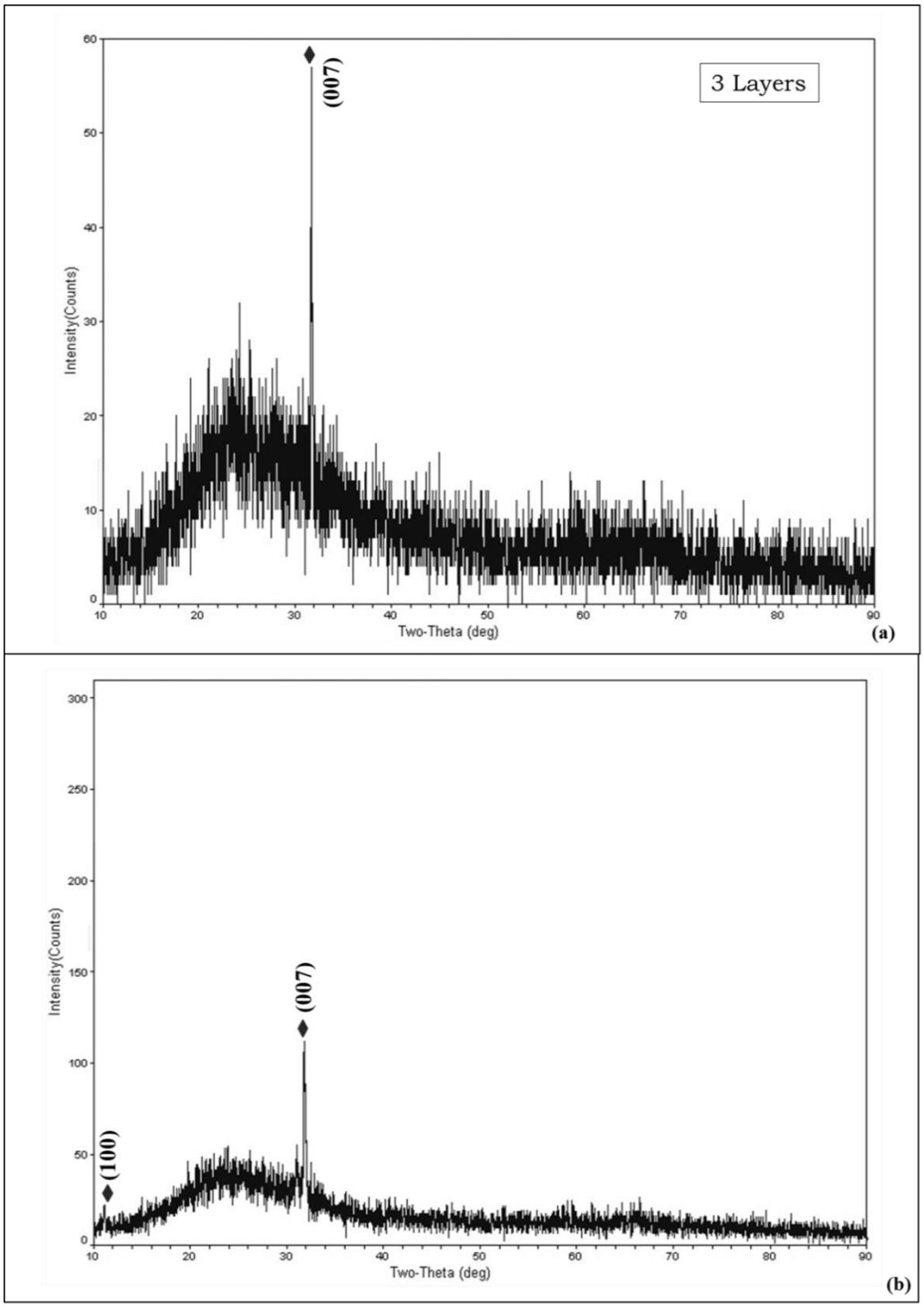

Figure 4.39 : XRD patterns of $Cu(In,Ga)Se_2$ thin-films deposited 3 layers **(a)** unirradiated **(b)** irradiated.

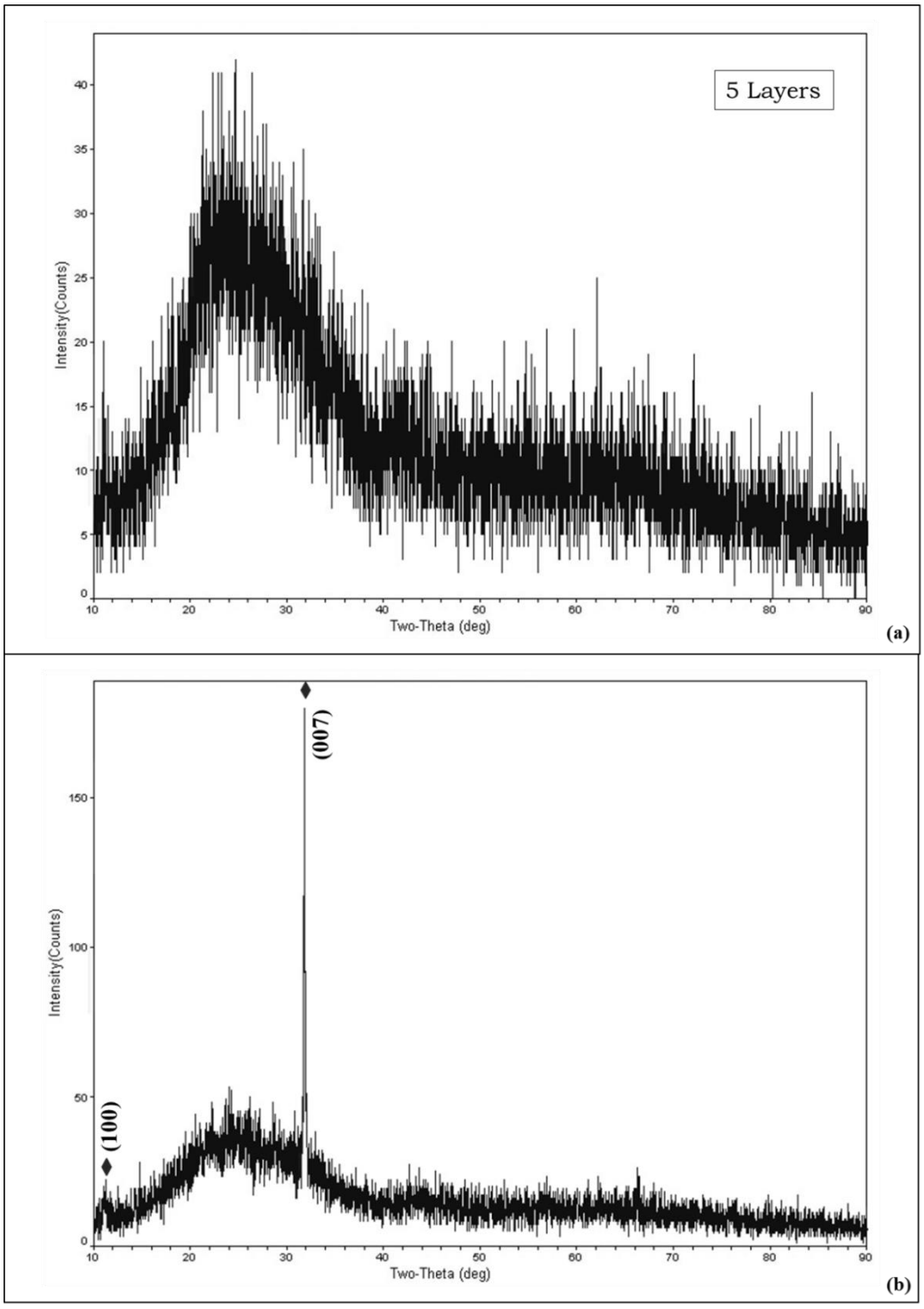

Figure 4.40 : XRD patterns of $Cu(In,Ga)Se_2$ thin-films deposited 5 layers **(a)** unirradiated **(b)** irradiated.

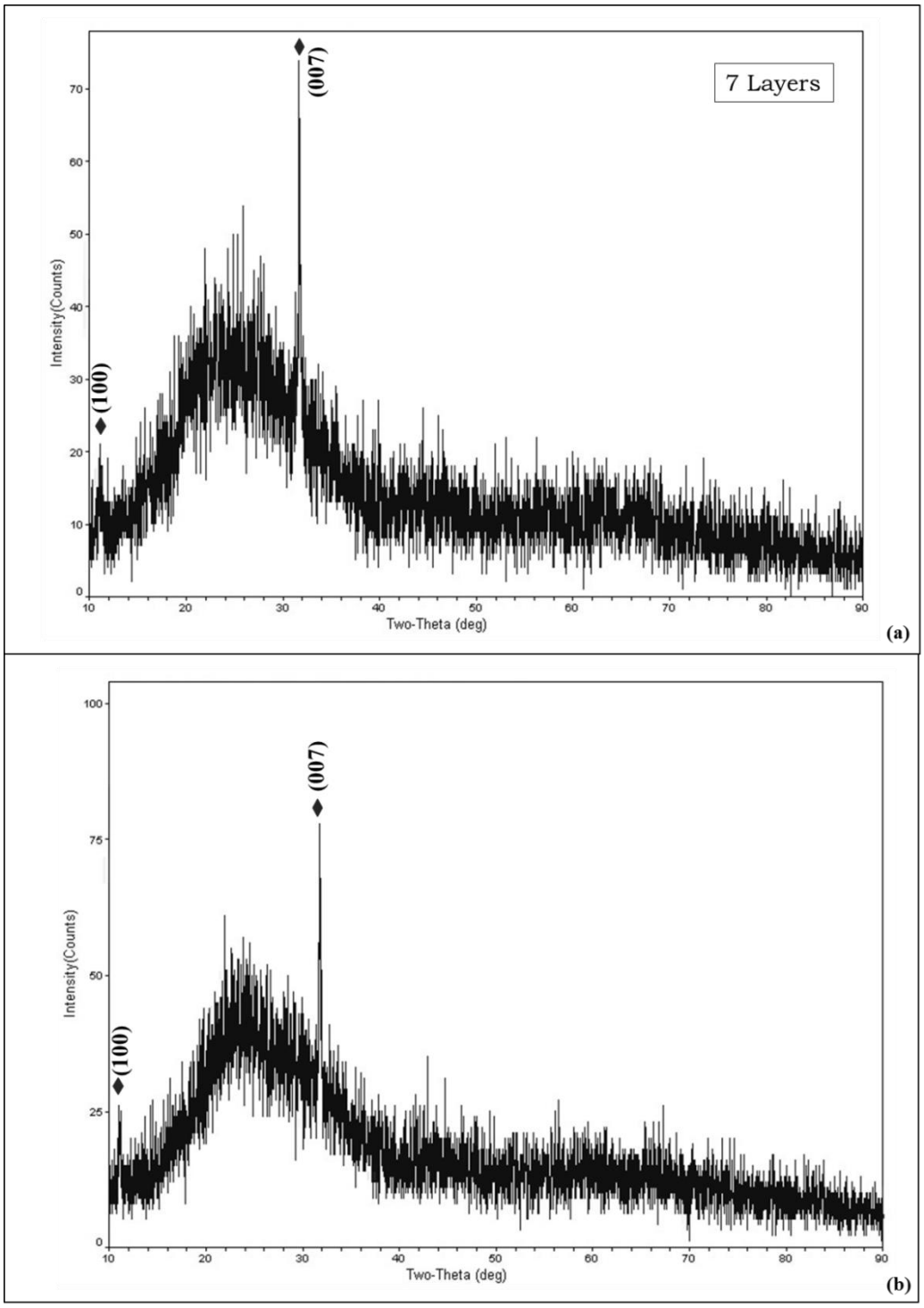

Figure 4.41 : XRD patterns of $Cu(In,Ga)Se_2$ thin-films deposited 7 layers **(a)** unirradiated **(b)** irradiated.

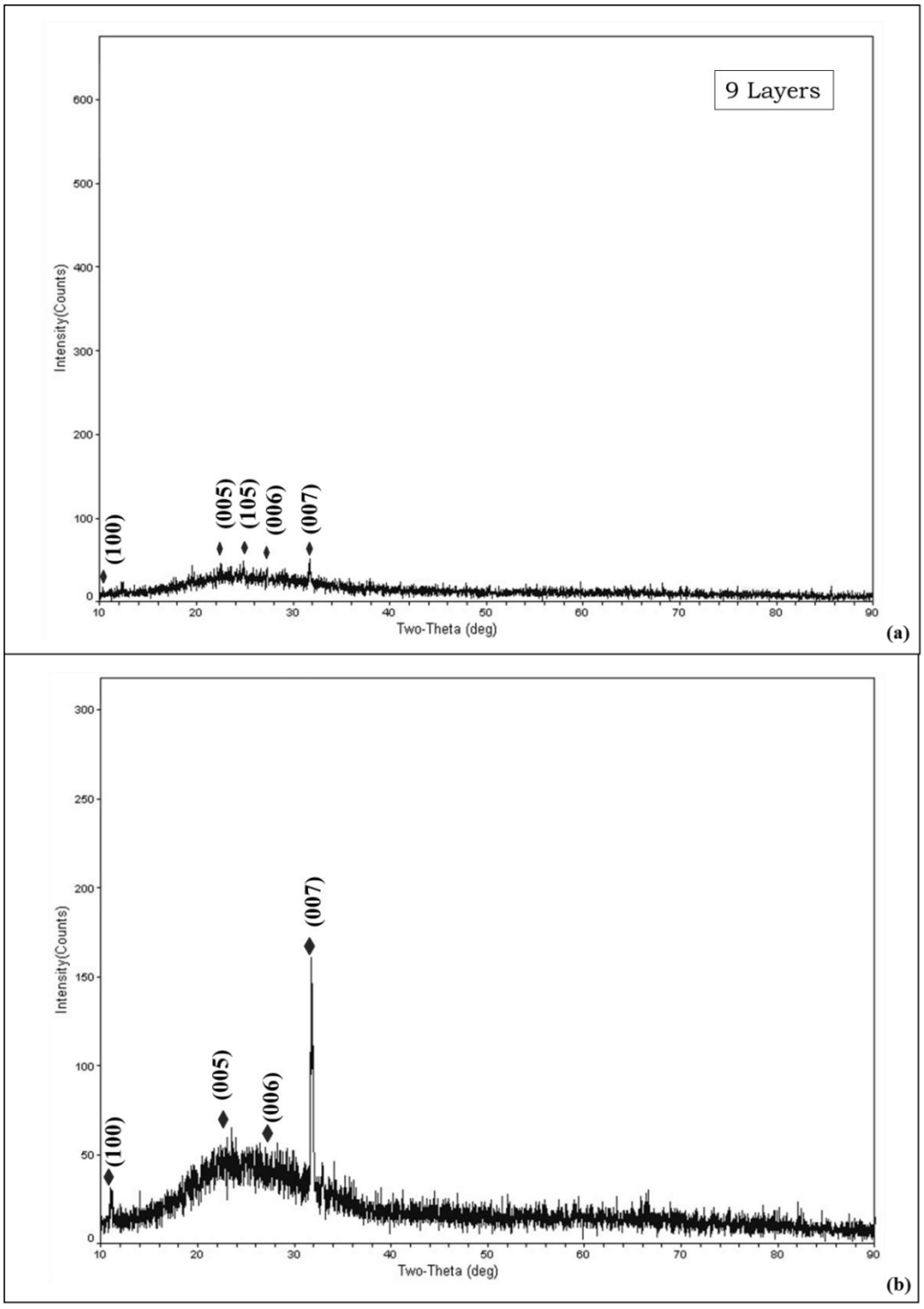

Figure 4.42 : XRD patterns of $Cu(In,Ga)Se_2$ thin-films deposited 9 layers **(a)** unirradiated **(b)** irradiated.

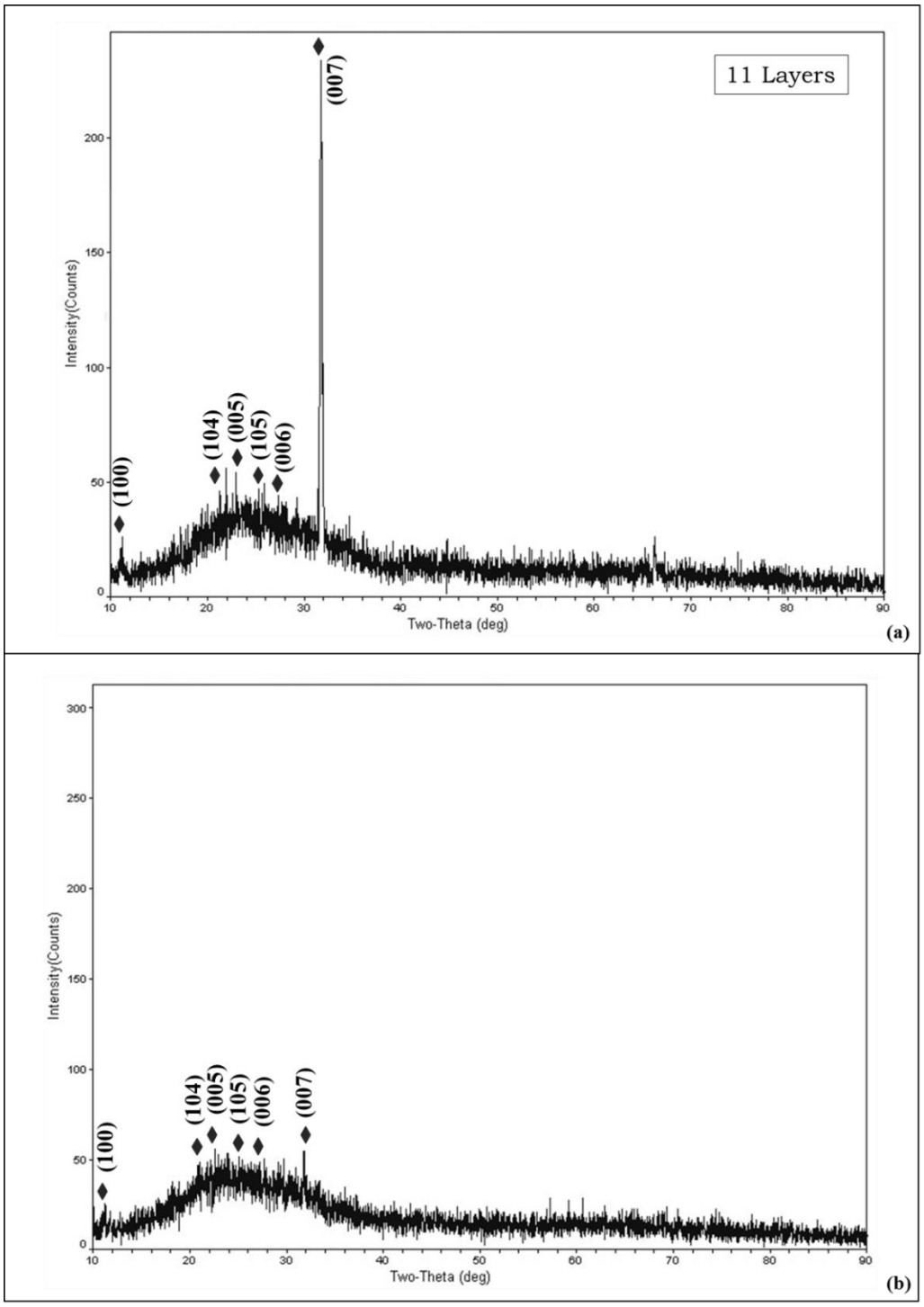

Figure 4.43 : XRD patterns of $Cu(In,Ga)Se_2$ thin-films deposited 11 layers **(a)** unirradiated **(b)** irradiated.

The sol-gel derived unirradiated thin-films of 5, 9 and 11 layers exhibit wider peaks of low intensity corresponding to the reflections of (007) planes of $Cu_{0.28}In_{1.72}Se_{2.72}$ (JCPDS 39-0758) (Figure 4.40;4.42;4.43) [107]. The CIGS thin-films are almost quasi-amorphous in nature; however, long-range order changes with increasing film thickness progressively [102]. After the beta irradiation the intensity of the

diffraction peaks increases slightly. The calculated interatomic distances and the measured diffraction angles of (007) reflection plane of unirradiated and irradiated films with different thicknesses are presented in Table 4.10.

Table 4.10 : X-Ray diffraction data of unirradiated and irradiated CIGS thin-films with different number of layers**.**

Samples	(*hkl*)	Calculated		JCPDS 39-0758	
		d (Å)	2θ	d (Å)	2θ
3 Layers-Unirr.	(007)	2.81	31.83	2.81	31.88
3 Layers-Irr. (9.0 Gy)	**(007)**	2.81	31.82		
7 Layers-Unirr.	(007)	2.81	31.78		
7 Layers-Irr. (9.0 Gy)	**(007)**	2.81	31.76		
9 Layers-Unirr.	(007)	2.82	31.74		
9 Layers-Irr. (9.0 Gy)	**(007)**	2.81	31.76		
11 Layers-Unirr.	(007)	2.82	31.74		
11 Layers-Irr. (9.0 Gy)	**(007)**	2.81	31.82		

The average size of CIGS nanocrystallites is determined using the Debye-Sherrer's formula **(3.5)** from the XRD pattern [82]. Table 4.11 depicts the variation in average crystallite sizes and the intensity of reflections of (007) plane of the unirradiated and irradiated films with the thickness increase. According to the Scherrer equation, the broadening of peaks implies a decrease in crystallite size.

Table 4.11 : The average nanocrystallite size and the intensity of (007) diffraction peak.

Samples	Layer	Thickness (nm)	I_0		Aver.Cryst. Size (nm)	
			Unirradiated	Irradiated	Unirradiated	Irradiated
A	3	80±5	57	113	232.02	85.30
B	5	140±5	35	180	-	138.30
C	7	195±5	74	78	185.59	50.80
D	9	235±5	50	162	115.98	92.60
E	11	300±5	56	234	231.97	58.08

The XRD diffraction of (007) preferred orientation shifts toward higher intensities with the increase of beta irradiation effect, as given in Table 4.11 [47]. The crystallite size of the sol-gel derived ultra thin CIGS films became smaller with exposing to beta irradiation. However, the larger grain sizes reduce grain boundary scattering and improve conductivity [Url-16]. The larger grain size plays a role at the decrease of grain boundaries. As the lattice mismatches occur at the grain boundaries, so that the defects reside at the grain boundaries according to literature [28]. Consequently, the lifetime of charge carriers is shorter. The more grain boundaries in the material, the shorter the lifetime of the charge carriers. The larger the grain size, the longer the charge carrier lifetimes and the larger the energy band gap utilization and the larger the open circuit voltage will be [31].

The chemical content is investigated by using EDS analyses for the unirradiated and irradiated of ~ 9 Gy absorbed dose of different thicknesses in Figure 4.44 - 4.53.

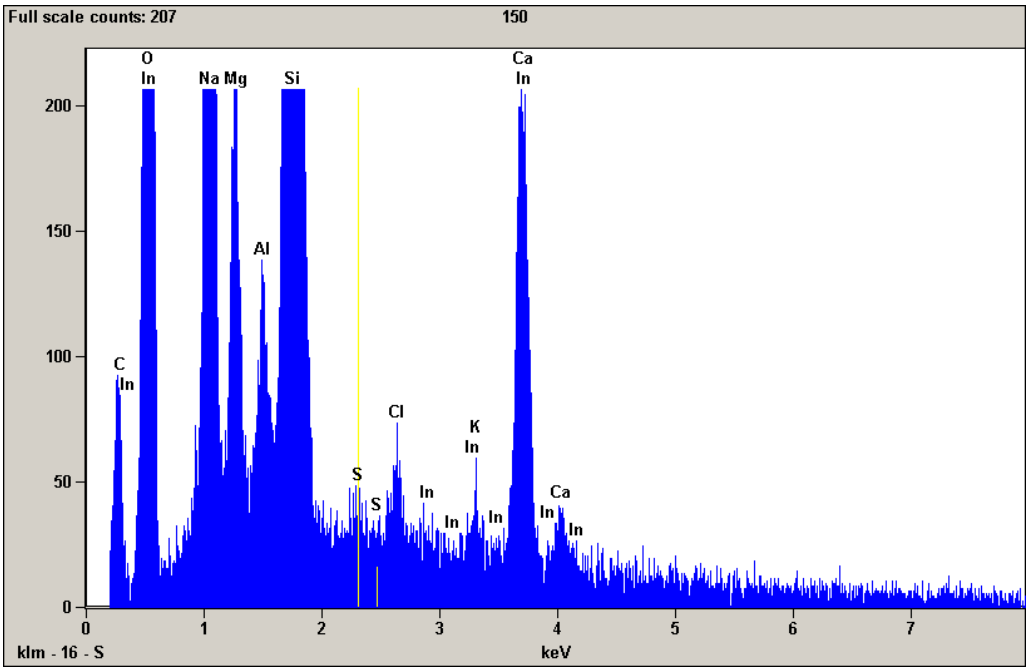

Element	*Weight %*	*Formula*	*Compound %*
O	46.78	***S***	---
Na	8.60	***Na_2O***	11.60
Mg	2.18	***MgO***	3.62
Al	0.74	***Al_2O_3***	1.39
Si	34.16	***SiO_2***	73.08
S	0.20	***SO_3***	0.49
Cl	0.57	***Cl***	0.57
K	0.17	***K_2O***	0.21
Ca	5.62	***CaO***	7.86
In	0.99	***In_2O_3***	1.19
Total	100.00		100.00

Figure 4.44 : EDS pattern of irradiated 3 layers CIGS thin-film.

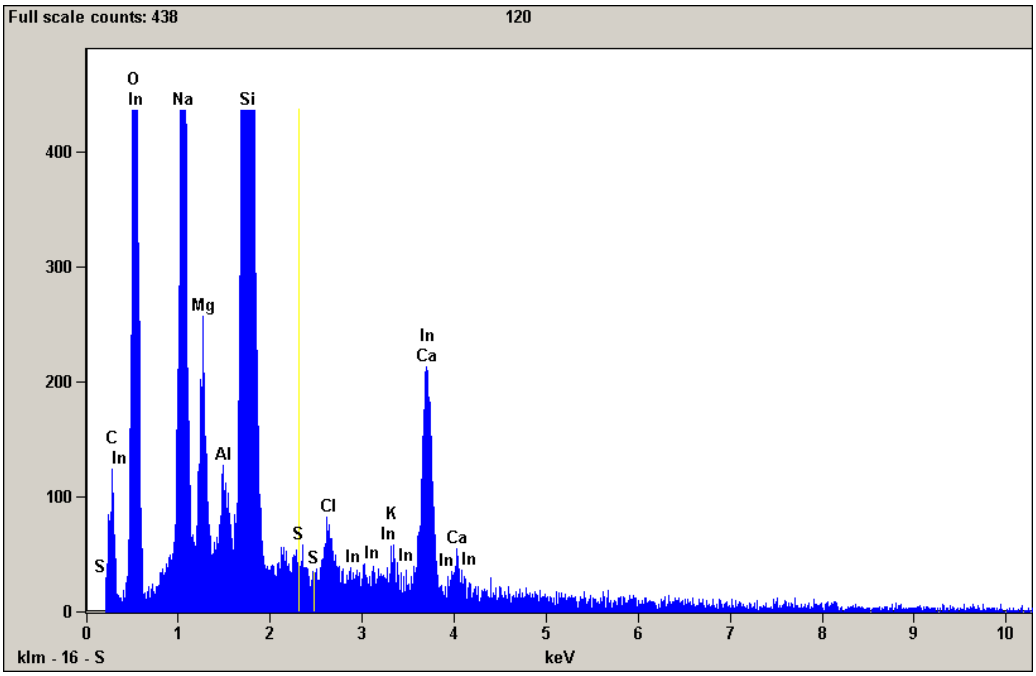

Element	*Weight %*	*Formula*	*Compnd %*
O	46.80	***S***	---
Na	8.67	***Na_2O***	11.68
Mg	2.13	***MgO***	3.53
Al	0.62	***Al_2O_3***	1.17
Si	34.55	***SiO_2***	73.91
S	0.06	***SO_3***	0.16
Cl	1.01	***Cl***	1.01
K	0.44	***K_2O***	0.53
Ca	5.73	***CaO***	8.01
In	0.00	***In_2O_3***	0.00
Total	100.00		100.00

Figure 4.45 : EDS pattern of unirradiated 3 layers CIGS thin-film.

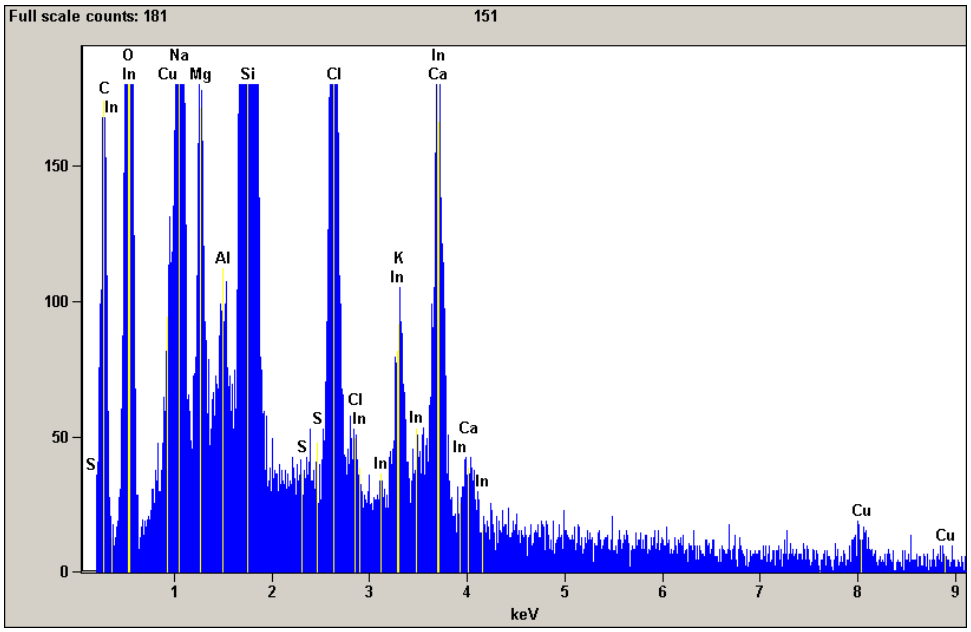

Element	*Weight %*	*Formula*	*Compound %*
O	42.16	***S***	---
Na	7.99	***Na_2O***	10.77
Mg	1.67	***MgO***	2.77
Al	0.58	***Al_2O_3***	1.09
Si	30.31	***SiO_2***	64.85
S	0.03	***SO_3***	0.09
Cl	5.13	***Cl***	5.13
K	0.61	***K_2O***	0.73
Ca	4.81	***CaO***	6.73
Cu	3.28	***Cu_2O***	3.70
In	3.43	***In_2O_3***	4.14
Total	100.00		100.00

Figure 4.46 : EDS pattern of irradiated 5 layers CIGS thin-film.

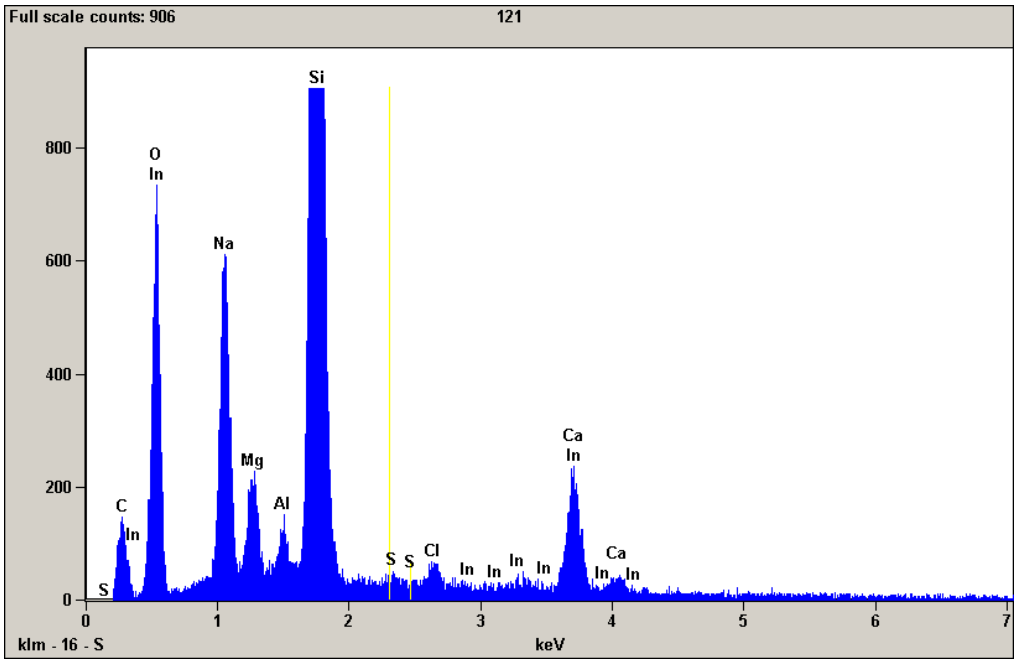

Element	*Weight %*	*Formula*	*Compnd %*
O	46.75	***S***	---
Na	8.92	***Na_2O***	12.03
Mg	2.25	***MgO***	3.74
Al	0.77	***Al_2O_3***	1.46
Si	33.93	***SiO_2***	72.59
S	0.23	***SO_3***	0.57
Cl	0.66	***Cl***	0.66
Ca	5.87	***CaO***	8.21
In	0.62	***In_2O_3***	0.75
Total	100.00		100.00

Figure 4.47 : EDS pattern of unirradiated 5 layers CIGS thin-film.

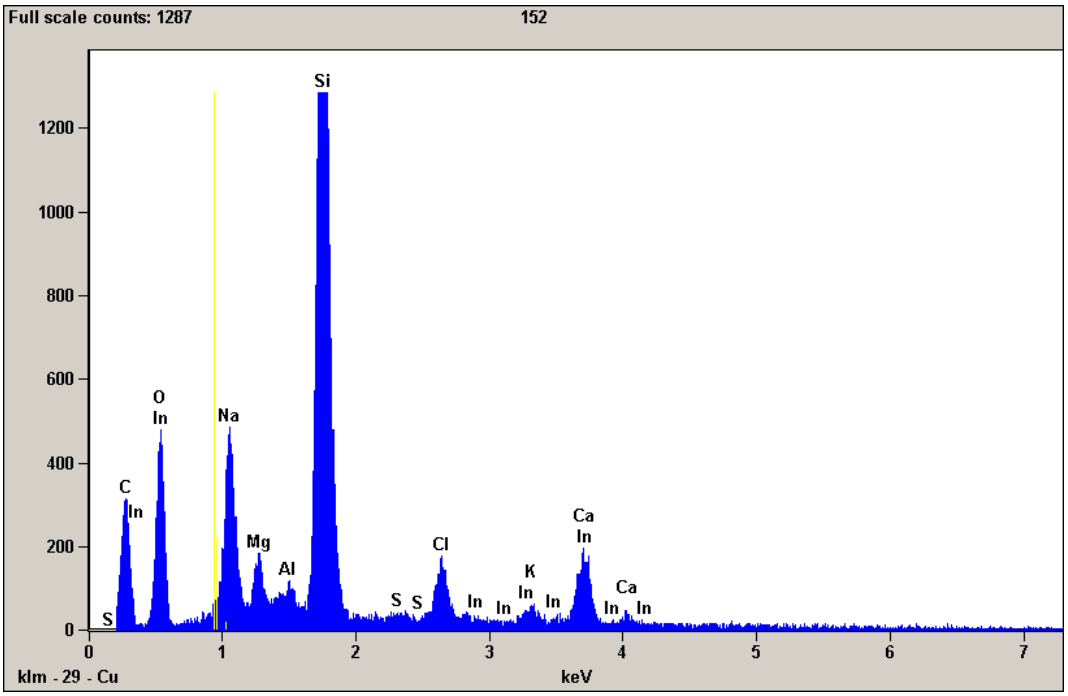

Element	*Weight %*	*Formula*	*Compound %*
O	44.99	***S***	---
Na	8.33	***Na_2O***	11.22
Mg	1.43	***MgO***	2.36
Al	0.62	***Al_2O_3***	1.16
Si	32.94	***SiO_2***	70.47
S	0.24	***SO_3***	0.59
Cl	3.48	***Cl***	3.48
K	0.37	***K_2O***	0.44
Ca	5.53	***CaO***	7.74
In	2.08	***In_2O_3***	2.51
Total	100.00		100.00

Figure 4.48 : EDS pattern of irradiated 7 layers CIGS thin-film.

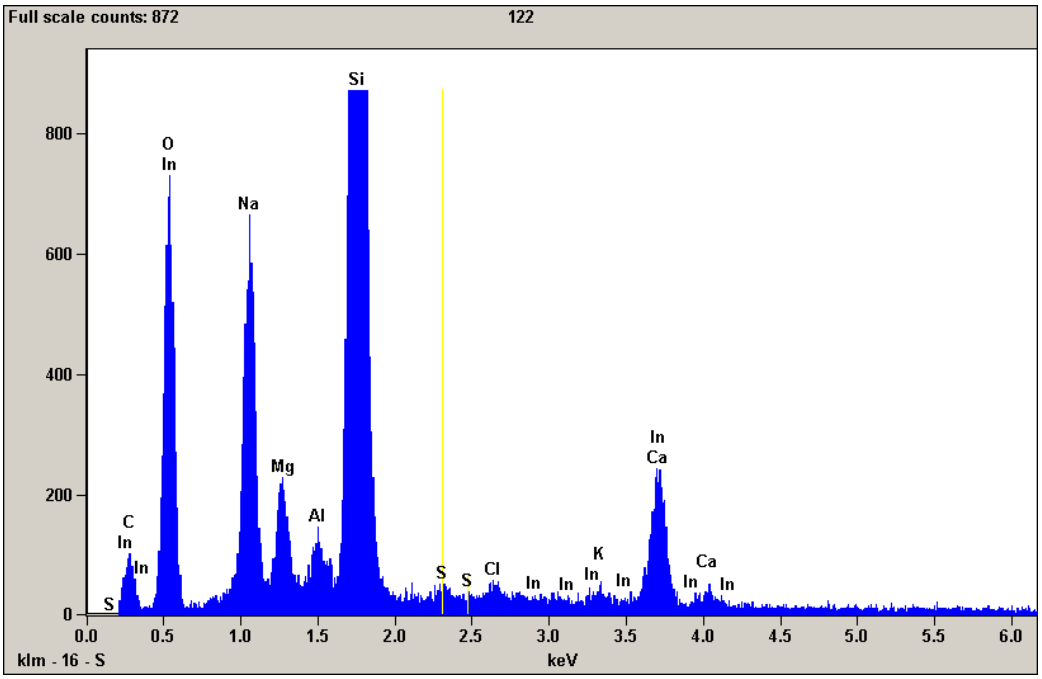

Element	*Weight %*	*Formula*	*Compound %*
O	47.08	***S***	---
Na	8.97	***Na_2O***	12.09
Mg	2.08	***MgO***	3.45
Al	0.73	***Al_2O_3***	1.38
Si	34.33	***SiO_2***	73.44
S	0.33	***SO_3***	0.81
Cl	0.36	***Cl***	0.36
K	0.43	***K_2O***	0.52
Ca	5.59	***CaO***	7.82
In	0.11	***In_2O_3***	0.13
Total	100.00		100.00

Figure 4.49 : EDS pattern of unirradiated 7 layers CIGS thin-film.

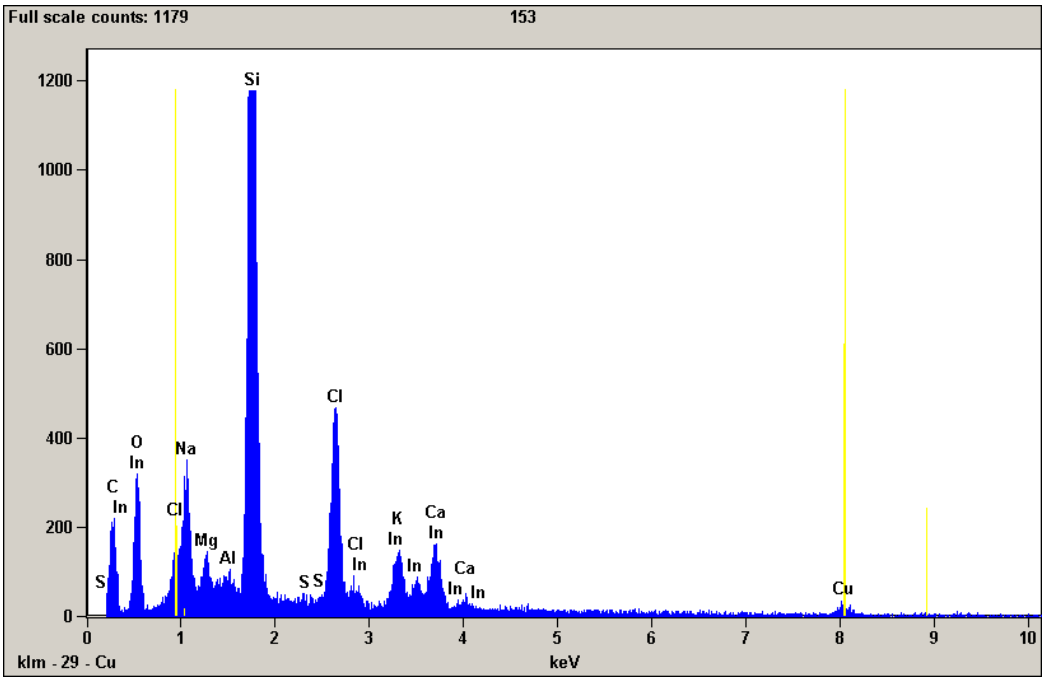

Element	*Weight %*	*Formula*	*Compound %*
O	36.51	***S***	---
Na	5.95	***Na_2O***	8.02
Mg	0.91	***MgO***	1.50
Al	0.43	***Al_2O_3***	0.81
Si	25.13	***SiO_2***	53.77
S	0.16	***SO_3***	0.39
Cl	10.02	***Cl***	10.02
K	0.36	***K_2O***	0.44
Ca	4.16	***CaO***	5.82
Cu	6.80	***Cu_2O***	7.66
In	9.58	***In_2O_3***	11.59
Total	100.00		100.00

Figure 4.50 : EDS pattern of irradiated 9 layers CIGS thin-film.

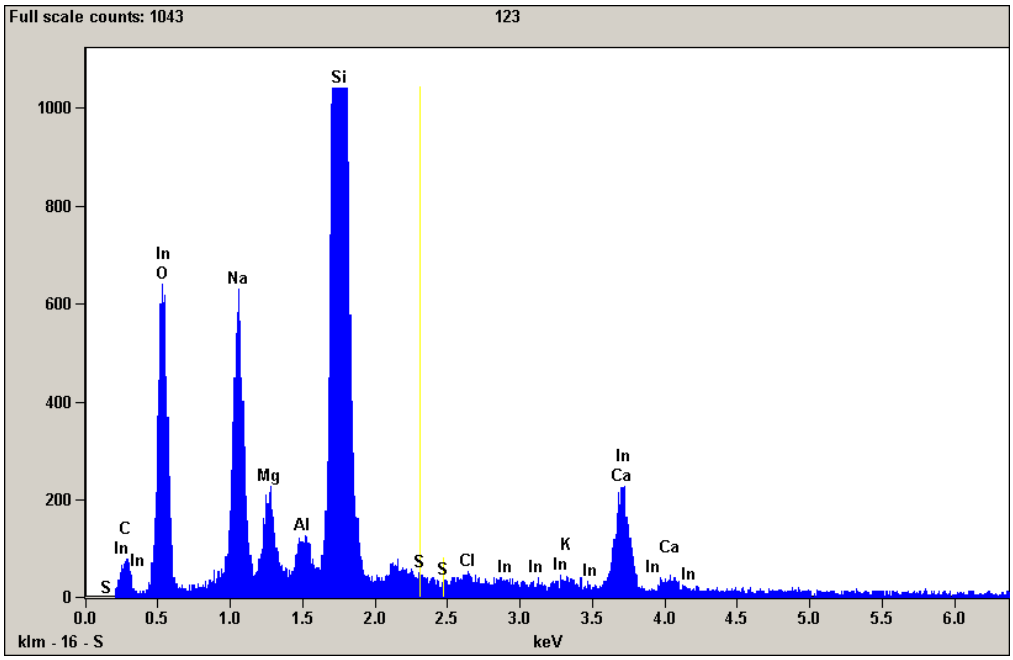

Element	*Weight %*	*Formula*	*Compound %*
O	47.16	***S***	---
Na	8.51	***Na_2O***	11.47
Mg	1.93	***MgO***	3.20
Al	0.77	***Al_2O_3***	1.45
Si	34.95	***SiO_2***	74.77
S	0.00	***SO_3***	0.00
Cl	0.34	***Cl***	0.34
K	0.25	***K_2O***	0.30
Ca	5.79	***CaO***	8.10
In	0.31	***In_2O_3***	0.37
Total	100.00		100.00

Figure 4.51 : EDS pattern of unirradiated 9 layers CIGS thin-film.

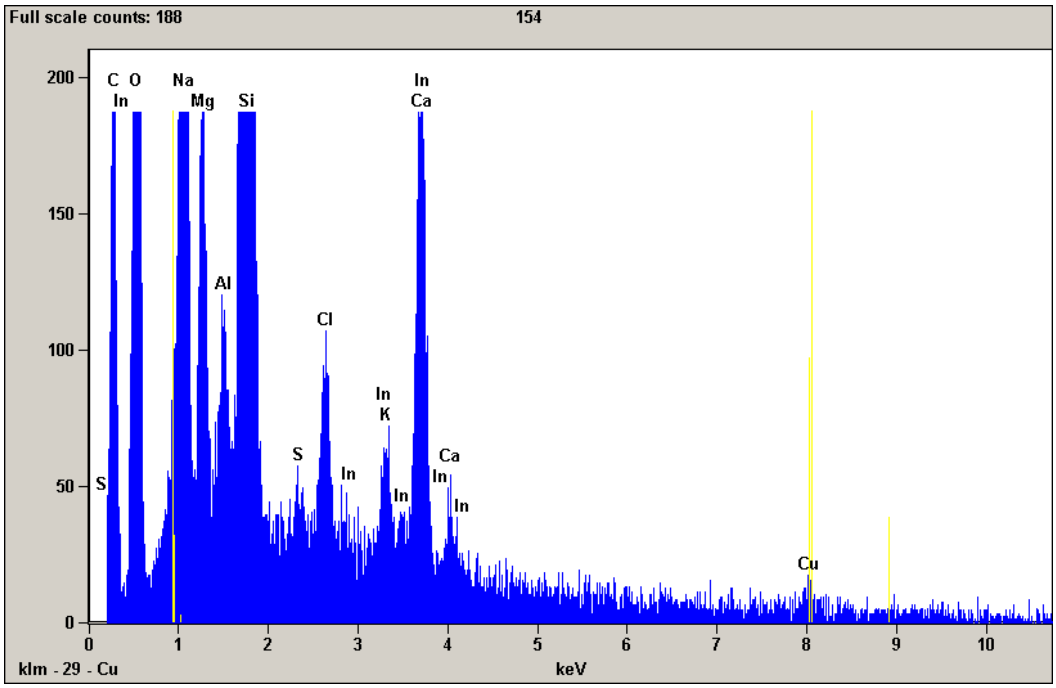

Element	*Weight %*	*Formula*	*Compound %*
O	45.37	***S***	---
Na	8.09	***Na_2O***	10.90
Mg	2.05	***MgO***	3.41
Al	0.70	***Al_2O_3***	1.31
Si	32.76	***SiO_2***	70.08
S	0.24	***SO_3***	0.60
Cl	1.31	***Cl***	1.31
K	0.34	***K_2O***	0.41
Ca	5.69	***CaO***	7.96
Cu	1.87	***Cu_2O***	2.11
In	1.58	***In_2O_3***	1.91
Total	100.00		100.00

Figure 4.52 : EDS pattern of irradiated 11 layers CIGS thin-film.

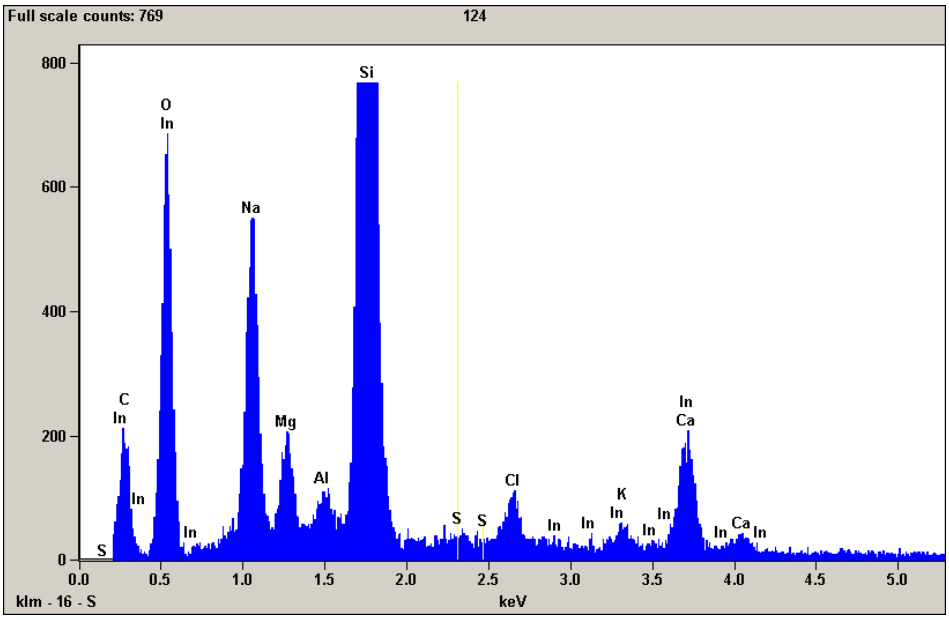

Element	*Weight %*	*Formula*	*Compound*
O	46.23	***S***	---
Na	8.65	***Na_2O***	11.66
Mg	1.89	***MgO***	3.14
Al	0.65	***Al_2O_3***	1.22
Si	33.88	***SiO_2***	72.48
S	0.24	***SO_3***	0.60
Cl	1.70	***Cl***	1.70
K	0.56	***K_2O***	0.67
Ca	5.41	***CaO***	7.57
In	0.79	***In_2O_3***	0.95
Total	100.00		100.00

Figure 4.53 : EDS pattern of unirradiated 11 layers CIGS thin-film.

There is a considerable variation in the amount of detected elements and compounds of the CIGS thin-film with increase of the thickness and radiation absorbed dose which is presented in Table 4.12.

Table 4.12 : EDS results of the unirradiated and irradiated CIGS thin-films for the different thicknesses.

Samples	Element (%)		Compound (%)	
	Cu	In	Cu_2O	In_2Cu_3
3 Layers-Unirr.	-	-	-	-
3 Layers-Irr. (9.0 Gy)	-	0.99	-	1.19
5 Layers-Unirr.	-	0.62	-	0.75
5 Layers-Irr. (9.0 Gy)	3.28	3.43	3.70	4.14
7 Layers-Unirr.	-	0.11	-	0.13
7 Layers-Irr. (9.0 Gy)	-	2.08	-	2.51
9 Layers-Unirr.	-	0.31	-	0.37
9 Layers-Irr. (9.0 Gy)	6.80	9.58	7.66	11.59
11 Layers-Unirr.	-	0.79	-	0.95
11 Layers-Irr. (9.0 Gy)	1.87	1.58	2.11	1.91

4.2.1.2 Optical characterizations

The transmittance and absorbance of CIGS thin-film deposited 3, 5 and 7 layers are illustrated in Figure 4.54 - 4.56. The irradiation effect for the different thicknesses can be seen clearly. With the increase of radiation absorbed dose the transmittance decrease obviously.

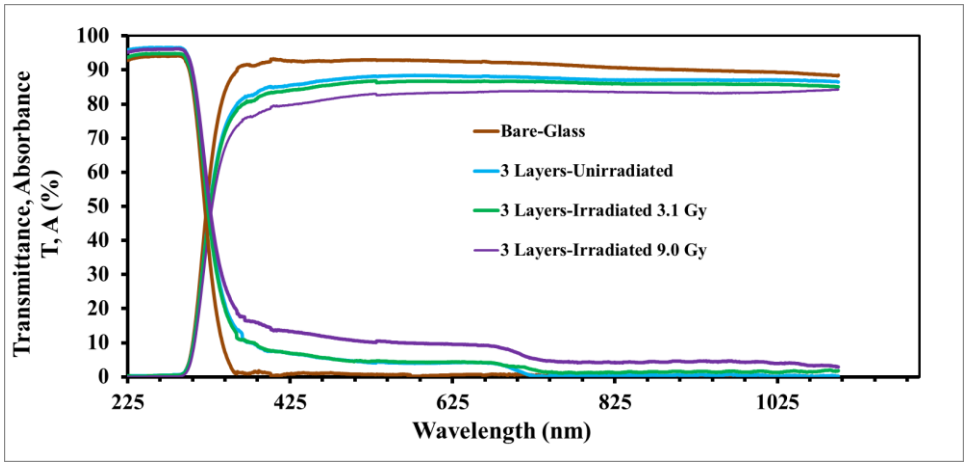

Figure 4.54 : Optical transmittance and absorbance spectra of unirradiated and irradiated 3 layers coated CIGS with different absorbed doses.

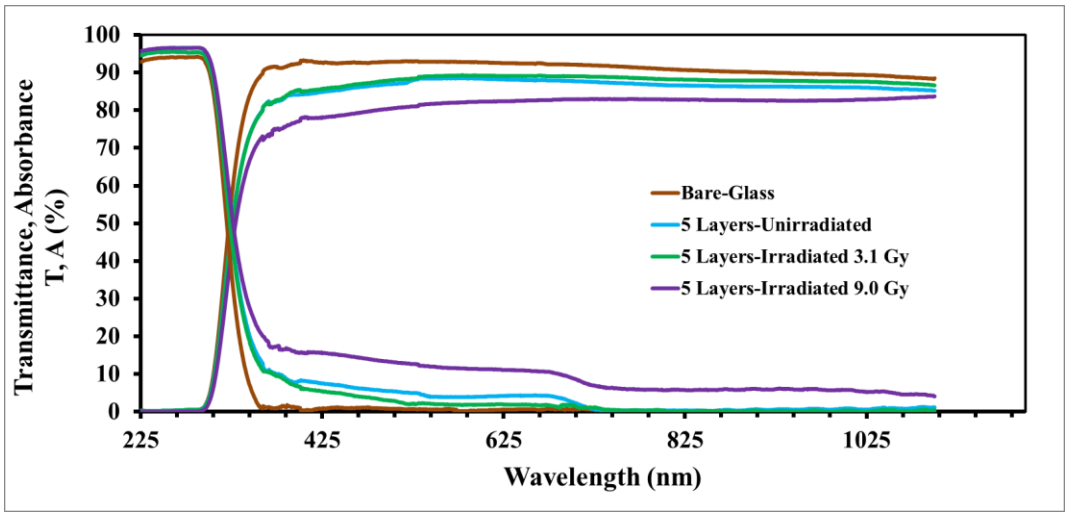

Figure 4.55 : Optical transmittance and absorbance spectra of unirradiated and irradiated 5 layers coated CIGS with different absorbed doses.

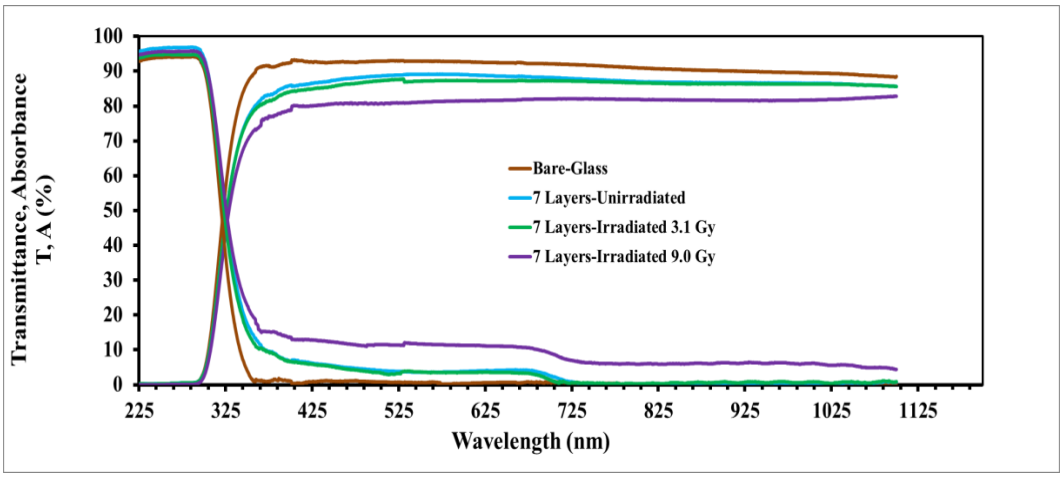

Figure 4.56 : Optical transmittance and absorbance spectra of unirradiated and irradiated 7 layers coated CIGS with different absorbed doses.

The effect of the each absorbed dose level the Figures 4.57 - 4.58 were illustrated seperately. The Figures 4.57 - 4.58 show that the effect of the beta irradiation with the same absorbed dose has similar amount of effect.

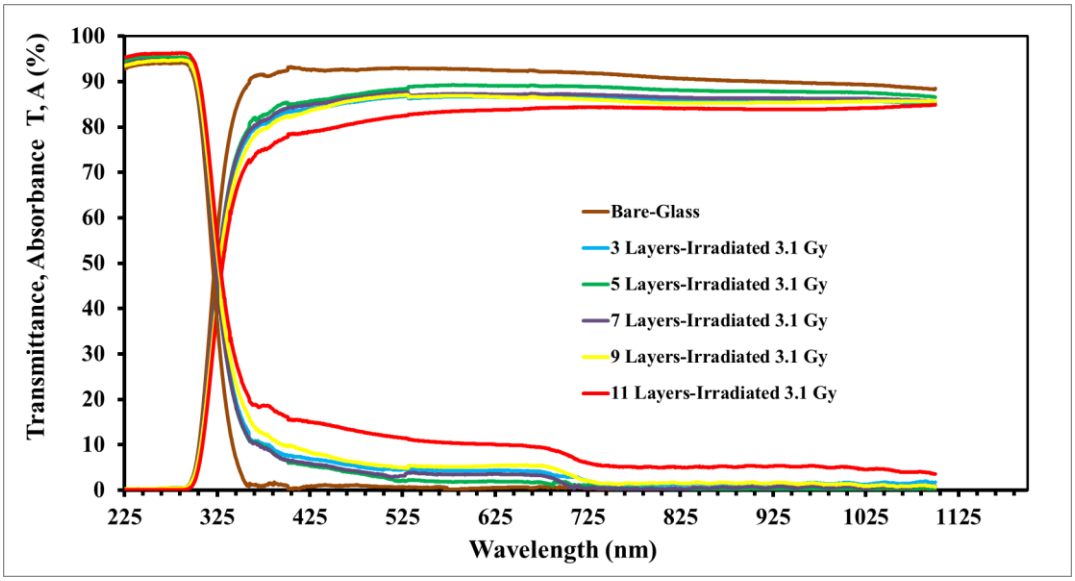

Figure 4.57 : Optical transmittance and absorbance spectra of 3.1 Gy absorbed dose CIGS thin-film with different thicknesses.

The transmittance of CIGS thin-films between 230 nm and 300 nm are also shown in Figure 4.58. The CIGS thin-films were non-absorbing beyond ~ 262 nm in the UV range of CIGS thin-film for the all 9.0 Gy irradiated with different number of layers (Figure 4. 58). The absorption edge of the CIGS thin-films raised slightly from ~ 246 to ~ 262 nm with the increase of irradiation absorbed dose of 9.0 Gy. The absorption spectra showed the blue shifting of absorption edge which indicates lower optical band.

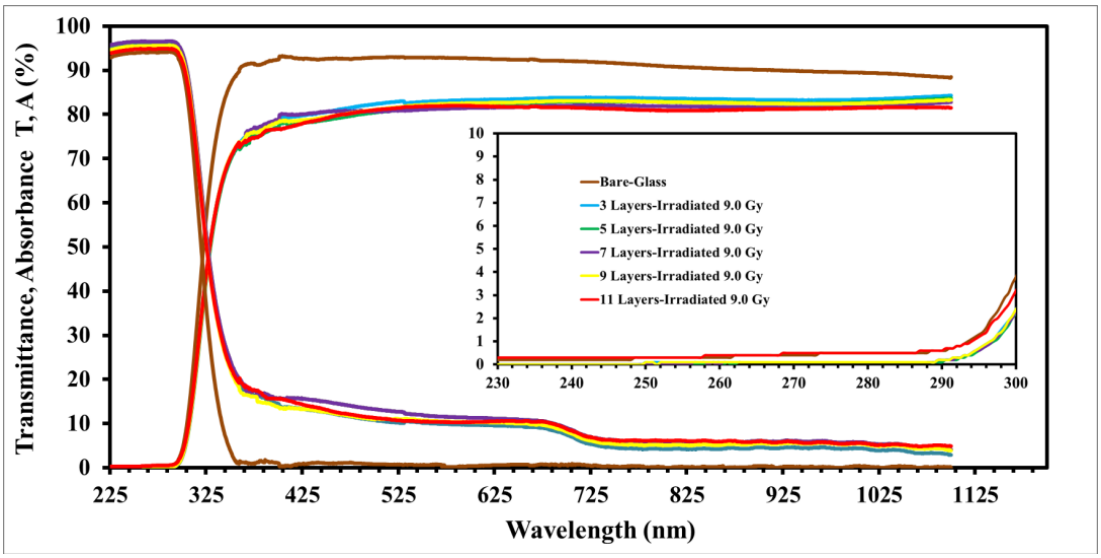

Figure 4.58 : Optical transmittance and absorbance spectra of 9.0 Gy absorbed dose CIGS thin-film with different thicknesses.

The average transmittance and absorbance of unirradiated and irradiated CIGS films at 3, 5, 7, 9 and 11 layers were presented at ultraviolet, visible and near infrared

ranges in Table 4.13. There was a decrease in transmittance of CIGS thin-film at ultraviolet range of electromagnetic spectrum as well as at the visible and the near-infrared ranges.

Table 4.13 : The average transmittance and absorbance of unirradiated and irradiated CIGS thin-film with different thicknesses.

	UV (190-380 nm)			**Visible (380-780 nm)**			**NIR (780-1100 nm)**		
	T (%)	**R (%)**	**A (%)**	**T (%)**	**R (%)**	**A (%)**	**T (%)**	**R (%)**	**A (%)**
3 Layers-Unirradiated	24.72	4.23	71.06	87.41	8.51	4.09	87.03	12.60	0.37
3 Layers-Irrad. 3.1 Gy	24.20	6.74	69.06	85.94	9.60	4.46	85.81	12.71	1.47
3 Layers-Irrad. 9.0 Gy	22.29	5.55	72.16	82.42	7.85	9.73	83.52	12.31	4.17
5 Layers-Unirradiated	24.76	4.68	70.56	87.10	8.54	4.36	86.19	13.24	0.57
5 Layers-Irrad. 3.1 Gy	24.68	6.11	69.21	88.08	9.31	2.62	87.74	12.04	0.22
5 Layers-Irrad. 9.0 Gy	21.88	5.22	72.90	81.17	7.28	11.56	82.81	11.56	5.62
7 Layers-Unirradiated	24.70	4.38	70.91	88.00	8.19	3.81	86.57	13.12	0.31
7 Layers-Irrad. 3.1 Gy	24.46	6.85	68.69	86.63	9.95	3.41	86.32	13.06	0.63
7 Layers-Irrad. 9.0 Gy	22.29	6.20	71.51	81.13	8.18	10.70	81.85	12.28	5.87
9 Layers-Unirradiated	22.18	6.17	71.65	82.29	8.62	9.09	81.97	12.96	5.07
9 Layers-Irrad. 3.1 Gy	23.11	6.22	70.67	85.79	8.82	5.39	85.47	13.13	1.39
9 Layers-Irrad. 9.0 Gy	22.12	6.32	71.56	81.56	8.26	10.18	82.68	12.20	5.13
11 Layers-Unirradiated	22.44	5.94	71.61	80.69	8.61	10.70	81.26	13.08	5.66
11 Layers-Irrad. 3.1 Gy	21.36	5.43	73.21	82.40	6.86	10.73	84.14	10.91	4.95
11 Layers-Irrad. 9.0 Gy	22.44	5.94	71.61	80.69	8.61	10.70	81.26	13.08	5.66
Bare-Glass	27.90	7.06	65.04	92.44	6.88	0.68	89.85	9.96	0.19

Figure 4.59 shows the plot of $(\alpha h\nu)^2$ versus $h\nu$ for the unirradiated and irradiated thin-films. The optical transition was determined as an allowed direct transition of $(\alpha h\nu)^2$ for CIGS thin-film. There was a change in optical energy band gap in CIGS thin-films with the increase of absorbed dose.

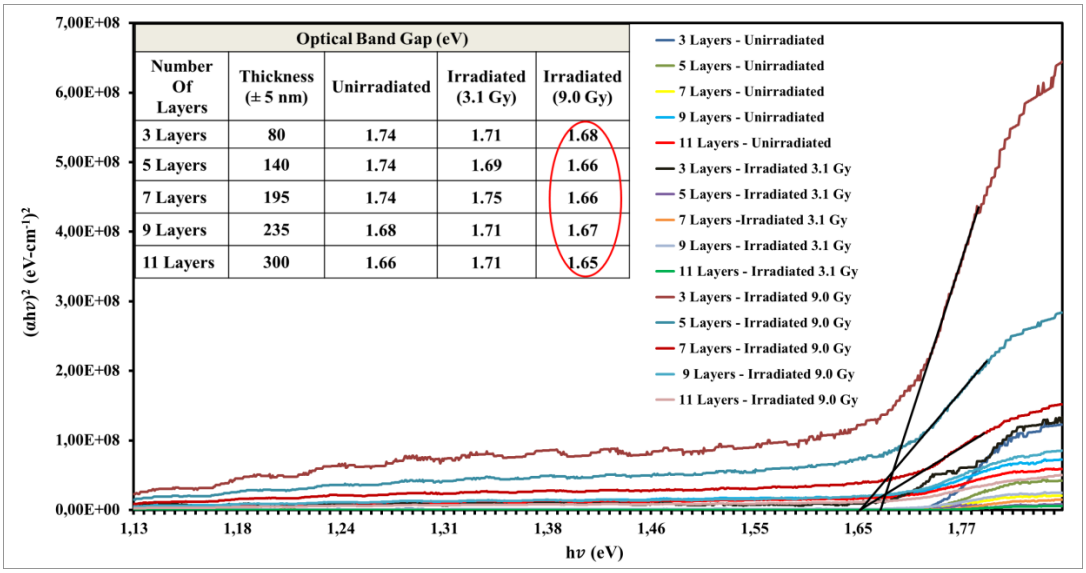

Figure 4.59 : The variation of optical energy band gap of the unirradiated and irradiated with the change of thickness.

The optical energy band gap of the 9.0 Gy irradiated CIGS absorber layer for the thicker sample with 11 layers is determined as ~ 1.65 eV by extrapolating the plot of $(\alpha h\upsilon)^2$ as a function of hυ. Figure 4.60 deplicts the optical energy band gap changes for the 9.0 Gy irradiated thin-films with the change of thickness.

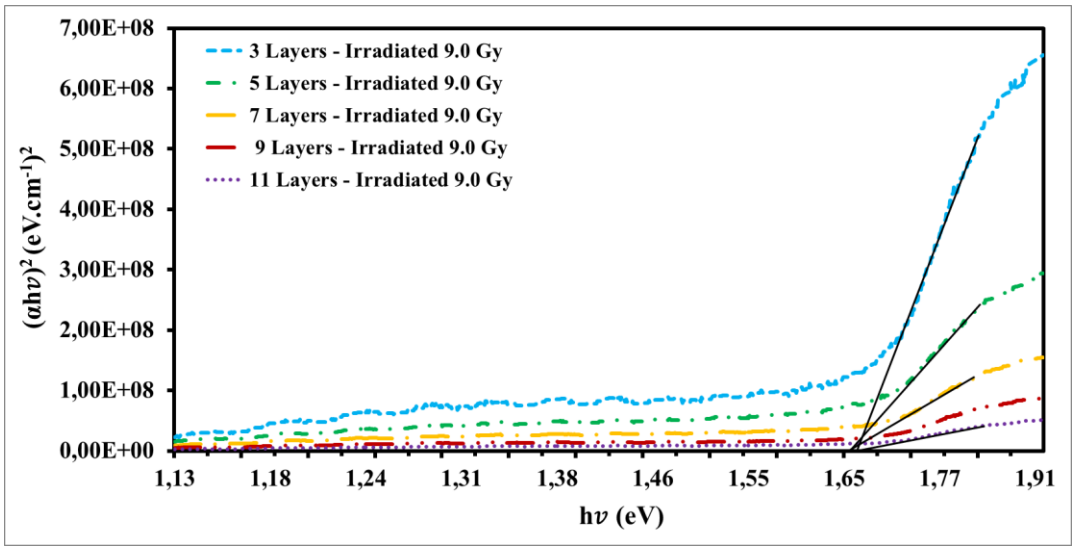

Figure 4.60 : The variation of optical energy band gap of the 9.0 Gy irradiated thin-films with the change of thickness.

The optical parameters of thin-films such as absorption coefficient (α), extinction coefficient (k) and refractive index (n) were calculated for the photon energy of 1.25, 2.25 and 3.54 eV (Table 4.14).

Table 4.14 : The calculated optical parameters of unirradiated and irradiated CIGS thin-film at different number of layers.

Samples	Wavelength (nm)	Photon Energy (eV)	Absorption Coeff. α (cm^{-1})	Extinction Coeff. (k)	Refractive Index (n)
3 Layer-Unirradiated	992	1.25	573.40	0.005	2.09
	550	2.25	5,673.36	0.025	1.72
	350	3.54	26,272.77	0.073	1.48
3 Layer-Irradiated 3.1 Gy	992	1.25	1,877.56	0.015	2.10
	550	2.25	6,339.39	0.028	1.81
	350	3.54	25,114.30	0.070	1.72
3 Layer-Irradiated 9.0 Gy	992	1.25	6,291.56	0.050	2.02
	550	2.25	14,370.55	0.063	1.59
	350	3.54	36,450.37	0.102	1.41
5 Layer-Unirradiated	992	1.25	578.37	0.005	2.14
	550	2.25	3,157.58	0.014	1.73
	350	3.54	14,350.62	0.040	1.61
5 Layer-Irradiated 3.1 Gy	992	1.25	81.40	0.001	2.07
	550	2.25	1,585.60	0.007	1.84
	350	3.54	13,069.82	0.036	1.76
5 Layer-Irradiated 9.0 Gy	992	1.25	4,847.31	0.038	1.98
	550	2.25	9,788.87	0.043	1.58
	350	3.54	21,569.14	0.060	1.51
7 Layer-Unirradiated	992	1.25	177.55	0.001	2.14
	550	2.25	2,031.24	0.009	1.72
	350	3.54	10,656.58	0.030	1.60
7 Layer-Irradiated 3.1 Gy	992	1.25	355.30	0.003	2.13
	550	2.25	2,133.46	0.009	1.86
	350	3.54	9,507.86	0.026	1.82
7 Layer-Irradiated 9.0 Gy	992	1.25	3,634.25	0.029	2.04
	550	2.25	6,910.96	0.030	1.68
	350	3.54	14,441.07	0.040	1.65
9 Layer-Unirradiated	992	1.25	4,384.36	0.03	2.08
	550	2.25	7,519.38	0.03	1.72
	350	3.54	22,381.79	0.06	1.61
9 Layer-Irradiated 3.1 Gy	992	1.25	1,117.80	0.01	2.13
	550	2.25	4,309.77	0.02	1.76
	350	3.54	18,535.93	0.05	1.65

9 Layer-Irradiated 9.0 Gy	992	1.25	4,612.09	0.04	2.03
	550	2.25	9,064.32	0.04	1.65
	350	3.54	20,673.95	0.06	1.62
11 Layer-Unirradiated	992	1.25	8,172.84	0.06	2.05
	550	2.25	14,960.36	0.07	1.65
	350	3.54	35,513.03	0.10	1.49
11 Layer-Irradiated 3.1 Gy	992	1.25	100.75	0.0008	2.11
	550	2.25	475.45	0.0021	1.85
	350	3.54	2,559.93	0.01	1.79
11 Layer-Irradiated 9.0 Gy	992	1.25	7,227.45	0.06	1.91
	550	2.25	15,273.21	0.07	1.50
	350	3.54	38,878.33	0.11	1.35

4.2.1.3 Electrical characterizations

The irradiated samples were investigated to obtain the conductivity quality. The sheet resistance was measured for the samples of ~ 9 Gy irradiated absorbed dose. CIGS thin-film of 11 layers irradiated sample has the highest conductivity value with $21.897\times10^{3}\,(\Omega\text{-cm})^{-1}$ (Figure 4.61).

The increase in conductivity does not match with the calculated average crystallite size. The crystal grain size is found to be inversely proportional to sheet resistance. The smaller crystal indicates more grain boundaries and defects. Thus, an electron encounters more barriers in the transmission process, and electric conductivity decreases [108]. The reason for the increase of the conductivity might be related with the EDS results (Table 4.11). The increase of Cu content indicates very important event that electrons emitted from Sr-90 radioisotope might created Cu-related defects in CIGS thin-film which increases the effective acceptor density. The types of defects, namely Cu, Ga, and Se Frenkel-pairs in CIGS were simultaneously generated by electron irradiaiton. These defects in CIGS solar cells induced by electrons and electrons increased the effective acceptor density. Electrons reduced the electrical resistivity as a result of the generated Frenkel-pairs in CIGS thin-film [109].

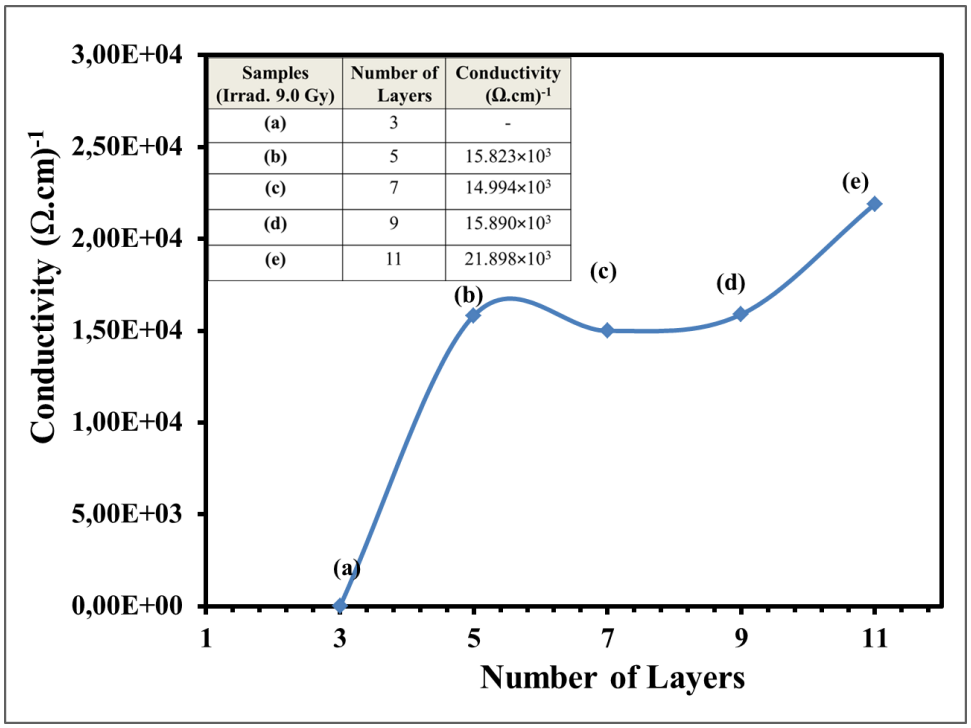

Figure 4.61 : The conductivity of the 9.0 Gray irradiated samples with the different number of layers.

4.2.2 Beta irradiation effect on aging

CIGS thin-films were fabricated by sol-gel dip-coating technique onto soda-lime-silicate glass substrates after 18 and 35 days aged of the colloidal solution. The solution was kept at - 5 °C in a dark environment in order to prevent precipitation and to extend the life of the solution. The films were immersed into the aged colloidal suspension and dried at 100 °C in an air ambiance for 10 min. This procedure was repeated five times. After the final drying, the samples were annealed at 175 °C, for 30 min, in an air ambiance. The sol-gel derived CIGS thin-films having thicknesses of about 140 ± 5 nm were exposed to the 1.5; 4.3 and 7.4 Gray (Gy) radiation doses.

4.2.2.1 Structural characterization

The CIGS thin-films are grown from the 18 and 35 days elapsed time CIGS solution and exposed to beta radiation. The structural properties were examined via SEM/EDS, X-Ray Diffraction analysis.

SEM/EDS analysis

The SEM images of the unirradiated and irradiated CIGS thin-films at 18 and 35 elapsed time is shown in Figure. 4.62.

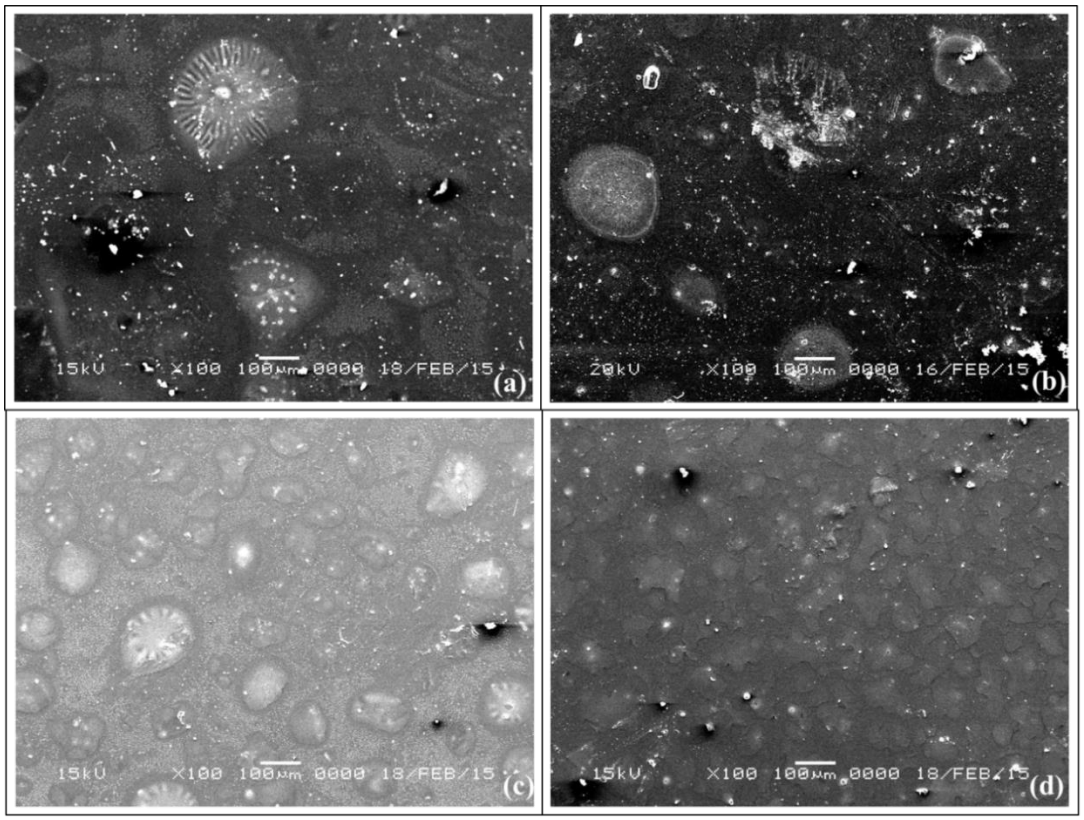

Figure 4.62 : SEM of CIGS thin-films grown with different elapsed time of solution
(a) 18 days unirradiated; **(b)** 18 days 7.4 Gy irradiated;
(c) 35 days unirradiated; **(d)** 35 days 7.4 Gy irradiated.

The SEM micrographs of the unirradiated samples proves that the aging time decreases the grain size (Figure 4.62 a and c). The irradiation can be investigated as well. The beta particles' colliscolourions effect can be seen with the change of the colour. The SEM micrographs of the irradiated samples are darker due to the beta particles' interaction. The irradiation causes the decrease of the grain size as well.

The EDS result of the 7.4 Gy irradiated 35 days aged CIGS thin-film is illustrated in Figure 4.63.

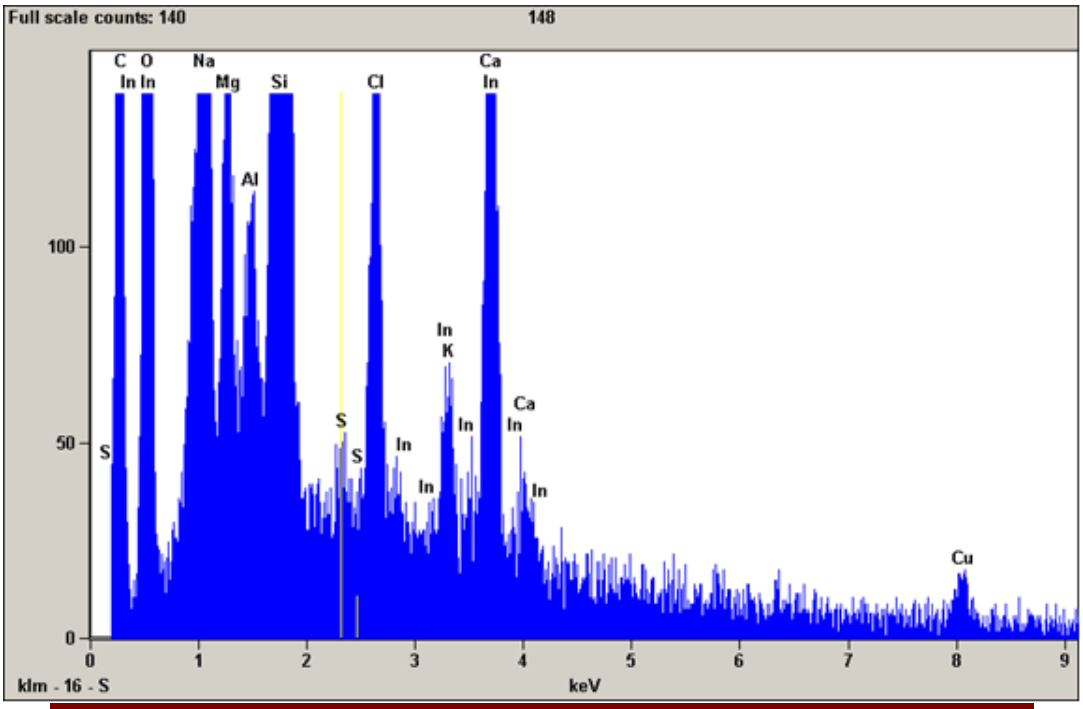

Element	*Weight %*	*Formula*	*Compound %*
O	43.86	***S***	---
Na	7.82	***Na_2O***	10.55
Mg	1.55	***MgO***	2.57
Al	0.57	***Al_2O_3***	1.07
Si	31.64	***SiO_2***	67.69
S	0.30	***SO_3***	0.74
Cl	2.79	***Cl***	2.79
K	0.24	***K_2O***	0.29
Ca	5.32	***CaO***	7.45
Cu	3.44	***Cu_2O***	3.88
In	2.46	***In_2O_3***	2.98
Total	100.00		100.00

Figure 4.63 : EDS pattern of CIGS thin-film grown from 35 days aged CIGS solution-7.4 Gy beta irradiated.

The Copper and Indium elements are detected. Due to the low amount of Gallium and Selenium, those elements might be not detected.

X-Ray diffraction analysis

The XRD patterns of the 7.4 Gy irradiated CIGS thin-films are given in Figure 4.64 - 4.65. "The X-Rays diffraction patterns for these films does not present any characteristic diffraction peak because the films deposited are amorphous or nanocrystalline. This is due to the small degree of crystallinity of these films" [107]. However, the improvement of the electrical conductivity indicated slight improvement of the crystallinity as nanocrystalline size for the aged solution during 35 days.

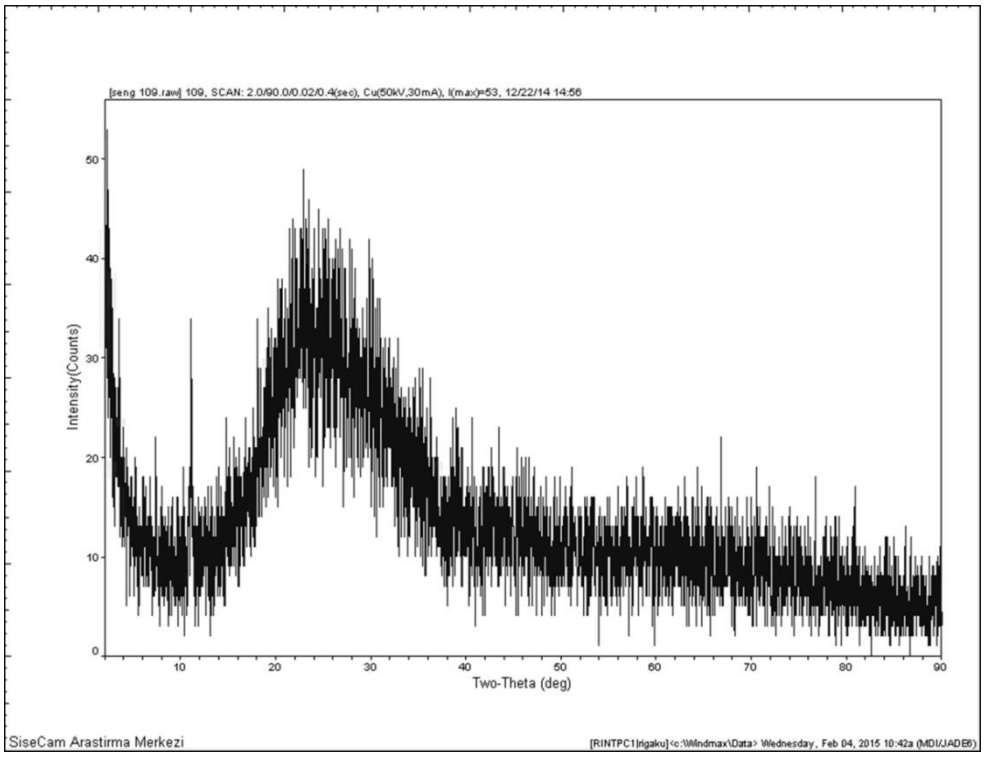

Figure 4.64 : XRD pattern of CIGS thin-film grown from 18 days aged CIGS solution - 7.4 Gy beta irradiated.

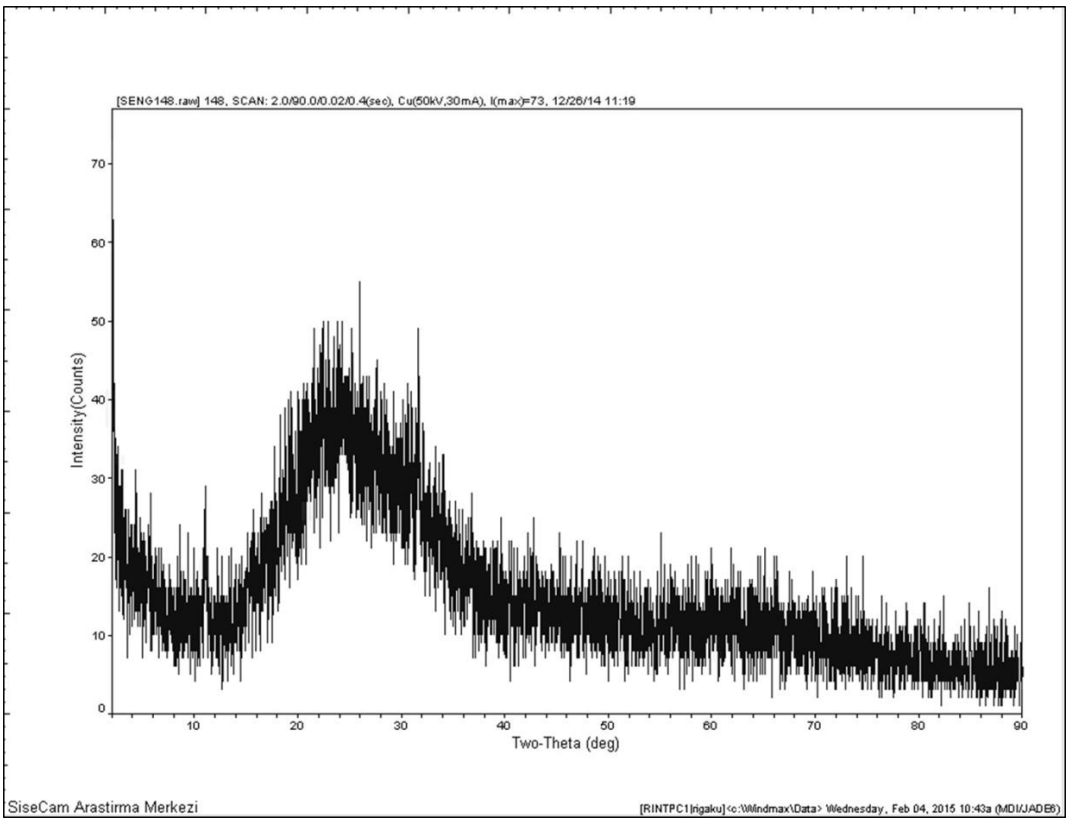

Figure 4.65 : XRD pattern of CIGS thin-film grown from 35 days aged CIGS solution - 7.4 Gy beta irradiated.

4.2.2.2 Optical characterizations

This section presents some data about beta irradiation effect on the aged CIGS solution and the response of CIGS thin-film to beta radiation in terms of the effect which generate radiation defects on optical properties. The changes of optical properties of the unirradiated CIGS thin-films were compared with the irradiated CIGS thin-films by beta radiation source. The optical properties at different dose levels as 1.5; 4.3 and 7.4 Gray (Gy) has taken to obtain the maximum changes.

The measured optical transmittance and reflectance values were considered with the spectral changes in the electromagnetic spectrum between 190 - 1100 nm (Table 4.15). The optical absorbance was calculated from the measured transmittance and reflectance values (Table 4.15).

Table 4.15 : The average optical transmittance, reflectance and absorbance of the unirradiated and irradiated aged CIGS thin-films in UV, Visible and Near-Infrared spectrums.

	UV (190-380 nm)			**Visible (380-780 nm)**			**NIR (780-1100 nm)**		
	T (%)	**R (%)**	**A (%)**	**T (%)**	**R (%)**	**A (%)**	**T (%)**	**R (%)**	**A (%)**
18 days aged-Unirradiated	23.61	6.01	70.38	86.99	8.69	4.31	86.54	12.20	1.26
35 days aged-Unirradiated	22.76	6.67	70.57	84.18	9.28	6.53	84.84	14.03	1.13
18 days aged-Irrad. (1.5 Gy)	23.15	5.39	71.46	83.34	9.65	7.01	84.03	14.49	1.49
35 days aged-Irrad. (1.5 Gy)	24.41	6.08	69.51	86.47	9.33	4.20	86.48	13.05	0.47
18 days aged-Irrad. (4.3 Gy)	21.45	6.25	72.29	79.88	9.24	10.88	81.19	14.10	4.71
35 days aged-Irrad. (4.3 Gy)	22.68	4.77	72.55	85.68	7.47	6.85	86.16	12.29	1.55
18 days aged-Irrad. (7.4 Gy)	21.46	4.79	73.76	81.11	7.66	11.23	82.80	12.21	4.99
35 days aged-Irrad. (7.4 G)y	21.95	5.38	72.67	82.65	7.92	9.43	84.88	12.38	2.74
Bare Glass	27.90	7.06	65.04	92.44	6.88	0.68	89.85	9.96	0.19

The increase of aging elapsed time and irradiated absorbed dose by the beta radiation source effect the change in the optical characteristic of the CIGS thin-films. The optical transmittance and absorbance of irradiated CIGS thin-films vary as a function of the aging elapsed time depending on the irradiation absorbed dose (Figure 4.66 - 68). Figure 4.66 - 68 illustrate transmittance (T %) and absorbance A(%) of CIGS thin-films that deposited at 18 days and 35 days and irradiated by beta radiation source.

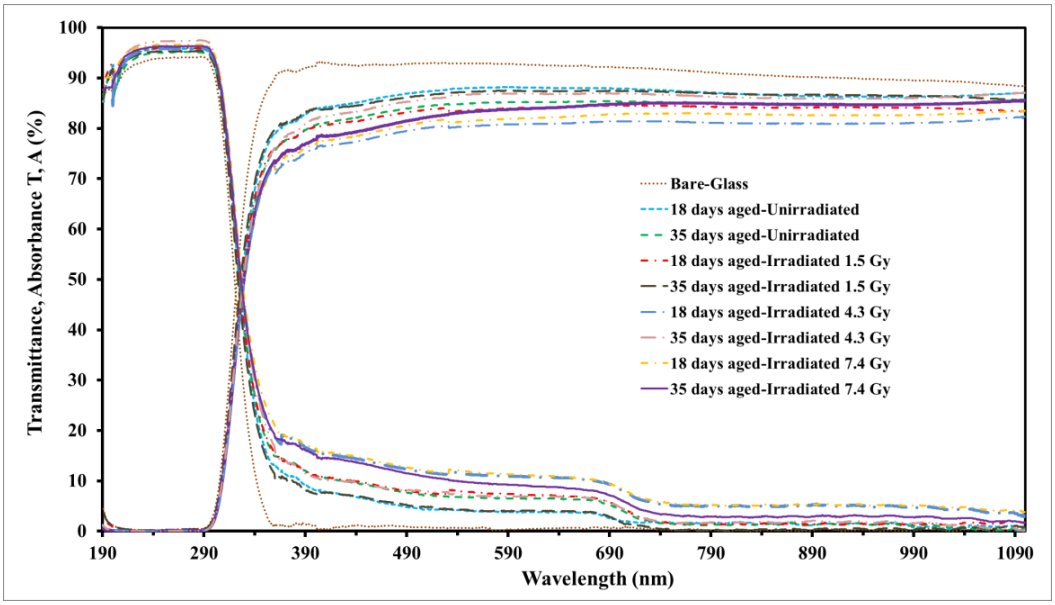

Figure 4.66 : Optical transmittance and absorbance spectra of unirradiated and irradiated different absorbed doses of CIGS thin-films at different elapsed aging time.

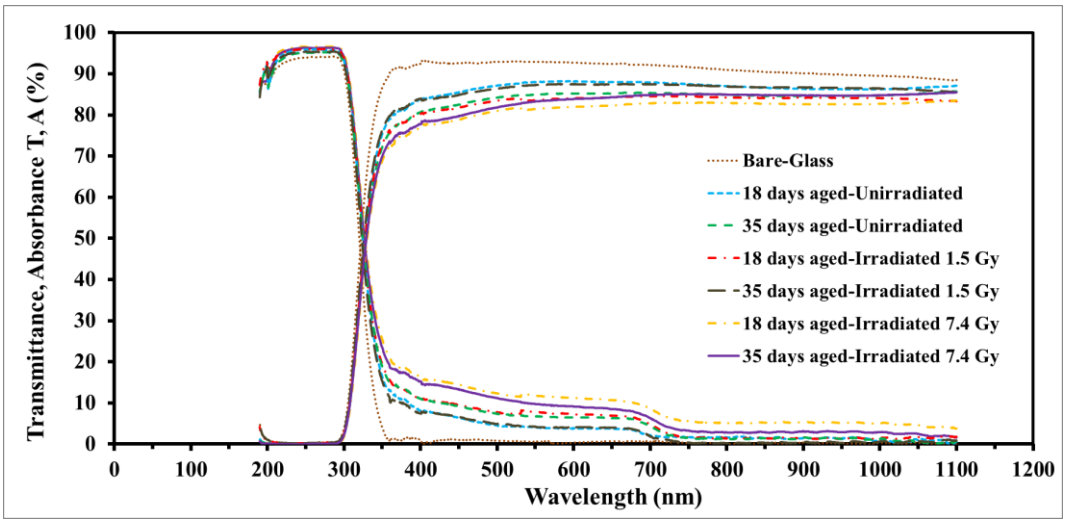

Figure 4.67 : Optical transmittance and absorbance spectra of unirradiated and 1.5 Gy and 7.4 Gy irradiated CIGS thin-films at different elapsed aging time.

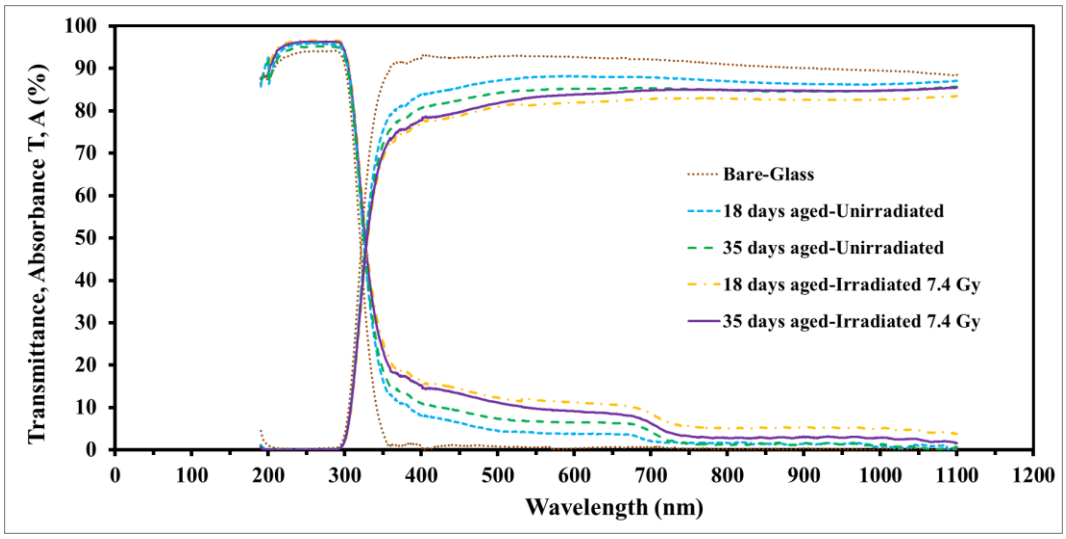

Figure 4.68 : Optical transmittance and absorbance spectra of unirradiated and 7.4 Gy irradiated CIGS thin-films at different elapsed aging time.

The variations of the optical properties indicate that the absorbed dose at ~ 1.5 Gy is enough to change optical performance of the beta irradiated thin-film.

Figure 4.69 illustrates the transmittance and absorbance spectrum of the examined unirradiated CIGS thin-films at different aging times. The transmittance of CIGS thin-films between 275 nm and 310 nm are also shown in Figure 4.69.

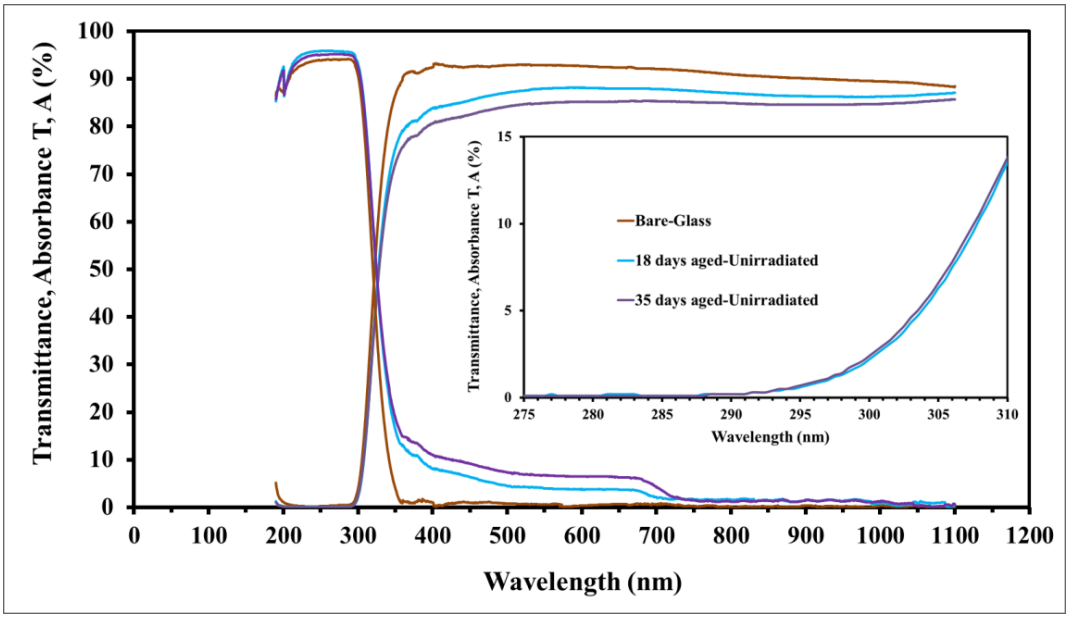

Figure 4.69 : Optical transmittance and absorbance spectra of unirradiated CIGS thin-films at different elapsed aging time.

As can be seen in Figure 4.69, it exhibits a slight decrease in the transmittance of the film. The transmission of the unirradiated samples decrease with the increase of aging elapsed time for all spectral region (UV, Visible and NIR) shown

in Table 4.15. The CIGS thin-films were non-absorbing beyond ~ 288 nm in the UV range of CIGS thin-film (Figure 4.69).

Figure 4.70 and 4.71 show the optical transmittance and absorbance spectra of unirradiated and irradiated CIGS thin-films of different absorbed doses at 18 days and 35 days elapsed time. There was a slight decrease of transmittance with the rise of absorbance and increase of the dose levels. At 18 days aged CIGS thin-films, the effect of the beta irradiation can be seen more clearly (Figure 4.70).

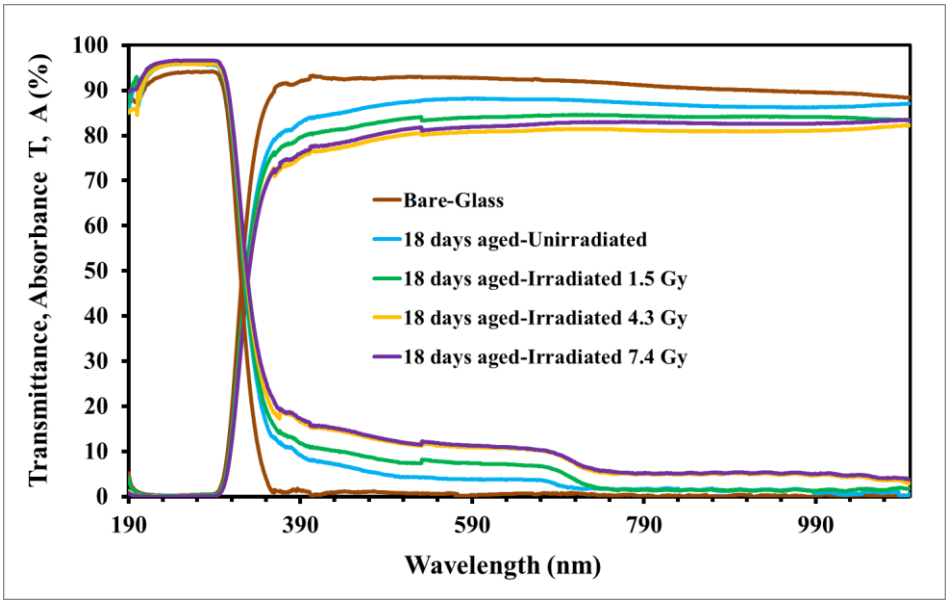

Figure 4.70 : Optical transmittance and absorbance spectra of unirradiated and irradiated CIGS thin-films of different absorbed doses at 18 days elapsed time.

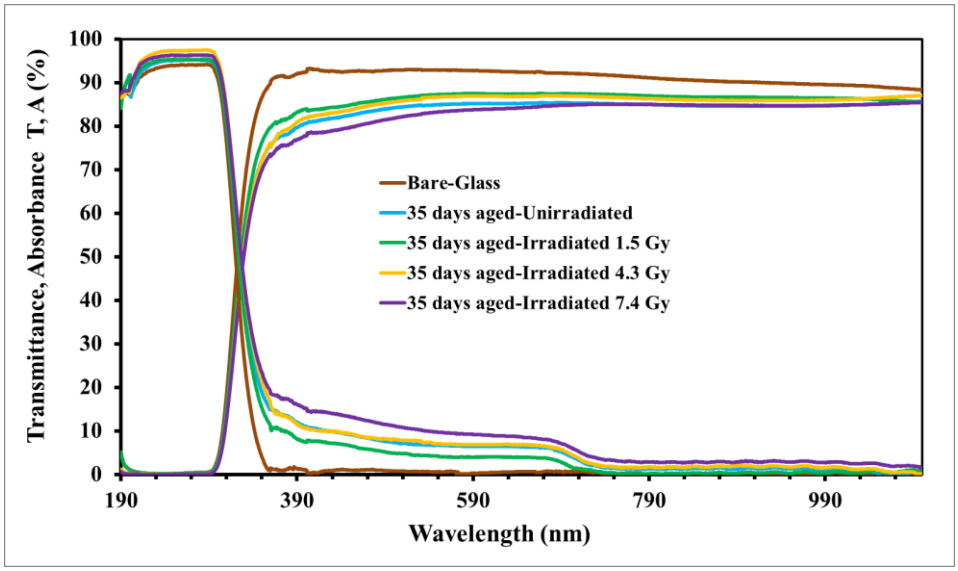

Figure 4.71 : Optical transmittance and absorbance spectra of unirradiated and irradiated CIGS thin-films of different absorbed doses at 35 days elapsed time.

To examine the effect of the each absorbed dose level the Figures 4.72 - 4.74 were illustrated seperately. These Figures 4.72 - 4.74 show that the effect of the beta irradiation becomes less significant with the increase of the aging time. That might be because of the increase of the density of the film. With the beta particle interaction, the scattering might be improved.

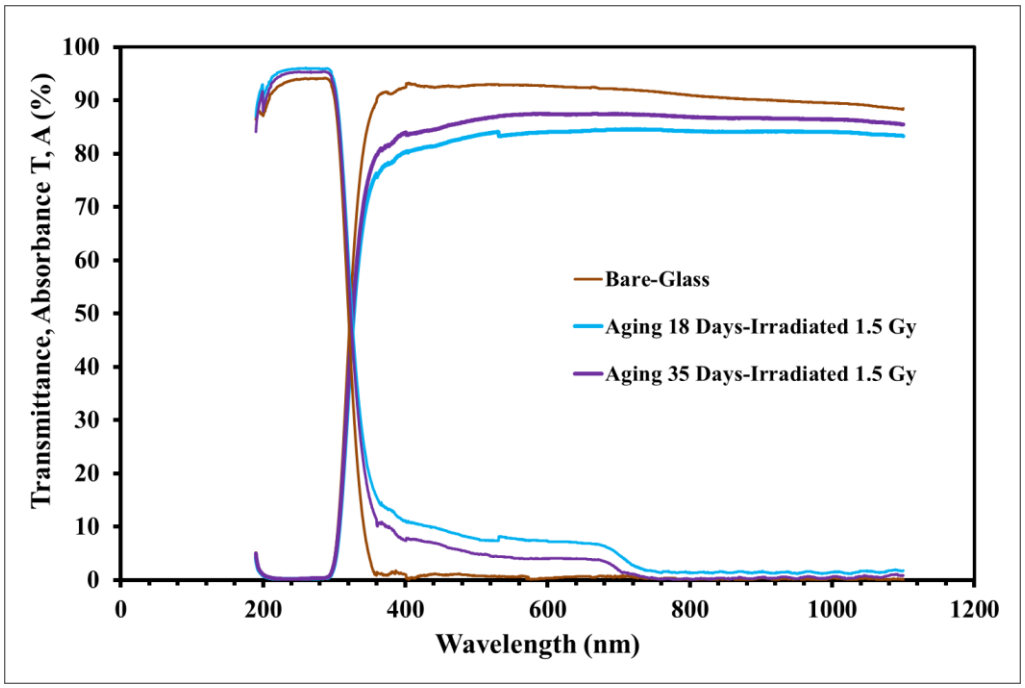

Figure 4.72 : Optical transmittance and absorbance spectra of 1.5 Gy absorbed dose CIGS thin-film.

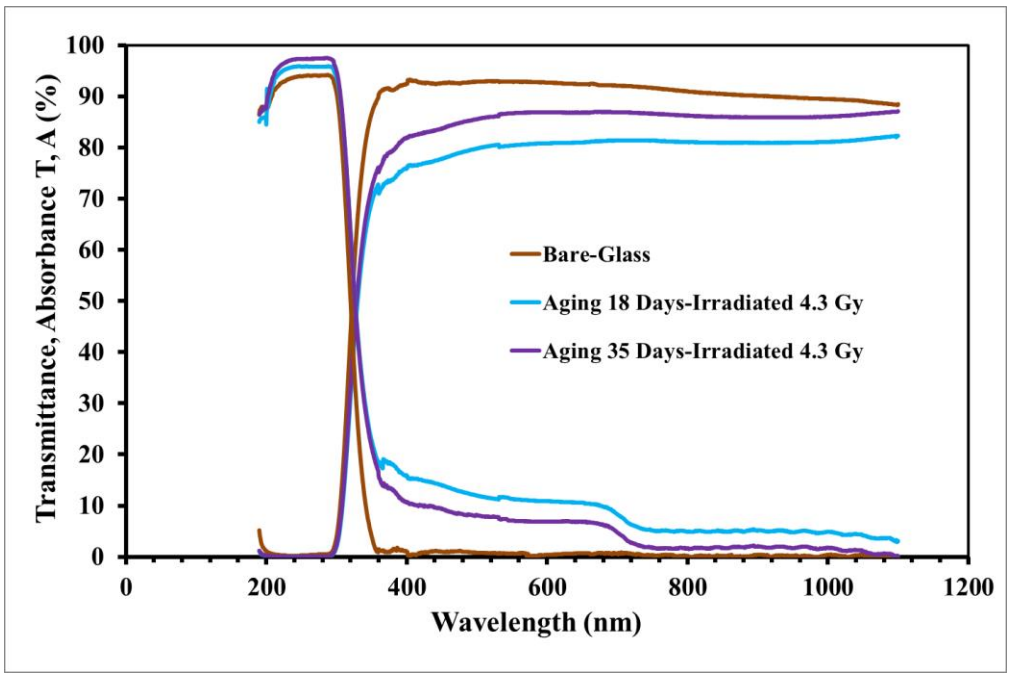

Figure 4.73 : Optical transmittance and absorbance spectra of 4.3 Gy absorbed dose CIGS thin-film.

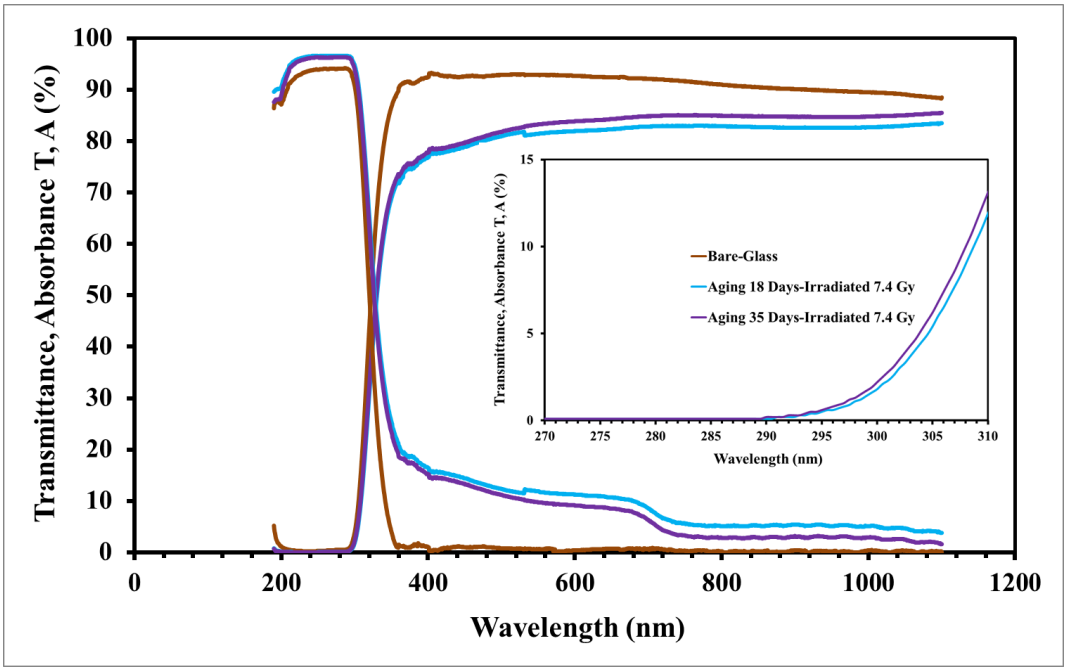

Figure 4.74 : Optical transmittance and absorbance spectra of 7.4 Gy absorbed dose CIGS thin-film.

The CIGS thin-films with the higher irradiated absorbed dose level at 7.4 Gy were non-absorbing beyond ~ 289.5 nm in the UV range (Figure 4.74).

The optical parameters of thin-films such as absorption coefficient (α), extinction coefficient (k) and refractive index (n) were calculated for the photon energy of 1.25, 2.25 and 3.54 eV (Table 4.16).

Table 4.16 : The calculated optical parameters of the unirradiated and irradiated CIGS thin-film of different aged solution.

Samples	Wavelength (nm)	Photon Energy (eV)	Absorption Coeff. α (cm^{-1})	Extinction Coeff. (k)	Refractive Index (n)
18 days aged-Unirrad.	992	1.25	279.02	0.002	1.94
	550	2.25	804.72	0.004	1.68
	350	3.54	5,782.19	0.016	1.85
18 days aged-Unirrad.	992	1.25	1,009.82	0.01	2.12
	550	2.25	5,556.47	0.02	1.75
	350	3.54	24,600.63	0.07	1.68
35 days aged-Unirrad.	992	1.25	1,758.53	0.01	2.19
	550	2.25	9,631.04	0.04	1.74
	350	3.54	28,927.43	0.08	1.71
18 days aged-Irradiated 1.5 Gy	992	1.25	1,917.44	0.02	2.22
	550	2.25	11,150.24	0.05	1.75
	350	3.54	29,458.44	0.08	1.59
35 days aged-Irradiated 1.5 Gy	992	1.25	721.29	0.01	2.13
	550	2.25	6,016.83	0.03	1.78
	350	3.54	22,844.79	0.06	1.70
18 days aged-Irradiated 4.3 Gy	992	1.25	7,042.01	0.06	2.14
	550	2.25	16,438.53	0.07	1.68
	350	3.54	35,598.46	0.10	1.59
35 days aged-Irradiated 4.3 Gy	992	1.25	2,304.21	0.02	2.06
	550	2.25	9,838.87	0.04	1.57
	350	3.54	32,488.42	0.09	1.47
18 days aged-Irradiated 7.4 Gy	992	1.25	7,337.79	0.06	2.00
	550	2.25	17,055.60	0.07	1.53
	350	3.54	39,409.68	0.11	1.28
35 days aged-Irradiated 7.4 Gy	992	1.25	4,065.40	0.03	2.05
	550	2.25	13,768.87	0.06	1.60
	350	3.54	36,228.21	0.10	1.44

The CIGS thin-films have the allowed direct energy band gap for unirradiated and irradiated states. Optical energy band gap, E_g for allowed direct transition was determined by extrapolating the linear part of $(\alpha h\nu)^2$ versus hν plot. There is a significant decrease in energy band gap of CIGS thin-films with the increase of the radiation absorbed dose (Figure 4.75). Beta irradiation causes a significant decrease of energy band gap of CIGS thin-film. The energy band gaps of 18 Days and 35 Days elapsed time are 1.76 eV and 1.72 eV, respectively.

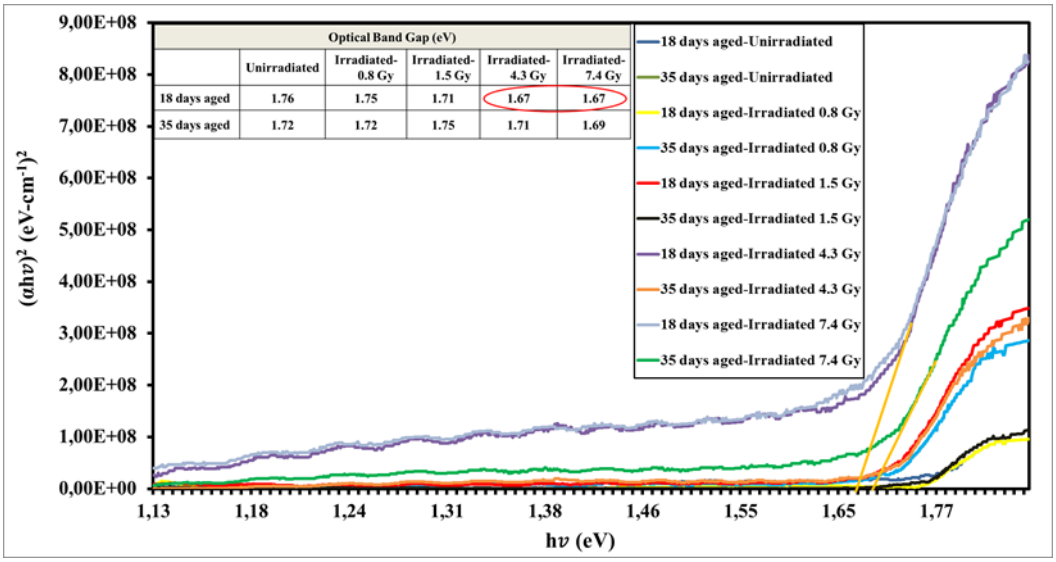

Figure 4.75 : The variation of optical energy band gap with the increase of radiaton absorbed dose.

To distinguish the energy band gap extrapolatings Figures 4.76 - 4.78 present optical energy band gap of unirradiated and 18 days of different absorbed radiation dose and 35 days of different absorbed radiation dose.

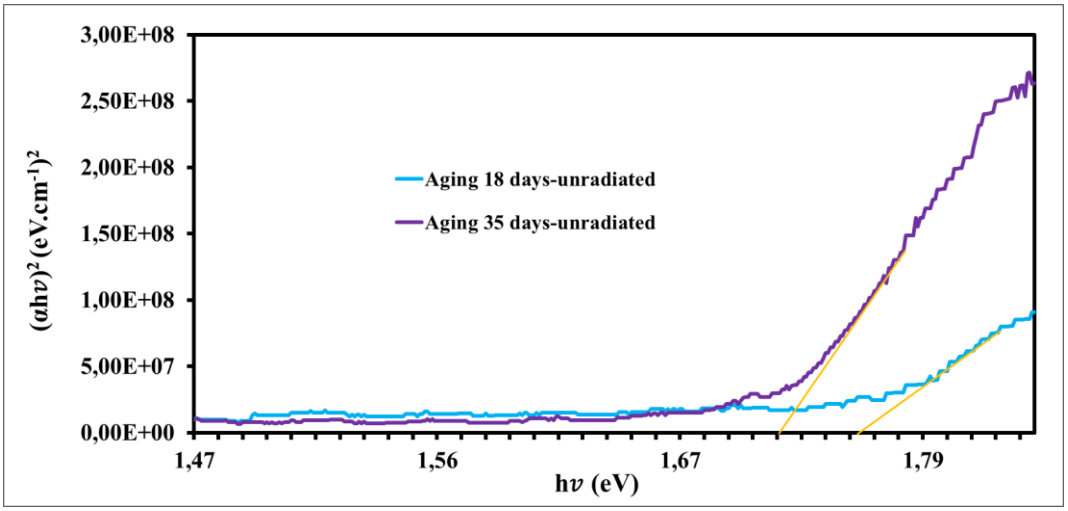

Figure 4.76 : The variation of optical energy band gap of unirradiated 18 days and 35 days aged thin-films.

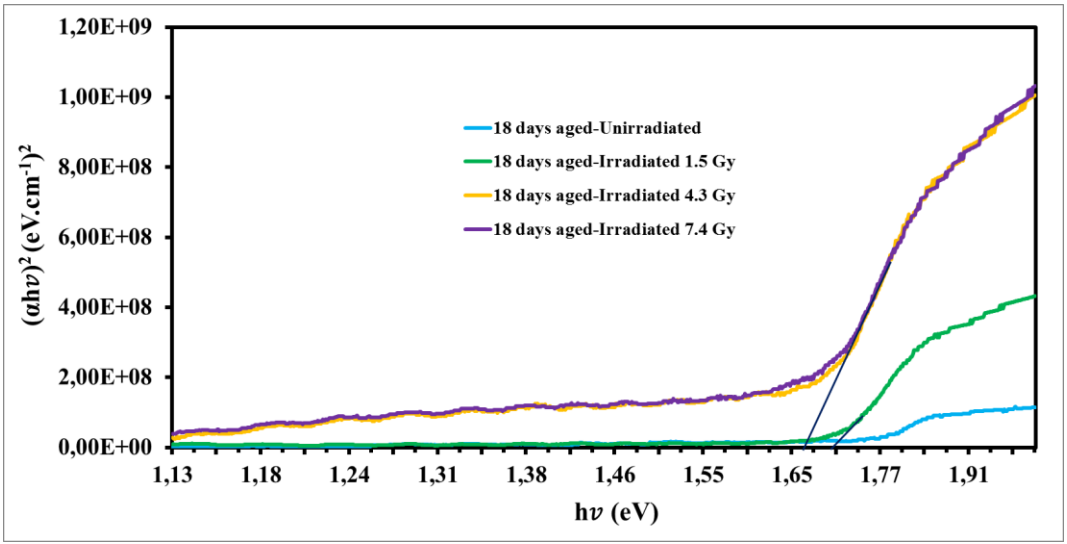

Figure 4.77 : The variation of optical energy band gap of 18 days aged thin-films with the increase of radiaton absorbed dose.

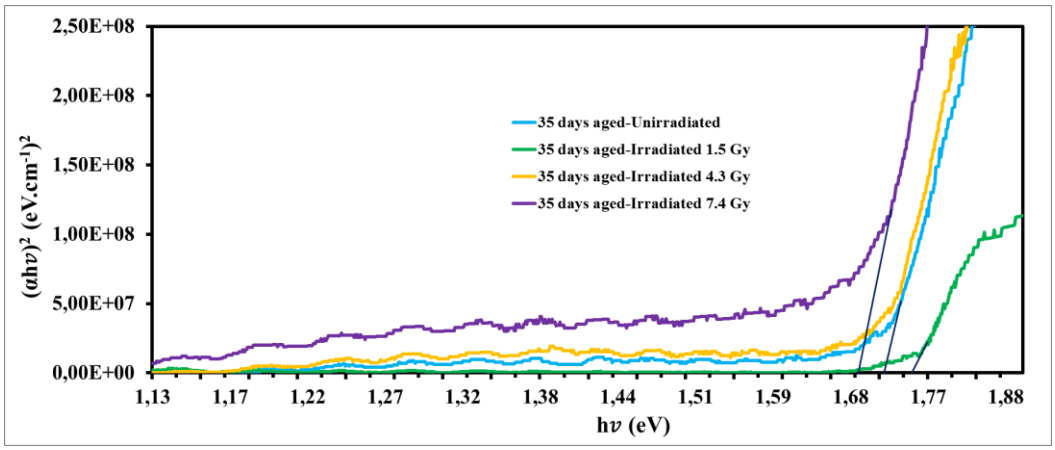

Figure 4.78 : The variation of optical energy band gap of 35 days aged thin-films with the increase of radiaton absorbed dose.

Figure 4.79 - 4.81 present the absorption coefficient of Cu(In,Ga)Se_2 thin-films with function of wavelength for 18 and 35 days aging of different absorbed doses. In each figure the increase of the absorption coefficient can be seen definitively.

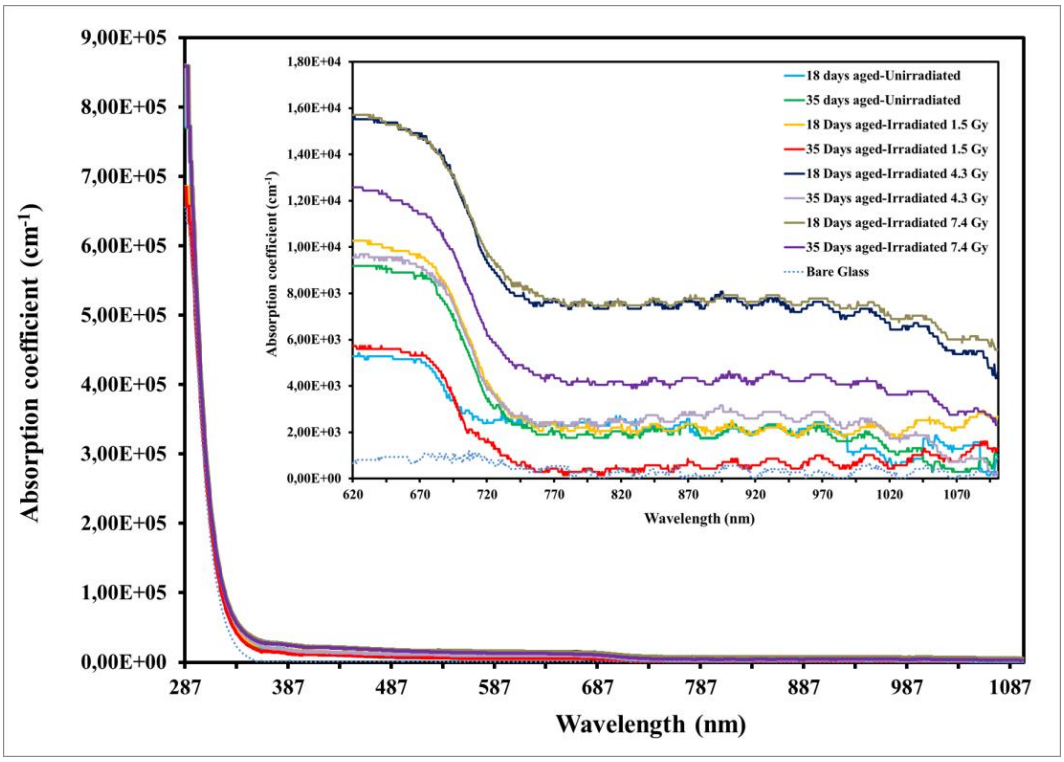

Figure 4.79 : Absorption coefficient of $Cu(In,Ga)Se_2$ thin-films with function of wavelength for 18 and 35 days aging of different absorbed doses.

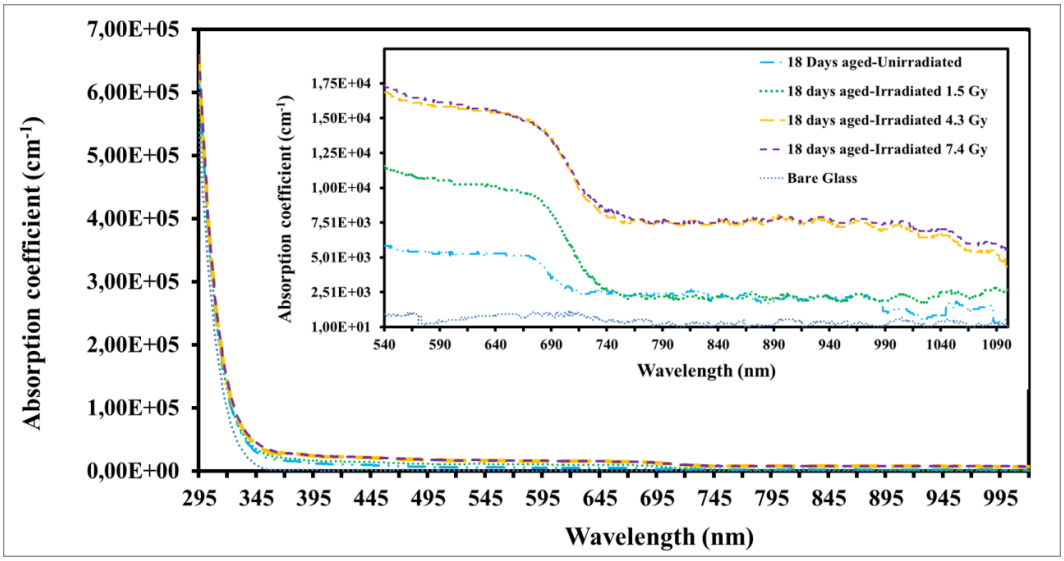

Figure 4.80 : Absorption coefficient of $Cu(In,Ga)Se_2$ thin-films with function of wavelength for 18 days aging of different absorbed doses.

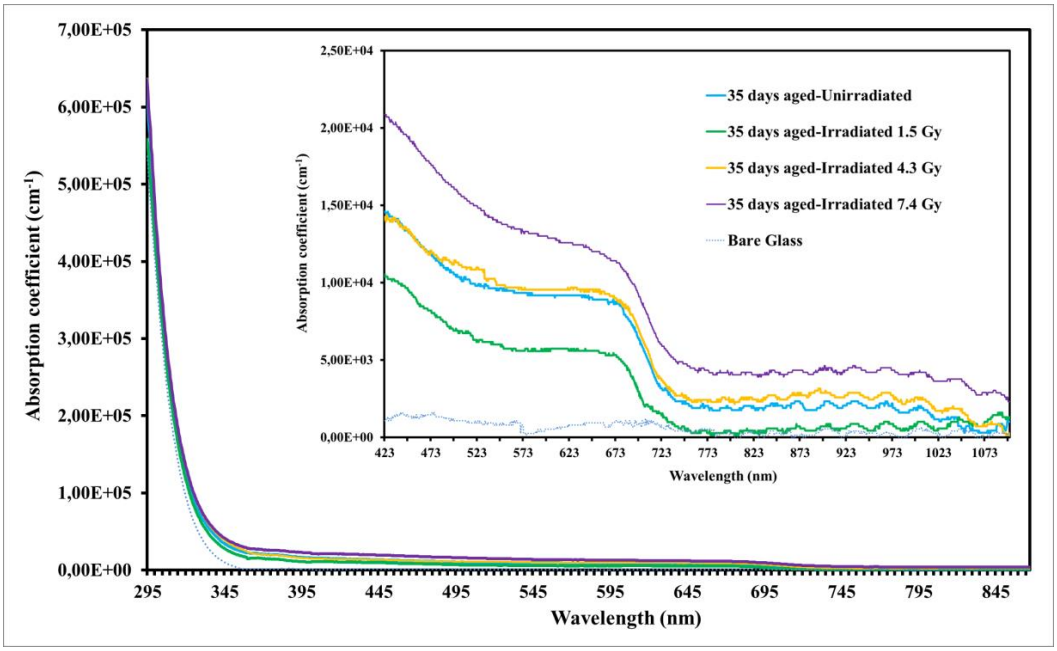

Figure 4.81 : Absorption coefficient of $Cu(In,Ga)Se_2$ thin-films with function of wavelength for 35 days aging of different absorbed doses.

4.2.2.3 Electrical characterizations

Sheet resistance measurements were carried out on all the samples and it was observed that the beta irradiation improved the conductivity of the thin-films. Due to the very thin-film in the nano-crystallite structure the resistance were not detected in most of the samples. Nevertheless, the basic conclusion was taken under the same physical measurement comditions for all the samples. The conductivity of the 35 days aged sample was calculated as $12.722x10^3$ $(\Omega\text{-cm})^{-1}$. The sheet resistance was not detected in the 35 days aged unirradiated sample. This shows the change in the conductivity was performed with the irradiation effect.

5. CONCLUSIONS

CIGS thin-films were deposited on soda-lime silicate glass substrates by the conventional sol-gel dip coating technique. Sol-gel technique is used to make contribution for the improvement of the cost-effective polycrystalline, which is a non-vacuum technology involving cheap equipment and lower temperature. CIGS solution was prepared via the sol–gel route employing diethanolamine, terpineol, ethyl-cellulose and hydrochloric acid.

The thin-film was grown via sol-gel experimental technique that the recipe of the sol was developed during this study. Besides, the production parameters were determined and the effect of beta irradiation on the CIGS thin-films were investigated systematically to obtain optical transparent CIGS thin-films and optimum electrical conductivity. As the CIGS layer is the absorber layer of the solar cell, the energy is required to be absorbed in all solar spectrum. So that, the semiconductor with the lower band gap is needed to be selected in this study. The energy band gap of the CIGS films is determined between 1,50-1,75 eV. The results indicate that the transparent CIGS thin-films derived by sol-gel process can be good candidates for the applications in optoelectronic devices.

The suitable pH-value of the solution for the optimum use of CIGS thin-film as a potential absorber material was determined. There was a match between electrical conductivity at the range of ~ 1.5 – 2.0 pH-value and optical transmittance at ~ 1.0 - 1.5 pH. The increase of pH-value ~ 2 contributes the noticeable increase of the electrical conductivity with a value of $8{,}69 \times 10^{2}$ $(\Omega\text{-cm})^{-1}$. The lowest optical band gap value is obtained at 2 pH-value with 1.24 eV. The favorable energy band gap between 1.2 - 1.6 eV was determined by considering the optical absorbance as a result of the fixing the pH-value of the CIGS solution at ~ 1.5 - 2.0 pH.

The sol-gel derived CIGS thin-films with determined thickness were thermally treated at different temperatures from 135 °C up to 200 °C with a colloidal solution prepared in an air ambiance under the standard laboratory conditions and under the inert gas atmosphere. The CIGS thin-films deposited from the colloidal solution

prepared under argon gas exhibited from amorphous structure to quasi-amorphous structure. While producing colloidal solution of CIGS under argon gas, the bonding of oxygen from air is inhibited.

XRD patterns of diffraction planes of CIGS thin-film presented principally the results of very thin-film similar with halo of amorphous material. The quasi-amorphous structure is determined slightly at very thin-film with 80 ± 5 nm thickness. The results indicate that the thicker CIGS film can give more crystalline structure which can be further to this study to examine the crystall structure.

The CIGS thin-films were exposured to beta particles of the Sr-90 radioisotope source. The beta irradiation was carried out to evaluate the cumulative dose effect on the CIGS thin-films having different thicknesses and with different aged elapsed time of colloidal solution.

Beta irradiation leads to variations in optical and electrical properties of CIGS thin-films, causes microstructural changes. The variations in structural, optical and electrical properties were considered according to the absorbed dose level. Hence, it is necessary to evaluate the effect of aggressive radiation environment at transparent conductive CIGS thin-film.

The observed effects in electrical resistivity are attributed to beta irradiation-induced formation of defects in the CIGS thin-film structure. The blue shift of absorption edge was improved by beta irradiation with the reduced of the elapsed time of colloidal solution and the increased of thickness.

The optical transition mechanism of CIGS thin-film was effected due to the radiation-absorbed dose. The optical transmittance of the thin-film decreased as the optical absorbance increased depending on the charge trapping of radiolytic-dissociation of molecules by radiation and the formation of defect centers and radiolytic electrons or holes. The emission of beta particles by Sr-90 source causes trapping at the holes of the film structure. There is a decrease in the optical transmission and the optical energy band gap of the CIGS thin-film. The creation of the induced colour centers leads to terminate the service life of the thin-films due to the creation of the exposure damages. As beta irradiation generates the colour centers

indirectly way in the structure with knock-on process there is an improvement of the optical density due to the creation of new colour centers by beta irradiation treatment.

The crystallite size of the CIGS thin-films became smaller with exposing to beta irradiation. On the other side, the beta irradiation improved conductivity. Although, the larger grain sizes reduce grain boundary scattering and improve conductivity, this detected result in this thesis can be associated with the defects formed by beta irradiation. Electrons emitted from Sr-90 radioisotope created Cu-related defects in CIGS thin-film. Hence, there was an increase in effective acceptor density. The types of defects, namely Cu, Ga, and Se Frenkel-pairs in CIGS were simultaneously generated by electron irradiation. These defects in CIGS solar cells induced by electrons and electrons increased the effective acceptor density. Electrons reduced the electrical resistivity as a result of the generated Frenkel-pairs in CIGS thin-film. The EDS analysis were conforming this consequences with the increase of the amount of Cu-related defects.

The irradiated samples were investigated to determine the changes in the electrical resistivity. The sheet resistance was measured for the samples of ~ 9 Gy irradiated absorbed dose. CIGS thin-film of 11 layers irradiated sample has the highest conductivity value with 21.897×10^{3} $(\Omega\text{-cm})^{-1}$.

REFERENCES

[1] **Singh, U. P. and Patra, S. P.** (2010). Progress in Polycrystalline Thin-Film Cu(In,Ga)Se_2 Solar Cells, *International Journal of Photoenergy Review*, Article ID 468147, doi:10.1155/2010/468147.

[2] **Nelson, V. C.** (2011). *Introduction to Renewable Energy*, CRC Press Taylor & Francis Group, USA, ISBN: 978-1-4398-3449-7.

[3] **Solanki, C. S.** (2011). *Solar Photovoltaics-Fundamentals, Technologies and Applications*, PHI Learning (second ed.), New Delhi, 978-8-120-34386-3.

[4] **Bruton, T. M.** (2002). General trends about photovoltaics based on crystalline silicon, *Solar Energy Materials and Solar Cells*,72, 1–4, P. 3–10.

[5] **Cox, A.** (2012). Solar-grade silicon at low cost, *University of Cambridge Research*, England.

[6] **Valderrama, R. C., Sebastian, P. J., Enriquez, J. P., Gamboa, S. A.** (2005). Photoelectrochemical characterization of CIGS thin-films for hydrogen production, *Solar Energy Materials & Solar Cells*, 88, 145–155.

[7] **Baydoğan, N., Matur, U. C., Akyol, Ş., Çimenoğlu, H.** (2014). Investigation of Electrical Properties of CIGS Thin-Films Derived by Sol-Gel Process, *TMS 2014 : 143rd The Minerals, Metals and Materials Society, Annual Meeting & Exhibition -Supplemental Proceedings*, pp.379-381, February 16-20, 2014 San Diego, California, USA.

[8] **Scheer, R., Schock, H. W.** (2011). *Chalcogenide photovoltaics:physics, technologies and thin-film devices*, Wiley-VCH, Weinheim, Germany.

[9] **Green, M. A., Emery, K., Hishikawa, Y., Warta, W.** (2011). Solar cell efficiency tables (version 37), *Progress In Photovoltaics: Research And Applications*, 19, 84–92.

[10] **Lin, G. J., Bi, J., Song, M., Liu, J., Xiong, W., Huang, M.** (2013). III-V Multi-Junction Solar Cells Optoelectronics, *Advanced Materials and Devices*, Prof. Sergei Pyshkin (Ed.), ISBN: 978-953-51-0922-8, InTech, DOI: 10.5772/50965.

[11] **Akyol, S., Baydogan, N., Çimenoglu, H.** (2015). Beta Irradiation Effect on Cu(In,Ga)Se_2 Thin-Films, *Defect and Diffusion Forum*, 365, 249-254, doi: 10.4028/www.scientific.net/DDF.365.249

[12] **Hergert, F.** (2007). Chemical Formation Reactions for Cu(In,Ga)Se_2 and Other Chalcopyrite Compounds-an in-situ X-ray Diffraction Study and Crystallographic Models, *Ph.D. Thesis*, Friedrich-Alexander University, Erlangen-Nürnberg.

[13] **Karaağaç, H.** (2010). Electrical, Structural And Optical Properties of $AgGaSe_{2-x}S_x$ Thin-films Grown By Sintered Powder, *Ph.D. Thesis*, METU, Ankara.

[14] **Jackson, P., Hariskos, D., Lotter, E., Paetel, S., Wuerz, R., Menner, R., Wischmann, W., Powalla, M.** (2011). New world record efficiency for $Cu(In,Ga)Se_2$ thin-film solar cells beyond 20%, *Progress in Photovoltaics*: *Research and Applications*, 19, 894–897.

[15] **Nishiwaki, S., Siebentritt, S., Walk, P., Lux-Steiner, M. C.** (2003). A Stacked Chalcopyrite Thin-film Tandem Solar Cell with 1.2 V Open-Circuit Voltage, *Progress in Photovoltaics : Research and Applications*, 11(4), 243-248, DOI:10.1002/pip.486.

[16] **Park, M. G., Ahn, S. J., Yuna, J. H., G., Jihye, Choa, A., Ahna, S. K., Shina, K., Namb, D., Cheongb, H., Yoona, K.** (2012). Characteristics of $Cu(In,Ga)Se_2$ (CIGS) Thin-films Deposited by a Direct Solution Coating Process, *Journal of Alloys and Compounds*, 513, 68– 74.

[17] **Brémaud, D. J. L.** (2009). Investigation and Development of CIGS Solar Cells on Flexible Substrates and with Alternative Electrical Back Contacts, *Ph.D. Thesis*, ETH Zurich, Switzerland.

[18] **Matur, U. C., Akyol, Ş., Baydoğan, N., Çimenoğlu, H.** (2014). The Characteristic Properties of Se Doped CuGa Thin-Films, *ISSTC 2014* : International Semiconductor Science & Technology Conference, Istanbul, Turkey, pp. 153.

[19] **Chung, Y. D., Cho, D. H., Chung, Y. D., Cho, D. H., Park, N. M., Lee, K. S., Kim, J.** (2011). Effect of annealing on $CdS/Cu(In,Ga)Se_2$ thin-film solar cells, *Current Applied Physics*, 11, 65-67.

[20] **Tolan, G.J., Chau, N.B., Heavens, S. N., Dharmadasa, I. M.** (2007). Development of p, i and n-type $CuInGa(Se_2)$ layers for applications in thin-film solar cells, Solar Energy Group, Materials & Engineering Research Institute, *22nd European Photovoltaic Solar Energy Conference and Exhibition*, Milan, Italy.

[21] **Akyol, Ş., Matur, U.C., Baydoğan, N., Çimenoğlu, H.** (2015). Effects of Production Parameters on Characteristic Properties of CIGS Thin-Film Derived by Sol-Gel Process, *Energy Systems and Management*, Springer, Switzerland, pp. 199-207, ISBN:978-3-319-16023-8, DOI:10.1007/978-3-319-16024-5_19.

[22] **Zhou, H., Hsu, W. C., Duan, H. S., Bob, B., Yang, W, Song, T. B., Hsu, C. J., Yang, Y.** (2013). CZTS nanocrystals: a promising approach for next generation thin-film photovoltaics, *Energy Environmental Science*, 6, 2822–2838, DOI:10.1039/c3ee41627e.

[23] **Zepf, V., Simmons, J., Reller, A., Ashfield, M., Rennie, C.** (2014). *Materials Critical to the Energy Industry: an Introduction*, BP p.l.c (second ed.), London, United Kingdom, ISBN:978-0-9928387-0-6.

[24] **Jaffe, B. and Price, J.** (2010). *Critical Elements for New Energy Technologies*, MIT (Massachusetts Institute of Technology) Energy Initiative Workshop Report.

[25] **Gschneidner, K. A.** (2015). The Rare Earth Crisis—The Supply/Demand Situation for 2010–2015, *Material Matters*, 6(2).

[26] **Harper, C. A.** (2003). *Electronic materials and processes handbook*, McGraw-Hill (third ed.), New York.

[27] **Kasap, S. O.** (2006). *Principles of electronic materials and devices*, McGraw-Hill (third ed.), Boston, ISBN:0-07-29579-1.

[28] **Askeland, D. R., Wright, W. J.** (2014). *Essentials of materials science and engineering*, University of Missouri, Rolla, Emeritus and Bucknell University, Stanford (third ed.), USA, ISBN:978-1-11157685-1.

[29] **Smith, W. F.** (1996). *Principles of materials science and engineering*, McGraw-Hill (third ed.), USA, ISBN:0-07-114717-9.

[30] **Grahn, T. H.** (1999). *Introduction to Semiconductor Physics*, World Scientific Publishing, Singapore, p2-3, ISBN:981-02-3302-7.

[31] **Smets, A.** (2015). ET3034TUx Solar Energy Course Notes, *Delft University of Technology*.

[32] **Nikijoo, H., Uehara, S., Emfietzoglou, D.** (2012). *Interaction of Radiation with Matter*, CRC Press, New York, p.45, ISBN:978-1-4398-5357-3.

[33] **Doğu, D.** (2012). The Photocatalytic Activity of Praseodymium Doped Titanium Dioxide, *Ph.D. Thesis*, METU, Ankara.

[34] **Möller, H. J.** (1993). *Semiconductors for Solar Cells*, Artech House, London, ISBN 0-89006-574-8.

[35] **Singh, Y.**, (2009). *Semiconductor Devices*, I. K. International Pvt Ltd., New Delhi.

[36] **Hummel, R. E.**, (2010). *Electronic Properties of Materials*, Springer (Fourth Edition), New York, ISBN:978-1-4419-8163-9.

[37] **Kondarides, I. D.**, (2010). *Photocatalysis*, *Encyclopedia of Life Support Systems (EOLSS)*, Developed under the Auspices of the UNESCO, EOLSS Publishers, Oxford, UK

[38] **Barrett, C. S. and Massalski, T. B.** (1980). *Structure of Metals*, Pergamon Press (third revised ed.), Oxford, UK.

[39] **Chen, S., Gong, X. G., Walsh, A., Wei, S. H.** (2009). Electronic structure and stability of quaternary chalcogenide semiconductors derived from cation cross-substitution of II-VI and I-III-VI_2 compounds, *Physical Review B*, 79, 165211

[40] **Shay, J. L. and Wernick, J. H.** (1975). *Ternary Chalcopyrite Semiconductors: Growth, Electronic Properties and Applications*, Pergamon Press, Oxford, UK.

[41] **Rockett, A. and Birkmire, R. W.** (1991). $CuInSe_2$ for Photovoltaic Applications, *Journal of Applied Physics*, 70(7), 81.

[42] **Schock, H. W.** (1996). Thin-film photovoltaics, *Applied Surface Science*, 92, p.606-616.

[43] **Soni, A., Gupta, V., Arora, C. M., Dashora, A., Ahuja, B. L.** (2010). Electronic structure and optical properties of $CuGaS_2$ and $CuInS_2$ solar cell materials, *Solar Energy*, 84, 1481–1489.

[44] **Karaagaç, H. and Parlak, M.** (2010). Investigation of physical properties of quaternary $AgGa_{0.5}In_{0.5}Te_2$ thin-films deposited by thermal evaporation, *Journal of Alloys and Compounds*, 503, 468–473.

[45] **Chen, S., Gong, X. G., Wei, S. H.** (2007). Band Structure anomalies of the chalcopyrite semiconductors $CuGaX_2$ versus $AgGaX_2$ (X=S and Se) and their alloys, *Physics Review B 75*, 205209.

[46] **Schmidt, S. S.** (2011). Microscopic properties of grain boundaries in $Cu(In,Ga)Se_2$ and $CuInS_2$ thin-film solar cells studied by transmission electron microscopy, *Ph.D. Thesis*, Helmholtz Zentrum Berlin Institut für Technologie, Berlin.

[47] **Kodigala, S. R.** (2010). *$Cu(In_{1-x}Ga_x)Se_2$ Based Thin-Film Solar Cells*, Elsevier, The Netherlands, ISBN:978-0-12-373697-0.

[48] **Green, M. A., Baillie, A. H., Snaith, H. J.** (2014). The emergence of perovskite solar cells, *Nature Photonics Review*, 8, 506–514, doi:10.1038/nphoton.2014.134.

[49] **Chuang, C. L.** (2011). Method of Preparing Sol-Gel Solution for CIGS Solar Cell, *United States Patent*, No: US 7,922,804 B2 dated 12.04.2011.

[50] **Abour-Ras, D., Kirchartz, T., Rau, U.** (2011). *Advanced Characterization Techniques for Thin-Film Solar Cells*, Wiley-VCH, Weinheim, Germany, ISBN:978-3-527-41003-3.

[51] **Roedern, B.** (2007). National Solar Technology Roadmap: CIGS PV, *Solar Energy Technologies Program*, U.S. Department of Energy, Management Report, NREL/MP-520-41737.

[52] **Rahaman, M. N.** (2005). *Ceramic Processing & Sintering*, Taylor & Francis e-Library (second ed.), New York, USA, p248.

[53] **Wright, J. D. and Sommerdijk, N. A. J. M.** (2001). *Sol-Gel Materials Chemistry and Application*, CRC Press, New York. p1,85,93.

[54] **Klein, L.C.** (1988). *Sol-Gel Technology for Thin-films, Fibers, Preforms, Electronics and Specialty Shapes*, Noyes Publications, New Jersey, p52, ISBN 0-8155-1154-X.

[55] **Tepehan, F.** (2011). *Physics of Thin-film Lecture Notes*, Physics Engineering Department, I.T.U., Istanbul.

[56] **Brinker, C. J., Scherer, G. W.** (1990). *Sol-Gel Science: the Physics and Chemistry of Sol-Gel Processing*, Elsevier (first ed.), San Diego.

[57] **Fahlman, B. D.** (2011). *Materials Chemistry*, Springer, Netherlands, page 22, ISBN:978-94-007-0692-7.

[58] **Uhlmann, D.R., Suratwala, T., Davidson, K., Boulton, J.M., Teowee, G.** (1997). Sol-gel derived coatings on glass, *Journal of Non-Crystalline Solids*, 218, 113-122.

[59] **Musat, V., Teixeira, B., Fortunato, E., Monteiro, R.C.C., Vilarinho, P.** (2004). Al-doped ZnO thin-films by sol-gel method, *Surface and Coatings Technology*, p.180-181, 659–662.

[60] **Cushing, B. L.,Kolesnichenko, V. L., O'Connor, C. J.** (2004). Recent Advances in the Liquid-Phase Syntheses of Inorganic Nanoparticles, *Chemical Reviews, Advanced Materials Research Institute*, University of New Orleans, New Orleans,104(9),3893−3946.

[61] **Kesim, M. T.** (2012). Sol-Gel Processing of Organically Modified ITO Thin-Films and Characterization of their Optoelectronic and Microstructural Properties, *M.Sc. Thesis*, M.E.T.U., Ankara.

[62] **Landau, L. D., Levich, B. G.** (1942). Dragging of a liquid by a moving plate, *Acta Physicochim U.R.S.S.*, 17, 42-54.

[63] **Brinker, C. J., Hurdi A. J., Ward, K. J.** (1988). *Ultrastructure Processing of Advanced Ceramics*, John Wiley& Sons, New York, p.223.

[64] **Mitzi, D. B.** (2008). *Solution processing of inorganic materials*, John-Wiley & Sons, New Jersey, USA.

[65] **Salama, R.** (2015). Lecture Notes, PhD Community Medicine, *Suez Canal University*, Egypt

[66] **Nikjoo, H., Uehara, S., Emfietzoglou, D.** (2012). *Interaction of Radiation with Matter*, CRC, Boca Raton, London, p.15,20, ISBN:978-14-39-85-35-73.

[67] **Rutherford, E.** (2007). *Radio-activity*, Juniper Grove, USA, ISBN:978-1-60355-058-1.

[68] **Turner, J. E.** (1995). *Atoms Radiation and Radiation Protection*, John-Wiley&Sons (second ed.), New York, p61.

[69] **Tavernier, S.** (2010). *Experimental Techniques in Nuclear and Particle Physics*, Springer, DOI 10.1007/978-3-642-00829-0_2.

[70] **Madison Safety Department's Chemical and Radiation Protection Office**, (2005). Radiation Safety for Radiation Workers, *University of Wisconsin*, ISBN: 0-9670043-4-9

[71] **Park, S. J., Lee, E., Jeon, H. S., Ahn, S. J., Oh, M. K., Min, B. K.** (2011). A comparative study of solution based CIGS thin-film growth on different glass substrates, *Applied Surface Science*, 258, 120-125.

[72] **Park, J. W., Choi, Y. W., Lee, E., Joo, O. S., Yoon, S., Min, B. K.** (2009). Synthesis of CIGS Absorber Layers via a Paste Coating, *Journal of Crystal Growth*, 311, 2621-2625.

[73] **Akyol, Ş., Baydoğan, N., Çimenoğlu, H., Matur, U. C., İzmirlioğlu, B.** (2014). The Effect of Annealing Temperature on CIGS Thin-Films, *ICEM 2014 : International Conference on Energy and Management*, June 5-7, 2014 Istanbul, Turkey.

[74] **Akyol, Ş., Matur, U. C., Baydoğan, N., Çimenoğlu, H.** (2014). Effect of pH on the Physical Properties of CIGS Thin-Films, *ISSTC 2014 : International Semiconductor Science & Technology Conference*, pp.154, January 13-15, 2014 Istanbul, Turkey.

[75] **Kesim, M. T.** (2012). Sol-Gel Processing of Organically Modified ITO Thin-Films and Characterization of their Optoelectronic and Microstructural Properties, *M.Sc. Thesis*, M.E.T.U., Ankara.

[76] **Baydoğan, N., Karacasu, O., Çimenoğlu H.** (2012). ZnO:Al thin-films used in ZnO:Al/p-Si heterojunctions, *Journal of Sol-Gel Science and Technology*, 61, 620–627.

[77] **Arvizu, D., Balaya, P.** (2010). IPCC, *Intergovernmental Panel on Climate Change*, Direct Solar Energy (Chapter 3), USA.

[78] **Instruction Manual** (2005). Innov-x Systems Alpha Series, X-ray Fluorescence Spectrometers, Version 2.1, *Innov-X Systems*, Inc., Woburn.

[79] **Candan, I.** (2009). Growth and Characterization of $CuIn_{1-x}Ga_xSe_2$ (CIGS) Thin-Films for Solar Cell Structures, *M.Sc. Thesis*, METU, Ankara.

[80] **Cullity, B. D.** (1956). *Elements of X-ray Diffraction*, Addison-Wesley Publishing (second ed.), USA.

[81] **Bragg, W. L.** (1915). The diffraction of X-rays by Crystals, *Nobel Lecture*.

[82] **Baydoğan, N., Özdemir, O., Çimenoğlu, H.** (2013). The improvement in the electrical properties of nano spherical ZnO:Al thin-film exposed to irradiation using a Co-60 radioisotope, *Radiation Physics and Chemistry*, 89, 20–27.

[83] **Manifacier, J. C., Murcia, M. D., Fillard, J. P.** (1977). Optical and Electrical Properties of SnO_2 Thin-films in Relation to their Stoichiometric Deviation and their Crystal-line Structure, *Thin Solid Films*, 41127–135.

[84] **Mott, N. F., Davis, E. A.** (1979). *Electronic processes in non-crystalline materials*, Clarendon (second ed.), Oxford University, New York.

[85] **Green, M.A.** (1982). *Solar Cells: Operating Principles, Technology, and System Applications*, Prentice-Hall, Inc., Englewood Cliffs, New Jersey.

[86] **Abass, W. H.** (2012). Annealing Effect on the Optical Properties of $(ZnO)_x(CdO)_{1-x}$ Films Obtained by Spray Pyrolysis, *Ibn Al-Haitham Journal for Pure and Applied Science*, 1, 25.

[87] **Çağlar, M., Ilıcan, S., Çağlar, Y., Yakuphanoğlu, F.** (2008). The effects of Al doping on the optical constants of ZnO thin-films prepared by spray pyrolysis method, *Journal of Material Science: Mater Electron*, 19, 704–708, DOI 10.1007/s10854-007-9386-2.

[88] **Bhat, J. S., Patil, A. S., Swami, N, Mulimani, B. G., Gayathri, B. R., Deshpande, N. G., Kim, G. H., Seo, M. S. and Lee, Y. P.** (2010). Electron Irradiation Effects on Electrical and Optical Properties of Sol-gel Prepared ZnO Films, *Journal Of Applied Physics*, 108, 043513.

[89] **Wai, M., Gong, X. G.** (2013). *Strontium Chemical Properties, Applications and Health Effects*, Nova Science Publishers, Inc., New York.

[90] **Draganic, I. G., Draganic, Z. D., Adloff, P. P.** (1993). *Radiation and Radioactivity on Earth and Beyond*, CRC Press (second ed.), Florida.

[91] **Baydogan, N. D., Tugrul, A. B.** (2006). Evaluation of the Optical Changes for a Soda–Lime–Silicate Glass Exposed to Radiation, *Glass Physics and Chemistry*, 32, 3, pp.309–314, ISBN:1087-6596, DOI:10.1134/S1087659606030096.

[92] **El-kameesy, S.U., El-Zaiat, S.Y., Hamid, A., El-Gamam, Y.** (2014), Neutron Irradiation Effects on Optical Properties of Sm-Doped Lead Borate Glasses, *Arab Journal of Nuclear Science and Applications*, 47(3), 124-129.

[93] **Magill, J., Galy, J.** (2005). *Radioactivity Radionuclides Radiation*, Springer, European Commission Joint Research Centre Institute for Transuranium Elements, ISBN: 3-540-21116-0.

[94] **Turner, J. E.** (2007). *Atoms, Radiation and Radiation Protection*, Wiley-VCH, Weinheim, ISBN:978-3-527-40606-7.

[95] **Zhao, J., Wang, P., Wei, L., Liu, Z., Zhang, J., Si, H., Mai, Y., Fang, X, Liu, X., Ren, D.** (2015). Enhanced Photocurrent by the Co-sensitization of ZnO with Dye and CuInSe Nanocrystals, *Dalton Transactions*, doi: 10.1039/C5DT01739D.

[96] **Carotenuto, G., Nicola, S. D., Palomba, M, Pullini, D, Horsewell, A, Hansen, T W , Nicolais, L.** (2012). Mechanical properties of low-density polyethylene filled by graphite nanoplatelets, *Nanotechnology*, 23, 485705, doi:10.1088/0957-4484/23/48/485705.

[97] **Database of computer program,** Windows-Qualitative Analysis Version 6.0.

[98] **Tüzemen, S., Gür, E.** (2007). Principal Issues in Producing New Ultraviolet Light Emitters Based on Transparent Semiconductor Zinc Oxide, *Optical Materials*, 30, 292–310.

[99] **Yu, Z., Yan, Y., Li, S., Zhang, Y., Yan, C., Liu, L., Zhang, Y., Zhao, Y.** (2013). Significant Effect of Substrate Temperature on the Phase Structure, Optical and Electrical Properties of RF Sputtered CIGS Films, *Applied Surface Science*, 264, 197–201.

[100] **Mahadeva, S. K., Fan, J., Biswas, A., Sreelatha, K. S., Belova, L., Rao, K. V.** (2013). Magnetism of Amorphous and Nano-Crystallized Dc-Sputter-Deposited MgO Thin Films Nanomaterials, 3(3), 486-497, doi:10.3390/nano3030486.

[101] **Eerikäinen, H.** (2005). Preparation of nanoparticles consisting of methacrylic polymers and drugs by an aerosol flow reactor method, *Ph.D. Thesis*, University of Helsinki, VTT PUBLICATIONS 563, ISBN:951-38-6444-8.

[102] **Behera, P. S., Rajesh, D., Karthikeyan, S., Sunandana, C.S., Mohan, D. B.** (2014). Study of Quasi-amorphous to Nanocrystalline Phase Transition in Thermally Evaporated $CuInS_2$ Thin-Films, *Journal of Material Research*, 29, 4.

[103] **Carotenuto, G., Nicola, S. D., Palomba, M, Pullini, D, Horsewell, A, Hansen, T W , Nicolais, L.** (2012). Mechanical properties of low-density polyethylene filled by graphite nanoplatelets, *Nanotechnology*, 23, 485705, doi:10.1088/0957-4484/23/48/485705.

[104] **Kang, S. H., Kim, Y. K., Choi, D. S., Sung, Y. E.** (2006). Characterization of Electrodeposited $CuInSe_2$ (CIS) Film, *Electrochimica Acta*, 51, 4433–4438.

[105] **Weijie, D.** (2013). Formation of High-Quality $BaSi_2$ Thin-Films with Large Photo Responsivity and the Structure Design for $BaSi_2$ Solar Cells, *Ph.D. Thesis*, University of Tsukuba, Japan.

[106] **Jamal, R., Osman, Y., Rahman, A., Ali, A., Zhang, Y., Abdiryim, T.** (2014). Solid-State Synthesis and Photocatalytic Activity of Polyterthiophene Derivates/TiO_2 Nanocomposites, Materials, 7(5), 3786-3801, doi:10.3390/ma7053786.

[107] **Chraibi, F., Fahoume, M., Ennaoui, A., Delplancke, J. L.** (2004). One Step Electrodeposition of $CuInSe_2$ Thin-films, *Moroccan Journal Of Condensed Matter*, 5, 1.

[108] **Wang, H. C., Wang, C. C., Feng, S.W., Chen, L. H., Lin, Y. S.** (2013). Synthesis of CIGS thin-film by solvothermal route, *Optical Materials Express*, 3,54-66.

[109] **Kawakita, S., Imaizumi, M, Ishizuka, S., Shibata, H., Niki, S., Okuda, S., Kusawake, H.** (2014). Influence of Electron Irradiation on Electroluminescence of Cu(In,Ga)Se_2 Solar Cells, *Japanese Journal of Applied Physics*, 53, 05FW08.

Url-1 <*http://ssd.phys.strath.ac.uk/index.php/Chalcopyrites*>, date retrieved 21.02.2015.

Url-2 <*http://archiv.aktuelle-wochenschau.de/2007/woche47/w47.html*>, date retrieved 21.11.2014, 14:15.

Url-3 <*http://www.nadetech.com/index.php/en/technologies*>, date retrieved 21.11.2014, 16:01.

Url-4 <*http://www.solgel.com/articles/Nov00/mennig.htm*>, date retrieved 21.11.2014, 15:28.

Url-5 <*http://web.princeton.edu/sites/ehs/osradtraining/radiationproperties/radiationproperties.htm*>, date retrieved 6.2.2015, 11:31.

Url-6 <*http://www.tesec-int.org/TechHaz-site%2008/Radiation-interaction.pdf*>, date retrieved 6.2.2015, 20:05.

Url-7 <*http://www.ehs.utoronto.ca/services/radiation/radtraining/module3.htm*>, date retrieved 7.2.2015, 09:31.

Url-8 <*http://www.physics.nus.edu.sg/pc2193/Experiments/INTERACTIONS%20WITH%20MATTER.pdf*>, date retrieved 10.2.2015, 14:11.

Url-9 <*http://serc.carleton.edu/research_education/geochemsheets/techniques/SEM.html*>, date retrieved 2.2.2015.

Url-10 <*http://www.fei.com/products/sem/quanta-sem/*>, date retrieved 5.2.2015.

Url-11 <*http://amrita.vlab.co.in/?sub=2&brch=190&sim=338&cnt=1*>, date retrieved 7.2.2015.

Url-12 <*http://www.nanoqam.uqam.ca/equipement.php?id=46&lang=en*>, date retrieved 9.2.2015.

Url-13 < *http://137.193.65.93/eng/theory.htm*>, date retrieved 1.3.2015.

Url-14 <*http://pveducation.org/pvcdrom/solar-cell-operation/quantum-efficiency*>, date retrieved 30.04.2015.

Url-15 <*http://shodhganga.inflibnet.ac.in:8080/jspui/bitstream/10603/3300/10/10_chapter%203.pdf*>, date retrieve 30.04.2015.

Url-16 <*http://shodhganga.inflibnet.ac.in:8080/jspui/bitstream/10603/3300/10/10_chapter%203.pdf*>, date retrieve 25.04.2015.

CURRICULUM VITAE

PUBLICATIONS, PRESENTATIONS AND PATENTS ON THE THESIS:

- **Akyol, Ş.**, Matur, U. C., Baydogan, N., Çimenoglu, H., (2015). Beta Irradiation Effect on Cu(In,Ga)Se_2 Thin-Films, *Defect and Diffusion Forum*, 365, 249-254, doi: 10.4028/www.scientific.net/DDF.365.249.

- **Akyol, Ş.**, Matur, U.C., Baydoğan, N., Çimenoğlu, H. (2015). Effects of Production Parameters on Characteristic Properties of CIGS Thin-Film Derived by Sol-Gel Process, *Energy Systems and Management*, Springer, Switzerland, pp. 199-207, ISBN:978-3-319-16023-8. doi:10.1007/978-3-319-16024-5_19.

- Matur, U. C., **Akyol, Ş.**, Baydoğan, N., Çimenoğlu, H. (2015). The Characteristic Behaviours of Sol-Gel Derived CIGS Thin-Films Exposed to the Specific Environmental Conditions, *Energy Systems and Management*, Springer, Switzerland, ISBN:978-3-319-16023-8. doi:10.1007/978-3-319-16024-5_17.

- Matur, U.C., **Akyol, Ş.**, Baydoğan, N., Çimenoğlu, H. (2015). The Optical Properties of CIGS Thin-Films Derived by Sol-Gel Dip Coating Process at Different Withdrawal Speed, *Elsevier Procedia - Social and Behavioral Sciences*, Article in press, doi: 10.1016/j.sbspro.2015.06.328.

- **Akyol, Ş.**, Matur, U. C., Baydogan, N., Çimenoglu, H. (2015). The Effect of Terpineol Addition on Characteristic Properties of the CIGS Thin-Film, *Elsevier Procedia - Social and Behavioral Sciences*, Article in press.

- Baydoğan, N., Matur, U.C., **Akyol, Ş.**, Çimenoğlu, H. (2014). Investigation of Electrical Properties of CIGS Thin-Films Derived by Sol-Gel Process, *TMS 2014:143rd The Minerals, Metals and Materials Society, Annual Meeting and Exhibition -Supplemental Proceedings*, pp. 379-381, February 16-20, 2014 San Diego, California, USA.

- **Akyol, Ş.**, Matur, U.C., Baydoğan, N., Çimenoğlu, H. (2014). Effect of pH on the Physical Properties of CIGS Thin-Films, *ISSTC 2014:International Semiconductor Science & Technology Conference*, pp. 154, January 13-15, 2014 Istanbul, Turkey.

- Matur, U.C., **Akyol, Ş.**, Baydoğan, N., Çimenoğlu, H. (2014). The Characteristic Properties of Se Doped CuInGa Thin-Films, *ISSTC 2014 International Semiconductor Science & Technology Conference*, pp. 153, January 13-15, 2014 Istanbul, Turkey.

- **Akyol, Ş.**, Baydoğan, N., Çimenoğlu, H., Matur, U.C., İzmirlioğlu, B (2014). Effect of Annealing Temperature on CIGS Thin-Films, *ICEM 2014:International Conference on Energy and Management*, pp. 125, June 5-7, 2014 Istanbul, Turkey.

- **Akyol, Ş.**, Baydoğan, N., Çimenoğlu, H., Matur, U.C. (2014). Effect of Film Thickness on the CIGS Thin-Films, *ICEM 2014:International Conference on Energy and Management*, pp.125, June 5-7, 2014 Istanbul, Turkey.

▪ Matur, U.C., **Akyol, Ş.**, Baydoğan, N., Çimenoğlu, H. (2014). Aging Effect of CIGS Solution on Optical and Electrical Properties, *ICEM 2014:International Conference on Energy and Management*, pp. 109, June 5-7, 2014 Istanbul, Turkey.

▪ Matur, U.C., **Akyol, Ş.**, Baydoğan, N., Çimenoğlu, H. (2014). Effect of Annealing Time on CIGS Thin-Films, *ICEM 2014:International Conference on Energy and Management* t, pp. 113, June 5-7, 2014 Istanbul, Turkey.

▪ Matur, U.C., **Akyol, Ş.**, Baydoğan, N., Çimenoğlu, H. (2014). İnsansız Hava Araçlarındaki CIGS İnce Filmlerin Ekonomik Bir Şekilde Üretimi, *HITEK 2014: 3. Ulusal Havacılıkta İleri Teknolojiler Konferansı*, 18-19 Haziran, 2014 Hava Harp Okulu, Istanbul, Turkey.

▪ Matur, U.C., **Akyol, Ş.**, Baydoğan, N., Çimenoğlu, H. (2015). The Production of Zno:Al/CIGS Heterojunction by Sol–Gel Dip Coating Technique, *9th International Physics Conference of the Balkan Physical Union-BPU9*, 24-27 August 2015, Istanbul University , Istanbul , Turkey (accepted for presentation).

▪ **Akyol, Ş.**, Matur, U. C., Baydoğan, N., Çimenoğlu, H. (2015). Production of Nano-Cu(In,Ga)Se_2 Film Solution Under Inert Gas Atmosphere, *9th International Physics Conference of the Balkan Physical Union-BPU9*, 24-27 August 2015, Istanbul University , Istanbul , Turkey (accepted for presentation).

Workshop

▪ 23rd European Workshop on Heterostructure Technology (HETECH 2014), 12-15 October 2014, Characterization of the Irradiated CIGS Thin-Film by Reactor Neutrons, Marburg, Germany.